Development of a novel LIBS-based Technique for Elemental Analysis and Harnessing Machine Learning for Real-time Applications using LIBS and Raman Spectroscopy

A thesis submitted to

University of Hyderabad

Towards partial fulfilment of the degree of

Doctor of Philosophy

in

Physics

By

Akash Kumar Tarai

(17ACPP01)

हैदराबाद विश्वविद्यालय
University of Hyderabad

प्रतिष्ठित संस्थान
INSTITUTION OF EMINENCE

Under the Supervision of

Prof. G. Manoj Kumar

Advanced Centre of Research in High Energy Materials (ACRHEM)

DRDO – Industry – Academia Centre of Excellence (DIA-CoE)

School of Physics, University of Hyderabad

Hyderabad, Telangana, India 500046

Feb 2024

Dedicated to

Bapa, Bou, Bhai & Pechikiri

Declaration

I, **Akash Kumar Tarai**, hereby declare that the work reported in this thesis entitled "**Development of a novel LIBS-based Technique for Elemental Analysis and Harnessing Machine Learning for Real-time Applications using LIBS and Raman Spectroscopy**" is original and has been carried out by me under supervision of **Prof. G. Manoj Kumar**, Professor in ACRHEM, School of Physics, University of Hyderabad, Hyderabad, Telangana, India, as per the Ph.D. ordinance of the University, which is also plagiarism free and the plagiarism statistics from the university librarian is enclosed. To my knowledge, no part of this thesis has been submitted for the award of a research degree or diploma from any other university. I hereby agree that my thesis can be deposited in Shodhganga/INFLIBNET.

Akash Kumar Tarai
Reg. No. 17ACPP01

Prof G. Manoj Kumar
Thesis Supervisor
ACRHEM, School of Physics
University of Hyderabad

Prof. G. MANOJ KUMAR
ACRHEM
DRDO Industry Academic
Centre of Excellence (DIA-COE)
School of Physics
University of Hyderabad
Hyderabad-500 046. Telangana, INDIA.

Prof. G. Manoj Kumar
Professor
Tel.: +91–40 2313 8837
Fax: +91–40 23012800
Email: manoj@uohyd.ac.in

ACRHEM, School of Physics
University of Hyderabad
Prof. C R Rao Road,
Gachibowli, Hyderabad
Telangana, India

Certificate

This is to certify that the thesis entitled **"Development of a novel LIBS-based Technique for Elemental Analysis and Harnessing Machine Learning for Real-time Applications using LIBS and Raman Spectroscopy"** being submitted to the University of Hyderabad by **Akash Kumar Tarai** (Regd. No. **17ACPP01**), for the award of the degree of **Doctor of Philosophy in Physics**, is a record of bonafide work carried out by him under my supervision and is free of plagiarism.

The thesis has not been submitted previously in part or in full to this or any other University or Institution for the award of any degree or diploma.

Prof. G. Manoj Kumar
Thesis Supervisor
Prof. G. MANOJ KUMAR
ACRHEM
DRDO Industry Academic
Centre of Excellence (DIA-COE)
School of Physics
University of Hyderabad
Hyderabad-500 046. Telangana, INDIA.

Krishnagopal Rao
02.02.2024

Director
ACRHEM
Director
ACRHEM

2/2/24

Dean
School of Physics
DEAN
School of Physics
University of Hyderabad
HYDERABAD - 500 046

Certificate

This is to certify that the thesis entitled **"Development of a novel LIBS-based Technique for Elemental Analysis and Harnessing Machine Learning for Real-time Applications using LIBS and Raman Spectroscopy"** being submitted to the University of Hyderabad by **Akash Kumar Tarai** (Regd. No. **17ACPP01**), for the award of the degree of **Doctor of Philosophy in Physics**, is a record of bonafide work carried out by him under my supervision and guidance. This thesis is free of plagiarism and has not been submitted previously in part or in full to this or any other University or Institution for the award of any degree or diploma.

Further, the student has the following publications before submission of the thesis for adjudication:

1. **Tarai, A. K.,** Rashkovskiy, S. A., & Gundawar, M. K. Simplified LIBS- based intensity-ratio approach for concentration estimation (SLICE): an approach for elemental analysis using laser induced breakdown spectroscopy. **Optics Express (In Press)**.
2. **Tarai, A. K.,** Junjuri, R., Dhobley, A., & Gundawar, M. K. (2023). Classification of human tooth using laser-induced breakdown spectroscopy combined with machine learning. **Journal of Optics**, 1-11.
3. **Tarai, A. K.,** & Gundawar, M. K. (2023). Raman spectroscopy combined with machine learning for the quantification of explosives in mixtures. **Journal of Optics**, 1-9.
4. **Tarai, A. K.,** Junjuri, R., Rashkovskiy, S. A., & Gundawar, M. K. (2022). Time- Dependent Intensity Ratio-Based Approach for Estimating the Temperature of Laser Produced Plasma. **Applied Spectroscopy**, 76(11), 1300-1306.
5. **Tarai, A. K.,** & Gundawar, M. K. (2022). Possibility of Plastic Discrimination using Picosecond Laser Induced Breakdown Spectroscopy. In 2022 Workshop on Recent Advances in Photonics (WRAP) (pp. 1-2). **IEEE**.
6. **Tarai, A. K.,** Junjuri, R., & Gundawar, M. K. (2021). Advances in applications of LIBS in India: A Review. **Asian Journal of Physics**, 30(6), 871-888.

The following courses have been taken as part of the course work:

Course No.	Course offered at	Title of the course	Credits	Pass/Fail
PY801	School of Physics	Research Methodology	4	Pass
PY802	School of Physics	Advanced Quantum Mechanics	4	Pass
PY803	School of Physics	Advanced Experimental Techniques	4	Pass
PY805	ACRHEM	Ultra Fast Optical Phenomena	4	Pass

Supervisor
Prof. G. Manoj Kumar
Professor
ACRHEM, University of Hyderabad
Hyderabad, India

Prof. G. MANOJ KUMAR
ACRHEM
DRDO Industry Academic
Centre of Excellence (DIA-COE)
School of Physics
University of Hyderabad
Hyderabad-500 046. Telangana, INDIA.

02.02.2024

Director
ACRHEM
University of Hyderabad
Hyderabad
India

Director
ACRHEM

2/2/24

Dean
School of Physics
University of Hyderabad
Hyderabad
India

DEAN
School of Physics
University of Hyderabad
HYDERABAD - 500 046

Acknowledgement

Profound gratitude and boundless appreciation are extended to the following individuals whose invaluable help and unwavering support have been instrumental in making this research possible.

Foremost, my heartfelt appreciation extends to my esteemed supervisor, **Prof. G. Manoj Kumar**, whose expertise, unwavering support, and consistent encouragement have not only facilitated my exploration of this topic but also enriched my academic and personal growth. His profound knowledge, meticulous guidance, and compassionate demeanour have been instrumental at every juncture of my doctoral journey, nurturing my analytical skills, refining my manuscript compositions, and enhancing my presentation acumen.

I express my gratitude to the current director, **Dr. V. Kameswara Rao**, and past directors of ACRHEM for their comprehensive support in all aspects toward the completion of this work. Additionally, I extend my thanks to the Dean of the School of Physics for their unwavering academic support.

I extend my heartfelt thanks to my doctoral committee members, **Prof. P Prem Kiran** and **Prof. Ashok Vudayagiri**, for their exemplary approach to problem-solving. Their ability to impart knowledge and skills with a straightforward approach has been both instructive and deeply inspirational to me.

I am profoundly grateful to **Prof. Sargey A. Rashkovskiy** of Tomsk State University, Russia, for his invaluable theoretical insights, and to **Dr. Narahara Chari Dingari** of Worcester Polytechnic Institute, USA, for their illuminating discussions on machine learning applications.

I extend my gratitude to **Prof. Koteswararao V. Rajulapati** of SEST for providing alloy samples and to Mr. Nandakishore for his assistance with sample preparation and hardness measurements. Gratitude also goes to Mr. Prashant, Centre for Nanotechnology for his support during the profilometer experiment.

I am deeply appreciative of my lab-mate, Arun Prakash, for his consistent assistance, as well as Dr. Rajendhar for his guidance. Special thanks to Dr. Lingamurthy, Dr. Samuel, Dr. Bharathi, and Dr. Reshma for their invaluable support in handling experimental systems.

I am indebted to Mr. Anubhab Sahoo of IIT Madras for his unconditional support and motivation throughout my Ph.D. journey.

My heartfelt appreciation extends to colleagues Dr. Prathap, Dr. Subrathu, Abinash, Arjun, Dr. Manikanta, Nagaraju, Chandan, and Supratik for their camaraderie and support.

Gratitude also flows to my friends Dr. Rudra, Jagmohan, Shashi, Dr. Mitesh, Dr. Atasi, Rashmi, Deepak, Sumit, Satya, Anurag, Jyoti, Rajkishore, Veeru, Dr. Shivaraju, Dinesh, Aishwarya, Rekha, Dr. Niladri, Dr. Hemadri, Dr. Ishwar, Bharath, Priya, and Papia for enriching my experiences at UoH campus.

I cherish the support of my friends Ms. Adyapuja and Late. Kaibalya for their unwavering encouragement.

I am profoundly grateful to my father, Mr. Abhiram Tarai, my mother, Mrs. Meenakshi Tarai, my brother, Mr. Anirudha Tarai, and my sister, Ms. Jyotirmayee Tarai, for their boundless love and unwavering support throughout every chapter of my life.

I extend my gratitude to all the faculty members and office staff of ACRHEM and the School of Physics for their support.

Special acknowledgment is given to the **Defence Research and Development Organisation (DRDO), Govt. of India**, for invaluable financial support. Finally, I express my gratitude to the **Institute of Eminence (IoE), University of Hyderabad** for providing International Travel Grant to participate in the LIBS2022 conference in Bari, Italy.

CONTENT

List of Figures

List of Tables

Abbreviations

AAS	Atomic Absorption Spectroscopy
ABS	Acrylonitrile butadiene styrene
ACRYLIC	Poly(methyl methacrylate)
AES	Atomic Emission Spectroscopy
AN	Ammonium Nitrate
ANN	Artificial Neural Network
AP	Ammonium Perchlorate
BPN	Boron Potassium Nitrate
CCD/CCDs	Charged Coupled Device /Charged Coupled Devices
CF-LIBS	Calibration-free LIBS
CL20	Hexanitrohexaazaisowurtzitane
CT	Czerny-Turner
CW/cw	Continuous wave
DFA	Discriminant Function Analysis
DL	Deep Learning
DNAN	2,4-Dinitroanisole
DNT	2,4-Dinitrotoluene
DSC	Differential Scanning Calorimetric
DTR	Decision Tree Regression
EDS	Electron Dispersive X-ray Spectroscopy
FN	False Negative
FP	False Positive
Fs/fs	Femtosecond
FTIR	Fourier Transform Infrared
H_2BTE	Diazomethane
HDPE	High-density polyethylene
HEMs	High Energy Materials
HGA	Harmonic Generation Assembly
HIP	High Impact Polystyrene
HMX	1,3,5,7-Tetranitro-1,3,5,7-tetrazocane
HV	Vickers Hardness Number
IB	Inverse Bremsstrahlung
ICA	Independent Component Analysis
ICCD	Intensified Charge-coupled Device
IEDs	Improvised Explosive Devices
IR	Infrared
kNN	k-nearest neighbours
LA-ICP-MS	Laser Ablation Inductively Coupled Plasma Mass Spectrometry
LASER	Light Amplification by Stimulated Emission of Radiation
LDA	Linear Discriminant Analysis
LDPE	Low-density polyethylene
LDs	Linear Discriminants
LHS	Left Hand Side
LIBS	Laser Induced Breakdown Spectroscopy

LIF	Laser Induced Fluorescence
LIP	Laser Induced Plasma
LOD/LoD	Limit of Detection
MD	Mahalanobis distance
ML	Machine Learning
MF	Manual feature selection
MLR	Multiple Linear Regression
MNT	Mononitrotoluene
MPI	Multiphoton Ionization
NA	Not Available
NCA	Nearest Component Analysis
Nd: YVO_4	Neodymium-doped yttrium orthovanadate
Nd:YAG	neodymium-doped yttrium aluminum garnet
NIR	Near Infrared
NIST	National Institute of Standards and Technology
Ns/ns	Nanosecond
NTO	Nitrotriazolone
PA	Polyamide
PBT	polybutylene terephthalate
PC	Polycarbonate
PCA	Principal Component Analysis
PCPP	polypropylene copolymer
PCs	Principal Components
PDPs	Plasma Decay Parameters
PE	Polyethylene
PET	Polyethylene terephthalate
PETN	Pentaerythritol tetranitrate
PLS-DA	Partial least square discriminant analysis
PLSR	Partial Least Square Regression
PMMA	Polymethylmethacrylate
POM	polyoxyethylene
PP	Polypropylene
PS	Polystyrene
Ps/ps	Picosecond
PTFE	Polytetrafluoroethylene
PU	Polyurethane
PVC	Polyvinylchloride
RBFNN	Residual Basis Function Neural Networks
RDX	1,3,5-trinitroperhydro-1,3,5-triazine
RF	Random Forest
RFR	Random Forest Regression
RHS	Right Hand Side
ROC	Receiver Operating Characteristic
SA	Self-absorption
SEM	Scanning Electron Microscopy
SIMCA	Soft Independent Modeling of Class Analogy

SLICE	Simplified LIBS-based Intensity-ratio approach for Concentration Estimation
SOM	self-organizing maps
TATB	Triaminotrinitrobenzene
TEM	Transverse Electromagnetic Mode
TN	True Negative
TNT	Trinitrotoluene
TP	True Positive
UA	Urea Nitrate
UV	Ultraviolet
VI	Variable Importance
VIS	Visible

Chapter 1

Introduction and Outline of Thesis

This chapter provides an introduction to spectroscopy, with a specific emphasis on two major techniques: Laser Induced Breakdown Spectroscopy (LIBS) and Raman Spectroscopy. The chapter aims to examine in detail these approaches, in order to uncover the underlying principles, technological breakthroughs, and many applications that define each spectroscopic methodology. This chapter concludes with an overview of the entire thesis and a summary of each individual chapter.

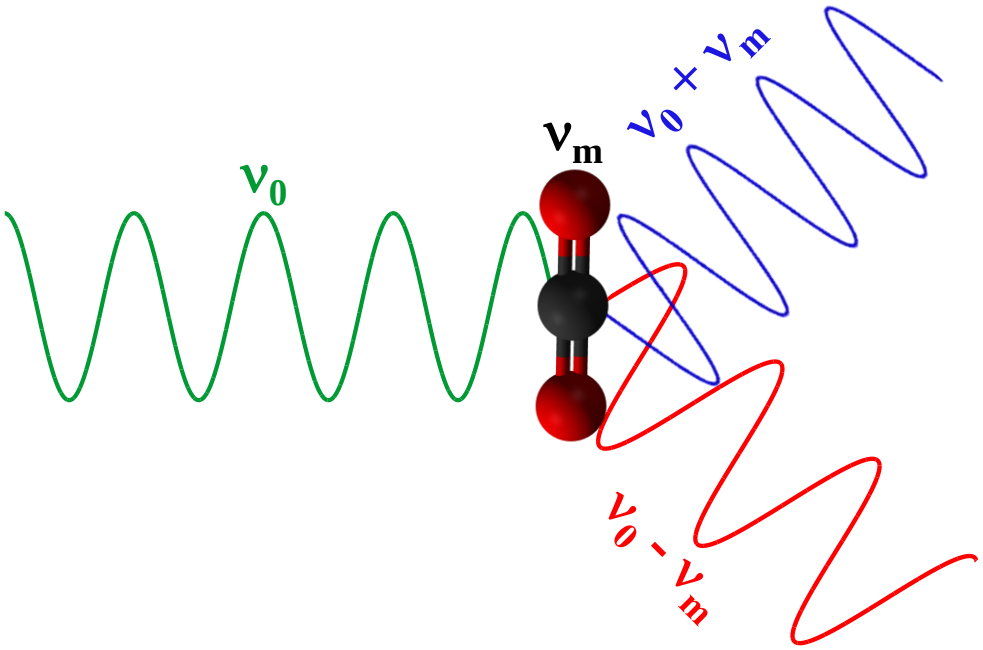

Spectroscopy is a scientific discipline that specifically investigates the interaction between electromagnetic radiation and matter. It involves the dispersion of light into its constituent colours and the measurement of absorbed or emitted radiation at specific wavelengths. The fundamental foundation of spectroscopy is the observation of light after the interaction with matter, i.e., when light encounters matter, it undergoes modifications of properties such as wavelength, intensity, or polarization. These modifications are due to the interaction of the molecules, atoms, electrons, or ions present in the material. The changes in the properties of light provide crucial insights into the material's chemical composition, molecular structures and various other physical properties. Therefore, spectroscopy is a very useful tool for the characterization of various materials and is widely used in many disciplines of science, including physics, chemistry, astronomy, biology, etc. Several spectroscopic techniques exhibit significant variations in their methodologies depending on the specific properties of interest of the material and the type of light source used. Some of the important spectroscopic techniques are Raman spectroscopy, fluorescence spectroscopy, atomic absorption spectroscopy (AAS), mass spectroscopy, infrared (IR) spectroscopy, laser induced breakdown spectroscopy (LIBS), etc.

1.1 Laser Induced Breakdown Spectroscopy (LIBS)

LIBS is an advanced analytical technique that offers real-time detection of elemental species. It is more convenient and versatile than other conventional methods because of its ability to identify and analyze various materials in any form with no or minimal sample preparation, and it is ideal for on-site analysis. LIBS is an atomic emission spectroscopy (AES) technique that employs a high-energy pulsed laser to generate laser-induced plasma (LIP). Due to its utilization of high-energy optical radiation for producing LIP, this method has several advantages compared to other conventional AES techniques that rely on adjacent physical devices (such as electrodes, coils, etc.) to generate vaporization/excitation sources like flames, arcs, sparks, etc.

The origins of LIBS can be traced back to the 1960s, just after the discovery of the laser, when researchers began studying LIP[1]. However, in the 1980s, LIBS began to get significant attention and development. In the early years, LIBS was focused on basic spectroscopic measurements and basic understanding of plasma formation dynamics. After that, LIBS was only used for the investigation of solid samples. Later, developments in laser, detectors, and spectroscopic instruments drove the advancement of LIBS towards a wide range of fields

beyond traditional material analysis, including environmental monitoring[2], forensic science[3], geological exploration[4], space exploration[5], waste management[6], biomedical research[7], food chemistry[8], homeland security[9], industrial and nuclear applications, etc. The traditional LIBS used only nanosecond (ns) lasers and with time, short pulse lasers like picosecond (ps) and femtosecond (fs) lasers were incorporated into LIBS to achieve enhanced spatial resolution with low energy damage threshold. Over time, LIBS analysis has become more sensitive, more resolved, and more accurate because of developments in advanced spectrometers. These days, the LIBS system is often incorporated with sophisticated spectrometers like echelle spectrometers or time-of-flight spectrometers, along with sensitive low-cost detectors like charged coupled devices (CCDs) or photomultiplier tubes (PMTs). Other significant developments have also been made, such as double pulse LIBS, standoff LIBS, microwave LIBS, etc. There are also numerous significant developments from an analytical perspective. Several researches have been carried out to understand the fundamental aspects of LIBS and enhance the limit of detection (LOD) to enable trace elemental analysis. Furthermore, the development of LIBS combined with machine learning (ML) opened up new possibilities for data analysis and interpretation, boosting the capabilities and efficacy of LIBS methods. Researchers also combine LIBS with various other analytical techniques like Raman spectroscopy, infrared (IR) spectroscopy, laser induced fluorescence (LIF), laser ablation inductively coupled plasma mass spectrometry (LA-ICP-MS), etc., to acquire complementary information about the sample with improvised sensitivity, LOD, and other analytical capabilities.

1.1.1 Process Involved in LIBS

The interaction between a high-energy pulsed laser beam and matter is an intricate and not completely understood phenomenon that continues to be extensively researched. When the laser pulse is focused on the surface of any material with irradiance over the breakdown threshold (often on the order of GW/cm^2), it leads to the removal of some materials from the surface of the material and the creation of shockwave. This process encompasses a diverse range of phenomena, including as rapid localised heating, liquefaction, and intense vaporisation. The vaporized materials then expand as a plume over the surface of the sample, where it encounters extremely high temperatures and laser induced plasma (LIP) is formed. Figure 1.1 provides a schematic of several mechanisms that contribute to the creation of the LIP.

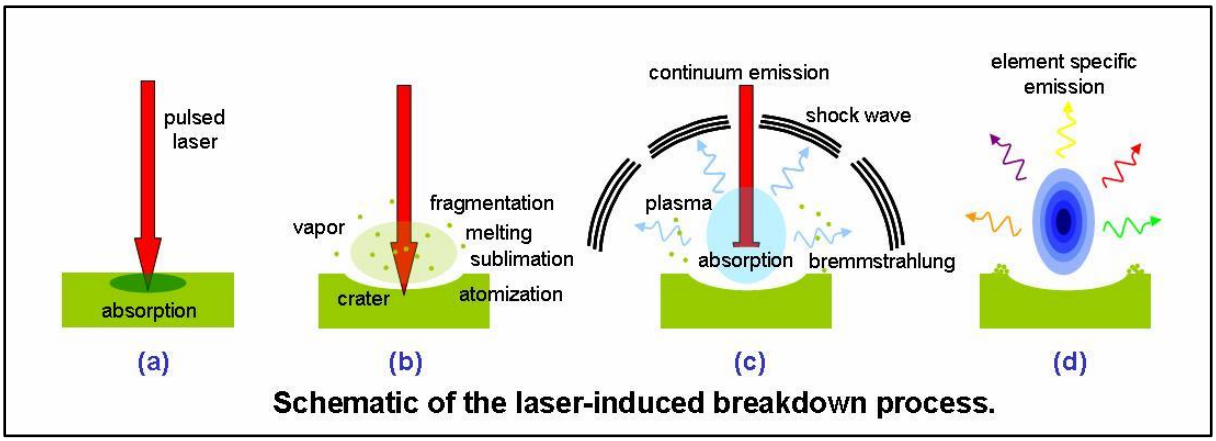

Figure 1.1. Various processes involved in the formation of LIP. (Figure adopted from Steven Rehse et al.[10])

LIP is a localized collection of free electrons, ions, atoms and molecules where the charged species often act collectively, yet the system as a whole is electrically neutral. LIP can be characterized by various parameters like degree of ionization, plasma electron temperature, plasma electron density, etc. Typically, LIP is a weakly ionized plasma, i.e., the ratio of electrons and other species is less than 10%[11]. A schematic explaining the formation and temporal evolution of LIP initiated by a single laser pulse is described in figure 1.2.

1.1.1.1 Ablation and Ionization

The ionization of species is primarily governed by two mechanisms, i.e., by multiphoton ionization (MPI) and inverse Bremsstrahlung (IB) absorption process[12–14].

MPI is required to achieve direct ionization of species with ionization energy far greater than the photons typically employed in the laser pulse[15]. The multiphoton ionisation (MPI) of electrons can take place when a significant number of photons are absorbed simultaneously by atoms or molecules (or when electrons are ejected from the valence to conduction band in the case of metals), which can be given by,

$$M + m(h\nu) \rightarrow M^{+} + e^{-} \tag{1.1}$$

where m is the photon population and M refers to the atom or molecule. MPI is significant at high laser irradiance (greater than10^{10} W/cm^2 for gases) and at shorter wavelengths (less than ~1 μm). The probability of an atom or molecule absorbing a sufficient number of photons with a wavelength much greater than ~1 μm to increase the energy of the neutrals beyond their ionization potential is statistically improbable. However, this procedure becomes

particularly significant at low pressure, when the low particle density of the medium results in low collision frequencies between species.

In the IB process, the photon is absorbed by one or more electrons (known as seed electrons) that are initially located within the focal volume at the begining of the laser pulse. The seed electrons can be produced by cosmic rays or by the interaction of the initial laser pulses with dust, oxygen, or organic vapors[11]. It can also originate from the atoms or molecules in the environment through MPI.

In the IB process, electrons acquire energy from photons in collision with ions, atoms or molecules. When the energy of the electron is greater than the ionization potential of neutral species, it can ionize atoms or molecules (M) through collision and produces two lower energy electrons which again acquire more energy and cause more ionization of other neutrals and two more electrons as

$$e + M \rightarrow 2e^{-} + M^{+} \tag{1.2}$$

With an increase in the number of electrons and ions, there is a corresponding rise in the collisions between electrons, photons, and ions. This leads to a greater probability of electron multiplication and, consequently, cascade ionization. During the IB process, all elemental species of the sample can be ionized to create plasma and the laser pulse energy can be coupled into the plasma which combinedly increases the plasma density to a point where it becomes optically thin. When the density of the plasma is more than the critical density (where plasma frequency becomes equal to laser frequency), the laser cannot enter inside the plasma; this is called plasma shielding.

An accurate description of the breakdown threshold of LIP is very difficult as it depends on many parameters, including laser parameters (wavelength, irradiance, pulse duration), nature of the medium (density, ionization threshold)[11]. The dominance of IB absorption mechanism occures at high pressures when the influence of collision is significant and wavelength is longer than 1 μm. In case of low-density molecules or at shorter wavelength ($\leq$ 1 μm), the possibility of electrons colliding with neutral species collision is minimal. In these cases, the MPI process dominates, i.e., in general, MPI will predominate if the breakdown threshold is independent of pressure. Ultimately, cascade ionization continues over the entire duration of the laser pulse until plasma shielding takes place.

1.1.1.2 Plasma Expansion

After the termination of the laser pulse, the luminous plasma expands outwards in all directions from the point of laser interaction. The expansion of the plasma depends on several factors, including the amount of mass ablated, energy transferred to the mass, laser spot size, nature of the environment (solid, liquid, or gas), and pressure. The laser energy can be transmitted, dispersed, or absorbed depending on the irradiance at the focus point. So, in that direction, photon absorption is asymmetric and the plasma expands more towards the laser pulse, resulting in the plasma's shape being slightly oval[11].

At the early time of plasma formation, the level of ionization in the LIP is extremely high, and there is a huge continuous background that decays rapidly over time, even quicker than the spectral lines. Continuum emission is generated by the transitions between free state and stationary state E_j of the atom whose frequencies are[15],

$$h\nu = \xi - E_j + \frac{1}{2}mv^2 \tag{1.3}$$

where ½ mv^2 and ξ are the kinetic energy of the free electron and ionization of the atom, respectively.

The plasma continuum is mainly caused by radiative recombination (free–bound) and Bremsstrahlung (free–free) processes. Recombination is the process in which a free electron is absorbed into an atomic or ionic energy state, E_j, by releasing its extra kinetic energy as radiation. Bremsstrahlung process refers to free–free emission transition which occurs when an electron is accelerated or decelerated in collision with other charged particles due to the loss of kinetic energy.

It is difficult to distinguish between emissions caused by radiative recombination and those caused by the Bremsstrahlung process. Besides, the former exhibits greater prominence at higher frequencies, whereas the latter is more pronounced at lower frequencies[15].

In vacuum, the LIP follows adiabatic expansion. The speed of the expansion can be expressed by[15,16]

$$v_p = \sqrt{\frac{4\gamma + 10}{3}\frac{E}{M_v}} \tag{1.4}$$

where v_p, γ, E and M_v are the specific heat ratio, plum energy and total vaporized sample mass, respectively.

When the laser ablation occurs, the surrounding media is compressed by the ablated mass and shockwave is produced. The plasma is the mixture of atoms and ions of both sample and surrounding media. The rate of plasma expansion decreases once it interacts with the surrounding media. The expansion distance of the shockwave can be described by Sedov's theory. The time-dependent expansion distance H(t) in air can be expressed as[15,17]

$$H(t) = \lambda_0 \left(\frac{E_0}{\rho} \right)^{1/(2+d)} t^{2/(2+d)} \tag{1.5}$$

where λ_0 represents a constant without units. E_0 represents the energy per area for one-dimensional expansion, energy per length for two-dimensional expansion, and energy for three-dimensional expansion. ρ is the density of air and d the symbol d represents the dimensionality of the propagation. For spherical propagation, d=3, for cylindrical propagation, d=2, and for planar propagation, d=1.

Once the pressure of the plasma plume equals the pressure of the surrounding media, the expansion of the shockwave ceases, and the ultimate distance determines the volume of the plasma plume. The duration and size of the vapour plume can be represented as[15,18]

$$t_s = \xi_s \left(\frac{E}{p} \right)^{1/3} \frac{1}{c_g} \tag{1.6}$$

$$R_s = \zeta_s \left(\frac{E}{p} \right)^{1/3} \tag{1.7}$$

where ξ_s and ζ_s are constants, p is the pressure and c_g is the sound velocity of the gas.

1.1.1.3 Plasma Emission

Emission of intense electromagnetic radiation occurs in the UV-VIS-NIR regions with generation of sound and shockwave as the plasma evolves. The ns laser generates a continuum that emerges during the laser pulse, which typically has a duration of several hundred nanoseconds. In the ns range, ionic emissions are most prominent, while atomic and molecular emissions are seen in the microsecond range (typically after 1 μs). Later the presence of molecular line emission observed resulting from the recombination of species within the plasma. In organic samples like explosives, plastics, drugs, etc., the CN violet and C_2 swan bands are often observed on the microsecond time scale. The formation of these molecules in LIP is complex to understand; however, extensive studies have reported that the molecular

formation of CN band could be due to the recombination of C and N atoms[19,20]. The C2 bond was observed due to the C = C linkage of the analyte[19,20].

1.1.2 Difference between short (ns) and Ultra-short (ps and fs) pulse LIBS

The difference between the ablation mechanism of short (ns) and ultra-short (ps and fs) pulses are different because of large variations in peak power and pulse duration. The formation of LIP involves ablation, atomization, and excitation. In short pulses (ns), the absorption process is initiated at the fs time scale by the seed electron in the focal region of the laser pulse, followed by the IB process[21]. And in the case of the short pulse, ionization, sample heating, and vaporization all occur during the formation of plasma and the matter undergoes a transient change in thermodynamic regime from solid to plasma state through liquid state[22]. In this case, the poor coupling of laser to material requires higher pulse energies, which forms scars on the material surface due to melting.

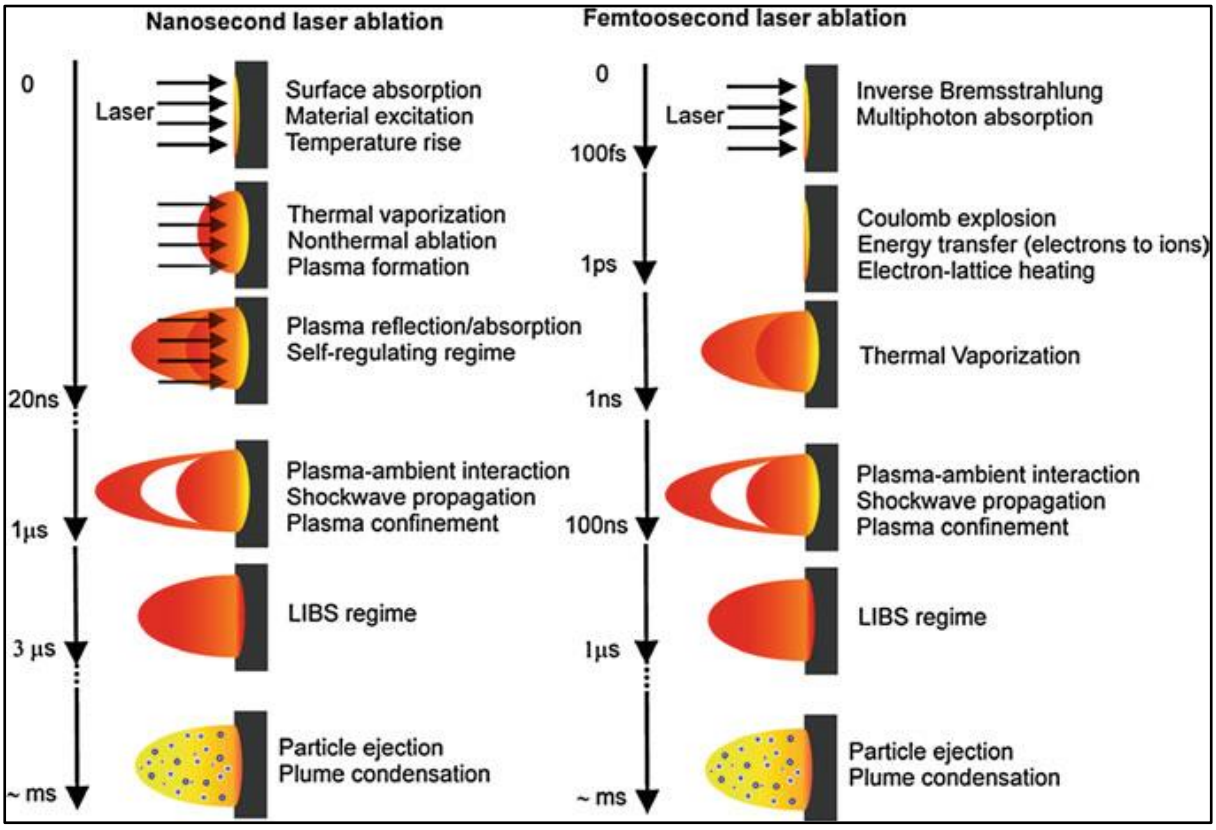

Figure 1.2. Time scale of various processes involved in ns and fs LIP during and after the laser – matter interaction. (Figure adopted from Harilal et al.[23])

In the case of ultra-short pulses (ps and fs), the ablation mechanism is driven by various mechanisms depending on the availability of free electrons i.e., multiphoton absorption, impact ionization, avalanche ionization, and coulomb expansion. Ultrafast pulses rapidly form a hot plasma without a liquid phase with a low ablation threshold and less damage threshold on the sample. Moreover, ultrafast interactions have exciting features as the plasma shielding effect is absent, leading to improvement in sensitivity compared to short pulse. Short pulses result in high temperature and dominance of ionic and atomic emissions at the initial time, whereas ultrashort pulses form plasma with low temperature and favor molecular emissions[19]. The time scale of short and ultra-short energy absorption, laser ablation, and other related processes that occur during or after the interaction of laser with matter exhibits significant variation. The approximate time scale of ns and fs plasma processes are depicted in figure 1.2, adopted from the work of Harilal et al.[23].

1.2 Raman Spectroscopy

Raman spectroscopy is a molecular spectroscopic technique that involves studying the vibrational (phonon) states of molecules by observing the inelastic scattering of light. This technique provides exceptional insights into molecular vibrations. This approach provides a powerful tool for molecular fingerprinting and monitoring changes in molecular bond structures. Raman spectroscopy offers unique advantages compared to other vibrational spectroscopy techniques like Fourier Transform Infrared (FTIR) and Near-infrared (NIR) spectroscopy. This is because Raman spectroscopy involves analyzing the light scattered off a material rather than the light absorbed by it. Consequently, Raman spectroscopy necessitates minimal sample preparation and is not affected by absorption bands in aqueous environments. This allows for direct measurement of solids, liquids, and gases, even when they are contained in transparent materials such as plastic, transparent crystals, glasses, etc. The great selectivity of this approach, similar to FTIR, enables the identification and discrimination of molecules and chemical species that have similar structures. Additionally, it allows for the exact assessment of small changes in materials.

Raman spectroscopy is an indispensable analytical technique used to identify and monitor changes in molecular bond structure across various materials, such as solids, liquids, and gases. Its non-destructive nature, minimal sample preparation requirements, and ability to identify substances make Raman spectroscopy indispensable in diverse scientific fields such as chemistry, materials science, pharmaceuticals, forensics, and biomedical research.

1.2.1 Theory of Raman Scattering

When studying Raman scattering, two viewpoints arise: classical wave and quantum particle interpretation. Each perspective provides a distinct and valuable understanding of the fundamental physics involved. Light is considered as electromagnetic radiation in the classical wave model, distinguished by a fluctuating electric field that interacts with molecules via their polarizability. The polarizability is dictated by the electron cloud's capacity to engage with an electric field. Softer molecules, such as benzene, exhibit pronounced Raman scattering, whereas harder molecules like water tend to display lesser scattering tendencies.

In contrast, the quantum particle perspective defines light as photons engaging in interactions with molecules, leading to inelastic scattering. In this scenario, the quantity of scattered photons is directly correlated with the size of the bonds. Consequently, molecules possessing a significant quantity of Pi bonds, such as benzene, exhibit a pronounced scattering of photons, whereas molecules with modest single bonds, such as water, display a feeble Raman scatterer.

1.2.1.1 Classical Theory of Raman Scattering

When a molecule is subjected to an electric field, it experiences polarization as the negatively charged electron cloud is drawn towards the positive pole, while the positively charged nuclei are drawn towards the negative pole. The induced polarization, denoted as P, has a direct proportionality to the amount of the applied electric field., E [24]. The expression can be given by,

$$P = \alpha E \tag{1.8}$$

where the proportionality constant, α represents the polarizability.

When electromagnetic radiation having frequency of ν_0 interacts with molecules, each molecule experiences a varying electric field,

$$E = E_0 \cos 2\pi \upsilon_0 t \tag{1.9}$$

To simplify, let us consider the vibrational motion of the molecule. Let Q be the normal coordinate associated with a specific mode of vibration of frequency ν_m. In the harmonic approximation, Q can be expressed as:

$$Q = Q_0 \cos 2\pi \upsilon_m t \tag{1.10}$$

Expanding α using Taylor expansion in the normal coordinate Q,

$$\alpha = \alpha_0 + \left(\frac{\partial \alpha}{\partial Q}\right)_0 Q + \ldots \tag{1.11}$$

Substituting equations 1.9, 1.10 & 1.11 in equation 1.8 and neglecting higher-order terms,

$$P = \left[\alpha_0 + \left(\frac{\partial \alpha}{\partial Q}\right)_0 Q_0 \cos 2\pi \upsilon_m t\right] E_0 \cos 2\pi \upsilon_0 t$$

$$= \alpha_0 E_0 \cos 2\pi \upsilon_0 t + \left(\frac{\partial \alpha}{\partial Q}\right)_0 Q_0 E_0 \cos 2\pi \upsilon_0 t \cos 2\pi \upsilon_m t$$

Using the trigonometric relation $2\cos\theta\cos\phi = \cos(\theta+\phi) + \cos(\theta-\phi)$,

$$P = \alpha_0 E_0 \cos 2\pi \upsilon_0 t + \frac{1}{2}\left(\frac{\partial \alpha}{\partial Q}\right)_0 Q_0 E_0 \left[\cos 2\pi(\upsilon_0 + \upsilon_m)t + \cos 2\pi(\upsilon_0 - \upsilon_m)t\right] \tag{1.12}$$

Therefore, the induced polarization comprises three distinct frequency comoponents.

(i) $\nu = \nu_0$ Rayleigh line

(ii) $\nu = \nu_0 - \nu_m$ Raman Stokes line

(iii) $\nu = \nu_0 + \nu_m$ Raman anti-Stokes line

1.2.1.2 Quantum Theory of Raman Scattering

In the quantum realm, electromagnetic radiations exhibit both wave and particle nature. In discussing Raman scattering, incident radiation with frequency ν_0 is considered as a continuous flow of particles (photons) that collide with molecules. In the case of a perfectly elastic collision, there is no exchange of energy between the photons and the molecule, called Rayleigh scattering. In an inelastic collision, energy is exchanged between the two entities. The molecule can undergo energy transfer by either gaining or losing an amount of energy equivalent to the disparity between its final and initial states. When the molecule absorbs energy, the frequency of the scattered photons becomes $\nu_0 - \nu_m$, known as the Stokes line. Conversely, when the molecule experiences a decrease in energy, the frequency of the scattered photon changes to $\nu_0 + \nu_m$, which is known as the anti-Stokes line. Figure 1.3 illustrates the different mechanisms responsible for the generation of Rayleigh, Stokes, and anti-Stokes lines.

When a system interacts with radiation of frequency ν_0, it has the potential to undergo a transition to a virtual state within the system. A virtual state, discrete from the stationary states of the molecule, represents a combined state of both the molecule and radiation. During Raman scattering, most molecules return to their initial state from the virtual state, leading to

the occurrence of Rayleigh scattering. Nevertheless, a small portion undergoes a change to states with greater and lesser levels of energy, resulting in the emergence of Stokes and anti-Stokes lines, respectively. When the virtual state coincides with the real state of the system, it leads to resonance Raman effect. It is worth mentioning that the annihilation of the incident photon and the formation of the scattered photon happen simultaneously.

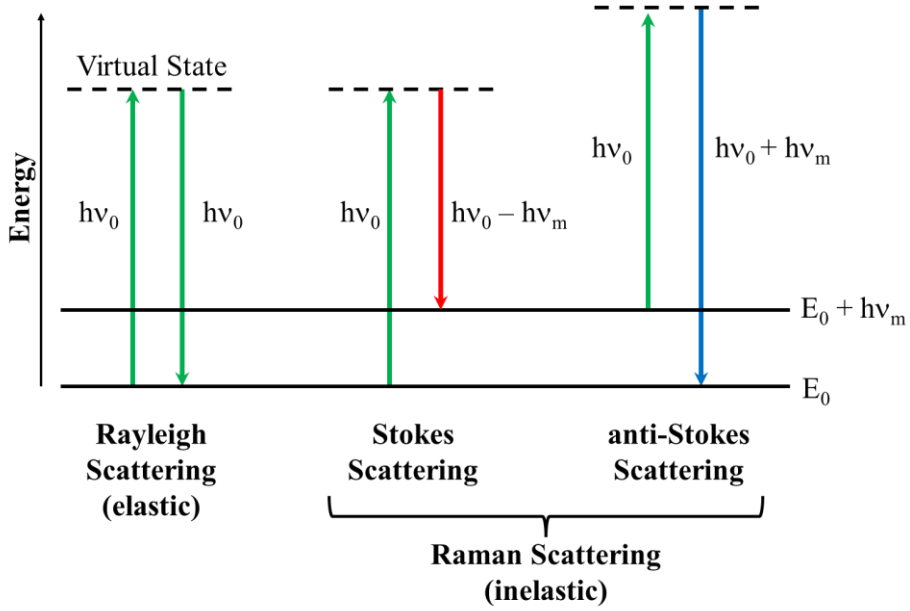

Figure 1.3. Energy level diagram of Rayleigh and Raman scattering.

The spectral line intensity depends on various parameters, with the primary factor being the initial population of the state from which the transition begins. The Stokes line, originating from $\nu = 0$, and the anti-Stokes line, originating from $\nu = 1$ exhibit same Raman shift ν_m.

1.3 Outline of the Thesis

The thesis focuses on the fundamental studies of LIBS towards development of Simplified LIBS-based Intensity-ratio approach for Concentration Estimation (SLICE) and harnessing machine learning for the classification of materials such as explosives and post-consumer plastics. It also discusses the dependence of various plasma parameters on the hardness of materials. Moreover, it delves into the applications of machine learning in Raman spectroscopy, aiming for the quantitative detection of explosives in mixtures.

Chapter 2 provides a comprehensive overview of the different instruments (lasers, spectrometers, etc.) and experimental configurations used for the thesis work.

Chapter 3 presents fundamental studies of LIBS towards temporal modeling of LIP for elemental analysis. Elemental analysis of materials is pivotal across diverse scientific domains and industries, serving several critical purposes. It plays a crucial role in identifying elemental composition and ensuring stringent product quality control across industries, including pharmaceuticals and food production. It is also used widely for characterizing materials in fields like materials science and nanotechnology while finding diverse applications in archaeology, environmental monitoring, pharmaceuticals, and more sectors. In essence, elemental analysis is indispensable for understanding the composition, properties, and behaviors of the materials, influencing a wide array of scientific studies, industrial processes, and practical applications.

Elemental analysis using LIBS is one of the most demanding disciplines due to its robust experimental setup since late 1980s[25–27]. Several LIBS techniques have been developed for the elemental analysis of various materials in different forms (solids, liquids, and gases). The first method proposed uses a calibration curve approach to estimate the concentration of each element present in a sample. This method, however, is constrained by the requirement of calibration curves for each matrix element, which can only be used for samples with the same matrix and must be reconstructed for samples with different matrices. Therefore, in real-life applications, while calibration LIBS excels in detecting species concentrations within a well-defined matrix, it is not suitable for complex situations like multi-elemental analysis of unknown materials. To overcome these limitations, A. Ciucci et al. introduced a new method called calibration-free LIBS (CF-LIBS), where the matrix-matched standard samples are not required for concentration estimation[28]. However, in CF-LIBS, the self-absorption (SA) effect is a major disruption of emission intensities at respective wavelengths. The SA of a certain emission line occurs when the emitted radiation of that atom is absorbed by another atom, resulting in a decrease in emission peak intensity. For CF-LIBS, it is essential to estimate plasma temperature using the Boltzmann/ Saha-Boltzmann plot method[28–30]. In principle, these methods require at least two SA free emission lines with a well-separated upper energy level for each constituent element in the sample. However, in the practical scenario, researchers always consider several emission lines from each element to retain accurate temperature values[29,31]. The availability of such quantities of SA free lines is difficult to observe for many elements (e.g., C, H, N, O, Na, B, etc.) in the UV – VIS – NIR range of LIBS spectrum. Also, the observable emission lines are scarce in the case of trace elements. Therefore, SA correction becomes essential for the universal adoption of CF-LIBS for elemental analysis. The involvement of the SA correction procedure makes the CF-LIBS

more complex and time-consuming. In specific scenarios where SA correction is not necessary, CF-LIBS may be quick and easy to use in practice.

To overcome these limitations, a new, robust, more straightforward method for fast quantitative elemental analysis was proposed which has several notable advantages. This method relies on the temporal modeling of intensity ratio using radiative relaxation mechanism of plasma[32,33]. Since the method relies on intensity ratios to determine concentrations, it is named Simplified LIBS-based Intensity-ratio approach for Concentration Estimation (SLICE). The major advantage of this technique is that it doesn't involve Boltzmann/Saha-Boltzmann plot in the calculation. The requirement of a few emission lines makes this method more robust and straightforward. To be precise, it demands only two emission lines from any one of the elements and a single line from all other elements. For example, a sample of n elements requires only n+1 emission intensity lines, giving an advantage for choosing emission lines conveniently. Since only one emission line is needed from every element except any element in the sample, now there is a great flexibility of choosing emission lines unaffected by SA. Also, SLICE reduces the complexity of the calculation as fewer steps are involved.

The LIBS experiment was performed on two Cu based alloys (binary and ternary). The kinetic LIBS spectra were recorded and the temporal behavior of emission intensity, plasma temperature and electron number density were studied. The radiative relaxation mechanism was used to model the temporal behavior of intensity ratio and plasma temperature in order to determine the plasma decay parameters (PDPs): the initial plasma temperature and the radiation decay constant. These estimated PDPs were used to estimate the concentration of each species in both samples using SLICE. Also, the results were cross-validated using CF-LIBS and electron dispersive X-ray Spectroscopy (EDS). The results obtained from SLICE show good agreement with CF-LIBS and EDS. At last, the advantages and limitations of SLICE were discussed.

Chapter 4 explores the dependence of plasma parameters on the hardness of the materials. Estimating the hardness of alloys stands as a critical endeavor across industries and scientific realms owing to its multifaceted significance. Beyond assessing durability and reliability, hardness testing guides material selection, aids in design precision and ensures quality control. The correlation between hardness and various mechanical properties empowers engineers to predict material behavior, wear resistance, and overall performance in diverse applications, from heavy machinery to critical aerospace components. Moreover, hardness estimation fosters

innovation in material development, enabling researchers to tailor alloys for specific requirements and enhance their mechanical characteristics. In essence, the assessment of alloy hardness serves as a linchpin in guaranteeing material integrity, safety, and reliability, fundamentally influencing product performance and longevity. Traditional methods for hardness estimation encompass several established techniques like the Vickers hardness test, Rockwell hardness test, Brinell hardness test, etc. Most of these techniques involve creating an indentation on the material surface and require specific sample preparations, such as smooth and flat surfaces, which might be challenging or impractical for certain materials or irregularly shaped samples. Additionally, the sample size or shape limitations can restrict the applicability of these methods. Moreover, these processes are time-consuming. Due to the rapid detection capability and requirement of no or minimal sample preparation, LIBS can provide insights into the relationship between various plasma parameters and material hardness, offering a non-invasive means to estimate hardness characteristics across different materials.

Several researchers tried to correlate the plasma parameters such as plasma temperature, electron number density, and intensity ratios (atomic to ionic), etc., with the hardness of materials[34–36]. Despite these efforts, a consistent relationship between plasma parameters and hardness is difficult to describe.

This chapter explores the dependence of plasma parameters with material hardness. For the experiment, five different iron-based alloys with same elemental compositions and varying hardness were considered. The hardness of each sample was initially determined by using Vicker's hardness tester. Then temporal LIBS spectra for each sample were recorded and subsequently, various parameters like plasma temperature, electron density, radiation decay constant, crater dimension, etc., were estimated for all five alloys. When the change in plasma parameters was compared against the change in hardness, a linear (both increasing and decreasing) trend of all the parameters were observed w.r.t. the change in hardness. The results serve to underline the capability of LIBS for rapid estimation of material hardness without or with minimal sample preparation.

Chapter 5 delves into the application of machine learning in conjunction with LIBS for the identification/classification of explosives and post-consumer plastics.

In the last few decades, the threat to homeland security around the world, as well as in India, urged the need for an automated portable device for the rapid detection of high energy materials (HEMs), including explosives, improvised explosive devices (IEDs), etc. Especially in crowded places like airports, railway stations, metro stations, shopping malls, worship places,

etc., an advanced explosive detection device based on modern analytical techniques is essential for detecting HEMs with high confidence. LIBS is a potential tool for the on-site detection of explosives with numerous advantages over other techniques. These advantages include robust signal acquisition, standoff detection, trace level identification, rapid prediction when combined with machine learning, etc., which can make LIBS an indispensable tool in explosive detection.

With increasing population and modernization, the widespread adaptation of plastics in our day-to-day lives has experienced a substantial surge. Human society heavily relies on plastics as it is widely used in packaging, food safety, domestic equipment, industry, transport, electronics, etc. Its demand and use are continuously increasing because of its notable advantages such as cost-effectiveness, durability, low weight, flexibility in shape, etc. [37]. On the contrary, due to its high durability and low-degrading nature, it generates large amount of waste every year[38]. Thus, the management of plastic waste has now become essential. Traditional plastic waste management techniques like incineration and landfills are inconvenient as they cause colossal resource waste and adverse effects on the environment and ecosystem. Also, the toxic substances released in these processes severely pollute the soil, water, and air. Therefore, recycling is the most viable way to reduce final waste output. Classification/sorting post-consumer plastics is the most critical step in recycling. The sorting process is essential to retain the quality and properties of recycled plastics [39]. The prevalent method for sorting plastics involves manual visual inspection, where identification relies on recognizing the recycling number assigned to each plastic type. However, this is labor-intensive, more time-consuming, and error-prone. Also, hazardous contamination is harmful to workers. Other classification techniques based on the physical properties are also developed, like the floating technique [40], an electrostatic technique [41], differential scanning calorimetric (DSC) [42], etc. These conventional methods greatly depend on the physical state of the sample and are more time-consuming and prone to errors. Besides these technologies, LIBS combined with machine learning can provide a promising solution for sorting plastic waste efficiently and accurately.

In the context of *in situ* application, an ideal classifying instrument should be cost-effective, compact, reliable, and capable of providing a fast identification rate with higher accuracy. This chapter explores the potential of handheld picosecond (ps) LIBS setup for discrimination of explosives and post-consumer plastics using artificial neural network (ANN), a robust machine learning classifier. Further, from a spectral perspective, it is noteworthy that in LIBS spectra,

most of the wavelength regions (more than 80%) contain only noise, especially in organic samples. All the wavelengths/ variables/ features representing noise are statistically insignificant. Therefore, it might be advantageous to confine the analysis to the chosen features of significance. There are two approaches to reducing the dimension of the input data, i.e., 1) feature selection, where unwanted features are removed from the dataset manually or by using statistical/machine learning models, and 2) feature extraction, where machine learning algorithms are used to transform the original data into a new smaller dataset. Feature selection/ extraction is crucial in real-time applications as it reduces the dimensionality of the data, improves model performance, mitigates overfitting, and expedites computational processes. Additionally, they enhance data interpretability and visualization, and address multicollinearity, thus enabling more effective decision-making and insights. Therefore, in this chapter, various feature selection and feature extraction approaches were explored in conjunction with ANN to determine the most effective classification strategy in terms of accuracy, computational time, and storage requirement.

Five explosive and 12 non-explosive samples with similar chemical composition were considered for detection. Multiple spectra (200 for each sample) were recorded for all the samples. The total spectra were divided randomly for training (70%), validation (15%), and testing (15%). Initially, every spectrum within both the train and validation datasets is categorized into their respective groups, either explosive or non-explosive. The test phase involves utilizing test data to predict whether a given spectrum corresponds to an explosive or non-explosive category. Following this, a separate training model is constructed specifically focusing on the explosive samples, which are labeled to explosive sample names. Once a spectrum is identified as explosive, it proceeds to a secondary model designed to determine the specific type of explosive it belongs. The same training, validation and testing architecture is used for all the feature selection and feature extraction approaches. The results were compared from full spectra and various feature selection and feature extraction approaches as input to the ANN model. And it has been observed that ANN combined with linear discriminant analysis (LDA) feature extraction achieved a flawless 100% accuracy in distinguishing between explosive and non-explosive. In classification within explosives, maximum accuracy (99.8%) was obtained for full spectrum and manual feature selection with peak area. Moreover, in this study, both the training and testing were performed on the LIBS spectra obtained from the same samples. However, in real-world scenarios, the model encounters unknown samples that haven't been seen by the model during the training process. Given the limited types of explosive samples available, the training and testing were conducted using the same set of

samples. Multiple spectra were recorded and then randomly divided for training, validation and testing purposes. However, it would be interesting to extend this considering a large set of samples and performing testing on unknown samples not seen by the trained network earlier.

Within the framework of plastic sorting, two distinct approaches were employed: firstly, nine different post-consumer plastics were collected from a local recycling unit, and both training and testing were performed on the same sample. Secondly, 30 post-consumer plastics representing six commonly used types (HDPE, LDPE, PP, PET, PS, and PVC), and five samples from each category were collected from garbage. Testing was performed on unknown plastic, mimicking real-world scenarios for identifying unfamiliar post-consumer plastics. ANN models were utilized, incorporating various feature selection and extraction methods. Their performances were compared in accuracy, testing time, data size, and model size to find the most effective strategy. The results demonstrate that in the first case (training testing on the same sample), nearly all feature selection and extraction methods achieved outstanding classification accuracy in distinguishing nine distinct plastics. However, when confronted with the second case involving testing on unfamiliar samples, the ANN model encountered difficulty in distinguishing between HDPE, LDPE, and PP. Remarkably, it effectively differentiated between PET, PS, and PVC.

In discussing the real-time implementation of LIBS combined with machine learning for sorting post-consumer plastics, it becomes evident that employing the same sample for training and testing purposes renders the former scenario ineffective when encountering unknown samples. Conversely, testing on unknown samples in real-time applications proves more relevant and practical. Despite this, it's important to note that this approach efficiently identifies three out of six types of plastics. As such, it currently stands as a viable solution for real-time identification of PET, PS, and PVC, which could significantly reduce the manual sorting workforce by half.

Chapter 6 discusses the development of a low-cost, compact, and portable Raman spectroscopic setup for detecting explosive mixtures. Initially, the Raman experiment was performed on the mixture of 1,3,5-trinitroperhydro-1,3,5-triazine (RDX) and ammonium nitrate (AN) mixed at different concentrations. Various machine learning regression analyses, such as linear regression, partial least square regression (PLSR), support vector regression (SVR), decision tree regression (DTR) and random forest regression (RFR) were employed on the Raman spectra of mixtures to quantify the amount of each sample present in the mixture. The Raman spectra were analyzed with and without background correction. Also,

various feature/variable selection strategies were explored to find out the best analysis protocol. Finally, results obtained from all the regression models in conjunction with various feature selection approaches with or without background correction were compared in terms of accuracy, computational time and limit of detection. The results demonstrate that Raman technique combined with machine learning can work as an efficient tool for rapid detection of explosive mixtures. Overall, a portable Raman spectroscopic tool is demonstrated for the quantitative detection of explosive mixtures with a high accuracy rate, which can have great importance in homeland security and the military.

Chapter 7 of this thesis presents the culmination of the research findings and outlines the future prospects based on this research work.

1.4 Reference

[1] D.A. Cremers, L.J. Radziemski, T.R. Loree, Spectrochemical analysis of liquids using the laser spark, Appl. Spectrosc. 38 (1984) 721–729.

[2] R. Kumar, A.K. Rai, D. Alamelu, S.K. Aggarwal, Monitoring of toxic elements present in sludge of industrial waste using CF-LIBS, Environ. Monit. Assess. 185 (2013) 171–180.

[3] A.K. Tarai, R. Junjuri, A. Dhobley, M.K. Gundawar, Classification of human tooth using laser-induced breakdown spectroscopy combined with machine learning, J. Opt. (2023) 1–11.

[4] S.-L. Lui, A. Koujelev, Accurate identification of geological samples using artificial neural network processing of laser-induced breakdown spectroscopy data, J. Anal. At. Spectrom. 26 (2011) 2419–2427.

[5] F. Colao, R. Fantoni, V. Lazic, A. Paolini, F. Fabbri, G.G. Ori, L. Marinangeli, A. Baliva, Investigation of LIBS feasibility for in situ planetary exploration: an analysis on Martian rock analogues, Planet. Space Sci. 52 (2004) 117–123.

[6] S.-B. Roh, S.-B. Park, S.-K. Oh, E.-K. Park, W.Z. Choi, Development of intelligent sorting system realized with the aid of laser-induced breakdown spectroscopy and hybrid preprocessing algorithm-based radial basis function neural networks for recycling black plastic wastes, J. Mater. Cycles Waste Manag. 20 (2018) 1934–1949.

[7] X. Chen, Y. Zhang, X. Li, Z. Yang, A. Liu, X. Yu, Diagnosis and staging of multiple myeloma using serum-based laser-induced breakdown spectroscopy combined with machine learning methods, Biomed. Opt. Express. 12 (2021) 3584–3596.

[8] R. Agrawal, R. Kumar, S. Rai, A.K. Pathak, A.K. Rai, G.K. Rai, LIBS: a quality control tool for food supplements, Food Biophys. 6 (2011) 527–533.

[9] J. Handke, F. Duschek, K. Gruenewald, C. Pargmann, Standoff detection applying laser-induced breakdown spectroscopy at the DLR laser test range, in: Chem. Biol. Radiol. Nucl. Explos. Sens. XII, SPIE, 2011: pp. 212–217.

[10] Steven Rehse, A LIBS Primer, (n.d.). https://www.uwindsor.ca/people/rehse/299/libs.

[11] D.A. Cremers, L.J. Radziemski, Handbook of laser-induced breakdown spectroscopy, John Wiley & Sons, 2013.

[12] Y.M. Li, J.N. Broughton, R. Fedosejevs, T. Tomie, Formation of plasma columns in atmospheric pressure gases by picosecond KrF laser pulses, Opt. Commun. 93 (1992) 366–377.

[13] D. Von der Linde, H. Schüler, Breakdown threshold and plasma formation in femtosecond laser–solid interaction, JOSA B. 13 (1996) 216–222.

[14] J.J. Camacho, J.M.L. Poyato, L. Diaz, M. Santos, Optical emission studies of nitrogen plasma generated by IR CO2 laser pulses, J. Phys. B At. Mol. Opt. Phys. 40 (2007) 4573.

[15] J.P. Singh, S.N. Thakur, Laser-induced breakdown spectroscopy, Elsevier, 2020.

[16] Y.B. Zel'Dovich, Y.P. Raizer, Physics of shock waves and high-temperature hydrodynamic phenomena, Courier Corporation, 2002.

[17] L.I. Sedov, Similarity and dimensional methods in mechanics, CRC press, 1993.

[18] N. Arnold, J. Gruber, J. Heitz, Spherical expansion of the vapor plume into ambient gas: an analytical model, Appl. Phys. A. 69 (1999) S87–S93.

[19] R. Junjuri, M.K. Gundawar, Femtosecond laser-induced breakdown spectroscopy studies for the identification of plastics, J. Anal. At. Spectrom. 34 (2019) 1683–1692.

[20] S.A. Kalam, N.L. Murthy, P. Mathi, N. Kommu, A.K. Singh, S.V. Rao, Correlation of molecular, atomic emissions with detonation parameters in femtosecond and nanosecond LIBS plasma of high energy materials, J. Anal. At. Spectrom. 32 (2017) 1535–1546.

[21] D.N. Patel, P.K. Pandey, R.K. Thareja, Stoichiometric investigations of laser-ablated brass plasma, Appl. Opt. 51 (2012) B192–B200.

[22] J.R. Freeman, S.S. Harilal, P.K. Diwakar, B. Verhoff, A. Hassanein, Comparison of optical emission from nanosecond and femtosecond laser produced plasma in atmosphere and vacuum conditions, Spectrochim. Acta Part B At. Spectrosc. 87 (2013) 43–50.

[23] S.S. Harilal, J.R. Freeman, P.K. Diwakar, A. Hassanein, Femtosecond laser ablation: Fundamentals and applications, Laser-Induced Break. Spectrosc. Theory Appl. (2014) 143–166.

[24] G. Aruldhas, Molecular structure and spectroscopy, PHI Learning Pvt. Ltd., 2007.

[25] D.A. Cremers, The analysis of metals at a distance using laser-induced breakdown spectroscopy,

Appl. Spectrosc. 41 (1987) 572–579.

[26] T.L. Thiem, R.H. Salter, J.A. Gardner, Y.I. Lee, J. Sneddon, Quantitative simultaneous elemental determinations in alloys using laser-induced breakdown spectroscopy (LIBS) in an ultra-high vacuum, Appl. Spectrosc. 48 (1994) 58–64.

[27] R.W. Wisbrun, I. Schechter, R. Niessner, H. Schroeder, Laser-induced breakdown spectroscopy for detection of heavy metals in environmental samples, in: Int. Conf. Monit. Toxic Chem. Biomarkers, SPIE, 1993: pp. 2–15.

[28] A. Ciucci, M. Corsi, V. Palleschi, S. Rastelli, A. Salvetti, E. Tognoni, New procedure for quantitative elemental analysis by laser-induced plasma spectroscopy, Appl. Spectrosc. 53 (1999) 960–964.

[29] V.K. Unnikrishnan, K. Mridul, R. Nayak, K. Alti, V.B. Kartha, C. Santhosh, G.P. Gupta, B.M. Suri, Calibration-free laser-induced breakdown spectroscopy for quantitative elemental analysis of materials, Pramana. 79 (2012) 299–310.

[30] L.M. John, R.C. Issac, S. Sankararaman, K.K. Anoop, Multi-element Saha Boltzmann plot (MESBP) coupled calibration-free laser-induced breakdown spectroscopy (CF-LIBS): an efficient approach for quantitative elemental analysis, J. Anal. At. Spectrom. 37 (2022) 2451–2460.

[31] E. Mal, R. Junjuri, M.K. Gundawar, A. Khare, Optimization of temporal window for application of calibration free-laser induced breakdown spectroscopy (CF-LIBS) on copper alloys in air employing a single line, J. Anal. At. Spectrom. 34 (2019) 319–330.

[32] A.K. Tarai, R. Junjuri, S.A. Rashkovskiy, M.K. Gundawar, Time-Dependent Intensity Ratio-Based Approach for Estimating the Temperature of Laser Produced Plasma, Appl. Spectrosc. (2022) 00037028221117534.

[33] R. Junjuri, S.A. Rashkovskiy, M.K. Gundawar, Dependence of radiation decay constant of laser produced copper plasma on focal position, Phys. Plasmas. 26 (2019) 122107.

[34] Z.A. Abdel-Salam, A.H. Galmed, E. Tognoni, M.A. Harith, Estimation of calcified tissues hardness via calcium and magnesium ionic to atomic line intensity ratio in laser induced breakdown spectra, Spectrochim. Acta Part B At. Spectrosc. 62 (2007) 1343–1347.

[35] R.D. Pilkington, J. Astin, J. Cowpe, Application of laser-induced breakdown spectroscopy for surface hardness measurements, Spectrosc. Eur. 27 (2015) 13–15.

[36] J.S. Cowpe, R.D. Moorehead, D. Moser, J.S. Astin, S. Karthikeyan, S.H. Kilcoyne, G. Crofts, R.D. Pilkington, Hardness determination of bio-ceramics using laser-induced breakdown spectroscopy, Spectrochim. Acta Part B At. Spectrosc. 66 (2011) 290–294.

[37] U.K. Adarsh, V.B. Kartha, C. Santhosh, V.K. Unnikrishnan, Spectroscopy: A promising tool

for plastic waste management, TrAC Trends Anal. Chem. (2022) 116534.

[38] Q. Zeng, J.-B. Sirven, J.-C.P. Gabriel, C.Y. Tay, J.-M. Lee, Laser induced breakdown spectroscopy for plastic analysis, TrAC Trends Anal. Chem. 140 (2021) 116280.

[39] J.A. Brydson, Plastics materials, Elsevier, 1999.

[40] S. Pongstabodee, N. Kunachitpimol, S. Damronglerd, Combination of three-stage sink–float method and selective flotation technique for separation of mixed post-consumer plastic waste, Waste Manag. 28 (2008) 475–483.

[41] G.L. Hearn, J.R. Ballard, The use of electrostatic techniques for the identification and sorting of waste packaging materials, Resour. Conserv. Recycl. 44 (2005) 91–98.

[42] B. Luijsterburg, H. Goossens, Assessment of plastic packaging waste: Material origin, methods, properties, Resour. Conserv. Recycl. 85 (2014) 88–97.

Chapter 2

Experimental Details

This chapter delves into the examination of laser systems, spectrometers, LIBS experimental setups, Raman spectroscopy settings, and LabVIEW program creation for spectrum measurements. The chapter thoroughly analyses the specifications and operational principles of nanosecond (ns) and picosecond (ps) laser systems, explaining in detail their components and functions. Moreover, it explores the technological attributes of Mechelle ICCD and Czerny-Turner CCD spectrometers, which are crucial for spectroscopic studies. The experimental configurations for both gated and non-gated LIBS detections are comprehensively explained, coupled with a meticulous description of the Raman experimental arrangement. One noteworthy aspect of the chapter is the creation of a LabVIEW program that aims to optimize spectrum measurements, improving productivity and reducing experimental inaccuracies.

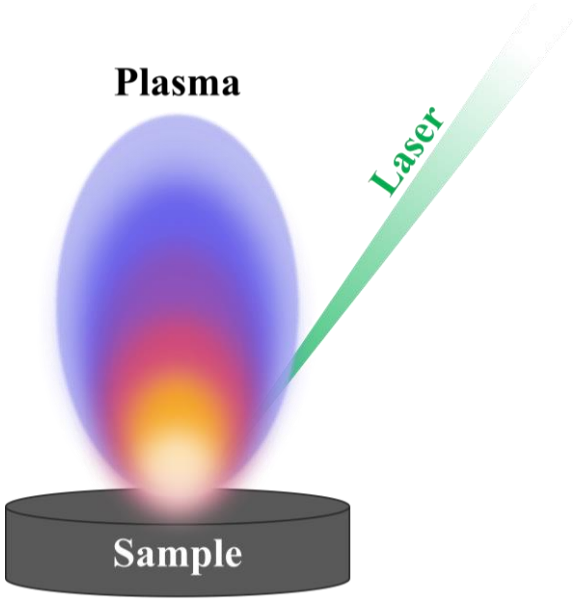

2.1 Details of Lasers

In the present thesis work, two high energy lasers were used for the LIBS experiments. The specifications of the two laser systems are presented in table 2.1.

Table 2.1. Specifications of nanosecond (ns) and picosecond (ps) laser systems.

Sl. No.	Parameters	Nanosecond laser	Picosecond laser
1	Laser model	SpitLight 1200 (M/s Innolas)	PL 2250 (M/s Ekspla)
2	Wavelength (nm)	1064 / 532 / 355 / 266	1064 / 532 / 355
3	Pulse duration	~ 7 ns	~ 30 ps
4	Maximum output energy at 1064 nm (mJ)	~ 1200	~ 100
5	Repetition rate (Hz)	1 – 10	10
6	Beam diameter (mm)	~ 6.5	~ 12

2.1.1 Nanosecond Laser

A Nd:YAG solid state laser (SpitLight 1200, M/s Innolas) was used for nsLIBS experiments in this thesis[1]. The laser system comprises of three main parts i.e., oscillator, pre-amplifier and amplifier. The schematic of the optical layout of the laser is depicted in figure 2.1.

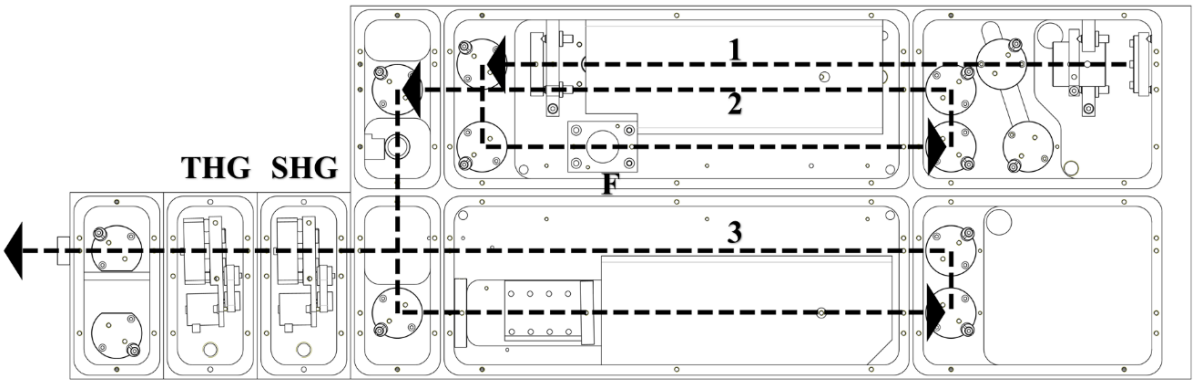

Figure 2.1. Schematic of optical layout of the nanosecond laser system. 1, 2 & 3 represent the beam path through oscillator, pre-amplifier and main amplifier respectively. F, SHG, and THG represent the Faraday isolator, second and third harmonic crystals, respectively.

The laser oscillator consists of a rear mirror of high reflectivity and a variable reflectivity output coupler (high reflectivity in the center, low reflectivity around the outside). This combination ensures well collimated monochromatic oscillator output which allows only TEM_{00} mode resulting a very smooth Gaussian beam profile. The gain medium of the cavity uses a Nd: YAG rod which is optically pumped by a single xenon-filled flashlamp driven by a

high stability power supply. Q-switching is achieved by a Pockels cell and a polarizer. The drive circuit is designed to produce one or two Q-switched pulses per flashlamp pulse and the pulse separation is adjustable between 1 – 10 Hz. In between the laser rod and output coupler, there is a mechanical shutter which is actuated by a rotary solenoid used to block or pass the oscillator output. The output of the oscillator passes through a pre-amplifier to further enhance the power. The pre-amplified rod is mounted in the same pumping chamber as the oscillator in a double elliptical cavity and share the same flashlamp. The output beam of the pre-amplifier is again directed to the amplifier chamber which consists of an amplifier rod pumped by two flashlamps in a double elliptical cavity. The laser works at fundamental wavelength 1064 nm and can achieve a maximum output power of 1200 mJ. However, it can be operated at first (532 nm), second (355 nm) or third (266 nm) harmonics with the help of harmonic generation assembly (HGA).

2.1.2 Picosecond Laser

A picosecond (ps) laser system (PL 2250, M/s Ekspla) was also used along with the ns laser[2]. The laser system is comprised of four functional parts, i.e. 1) master oscillator, 2) regenerative amplifier, 3) power amplifier, and 4) harmonic generators. The schematic of the optical layout of the ps laser system is depicted in figure 2.2.

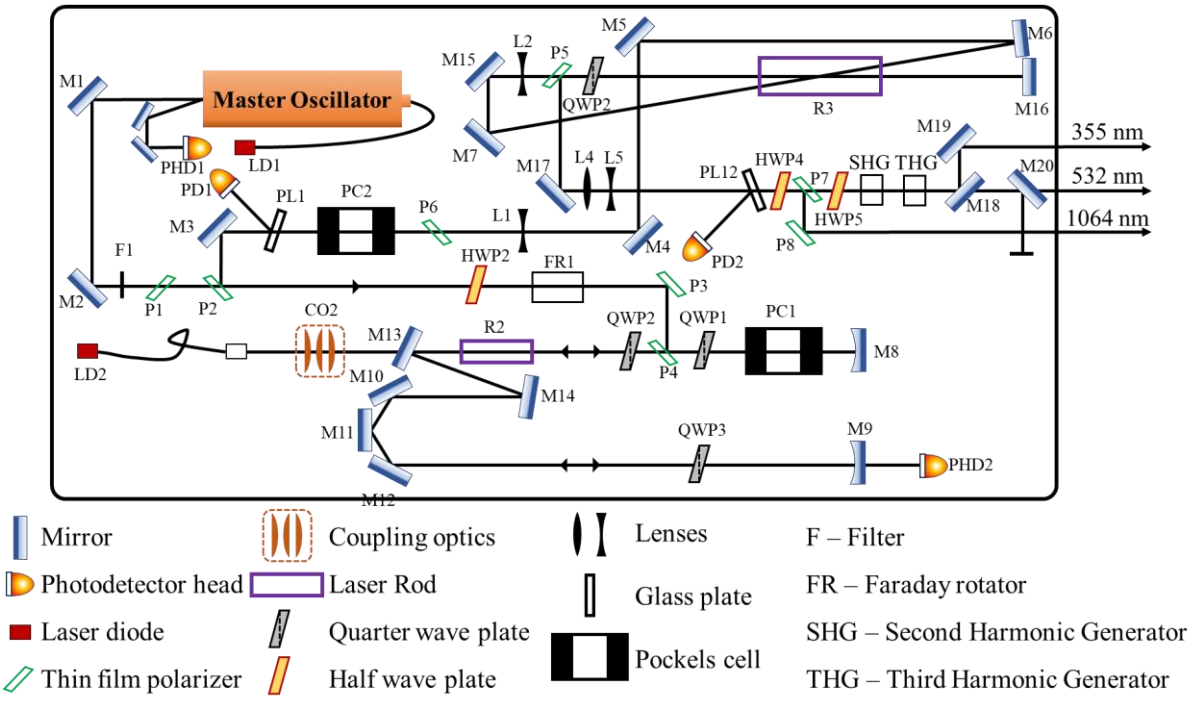

Figure 2.2: Schematic of optical layout of picosecond laser system.

The master oscillator uses Nd: YVO_4 laser material as the gain medium which is pumped by a temperature controlled 2.5 W laser diode. The mode-locking is achieved by means of a saturable absorber. The master oscillator generates two output beams, with one beam serving as a seed for the regenerative amplifier and the other beam used to signal a photo-detector to ensure synchronization with the Pockels cell. The seed pulse passes through a sequence of optical elements: polarizers P1 & P2, half-wave plate HWP2, and Faraday rotator FR1, before being guided into a regenerative amplifier through polarizers P3 & P4. Within the regenerative amplifier system, a laser diode functions as the pump for the Nd: YAG rod R2. The configuration has two mirrors, M8 and M9, which serve as cavity mirrors, while M10-M12 act as a retroreflector pair to enhance stability. The utilization of polarizer P4 and Pockels cell PC1 enables the injection and extraction of pulses into and out of the regenerative amplifier cavity. To prevent the occurrence of free-running mode while allowing pulse injection, a quarter-wave plate QWP1 is utilized. The procedure entails injecting an oscillator pulse from a series of pulses, rapidly increasing the voltage on PC1 to confine the beam within the cavity. The highest level of amplification usually happens after 25-28 cycles, at which point the PC1 voltage is turned off, allowing the fully amplified pulse to be released. In order to avoid the amplified pulse from returning to the master oscillator, Faraday rotator FR1, half-wave plate HWP2, and polarizer P1 were used. These components also help to guide the amplified pulse towards the power amplifier. The regenerative amplifier emits picosecond pulses which are then guided towards the three-pass amplification stage using mirrors M3 - M6. In this stage, a flash lamp is used to pump a Nd: YAG rod R3, which has dimensions of Ø12 × 85 mm. The Pockels cell PC2 and polarizer P6 work together as a pulse picker. When a high voltage is provided to PC2, it rotates the vertical polarization to horizontal. This rotation enables the amplified pulse from the regenerative amplifier to pass through polarizer P6. The pulse can then undergo additional amplification in the power amplifier. Afterward, the amplified pulse with vertical polarization is reflected by polarizer P5 and mirror M17 towards the harmonic generation stage.

The laser emits with fundamental wavelength of 1064 nm and has vertical polarization. The use of nonlinear crystals enables the creation of the second (532 nm) and third (355 nm) harmonics. The mirrors M18-M20 are deliberately placed to separate the harmonics from the primary radiation. The output pulses of the fundamental, second, and third harmonics are directed via three openings on the laser frame. The second harmonic is characterized by a horizontal polarization, while the third harmonic has a vertical polarization.

2.2 Details of Spectrometers

The LIBS studies performed in this thesis utilize a Mechelle spectrometer coupled with an intensified charge-coupled device (ICCD) detector and a Czerny-Turner (CT) spectrometers coupled with charge-coupled device (CCD) detector. All spectrometers are constructed to be durable and do not have any moving components in their optical elements, which ensures strong performance during experiments. Table 2.2 contains detailed technical characteristics for all the spectrometers.

Table 2.2. Various parameters of the Mechelle ICCD spectrometer and Czerny-turner (CT) CCD spectrometer.

S. No.	Parameter	ICCD System	CCD System
1	Spectrograph model	ME-5000 (M/s Andor) istar, DH334T-18U-E3, & DH734-18U-03	AvaSpec ULS2048L-USB2 (M/s Avantes)
2	Resolution @ 500 nm	0.1	0.29
3	Spectral range (nm)	220-850	200-750
4	Weight (Kg)	~ 15	~1
5	Size (10^3 cm^{-3})	~ 9.1	~1
6	Minimum integration time	2 ns	9 μs

2.2.1 Mechelle Spectrometer

The Mechelle spectrometer (ME-5000, M/S Andor) connected to ICCD has become a crucial instrument in gated LIBS investigations, providing exceptional durability and a wide range of spectral options for various applications. The iStar ICCD (DH334T-18U-E3, M/S Andor) is utilized for ps LIBS, while the iStar ICCD (DH734-18U-03, M/S Andor) is used for ns LIBS experiments. This system offers an impressive minimum time resolution of 2 nanoseconds, allowing for accurate study of elemental emissions across time. The spectrometer utilizes an Echelle grating and prism structure to disperse light in a two-dimensional space, which is effectively caught by the ICCD. The spectrometer has 0.1 nm optical resolution at 500 nm wavelength. The device is capable of capturing a broad spectrum of wavelengths, spanning from ultraviolet (220 nm) to near-infrared (850 nm), in a single measurement. The process of calibration involves the use of a standard lamp containing Hg-Ar to assure accurate measurement of wavelengths. Additionally, a Deuterium-Halogen lamp is used for calibration of the intensity. The calibration operations are performed at a constant temperature of 25 degrees Celsius. As a result, the system runs within a restricted temperature range of 25 ± 3 degrees Celsius, which guarantees optimal performance.

2.2.2 Czerny-turner (CT) Spectrometer

A Czerny-Turner CCD spectrometers, namely AvaSpec ULS2048L-USB2 (M/s Avantes), was used for non-gated detection systems in the LIBS experiments. These spectrometer offers promising advantages that make them suitable for real-time use in various applications. Their high cost-effectiveness makes them very appealing for real-time use, while their small size and lightweight design enhance portability, making them perfect for miniaturized LIBS applications. The spectrometer has the capability to measure wavelengths ranging from 200 to 750 nm. It has a remarkable resolution of 0.29 nm at 500 nm and requires a minimum integration time of 9 microseconds to capture spectra. Another benefit of this spectrometer is its capacity to function without a cooling system for the CCD, which improves its practicality and usability in different experimental environments.

2.3 LIBS Experimental Setup

This thesis involved conducting LIBS experiments using both ns and ps lasers. The spectra were obtained using both gated and non-gated detectors. Figure 2.3 depicts the temporal processes that take place in LIBS over time in relation to the laser pulse, but the time scale shown is not to scale.

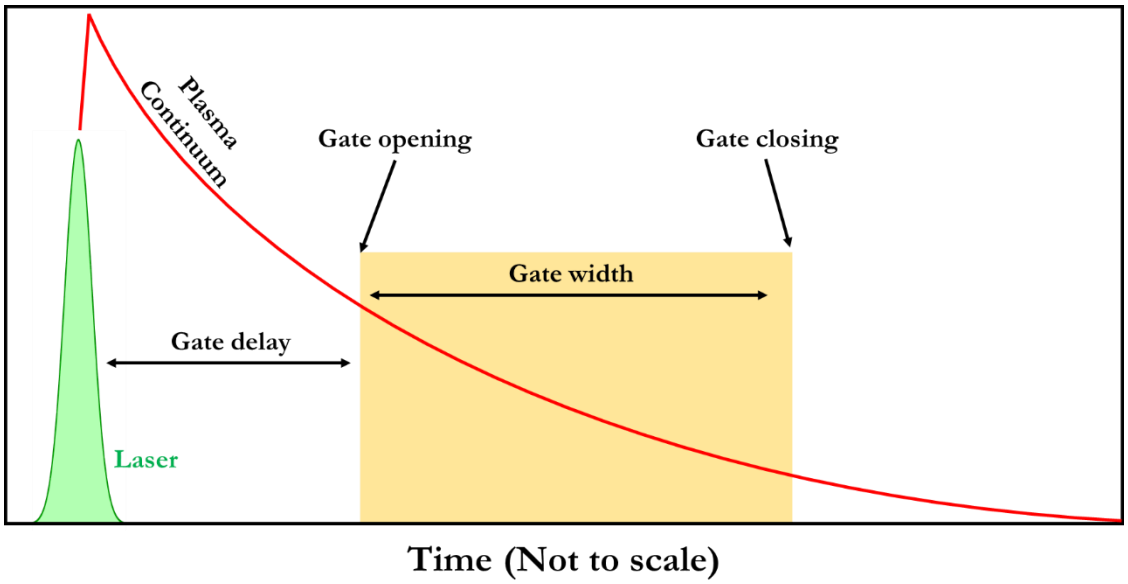

Figure 2.3: Timing diagram for data acquisition using gated LIBS setup.

Gating functionality proves crucial as it effectively mitigates the overwhelming continuum emissions from the plasma during earlier time intervals, preventing detector saturation and damage. In this thesis, delay periods ranging from around 0.2 to 0.5 μs were employed for the

experiments. The implementation of the gated detection system enables the capture of spectra at different delay periods, which is essential for accurately characterizing the temporal behavior of plasma parameters such as plasma temperature, intensity ratio, etc. Comprehending the temporal changes in plasma characteristics is especially relevant in elemental analysis.

2.3.1 Gated LIBS Setup

The typical diagram of the gated LIBS experimental setup, shown in Figure 2.4, demonstrates the primary components used in the experimental setup. The experimental setup for the ns and ps setups is largely similar, with the exception of the laser wavelength and the ICCD camera used. Essentially, the laser beam (ns/ps) is guided by a sequence of mirrors originating from the laser head, and a Plano-convex lens focuses it onto the surface of the sample. The sample, placed on an X-Y translational stage, is controlled by a motion controller (ESP-300 M/s Newport), which is interfaced by a self-developed LabView program in order to provide a fresh spot for every laser shot. This prevents the creation of deep craters on the surface of the sample and improves the consistency of acquiring LIBS spectra, shot by shot.

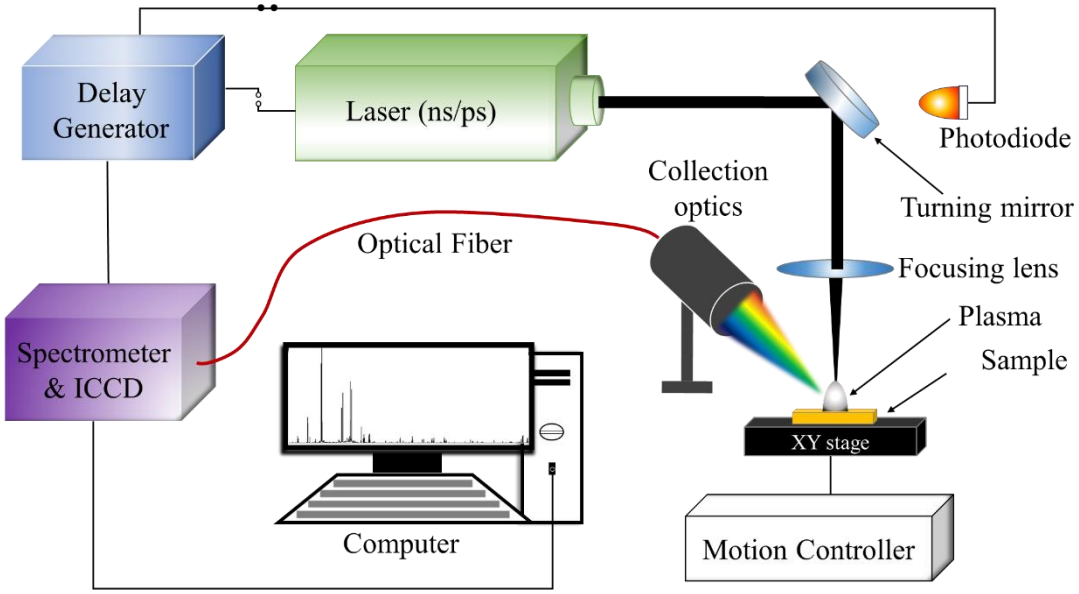

Figure 2.4: Schematic of gated LIBS experimental setup.

The speed of movement of the stage varies in accordance with the experimental settings. The emissions were accumulated by a collection optics assembly (ME-OPT-007, M/s Andor) and transmitted to spectrometers via an optical fibre with a core diameter of 600 μm. The collecting system was oriented at a 45° angle in accordance with the incident laser beam.

The spectra were recorded using a Mechelle spectrograph that was configured with ICCD detectors. The 'i-Star DH334T-18U-E3' detector was used for ps measurements, while the 'i-

Star DH734-18U-03' detector was used for ns measurements. The laser pulse was synchronized to the ICCD using a delay generator (DG-645, M/S Stanford Research Systems). Initially, the delay generator was triggered by by a photodiode or the Pockels cell signal of the laser. Then, it produced a TTL pulse (0-5 V, rise time approximately 2 ns) which further triggers the ICCD. The temporal events were seen and recorded using an oscilloscope (TDS-2024B by M/S Tektronix). A visual representation of the different temporal events of data acquisition can observed from the oscilloscope as displayed in figure 2.5.

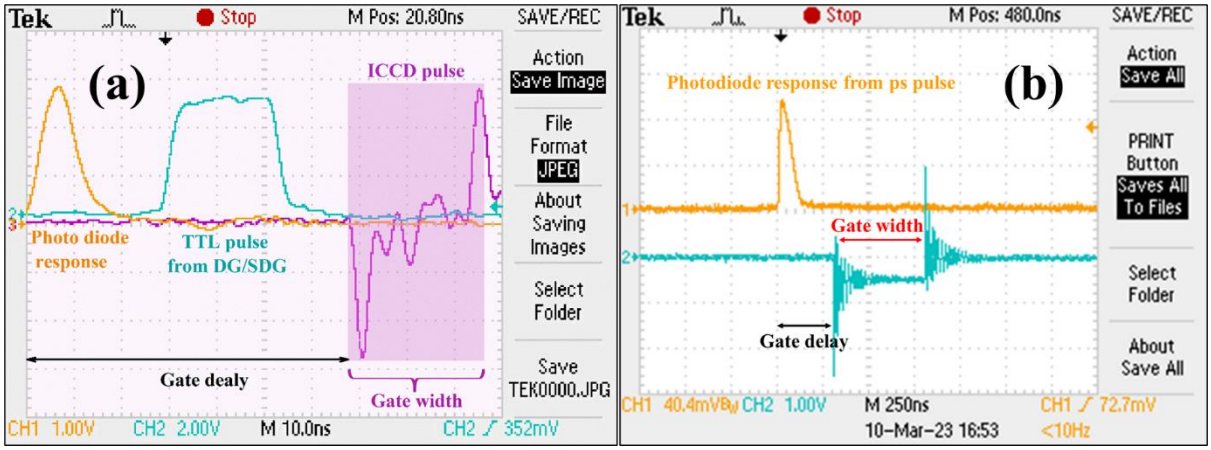

Figure 2.5: Oscilloscope screenshots for monitoring the gate delay and gate width for (a) ns and (b) ps LIBS data acquisition [figure (a) adopted from Ph.D. thesis of Dr. Rajendhar Junjuri].

2.3.2 Non-gated LIBS Setup

Figure 2.6 illustrates the optical configuration of the non-gated LIBS experimental setup. It comprises a ps laser delivering energy of 10 mJ per pulse at 10 Hz repetition rate. The laser operated at its fundamental wavelength of 1064 nm with a pulse duration of ~30 ps. The laser pulse was focused on the sample surface through a plano-convex lens (focal length of 15 cm) to produce the plasma. An XY-translation stage controlled by a motion controller (Newport, ESP 300) was used to move the sample to avoid deep crater formation at the same spot. The emissions from the plasma were collected by a collection optics assembly (Andor, ME OPT 007) and sent through an optical fiber of core diameter 600 μm to a non-gated Czerny Turner CCD spectrometer (Avantes, AvaSpec – ULS2048L – USB2) of optical resolution of ~0.29 nm. The spectrometer produces the LIBS spectra in the 200 – 750 nm wavelength range.

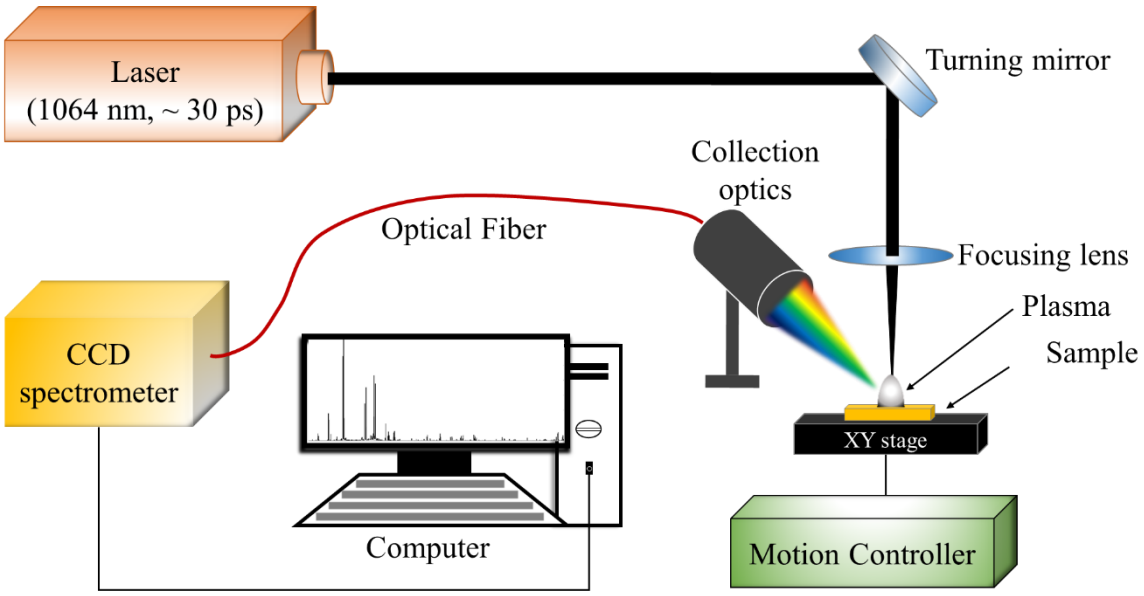

Figure 2.6: Schematic of non-gated LIBS experimental setup.

2.4 Raman Experimental Setup

The schematic diagram of the Raman experimental setup is pictured in figure 2.7. In detail, a compact portable diode-pumped continuous-wave (CW) laser (M/s, OceanOptics – I0785MM0350MS) emitting monochromatic light at 785 nm and delivering a maximum power of ~350 mW was used[3]. The laser light was focused onto the sample surface using a Raman probe (M/s, (OceanOptics – RIP-RPB-785-FC-SMA) of a working distance of 7.5 mm and spectral range of 300 – 3900 cm^{-1}. The same probe collects the Raman scattering and delivers them to a Czerny-Turner CCD spectrometer (M/s, Ocean Optics – QEPro) which has a detection range of 300 – 3000 cm^{-1} and optical resolution of 11 cm^{-1}.

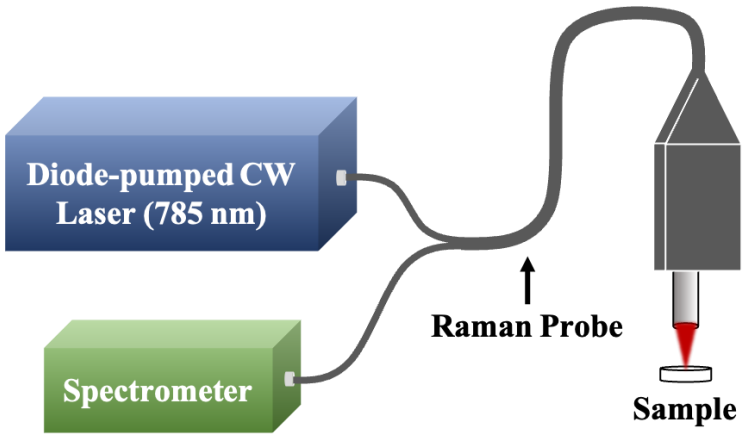

Figure 2.7: Schematic of Raman experimental setup.

The manufacturer provided software for capturing spectra, which was synchronized with the PC using a USB link. Nevertheless, the act of conserving is both time-consuming and tedious.

In order to optimize this task, a LabVIEW program was specifically designed for spectrum measurements. This customized software not only speeds up the process of obtaining Raman spectra but also decreases the probability of experimental errors occurring during the acquisition process. Figures 2.8 and 2.9 depict the LabVIEW graphical user interface (GUI) and block diagram, respectively.

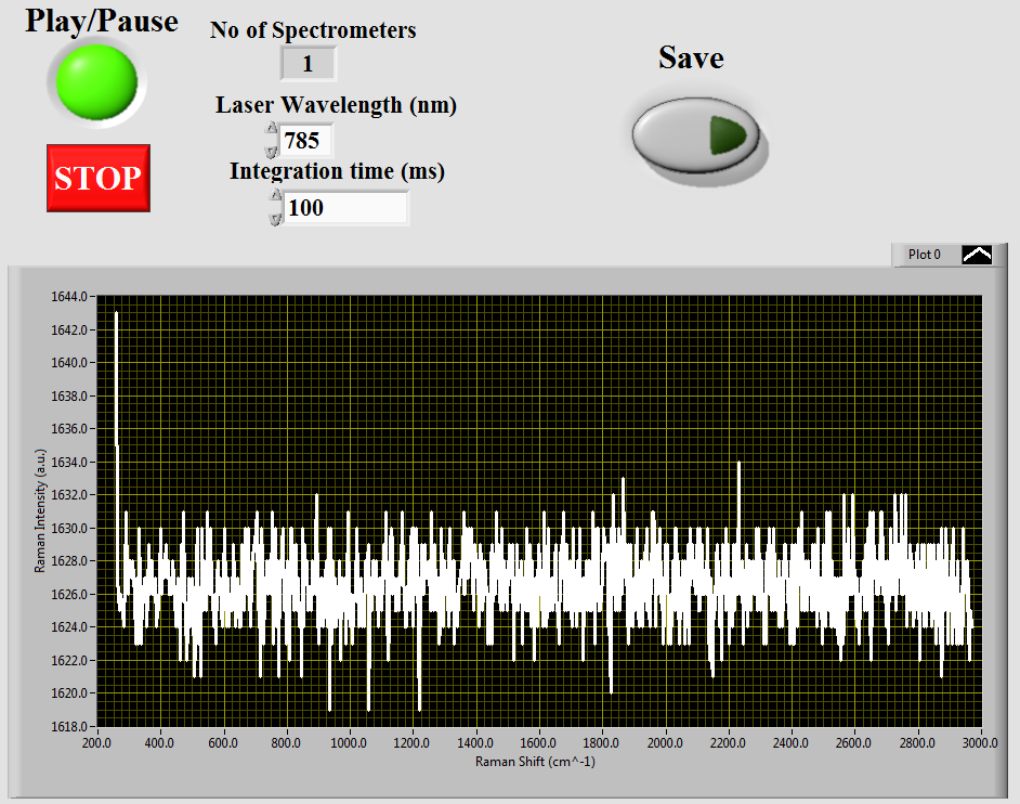

Figure 2.8: LabView GUI for recording Raman spectra.

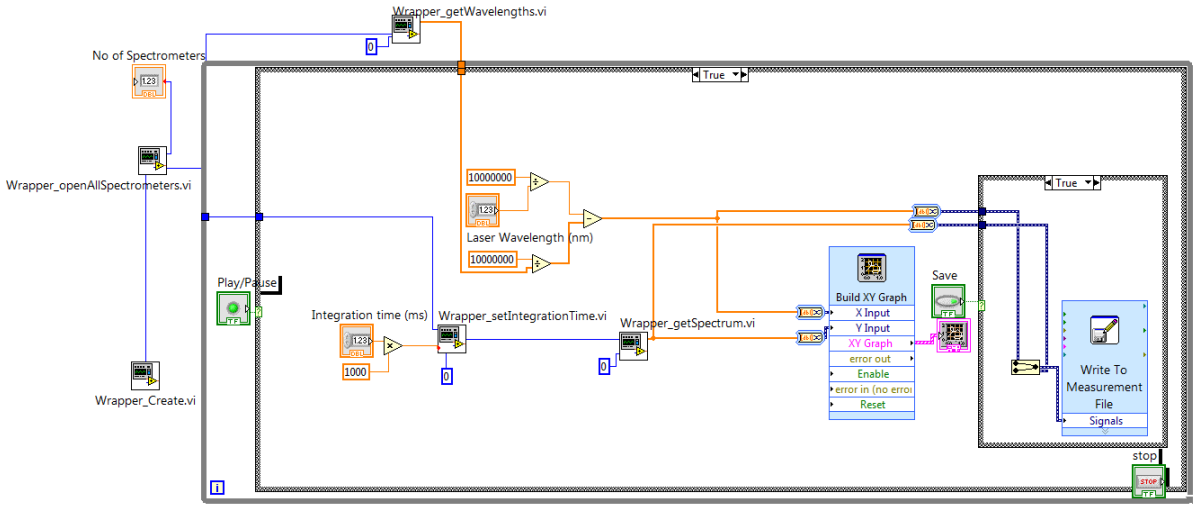

Figure 2.9: LabView block diagram for recording Raman spectra.

2.5 Summary

This chapter explores the complex aspects of laser systems used, with a specific emphasis on nanosecond (ns) and picosecond (ps) laser configurations. Table 2.1 presents a comprehensive comparison of their specifications, encompassing the laser model, pulse duration, wavelength, repetition rate and maximum output energy,. The nanosecond laser system, SpitLight 1200 manufactured by Innolas, and the picosecond laser system, PL 2250 manufactured by Ekspla, are thoroughly explained, providing detailed information about their structures and operational principles. The chapter delves more into the spectrometers used in the experiments, specifically focusing on the Mechelle ICCD spectrometer and the Czerny-Turner CCD spectrometer. It discusses their technical features and many applications. In addition, this text provides detailed explanations of the experimental setups for both gated and non-gated detections in LIBS, including information about their temporal processes and instrumental configurations. The Raman experimental setup includes a diode-pumped continuous-wave laser and a Czerny-Turner CCD spectrometer, which are described in detail. The chapter focuses on the creation and operation of a LabVIEW program designed specifically for spectrum measurements, with the goal of improving efficiency and reducing experimental mistakes.

2.6 Reference

[1] A.K. Tarai, R. Junjuri, S.A. Rashkovskiy, M.K. Gundawar, Time-Dependent Intensity Ratio-Based Approach for Estimating the Temperature of Laser Produced Plasma, Appl. Spectrosc. (2022) 00037028221117534.

[2] A.K. Tarai, M.K. Gundawar, Possibility of Plastic Discrimination using Picosecond Laser Induced Breakdown Spectroscopy, in: 2022 Work. Recent Adv. Photonics, IEEE, 2022: pp. 1–2.

[3] A.K. Tarai, M.K. Gundawar, Raman spectroscopy combined with machine learning for the quantification of explosives in mixtures, J. Opt. (2023) 1–9.

Intentional Blank Page

Chapter 3

Simplified LIBS-based Intensity-ratio approach for Concentration Estimation

This chapter presents the application of plasma diagnostics and elemental analysis in the examination of two distinct alloy samples, one binary and one ternary. A brief summary of the experimental methods and the spectral interpretation of plasma is provided in the initial sections. The basics of thermodynamic equilibrium, as well as the determination of plasma parameters and plasma decay parameters (PDPs), are covered in depth. The temporal behavior of LIP is characterized by modeling the decay of plasma temperature and intensity ratio. The last section focuses on the elemental analysis using calibration-free LIBS (CF-LIBS), Electron Dispersive X-ray Spectroscopy (EDS), and a newly proposed method, Simplified LIBS-based Intensity-ratio approach for Concentration Estimation (SLICE). The elemental concentrations estimated by SLICE for both binary and ternary alloys are in good agreement with CF-LIBS and EDS. Additionally, the chapter briefly discusses the benefits and drawbacks of these analytical techniques, providing insightful information on how they might be used for elemental analysis.

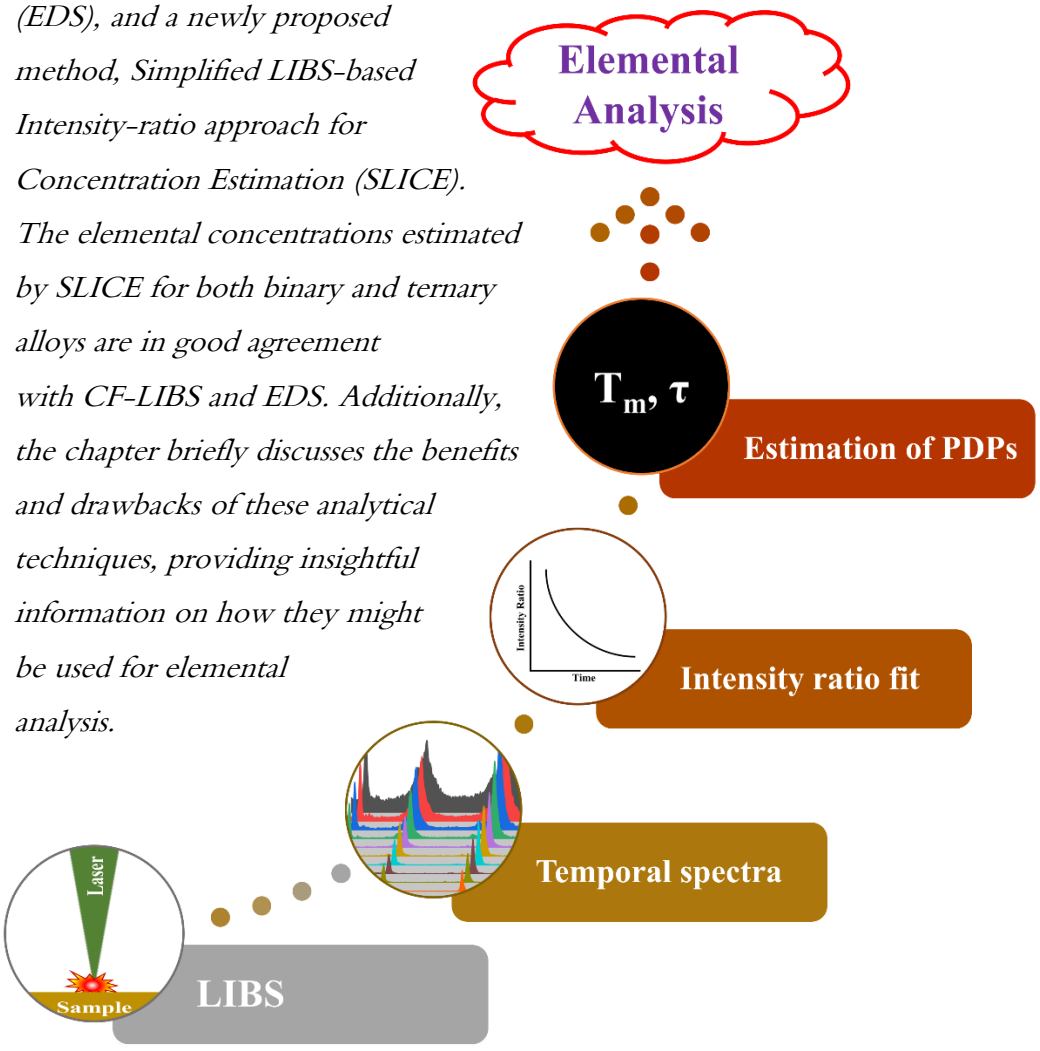

3.1 Introduction

Elemental analysis using LIBS is one of the most demanding disciplines due to its robust experimental setup. Several LIBS techniques have been developed for elemental analysis of various materials in different forms (solids, liquids, and gases). Quantitative elemental analysis was first introduced in LIBS in the late 1980s and early 1990s[1–3]. The first method uses calibration curve to estimate the concentration of each element in a sample. This method, however, is constrained by the need for calibration curves for each matrix element, which can only be used for samples with the same matrix and must be reconstructed for samples with different matrices. Therefore, in real-life applications, while calibration LIBS excels in detecting species concentrations within a well-defined matrix, it is not suitable for complex situations like multi-elemental analysis of unknown materials.

To overcome these problems, A. Ciucci et al. introduced a new method called calibration-free LIBS (CF-LIBS), where the need for a calibration curve or matrix-matched standard was eliminated in the concentration estimation[4]. Since then, this technique has been extensively used to analyze alloys[5], meteorites[6], soils[7], rocks[8], minerals[9], organic materials[10], etc. This technique has been evolving as a powerful multi-elemental analysis tool enabling quantitative analysis of various materials in laboratory setups. However, in CF-LIBS, the self-absorption (SA) effect is a major disruption of emission intensities at respective wavelengths. The SA of a certain emission line occurs when the emitted radiation of that atom is absorbed by another atom, resulting in a decrease in emission peak intensity. For CF-LIBS, it is essential to estimate plasma temperature using the Boltzmann/ Saha-Boltzmann plot method[4,11,12]. In principle, these methods require at least two SA free emission lines with a well-separated upper energy level for each constituent element in the sample. Still, in the practical scenario, researchers always consider several emission lines from each element to retain accurate temperature values[11,13]. The availability of such quantities of SA free lines is difficult to observe for many elements (e.g., C, H, N, O, Na, B, etc.) in the UV – VIS – NIR range of LIBS spectrum. Also, the observable emission lines are scarce in the case of trace elements. Therefore, SA correction becomes essential for the universal adoption of CF-LIBS for elemental analysis.

Several approaches and techniques have been devoted to literature for correcting the self-absorbed lines in the spectra of LIP. Initially, D. Bulajic et al. developed the curve of growth (COG) technique[14], which estimates the SA coefficient by an iterative simulation. The SA

coefficient was also determined by calculating the ratio of the observed emission intensity to the theroretical intensity in the absence of the SA effect[15]. Later, L. Sun et al.[16] introduced a technique less complicated than the COG technique, namely the internal reference for SA correction (IRSAC). This technique chooses an internal reference line from each species and based on its intensity, corrects all other SA lines through a regressive algorithm. F. Rezaei et al.[17] used artificial neural network and J. Dong et al.[18] used genetic algorithm to correct the self-absorbed lines. Apart from these, I. Karnadi et al.[19] proposed a technique to suppress the SA effect by making some modifications to the experimental setup, i.e., they used a double pulse LIBS setup to create a vacuum-like condition in the air for recording the spectra. Y. Zhang et al.[20] developed SA correction method using plasma images and employed it in underwater LIBS. Numerous other methods or approaches were devoted to literature concerning SA correction[21–23]. However, these techniques are more time-consuming and increase the complexity of the analysis. Certain individuals meet challenges in practical use, such as the IRSAC approach, which experiences issues when emission lines of various elements are affected by SA differently, resulting in inconsistent plasma temperatures. The genetic algorithm method is also not optimum as it requires a standard sample. Moreover, most of these studies require different theoretical parameters which may not be available for the emission lines of interest limiting the SA correction. More importantly, the involvement of the SA correction procedure makes the CF-LIBS more complex and time-consuming. In specific scenarios where SA correction is not necessary, CF-LIBS may be quick and easy to use in practice. Likewise, CF-LIBS several other calibration-free approaches have been developed like columnar density CF-LIBS, one line CF-LIBS (OLCF-LIBS), inverse CF-LIBS etc. However, the above-mentioned techniques also follow Boltzmann or Saha-Boltzmann plot method for estimation of plasma temperature in its procedure likewise CF-LIBS and also share its limitations.

To overcome these limitations, a new, robust, more straightforward method for fast quantitative elemental analysis is proposed in this chapter. The major advantage of this technique is that it doesn't involve Boltzmann/Saha-Boltzmann plot in the calculation. The requirement of a few numbers of emission lines makes it a more robust and straightforward technique. It demands only two emission lines from any one of the elements and a single line from all other elements. For example, a sample of n elements requires only n+1 emission intensity lines. Since only one emission line is needed from every element except any one element in the sample, now there is a great flexibility of choosing emission lines that are not affected by SA. Also, this approach significantly reduces the complexity of the calculation as

fewer steps are involved. Since the method relies on intensity ratios to determine concentrations, it is named as SLICE (Simplified LIBS-based Intensity-ratio approach for Concentration Estimation).

In this chapter, the plasma diagnostics and temporal characterization of plasma parameters are discussed briefly. The estimation of plasma temperature and plasma decay parameters (PDPs) of LIP using intensity ratio and radiative relaxation mechanism is discussed, followed by elemental analysis of two copper-based alloys using the CF-LIBS and SLICE techniques. The theory, working procedure, advantages and limitations of these methods were elaborated.

3.2 Experimental Details

The schematic of the experimental setup is shown in chapter 2 (figure 2.4). In brief, it comprises a Q-switched Nd:YAG laser (Spitlight 1200, M/s Innolas,) that produces ~7 ns laser pulses of energy ~50 mJ/pulse at a wavelength of 532 nm with a repetition rate of 1 Hz. The laser pulse was guided by a mirror and focused onto the sample surface using a plano-convex lens (focal length: 10 cm) in ambient atmosphere. The sample was mounted on an XY translation stage, controlled by a motion controller (Newport, ESP-300) to ensure a fresh surface spot for each laser pulse. A collection optics assembly (Andor, ME-OPT-0007) was aligned at approximately 45 degrees to the incident laser beam to collect the LIP emission light. Further, the light was directed towards an echelle spectrograph (Andor, Mechelle ME-5000) through an optical fiber of 600 μm core diameter and 2 m length. The spectrograph has been equipped with an ICCD (Intensified charge-coupled device) camera as a detector (Andor, iSTAR DH734). A delay generator (SRS-DG-645) was used to electronically trigger the ICCD with respect to the Pockels cell of the laser in order to avoid electronic interference and jitters. The spectrograph covers the spectral range of 220-850 nm.

LIBS experiment was conducted on two Cu alloys (binary and ternary). The binary alloy consists Cu and Zn, whereas the ternary alloy contains Cu, Zn and Ni as elemental composition. Temporal kinetic series spectra of the alloys were recorded in ambient air at atmospheric pressure. Each spectrum was collected after an initial delay of 0.5 μs to avoid the high intensity of continuum radiation at the initial period of plasma formation. The ICCD gain was set to 100 to obtain a strong signal. Time evolution spectra were collected in the 0.5 – 5 μs temporal window with a constant step and gate width of 0.5 μs. Each spectrum was

averaged over 10 spectra to increase the signal-to-noise ratio. Likewise, 10 sets of time evolution spectral data were recorded for each alloy.

3.3 Spectral interpretation

The emission spectra of LIP have been recorded in the temporal window of plasma relaxation (0.5 – 5 μs). The spectra corresponding to both the alloys recorded at 1 μs delay with 0.5 μs gate width is graphically presented in figure 3.1. Originally, the spectrum was recorded in the wavelength range of 220 – 850 nm, where those wavelength ranges having intensity emission lines of interest (i.e., 230 – 570 nm) are depicted. All the spectral emission lines in the spectrum were identified with the help of the NIST atomic database[24]. After identifying all the lines, it has been observed that binary alloy contains Cu and Zn, whereas ternary alloy contains Cu, Zn, and Ni as expected. Some of the prominent emission lines were marked in the spectra. Very less intense emission signatures of N and O were also observed due to the contribution of atmospheric air. It is obvious from Fig. 3.2 that Cu- 324.80, 327.27, 393.39, 427.58, 465.18, 510.55, 515.29, and 521.86 and Zn- 328.25, 330.27, 334.51, 472.30, and 481.13 emission lines emit intense radiation. The energy level diagram of some prominent transitions is presented in figure 3.2.

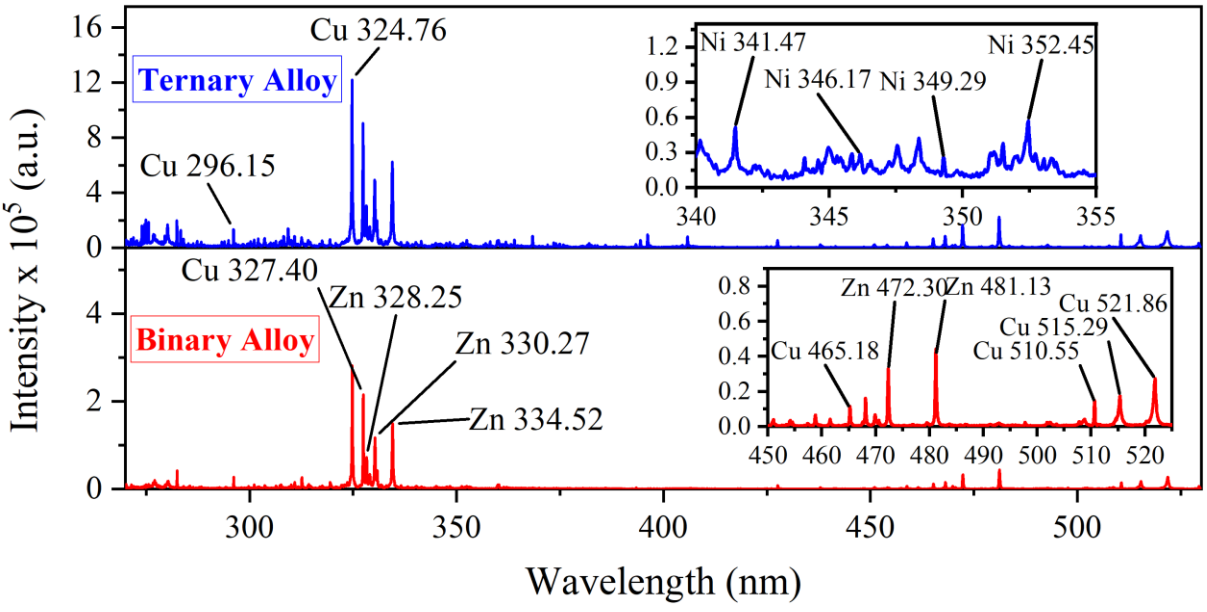

Figure 3.1. Emission spectra of binary and ternary alloy recorded at 1 μs delay.

Investigating the time dependence of LIP emission intensity is crucial because, after plasma formation (termination of laser pulse), it expands, resulting in plasma cooling due to thermal energy loss. As a result, the plasma temperature and hence the emission intensities gradually decrease over time. The time-dependent spectra of both alloys are depicted in figure 3.3 and

3.4. From the figures, it can also be noticed that there is a background in the spectra of both the alloys at the early stage, i.e., up to 1 μs which is completely absent in the later stage. This could be due to the dominance of the plasma continuum at the early stage of plasma relaxation. Also, a high signal-to-noise ratio is observed at the early time which decreases gradually with the decrease in emission intensities.

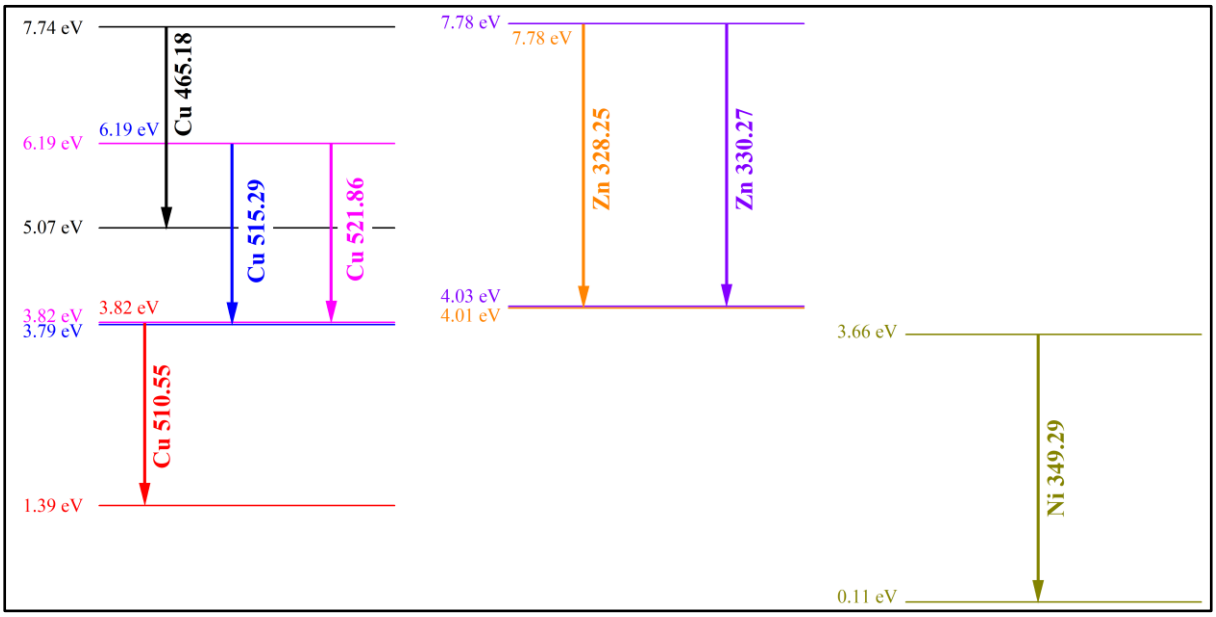

Figure 3.2. Energy level diagram of Cu, Zn and Ni transitions.

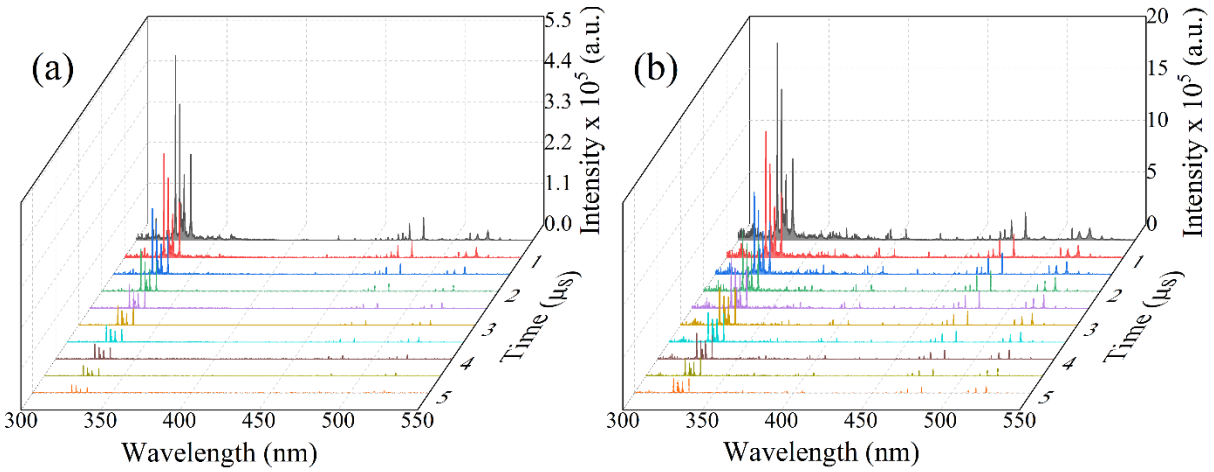

Figure 3.3. Time-dependent spectra of (a) binary and (b) ternary alloy.

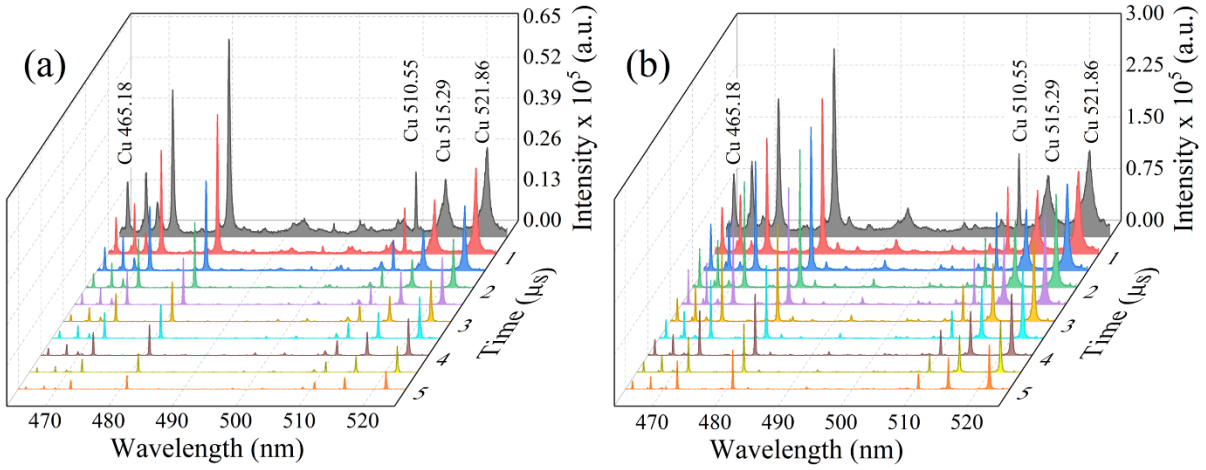

Figure 3.4. Expanded view of the time-dependent spectra of (a) binary and (b) ternary alloy in the range of 464 – 525 nm.

3.4 Plasma diagnostic studies

3.4.1 Thermodynamic equilibrium (TE) and local thermodynamic equilibrium (LTE) in LIP

LIP refers to a localised assembly of atoms, ions, electrons, and radiations. In a condition of thermodynamic equilibrium (TE), the distribution of energy among the many states of the particle assembly can be characterised by a single temperature. It is possible when the 'principle of detailed balance' holds, i.e., the rate of forward and reverse processes at a given energy level is equal. Also, the plasma should be optically thick in order to achieve radiative equilibrium. In practice, this situation is rarely complete, so physicists have adopted some approximations to to characterize the condition of the plasma, known as local thermodynamic equilibrium(LTE)[25,26]. According to LTE approximation, the plasma is in thermal equilibrium in a small region of the LIP.

Under LTE, the velocity distribution of particles follows classical Maxwellian distribution as,

$$f(v)dv = \left(\frac{m}{2\pi k_B T}\right)^{\frac{3}{2}} \exp\left(\frac{-mv^2}{2k_B T}\right) 4\pi v^2 dv \qquad (3.1)$$

where k_B is the Boltzmann constant, T is the temperature, v and m are the speed and mass of the particle, respectively.

The relative population of the plasma species (electrons and ions) in the excitation state is given by the Boltzmann distribution,

$$N_i = N_0 \frac{g_i}{Z(T)} \exp\left(\frac{-E_i}{k_B T}\right) \tag{3.2}$$

where N_i, N_0, g_i, $Z(T)$, E_i are the population of i^{th} level, population of the total species, statistical weight of the i^{th} level, partition function, energy of the i^{th} level respectively.

The LTE plasma exhibits a single temperature that accounts for the arrangement of species across energy levels, the kinetic energy of electrons or ions, and the population of ionization states. Hence, the excitation temperature, which regulates the population of atomic energy levels, must be equivalent to the ionization temperature, which dictates the distribution of atoms across various ionization states.

The elemental species are populated in ionization states according to by Saha – Eggert equation which can be expressed as,

$$n_e \frac{N^{j+1}}{N^j} = \left(\frac{2\pi m k_B T}{h^3}\right)^{\frac{3}{2}} \frac{2Z^{j+1}(T)}{Z^j(T)} \exp\left(\frac{-E_j + E_{j+1} - \chi}{k_B T}\right) \tag{3.3}$$

where N^j and N^{j+1} are the number density of j^{th} and $(j+1)^{th}$ ionization state respectively. n_e, h and χ are the electron number density, Planck's constant and first ionization energy of an isolated system.

3.4.2 Estimation of plasma temperature (Boltzmann plot)

Plasma temperature is a characteristic parameter of LIP that influence the spectral emissions of the plasma. Under LTE approximation, the population of a neutral ionic species at a particular temperature follows Boltzmann distribution as mentioned in equation 3.2. The spectral line intensity of the emitted radiation is given by the following expression,

$$I_{ij} = \frac{h\nu A_{ij} N_i}{4\pi} \tag{3.4}$$

where I_{ij} represents the intensity of emission due transition of species from i^{th} to j^{th} energy level, ν is the frequency of the emission and A_{ij} is the transition probability of the emission line. Substituting equation 3.2 in equation 3.4,

$$I_{ij} = \frac{hcN_0 A_{ij} g_i}{4\pi\lambda_{ij} Z(T)} \exp\left(\frac{-E_i}{k_B T}\right) \tag{3.5}$$

where c and λ are the speed of light and wavelength of emission, respectively.

Simplifying equation 3.5,

$$\ln\left(\frac{I_{ij}\lambda_{ij}}{A_{ij}g_i}\right)=\frac{-E_i}{k_BT}+\ln\left(\frac{FC}{Z(T)}\right) \tag{3.6}$$

where F and C are the experimental factor and elemental concentration of the species, respectively.

In equation 3.6, A_{ij}, g_i and E_i are the spectroscopic parameters that are available in NIST atomic database, I_{ij} and λ_{ij} are experimental parameters that are observed in the spectra and k_B is the constant. A plot of the LHS of equation 3.6 vs E_i has a slope of -1/kBT; therefore, plasma temperature T can be inferred by straight line fit.

In the current experimental picture, for the estimation of plasma temperature using the Boltzmann plot method (equation 3.6), four neutral emission lines of copper at 465.18, 510.55, 515.29 and 521.86 nm were considered. These lines were assumed to be self-absorption free emission lines based on earlier reports[13,27]. The energy level diagram of these lines are depicted in figure 3.3 and the spectrometric parameters are listed in table 3.1.

Table 3.1. Spectroscopic parameters of copper emission lines.

Sl. No.	λ_{ij} (nm)	E_i (eV)	E_j (eV)	A_{ij} (10^8 s^{-1})	g_i	g_j
1	465.18	7.737	5.072	0.38	8	10
2	510.55	3.816	1.388	0.02	4	6
3	515.29	6.192	3.785	0.60	4	2
4	521.86	6.192	3.816	0.75	6	4

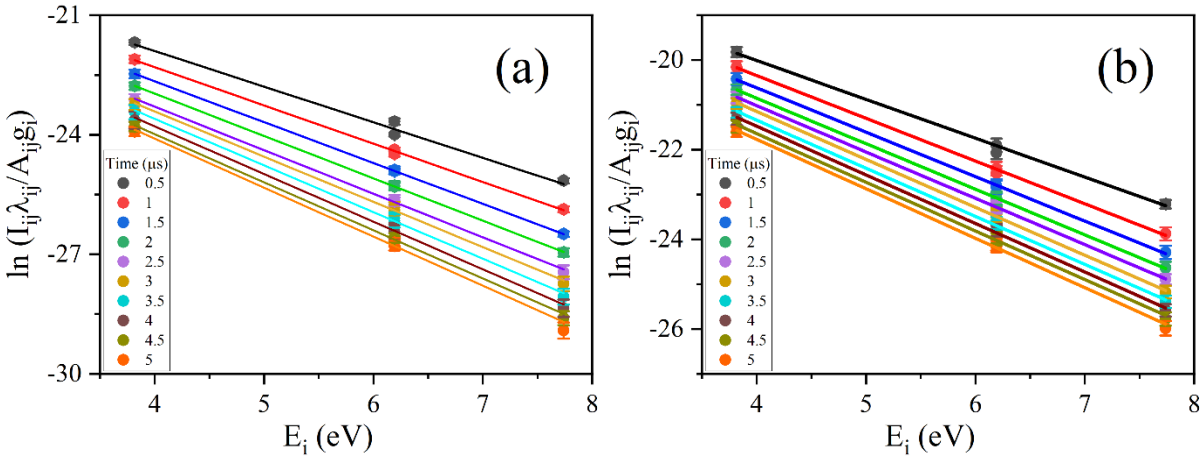

Figure 3.5. Boltzmann plot of Cu emission lines for (a) binary and (b) ternary alloy.

The Boltzmann plot of Cu emission lines for both the alloy sample at each delay is depicted in figure 3.5. From the figure, it can be noticed that the straight line fitted well w.r.t. the

experimental data at every delay for both the samples and have high R square value close to one. The temporal variation of plasma temperature of LIP of both the samples are represented in figure 3.6. It is observed that the plasma temperature decreases gradually with time. The temperature and intercept obtained from the Boltzmann plot also serve as essential parameters for elemental analysis when employing CF-LIBS, a topic that will be further elaborated upon in the upcoming sections.

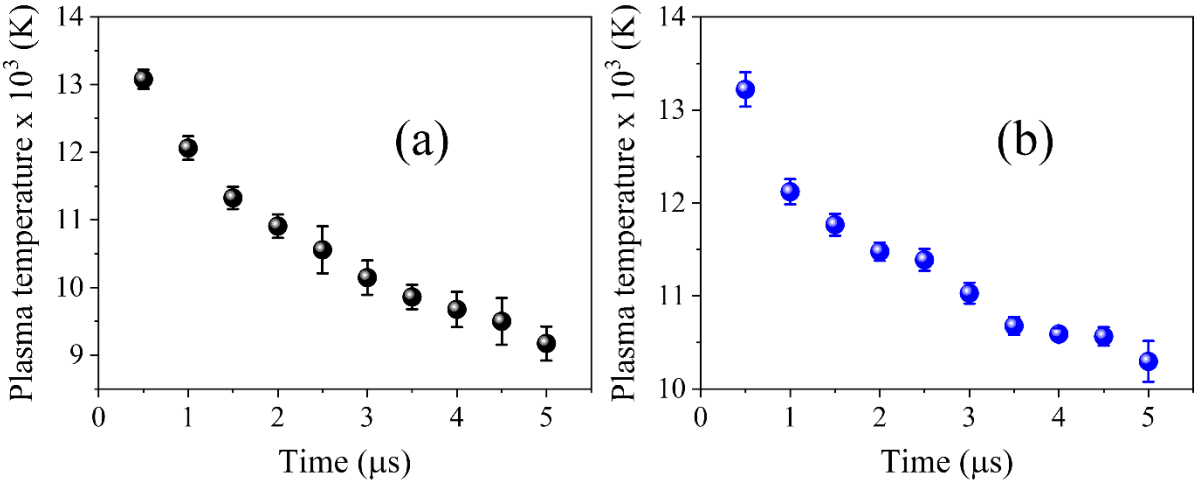

Figure 3.6. Temporal evolution of plasma temperature of LIP of (a) binary and (b) ternary alloy.

3.4.3 Estimation of electron number density

Electron number density is another characteristic parameter of LIP that can be determined from the width of the spectral line. The primary factor responsible for the broadening of the emission lines is the combined effect of natural, Doppler, and Stark broadening. The spectral transition's minimum linewidth is determined by its inherent natural linewidth, which is caused by the finite lifetime of species (atoms/ions) in their excited states. The natural broadening of the linewidth is very samll can be ignored. Doppler broadening occurs due to the Doppler effect caused by the varying velocities of atoms, ions, or molecules. The emitted radiation is dependent on the spectral line's frequency (or wavelength), plasma temperature, and the mass of the emitting particles.The expression for Doppler broadening ($\Delta\lambda_D$) is given by,

$$\Delta\lambda_D = 7.16 \times \lambda_{ij} \times 10^{-7} \sqrt{\frac{T}{M}} \tag{3.7}$$

where T and M are the plasma temperature and atomic mass of the species, respectively. The value of $\Delta\lambda_D$ is found to be in the order of few picometers which is much less compared to

the resolution of spectrometers used for LIBS experiments (For example, Andor Mechelle 5000 spectrometer has resolution of 100 pm at 500 nm), thus, the contribution of Doppler broadening can also be neglected. Therefore, only Stark broadening is responsible for the broadening of LIBS emission lines.

The interaction between charged particles within the plasma and the electric field induces perturbations in the energy levels of the particles, resulting in the broadening of spectral lines, commonly referred to as Stark broadening. This broadening is directly proportional to the electron density. The full width at half maximum (FWHM), $\Delta\lambda_{1/2}$ of the Stark broadened line is given by the following expression,

$$\Delta\lambda_{1/2} = 2w\left(\frac{n_e}{10^{16}}\right) + 3.5A\left(\frac{n_e}{10^{16}}\right)^{\frac{1}{4}}\left(1-1.2N_D^{\frac{-1}{3}}\right)w\left(\frac{n_e}{10^{16}}\right) \tag{3.7}$$

where w, n_e, A and N_D are the electron impact width parameter, electron density, ion broadening parameter and number of particles in Debye sphere, respectively. w and A can be obtained from literature and N_D can be calculated using the following expression[28],

$$N_D = 1.72\times10^9 \frac{T^{3/2}}{n_e^{1/2}} \tag{3.8}$$

The first term on the right-hand side of equation 3.7 pertains to electron broadening, while the second term corresponds to ion broadening. Given that the impact of ion broadening is minimal, equation 3.7 simplifies to,

$$\Delta\lambda_{1/2} = 2w\left(\frac{n_e}{10^{16}}\right) \tag{3.9}$$

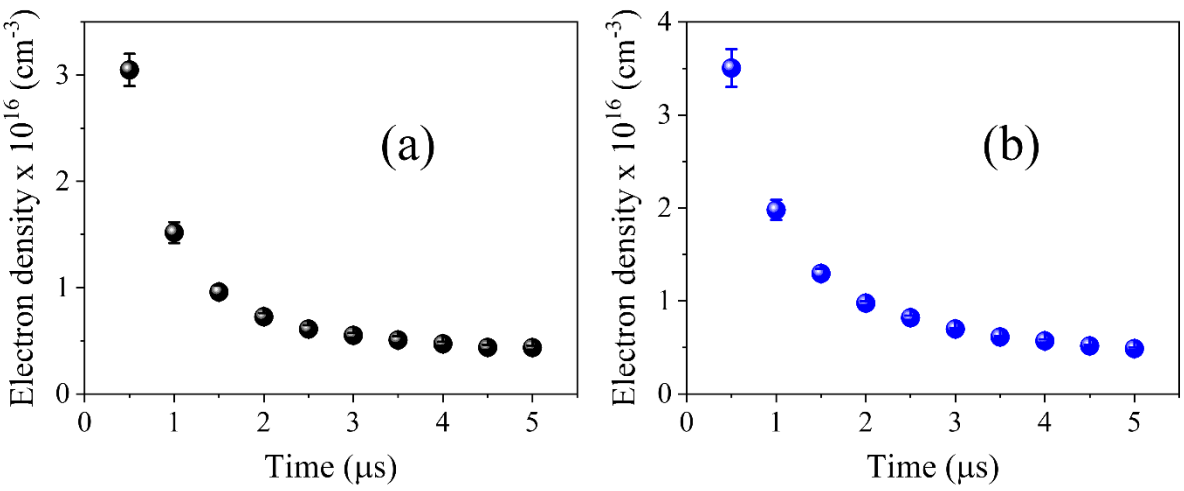

Figure 3.7. Temporal evolution of electron density (a) binary and (b) ternary alloy.

Therefore, the electron density n_e can be calculated using equation 3.9 where $\Delta\lambda_{1/2}$ is the FWHM of the observed emission line. The electron density values at each temporal delay for both the alloy samples were estimated using the Cu emission lines at 515.29 nm. The temporal variation of electron density of both the samples are represented in figure 3.7. The electron density exhibits a rapid decay during the initial phase of plasma expansion (within the first 2 μs), followed by a gradual reduction. Following the creation of plasma, the electrons inside the plasma undergo recombination with the ions as the plasma expands, resulting in a reduction in plasma temperature.

3.4.4 Theoretical model for temporal evolution of plasma temperature and estimation of PDPs

As the LIP expands in ambient gas, it cools down by emitting electromagnetic radiation and generating shockwave[29–31]. The temporal relaxation of LIP depends on various factors, including nature of the material, experimental parameters (e.g., laser energy, focusing distance, etc.), ambient environment, etc. Temporal dynamics is a complex and not yet completely understood phenomenon. At the initial stages of relaxation, the plasma becomes opaque or optically thick, leading to the emission of a plasma continuum. Subsequently, it becomes semi-opaque/ semi-transparent and at the later time, it becomes transparent or optically thin[32–34]. Nonetheless, for elemental analysis (CF-LIBS), LIP is always assumed as optically thin for duration spanning several microseconds. But, the relation between CF-LIBS and optically thin approximation is not understood properly. In spite of this, CF-LIBS remains a very successful analytical method for precise determination of concentrations and is widely accepted. However, according to the recent report by the same group who originally developed the CF-LIBS, the optically thin approximation may not be a necessary condition for elemental analysis [35].

Owing to the intricate nature of comprehending the temporal dynamics of plasma, the temporal decay of plasma temperature was always approximated to exponential decay which lacking proper theoretical foundation[36–41]. However, Rajendhar et al. made a significant breakthrough by introducing a theory based on radiative cooling of the plasma[42]. This approach is based on the optically thick approximation of the LIP which describes the relaxation using a one-third power-law expression that incorporates two plasma decay parameters (PDPs), namely the initial temperature T_m and radiation decay constant τ. This

theoretical model offers a thorough depiction of the kinetic evolution of LIP, taking into account the radiative relaxation mechanism.

In the context of the present experiment, the duration of the laser pulse (Δt_L) is ~7 ns which is the characteristic time for the formation of LIP whereas the duration of the plasma relaxation (Δt_R) is more than 5 μs; which implies, $\frac{\Delta t_L}{\Delta t_R} \gg 1$. That means the time taken for formation of LIP is much smaller compared to the plasma relaxation time and hence, the time at which the laser pulse is terminated and plasma is formed can be considered as time, t=0 and the temperature at that time can be assumed to be the initial temperature (T_m) of the LIP.

The heat flux density due to thermal conductivity can be estimated by the following expression[27],

$$Q_k \sim \frac{kT}{z} \tag{3.10}$$

where k is the coefficient of thermal conductivity of the medium; T is the plasma temperature; z is the characteristic distance at which the temperature drops from T to the ambient temperature $T_0 << T$.

The energy flux density due to thermal radiation can be represented by the expression,

$$Q_r \sim \sigma T^4 \tag{3.11}$$

where σ is the Stefan-Boltzmann constant.

The ratio between heat flux density due to thermal conductivity and energy flux density due to thermal radiation can be rewritten as the following expression,

$$\frac{Q_k}{Q_r} \sim \frac{k}{z\sigma T^3} \tag{3.12}$$

Considering k ≈ 0.5 $Wm^{-1}K^{-1}$ (which for air corresponds to a temperature of > 3000 K) and T = 10,000 K we obtain the estimation $\frac{Q_k}{Q_r} \sim 0.01$, which shows that in the process under consideration, the thermal conductivity can be neglected in comparison with thermal radiation. Hence, by only accounting for the radiative mechanism governing the plasma temperature decay, the energy conservation law for the plasma can be expressed as[42],

$$mc_v \frac{dT}{dt} = -S\sigma T^4 \tag{3.13}$$

where m, c_v, T, t, S and σ are the mass of the plasma, specific heat of the plasma cloud, plasma temperature, time, surface area of the plasma plume and Stefan-Boltzmann constant, respectively. Assuming m, c_v, and S constant, the solution to the equation 3.13 can be obtained as follow,

$$\int \frac{dT}{T^4} = -\frac{S\sigma}{mc_v}\int dt \tag{3.14}$$

$$\Rightarrow \quad -\frac{T^{-3}}{3} + C = -\frac{S\sigma}{mc_v}t \tag{3.15}$$

where C is the integration constant. By applying boundary condition to equation 3.15, i.e., at time t=0, $T=T_m$,

$$C = \frac{T^{-3}}{3} \tag{3.16}$$

By substituting equation 3.16 in equation 3.15,

$$-\frac{T^{-3}}{3} + \frac{T_m^{-3}}{3} = -\frac{S\sigma}{mc_v}t \tag{3.17}$$

$$\Rightarrow \quad \frac{T^{-3}}{3} = \frac{T_m^{-3}}{3}\left(1 + \frac{3S\sigma T_m^3}{mc_v}t\right) \tag{3.18}$$

$$\Rightarrow \quad \frac{T^{-3}}{3} = \frac{T_m^{-3}}{3}\left(1 + \frac{t}{\tau}\right) \tag{3.19}$$

where $\tau = \frac{mc_v}{3S\sigma T_m^3}$ is the radiation decay constant of the plasma or the characteristic time of the radiation cooling.

Simplifying equation 3.19,

$$T(t) = T_m\left(1 + \frac{t}{\tau}\right)^{-\frac{1}{3}} \tag{3.20}$$

The value of PDPs (T_m and τ) can be estimated by comparing the theoretical dependence (equation 3.20) with temperature derived from experimental data using the Boltzmann plot (section 3.4.2). During data processing, T_m and τ can be considered as the fitting parameters and followed by fitting of experimental data as shown in figure 3.8.

From figure 3.8, it can be observed that the theoretical dependence fitted well with that of the experimental data. In case of binary alloy, the R square of the fitting line is 0.99 and the value of T_m and τ were estimated to be 13900 ± 200 K and 1.96 ± 0.23 μs respectively. Similarly, for ternary alloy the value of R square, T_m and τ are 0.95, 13300 ± 200 and 4.07 ± 0.34 μs respectively. Once PDPs were estimated, the plasma temperature can be calculated at any temporal delay using equation 3.20 irrespective of the experiment.

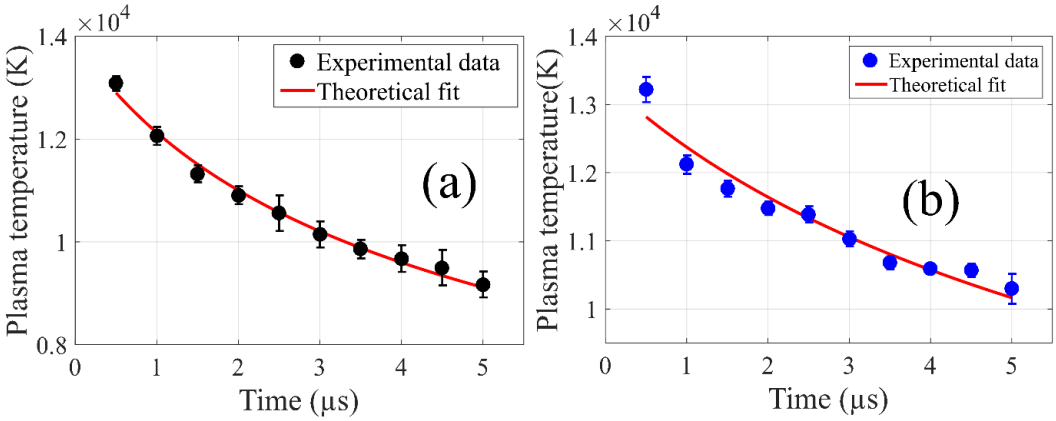

Figure 3.8. Dependence of plasma temperature on time for (a) binary and (b) ternary alloy.

3.4.5 Theoretical model for temporal evolution of intensity ratio and estimation of PDPs

Using equation 3.20 in equation 3.5, the temporal dependence of intensity ratio can be given by,

$$I_{ij}(t) = \frac{hcN_0 A_{ij} g_i}{4\pi\lambda_{ij} Z(T(t))} \exp\left(\frac{-E_i}{k_B T_m}\left(1+\frac{t}{\tau}\right)^{\frac{1}{3}}\right) \tag{3.21}$$

Considering the ratio of emission lines correspond the same species, it is possible to cancel out the common parameters from equation 3.21. The temporal dependence of intensity ratio can be written as,

$$\frac{I_{ij}(t)}{I_{mn}(t)} = \frac{\lambda_{mn} A_{ij} g_i}{\lambda_{ij} A_{mn} g_m} \exp\left(\frac{-(E_i - E_m)}{k_B T_m}\left(1+\frac{t}{\tau}\right)^{\frac{1}{3}}\right) \tag{3.22}$$

Now equation 3.22 is completely free from the temperature term. The nature of the intensity ratio will depend on the emission line chosen, i.e., the intensity ratio will decay with time if $E_i > E_m$ and increase with time if $E_i < E_m$.

Hence, equation 3.22 allows determining PDPs without estimating the plasma temperature using the Boltzmann/ Saha-Boltzmann plot method. Now, comparing the theoretical dependence (equation 3.22) with the experimental data on the intensity ratio, we can estimate PDPs as fitting parameters. If the upper energy level of the two emission lines are same i.e. $E_i = E_m$, then the equation 3.22 turns out to be

$$\frac{I_{ij}(t)}{I_{mn}(t)} = \frac{\lambda_{mn} A_{ij} g_i}{\lambda_{ij} A_{mn} g_m} = Constant \tag{3.23}$$

Under the special case (equation 3.23), the intensity ratio becomes a constant which is independent of time and also it doesn't contain PDPs. Therefore, in order to estimate PDPs accurately, the choice of emission lines is crucial. The emission lines should satisfy the following two conditions:

i. The emission lines should be free from self-absorption.

ii. The upper energy level of the two emission lines should be well separated.

In this context, four emission lines of Cu (465.18, 510.55, 515.29, and 521.86) correspond to binary and ternary alloy were considered for estimation of PDPs using intensity ratio fit (equation 3.22). The spectroscopic parameters of the emission lines are given in table 3.1.

From table 3.1, it can be seen that upper-level energy Cu-515.38 and Cu 521.86 are same. Therefore, except this combination of Cu lines, PDPs were estimated using all other five possible intensity ratio combinations for both the samples. The theoretical equation of intensity ratio (equation 3.22) is fitted with the experimental data for each combination of emission lines as shown in figure 3.9.

The theoretical dependence of the intensity ratio with time is represented by the solid black line in figure 3.9 while the markers indicate the experimental values. The error bars represent the standard deviation of 10 measurements. It is evident from figure 3.9 that the proposed theoretical model fitted well with the experimental data for different combinations of emission lines with R square close to one. The estimated values of PDPs obtained using the intensity ratio fit of various combinations of emission lines is represented in figure 3.10.

From figure 3.10, it can be observed that PDPs estimated using the intensity ratio model show good agreement with that of the plasma temperature model. It is expected that the error in the estimated values to be smaller compared to the temperature model; however, only few cases

resulted in a comparable error. This could be due to the effect of experimental parameters and optimization of these parameters may reduce the error.

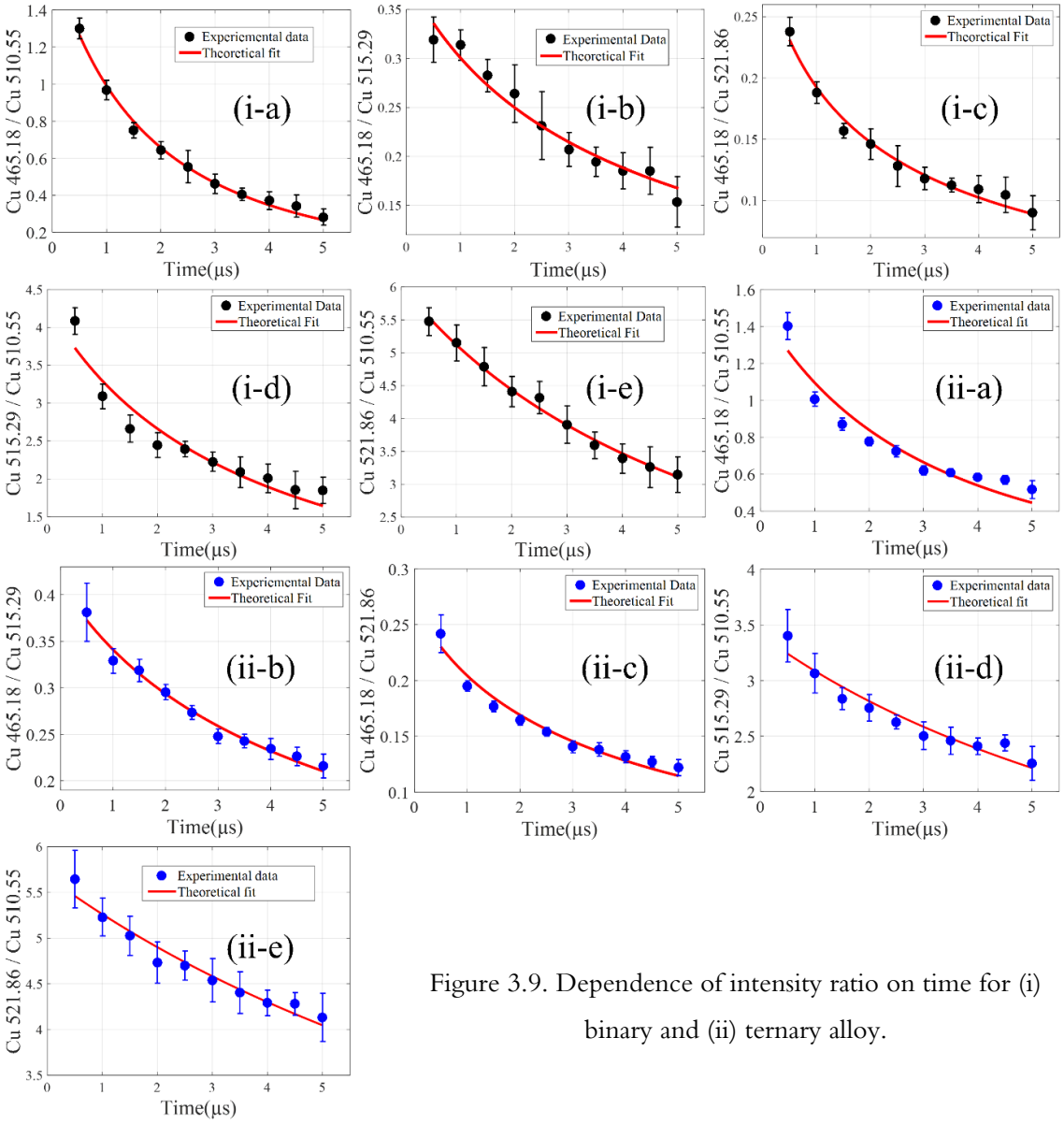

Figure 3.9. Dependence of intensity ratio on time for (i) binary and (ii) ternary alloy.

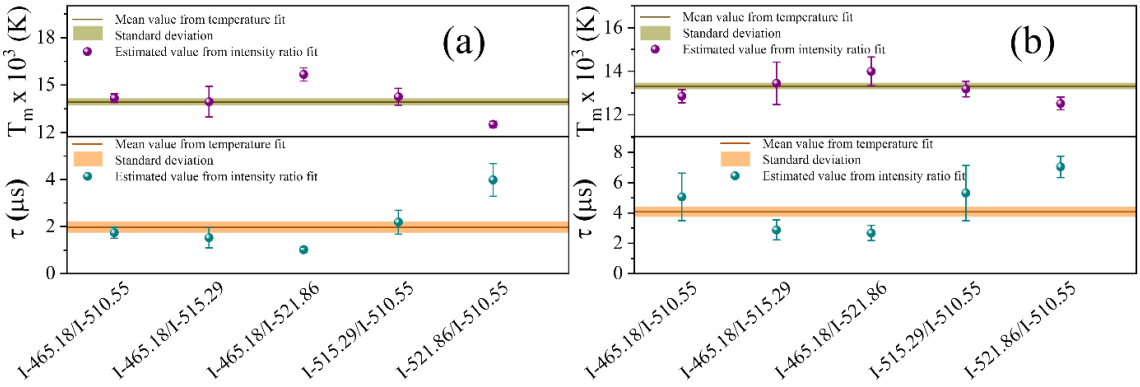

Figure 3.10. Comparison of PDPs obtained using temperature model vs intensity ratio model for (a) binary and (b) ternary alloy.

Moreover, the intensity ratio method has an edge over the temperature method as it determines the parameters directly from the intensities of the emission lines. This model reduces the complexity in the estimation of temperature by avoiding the intermediate calculations and can reduce the errors that inevitably arise at each step of the iteration. Apart from the various advantages over the existing plasma temperature estimation techniques, the proposed model only has one limitation, i.e., it requires the acquisition of temporal evolution of LIP spectra which will consume some extra time for the experiment compared to the conventional method. However, considering the fact that any calibration-free elemental analysis study using LIBS compulsorily uses a gated spectrometer and performs preliminary studies to find the best temporal window, this drawback is only artificial. More importantly, as will be discussed in the future sections, this analysis can significantly simply the process of estimation of concentration.

3.5 Elemental analysis

Elemental analyses were performed on two alloy samples (binary and ternary) using electron dispersive X-ray spectroscopy (EDS), CF-LIBS, and the newly proposed SLICE technique. Subsequently, the results obtained from the SLICE were compared with those from EDS and CF-LIBS.

3.5.1 Elemental analysis using electron dispersive X-ray spectroscopy (EDS)

EDS stands as a firmly established analytical method employed for determining the elemental composition of a given sample. It is a non-destructive technique that offers important insights into the micro- and nanoscale chemical composition of materials. EDS complements techniques like scanning electron microscopy (SEM) by allowing precise identification and quantification of the elements present within a sample.

The basic principle of EDS involves the interaction between high-energy electrons and a sample. When a focused electron beam strikes the sample, it generates characteristic X-rays by exciting inner-shell electrons of the atoms within the material. These emitted X-rays are unique to each element and contain the elemental information. Through the collection and analysis of these X-rays, EDS provides a complete elemental profile of the sample enabling to study the distribution of elements, detect trace elements, etc.

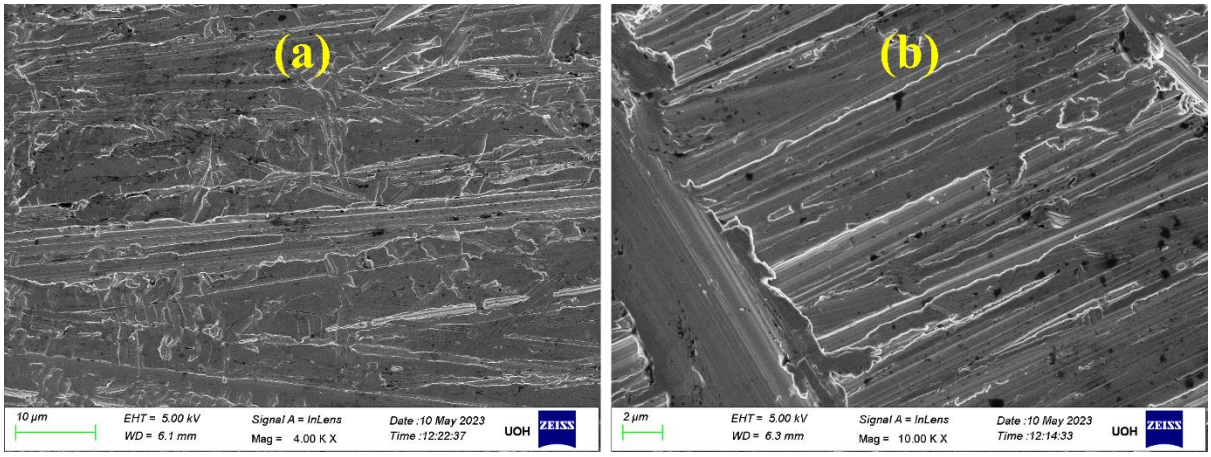

Figure 3.11. SEM image of the surface of (a) binary and (b) ternary alloy.

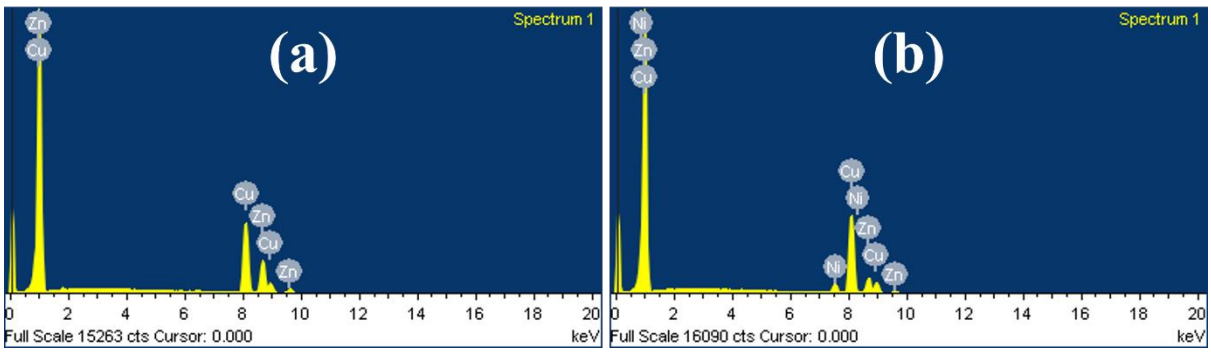

Figure 3.12. EDS spectra showing the elemental composition of (a) binary and (b) ternary alloy.

Table 3.2. Elemental concentrations obtained from EDS analysis.

Concentration (wt%)	Binary alloy	Ternary alloy
Cu	62.78 ± 0.72	76.67 ± 0.20
Zn	37.22 ± 0.72	17.73 ± 0.21
Ni		5.60 ± 0.18

EDS analysis was performed on five different regions of each sample. Figure 3.11 shows SEM images of one of the regions of each sample where EDS measurements were performed. Figure 3.12 represents the EDS spectrum of both the samples. From the spectra, it can clearly observe that in case of binary alloy only Cu and Zn are present whereas in case of ternary alloy Cu, Zn and Ni are present. The elemental concentrations of both the samples obtained using EDS are represented in table 3.2. Here the error factor represents the standard deviations of five measurements for each sample.

Advantages and Limitations of EDS

EDS has several advantages including capable of elemental analysis of a wide range of elements, offers excellent spatial resolution in micro- and nanoscale, highly sensitive in nature,

fast and non-destructive, etc. However, it has some limitations in which include necessity of sample preparation, imitated to surface investigation only, expensive instrumental setup, etc.

3.5.2 Calibration-free laser induced breakdown spectroscopy (CF-LIBS)

According to CF-LIBS, the concentration of each elemental species can be estimated from the intercept of the Boltzmann plot (see equation 3.6 and figure 3.6). The intercept of the Boltzmann plot can be represented as,

$$q = \ln\left(\frac{FC}{Z(T)}\right) \tag{3.24}$$

Simplifying,

$$C = \frac{1}{F} Z(T) \exp(q) \tag{3.25}$$

In this equation, Z(T) and q can be obtained from NIST atomic database and Boltzmann plot respectively. Therefore, F is the only parameter that needs to be estimated in order to calculate the elemental concentration of individual species.

According to closure condition, the sum of concentrations of all elements detected in a sample is 100% or 1 (in fraction). Therefore,

$$\sum C = \frac{1}{F} \sum Z(T) \exp(q) = 1 \tag{3.26}$$

$$\Rightarrow \quad F = \sum Z(T) \exp(q) \tag{3.27}$$

Hence, after calculation of F, the elemental concentration of each element in the sample can be estimated using equation 3.25.

The concentration of all the species were calculated at each time delay for both binary and ternary alloy. However, it is necessary to quantify the overall accuracy of this technique for which actual value of the elemental composition should be known. The overall accuracies have been quantified by distance measure[43] –

$$Distance = \sum_{i=1}^{N} abs(M_i - C_i) \tag{3.28}$$

where N, M and C are the number of elements in the sample, measured and standard/certified concentrations, respectively. The distance of few units is considered a reasonably good result, whereas the distance of the order of tens is a poor result[43]. In this case, the concentrations obtained from EDS are considered as actual/reference concentration since EDS is a well-established technique for the elemental analysis. The elemental concentrations obtained from CF-LIBS at each delay are tabulated in table 3.3. From the table, it can be observed that for binary alloy, the Cu concentration ranges from 60.83 to 67.90 whereas the actual (EDS concentration) value is 62.78. However, considering the standard deviation of both the techniques, CF-LIBS results agree well with that of EDS within the error range. Similar observations were also noticed in case of Zn and all the elements in ternary alloy. Therefore, it can be concluded that the CF-LIBS provides accurate estimation of elemental concentrations of the alloys.

Table 3.3. Elemental concentrations of binary and ternary alloy estimated from CF-LIBS.

Time (μs)	Binary alloy		Ternary alloy		
	Cu (wt%)	Zn (wt%)	Cu (wt%)	Zn (wt%)	Ni (wt%)
0.5	67.9 ± 3.73	32.1 ± 3.73	75.84 ± 2.09	19.76 ± 2.36	4.4 ± 1.74
1	63.49 ± 1.9	36.51 ± 1.9	75.43 ± 1.45	20.41 ± 1.96	4.16 ± 1.04
1.5	61.6 ± 2.28	38.4 ± 2.28	76.63 ± 0.8	19.23 ± 0.98	4.14 ± 1.19
2	63.14 ± 1.94	36.86 ± 1.94	77.04 ± 1.24	18.15 ± 0.42	4.81 ± 1.07
2.5	60.95 ± 3.45	39.05 ± 3.45	77.52 ± 0.94	18.07 ± 0.74	4.41 ± 0.57
3	60.83 ± 2.25	39.17 ± 2.25	77.07 ± 1.26	18.55 ± 1.05	4.38 ± 0.85
3.5	62.34 ± 3.81	37.66 ± 3.81	78.19 ± 0.95	17.91 ± 0.91	3.9 ± 0.72
4	62.02 ± 3.89	37.98 ± 3.89	77.69 ± 1.2	17.36 ± 1.07	4.95 ± 1.65
4.5	62.35 ± 4.06	37.65 ± 4.06	78.35 ± 0.94	17.63 ± 0.84	4.01 ± 0.81
5	61.35 ± 5.32	38.65 ± 5.32	77.68 ± 1.67	17.56 ± 1.4	4.77 ± 0.95

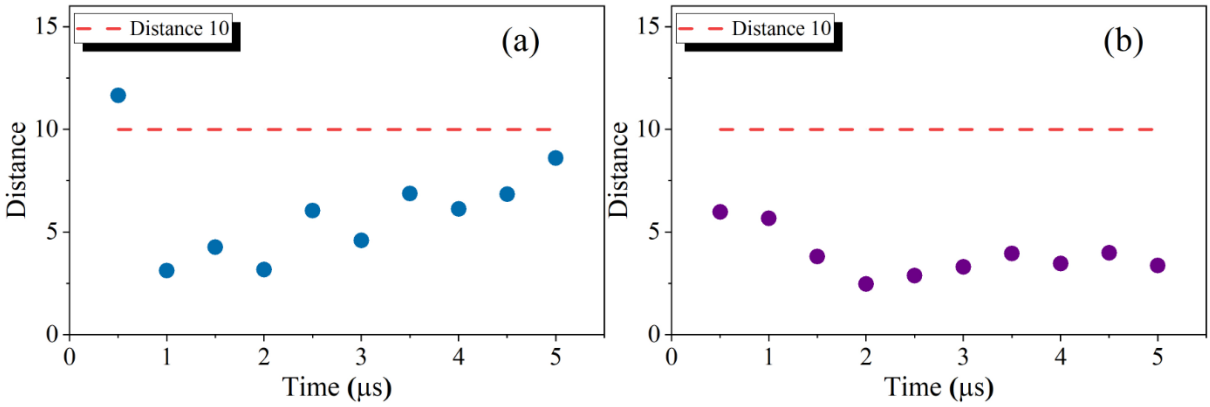

Figure 3.13. CF-LIBS distance at each temporal delay for (a) binary and (b) ternary alloy.

Moreover, figure 3.13 represents the CF-LIBS distance w.r.t. EDS explaining the overall accuracies of CF-LIBS. In the figure, the red dashed line represents the distance value of 10, below which the results can be considered as good. From figure 3.13a, it can be noticed that in case of binary alloy, the accuracy is poor at 1 μs delay which could be due to the effect of the plasma continuum at the early stage of plasma relaxation, as observed in figure 3.3 and 3.4. However, except this time window, the results are good for all other temporal regions. Furthermore, in case of ternary alloy, the results are good in all the cases as seen in figure 3.13b.

Advantages and Limitations of CF-LIBS

The advantage of CF-LIBS is that it circumvents the requirement of matrix matched standards and reference samples, which is a significant challenge in calibration-based LIBS. However, a notable limitation of this method is the necessity to identify few spectral lines of every element within the plasma with established atomic data and those line shouldn't be affected by self-absorption.

3.5.3 Simplified LIBS-based Intensity-ratio approach for Concentration Estimation (SLICE)

SLICE is significantly easier and straightforward method for elemental analysis using LIBS since it requires fewer emission lines. At first, two emission lines from any one of the elemental species are needed in order to estimate PDPs using temporal modeling of intensity ratio (section 3.4.5). Once the PDPs have been estimated, a single line from each element is all that is needed to calculate their concentration. Since a small number of emission lines are required, there is a great flexibility in picking lines that are not affected by the self-absorption.

After the deduction of PDPs, the only difficulty in estimating elemental concentration using equation 3.20 is the estimation of experimental factor F. The experimental factor F has been taken into account to balance the disruption caused by the optical deficiency of the collection system along with plasma density and volume. As a result, this factor affects the entire plasma and is unrelated to the emitting species. So, F can be easily ruled out by looking at the intensity ratio of two spectral lines that correspond to two different species. In simplified form, the intensity ratio of two spectral lines corresponding to different species can be written as,

$$\frac{I_{ij}^{P}(t)}{I_{xy}^{Q}(t)} = \frac{C^{P}\lambda_{xy}^{Q}Z^{Q}(T_m,\tau,t)A_{ij}^{P}g_{i}^{P}}{C^{Q}\lambda_{ij}^{P}Z^{P}(T_m,\tau,t)A_{xy}^{Q}g_{x}^{Q}}\exp\left(-\frac{E_i^P - E_x^Q}{k_B T_m}\left(1+\frac{t}{\tau}\right)^{\frac{1}{3}}\right) \tag{3.29}$$

Simplifying,

$$\frac{C^{P}}{C^{Q}} = \frac{I_{ij}^{P}(t)\lambda_{ij}^{P}Z^{P}(T_m,\tau,t)A_{xy}^{Q}g_{x}^{Q}}{I_{xy}^{Q}(t)\lambda_{xy}^{Q}Z^{Q}(T_m,\tau,t)A_{ij}^{P}g_{i}^{P}}\exp\left(\frac{E_i^P - E_x^Q}{k_B T_m}\left(1+\frac{t}{\tau}\right)^{\frac{1}{3}}\right) \tag{3.30}$$

Here the subscripts x and y represent the emissions from x^{th} to y^{th} energy level and the superscripts P and Q represent two species in the sample. All other parameters have the same meaning as before. Now, all the values corresponding to the parameters in the R.H.S. are known, so the ratio of elemental concentration between two different species in the same sample becomes a constant, i.e.,

$$\frac{C^{P}}{C^{Q}} = \alpha \tag{3.31}$$

where α is a constant. Again, for binary alloys, the closure condition implies[43],

$$C^{P} + C^{Q} = 100\% \tag{3.32}$$

Finally, by solving equation 3.31 & 3.32, we can obtain the individual elemental concentration.

Similarly, for ternary alloy,

$$\frac{C^{P}}{C^{Q}} = \alpha_1, \tag{3.33}$$

$$\frac{C^{P}}{C^{R}} = \alpha_2, \tag{3.34}$$

$$\text{and} \qquad C^{P} + C^{Q} + C^{R} = 100\% \tag{3.35}$$

where the superscript R corresponds to the third species. Again, by solving equation 3.33 to 3.35, the elemental concentration of each species can be determined. The flow chart of the working procedure of the proposed SLICE technique is summarized in figure 3.14.

In this context, the PDPs estimated using Cu 465.18 and Cu 510.55 lines (section 3.4.5) were selected for the estimation concentration estimation. For binary sample, the value of PDPs were estimated to be 14,183 ± 277 K and 2.37 ± 0.46 μs, respectively, whereas, for ternary sample, it was estimated to be 12,853 ± 300 K and 5.06 ± 1.57 μs, respectively.

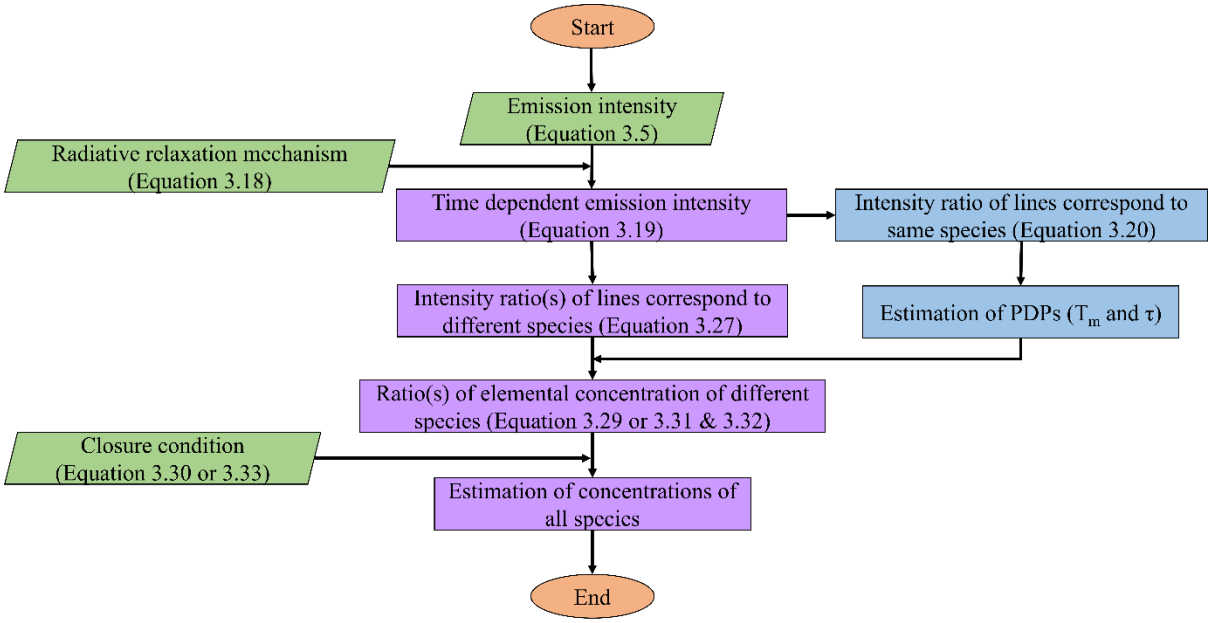

Figure 3.14. Flow chart of the working procedure of SLICE.

After the estimation of PDPs, the intensity ratio of Cu 465.18 / Zn 328.25 was considered to estimate the concentration of Cu and Zn in the binary alloy sample (using equation 3.30 to 3.32). Similarly, for ternary alloy, ratios of Cu 465.18 / Zn 328.25 and Cu 465.18 / Ni349.29 were used. The concentrations were obtained at 2 μs delay for both samples. The SLICE results are compared to that of CF-LIBS and EDS in table 3.4. Table 3.4 shows that, within the margin of error, the quantitative results from SLICE show excellent agreement with the other two techniques, one based on LIBS and another a standard technique. Considering the EDS result as a standard, the SLICE distance (equation 3.28) for binary alloy was evaluated to be 2.5 and for ternary alloy, it is 2.4. Similarly, for CF-LIBS, the distance is 3.2 and 2.5, respectively. A small distance of a few units for both binary and ternary samples explain the potential of SLICE for quantitative elemental analysis, likewise CF-LIBS. It is worth emphasizing that SLICE requires time evolution LIBS signal for estimating PDPs. However, in the next step, a spectrum from any one-time window is sufficient, provided the LIBS assumptions are valid in that time window. Also, multiple emission lines satisfy the self-absorption criterion of which Cu 465.18 / Zn 328.25 at 2 μs were considered for estimation of concentration. However, it is worth exploring this technique when different combinations of emission lines are used to estimate PDPs and then different lines for each species are used at different time windows of collection. The next section presents the results considering these parameters.

Table 3.4. Comparison of SLICE results with CF-LIBS and EDS. Here the results correspond to SLICE and CF-LIBS is the mean ± standard deviation of 10 measurements, and EDS is the mean ± standard deviation of 5 measurements.

Element	Binary alloy			Ternary alloy		
	SLICE	CF-LIBS	EDS	SLICE	CF-LIBS	EDS
Cu	63.08 ± 1.74	63.14 ± 1.94	62.78 ± 0.72	77.21 ± 1.21	77.04 ± 1.24	76.67 ± 0.20
Zn	36.92 ± 1.74	36.86 ± 1.94	37.22 ± 0.72	17.90 ± 0.49	18.15 ± 0.42	17.73 ± 0.21
Ni	-	-	-	4.89 ± 1.14	4.81 ± 1.07	5.6 ± 0.18

Robustness of SLICE

In order to investigate the potential of this technique for different emission lines at different delays, the PDPs estimated for all different possible combinations of intensity ratios were considered. For each pair of PDPs, the elemental analyses have been performed for eight combinations of emission lines (as mentioned in table 3.5) at ten different delays for each sample. And at each delay, ten spectra were recorded. This implies that in total 4000 concentrations have been estimated (5 PDPs × 8 combinations of emission lines × 10 delays × 10 spectra).

Table 3.5. Various combinations of intensity ratios considered for SLICE analysis.

Sl. No.	Binary alloy		Ternary alloy	
	Ratios	Label	Combinations of ratios	Label
1	Cu 465.18 / Zn 328.25	R1	Cu 465.18 / Zn 328.25 & Cu 465.18 / Ni 349.29	C1
2	Cu 465.18 / Zn 330.27	R2	Cu 465.18 / Zn 330.27 & Cu 465.18 / Ni 349.29	C2
3	Cu 510.55 / Zn 328.25	R3	Cu 510.55 / Zn 328.25 & Cu 510.55 / Ni 349.29	C3
4	Cu 510.55 / Zn 330.27	R4	Cu 510.55 / Zn 330.27 & Cu 510.55 / Ni 349.29	C4
5	Cu 515.29 / Zn 328.25	R5	Cu 515.29 / Zn 328.25 & Cu 515.29 / Ni 349.29	C5
6	Cu 515.29 / Zn 330.27	R6	Cu 515.29 / Zn 330.27 & Cu 515.29 / Ni 349.29	C6
7	Cu 521.86 / Zn 328.25	R7	Cu 521.86 / Zn 328.25 & Cu 521.86 / Ni 349.29	C7
8	Cu 521.86 / Zn 330.27	R8	Cu 521.86 / Zn 330.27 & Cu 521.86 / Ni 349.29	C8

The elemental analyses were performed for both the samples for every combination of PDPs and intensity ratios at each temporal delay. The distances were estimated for each combination by considering EDS as standard/reference. The mean distance estimated using various combinations of PDPs and intensity ratios at each delay is depicted in figure 3.15 and 3.16 for binary and ternary alloys, respectively. The distance value of 10 is shown by the dashed lines in each graph. Distances of fewer than ten units can be regarded as good results, while distances of 10 or more are considered poor results[43]. As can be seen from figure 3.15 and 3.16, a very large number of values fall below the line, which is 3026 (75.65 %) and 3789

(94.72 %) of the estimated concentrations out of a total possible 4000 for binary and ternary alloy respectively. This implies that any combination of the emission lines and delay can be chosen for the estimation of concentration.

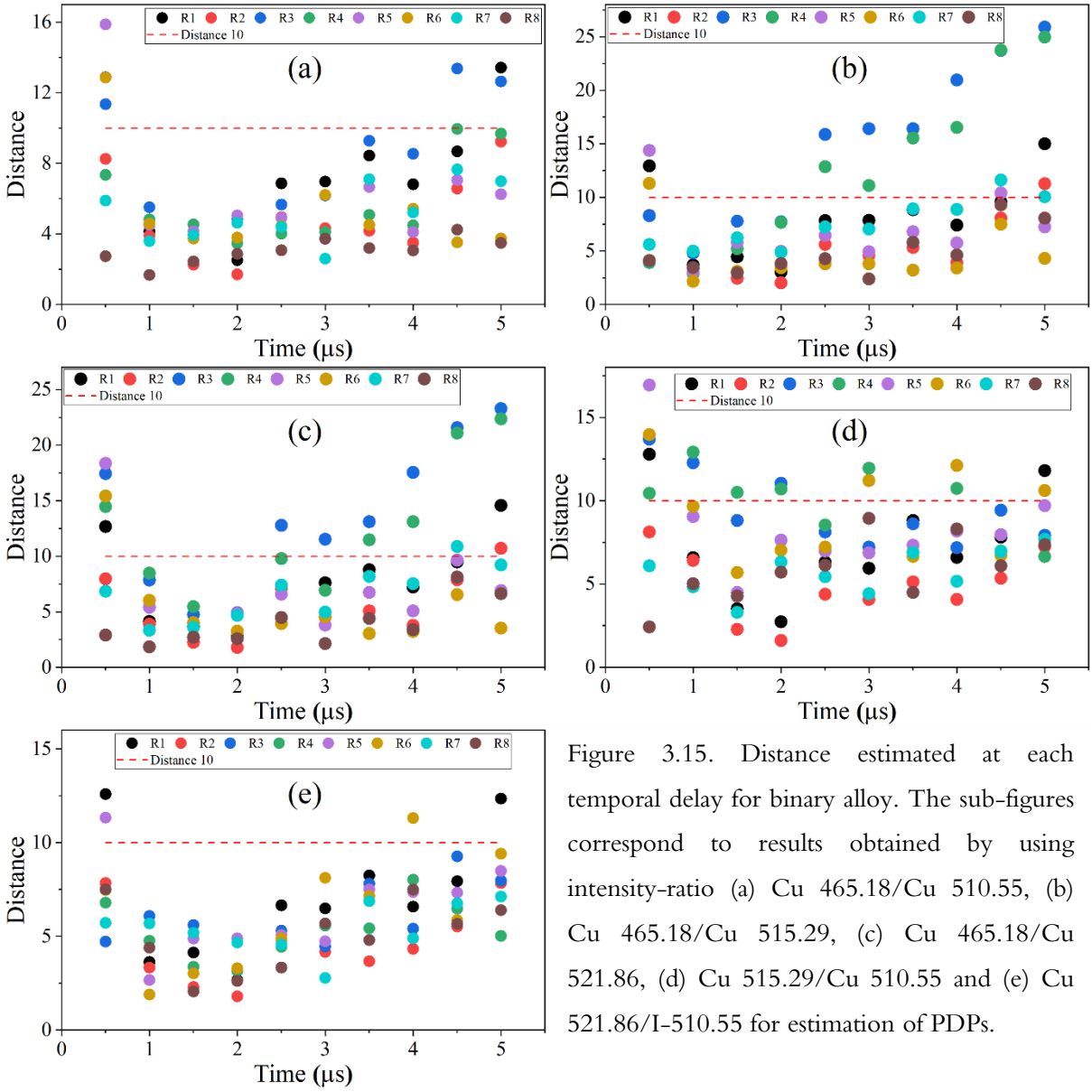

Figure 3.15. Distance estimated at each temporal delay for binary alloy. The sub-figures correspond to results obtained by using intensity-ratio (a) Cu 465.18/Cu 510.55, (b) Cu 465.18/Cu 515.29, (c) Cu 465.18/Cu 521.86, (d) Cu 515.29/Cu 510.55 and (e) Cu 521.86/I-510.55 for estimation of PDPs.

Also, it is evident that the SLICE distance in the temporal window of 1.5 – 4 μs, the distance value is minimum for almost all combinations for both the samples. To be specific, out of 2400 possible measurements, 1955 (81.46 %) and 2371 (98.79%) of the estimated concentrations fall below the threshold distance for binary and ternary alloy, respectively. The larger distance at the initial time (0.5 – 1 μs) could be due to the effect of the plasma continuum at the early stage of plasma relaxation, as observed in figure 3.3 and 3.4. And after

4 μs, the signal-to-noise ratios of emission intensities are low, which may be the reason for larger distance at later time. CF-LIBS also showed such behavior in the initial time window.

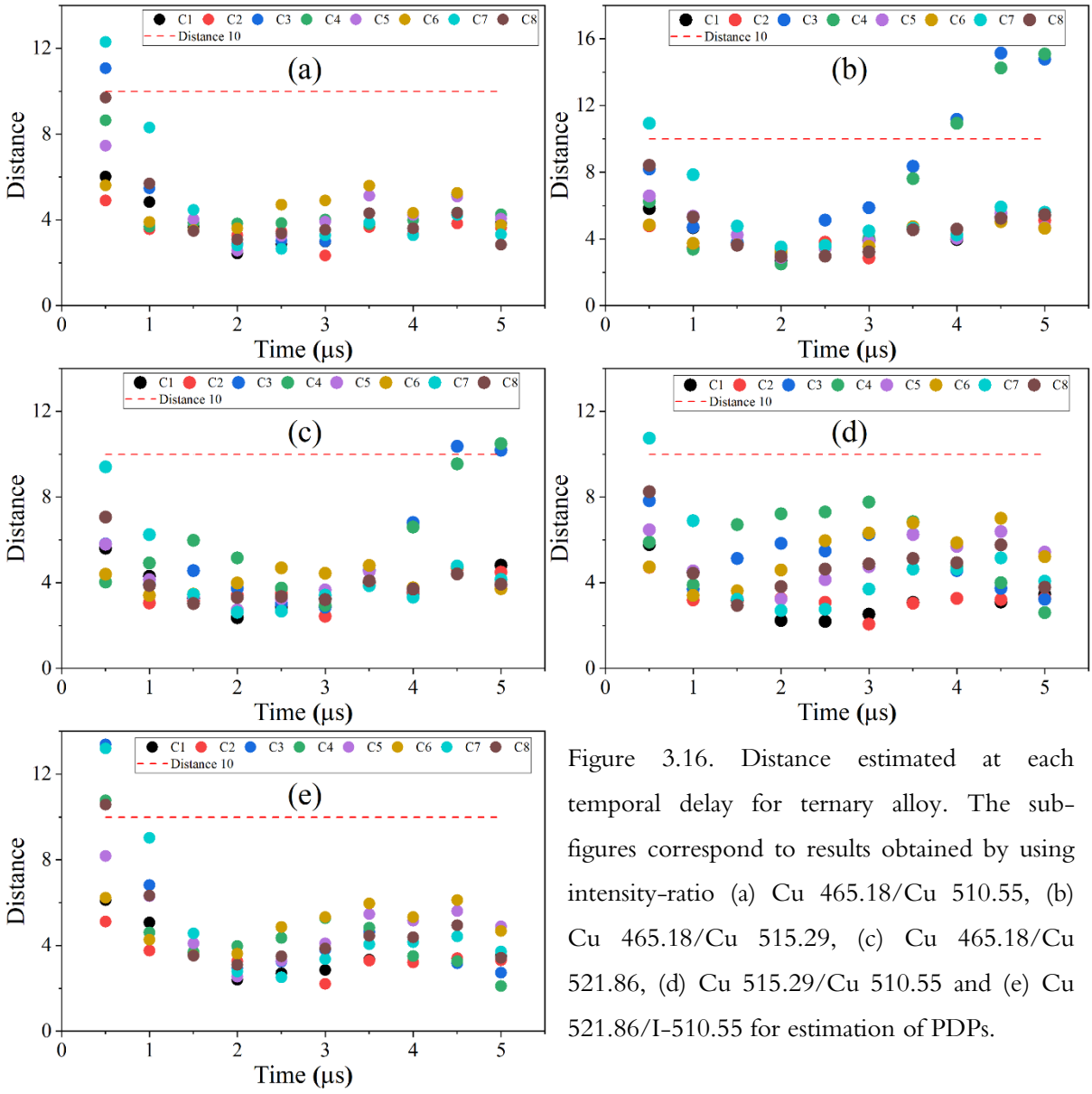

Figure 3.16. Distance estimated at each temporal delay for ternary alloy. The sub-figures correspond to results obtained by using intensity-ratio (a) Cu 465.18/Cu 510.55, (b) Cu 465.18/Cu 515.29, (c) Cu 465.18/Cu 521.86, (d) Cu 515.29/Cu 510.55 and (e) Cu 521.86/I-510.55 for estimation of PDPs.

The results of this section have two important implications. Firstly, for any combination of parameters, this technique gives an accurate estimation. Secondly, given data of one temporal scan, it is possible to repeat the process of estimation, thereby increasing the precision. In the case of binary alloy, there are five different combinations (m) for estimation of PDPs and ten different time windows (n), and eight combinations for considering ratios (p). Hence, a total of m×n×p estimations (400 in the present case) can be performed. Additionally, if one chooses to repeat the data N times (10 times in this case), then a total of N×m×n×p estimations (here 4000) can be performed. This is crucial as the precision or standard deviation of the mean is proportional to $1/\sqrt{N}$.

Figure 3.17 shows the distribution of Cu and Zn concentrations estimated for binary with only one time-evolution data and ten recordings. In all the cases, the distribution shows strong bell-shaped curve. In a typical concentration estimation experiment, one can perform any one of these estimations which is very fast and simple. In such a scenario, the error in the estimation of the concentration would be the standard deviation obtained from figure 3.17. However, if one is interested in finding the concentration with higher precision, one can perform either m×n×p estimations or N×m×n×p estimations. The estimated concentration in such a scenario can be expected to be very close to the actual value. Similar results were also obtained in case of ternary alloy as shown in figure 3.18.

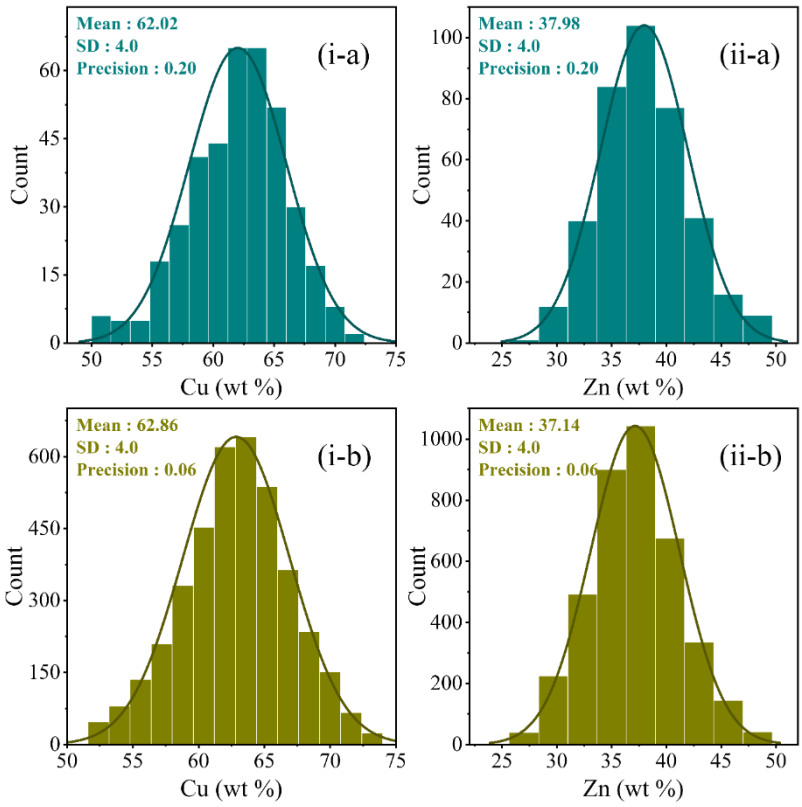

Figure 3.17. Histogram of (i) Cu and (ii) Zn concentrations correspond to binary alloy estimated using (a) single time evolution data (400 values) and (b) 10 sets of time evolution data (4000 values). SD represents standard deviation.

SLICE provides the flexibility of multiple measurements for elemental concentration which results in better precision. Also, this technique has several other notable advantages, as discussed in table 3.6 The accuracy and precision of this technique can further be improvised by optimizing different factors that play significant roles in the evolution of laser produced plasma. An extensive exploration for the future prospects for enhancing the accuracy and precision of SLICE is elaborated in Chapter 7.

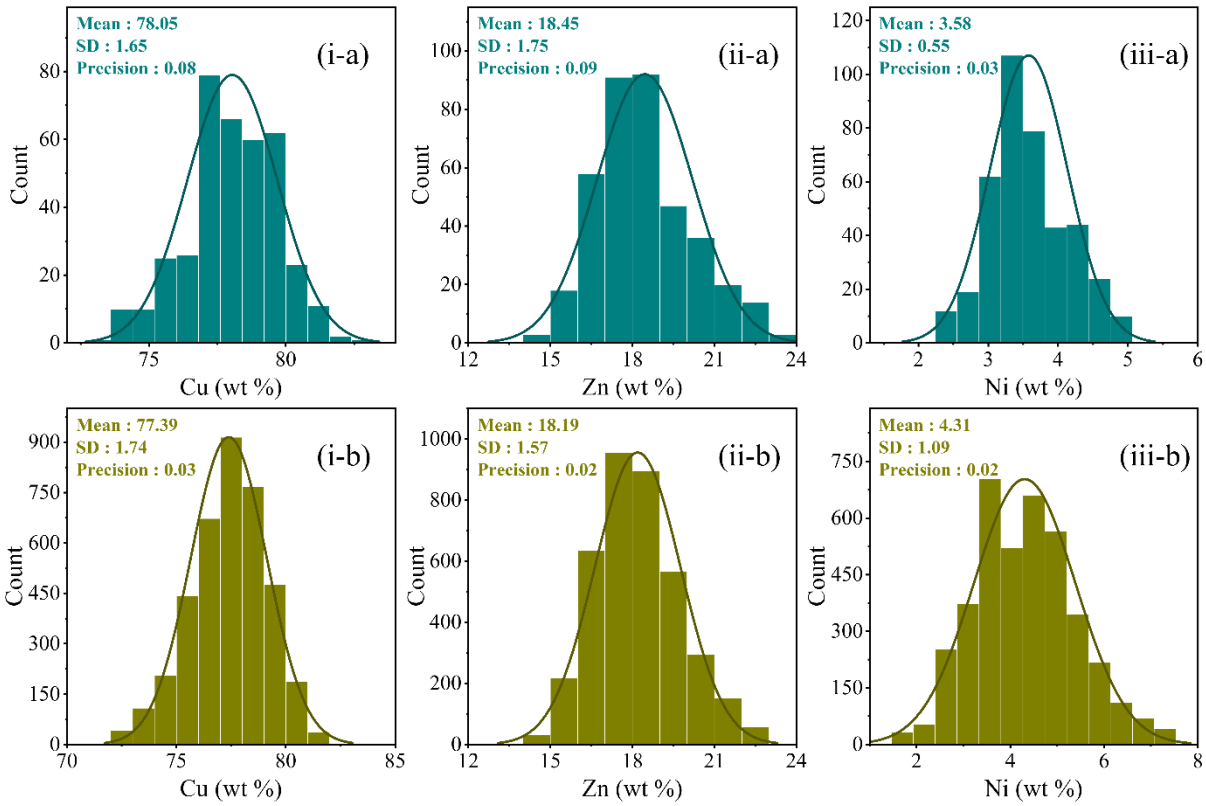

Figure 3.18. Histogram of (i) Cu, (ii) Zn and (iii) Ni concentrations correspond to ternary alloy estimated using (a) single time evolution data (400 values) and (b) 10 sets of time evolution data (4000 values). SD represents standard deviation.

Advantages and limitations of SLICE

SLICE has several notable advantages over other LIBS-based technique for elemental analysis. SLICE retains all the benefits of CF-LIBS and offsets some of its limitations. First of all, SLICE doesn't require Boltzmann/Saha-Boltzmann plot methods for the determination of concentration. Secondly, it requires fewer spectral lines to perform comprehensive elemental analysis; specifically, only n+1 emission lines are sufficient for a sample containing n elemental species. This offers a great flexibility in the choice of emission lines which do not suffer from self-absorption. Moreover, it is an intensity-ratio based approach and allows estimation of concentrations directly from the intensity-ratio of emission lines making it robust, straightforward and less time-consuming technique.

This technique only has one limitation so far i.e., it requires multiple time-dependent spectra in order to estimate the PDPs which is the first step in this approach. Nevertheless, the CF-LIBS approach necessitates the acquisition of temporal window measurements of the spectrum, utilizing an ICCD, which can also record time-dependent data for SLICE. Considering the rapid pace of LIBS experiments, the additional time required for recording

multiple spectra is relatively minimal. The advantages and disadvantages of SLICE compared to CF-LIBS are briefly discussed in table 3.6.

Table 3.6. Comparison of the advantages and disadvantages of SLICE with CF-LIBS technique.

Sl. No.	Properties	SLICE	CF-LIBS[35,43]
1	Spectral data acquisition	Time-dependent spectra required	Single spectrum is sufficient
2	Temperature estimation through Boltzmann/ Saha-Boltzmann Plot	Not required	Essential
3	Can self-absorbed emission lines be avoided?	Yes	No (In many cases)
4	Number of spectral lines involved	Few	Many
5	Number of steps involved	Comparably less	More
6	Time requires for quantitative analysis	Very Less	More
7	Complexity in analysis	Very Less	More
8	No. of possible measurements	Numerous	Limited
9	Accuracy/Precision	High/High	High/ -

⋆ The green colored text represents the advantages of one technique over other whereas the red colored text represents the disadvantages of the technique.

3.6 Summary

In this chapter, plasma diagnostics and elemental analysis are applied to two alloy samples, one binary and one ternary. The initial sections provide a concise overview of the experimental procedures and spectral interpretation of Laser-Induced Plasma (LIP) for both the samples. Subsequently, this chapter provides an overview of thermodynamic equilibrium and estimation of plasma parameters and plasma decay parameters (PDPs). The temporal behavior of LIP is characterized through the modeling of plasma temperature and intensity ratio decay. The concluding section of the chapter focuses on elemental analysis, employing EDS, CF-LIBS, and SLICE techniques. The elemental concentrations estimated using the proposed SLICE method for both binary and ternary alloys demonstrate excellent agreement with those obtained using CF-LIBS and EDS. Additionally, the chapter briefly discusses the advantages and limitations associated with these analytical techniques.

3.7 References

[1] D.A. Cremers, The analysis of metals at a distance using laser-induced breakdown spectroscopy, Appl. Spectrosc. 41 (1987) 572–579.

[2] T.L. Thiem, R.H. Salter, J.A. Gardner, Y.I. Lee, J. Sneddon, Quantitative simultaneous elemental determinations in alloys using laser-induced breakdown spectroscopy (LIBS) in an ultra-high vacuum, Appl. Spectrosc. 48 (1994) 58–64.

[3] R.W. Wisbrun, I. Schechter, R. Niessner, H. Schroeder, Laser-induced breakdown spectroscopy for detection of heavy metals in environmental samples, in: Int. Conf. Monit. Toxic Chem. Biomarkers, SPIE, 1993: pp. 2–15.

[4] A. Ciucci, M. Corsi, V. Palleschi, S. Rastelli, A. Salvetti, E. Tognoni, New procedure for quantitative elemental analysis by laser-induced plasma spectroscopy, Appl. Spectrosc. 53 (1999) 960–964.

[5] H. Shakeel, S.U. Haq, G. Aisha, A. Nadeem, Quantitative analysis of Al-Si alloy using calibration free laser induced breakdown spectroscopy (CF-LIBS), Phys. Plasmas. 24 (2017) 63516.

[6] M. Horňáčková, J. Plavčan, J. Rakovský, V. Porubčan, D. Ozdín, P. Veis, Calibration-free laser induced breakdown spectroscopy as an alternative method for found meteorite fragments analysis, Eur. Phys. Journal-Applied Phys. 66 (2014).

[7] M.A. Khoso, N.M. Shaikh, M.S. Kalhoro, S. Jamali, Z.A. Ujan, R. Ali, Comparative elemental analysis of soil of wheat, corn, rice, and okra cropped field using CF-LIBS, Optik (Stuttg). 261 (2022) 169247.

[8] M.D. Assefa, A.K. Chaubey, A.T. Hailu, A.Y. Hibstie, Multi-elemental INAA and CF-LIBS techniques for analysis of rocks of Ethiopian Tropical forest area of Tepi, Eur. Phys. Journal-Applied Phys. 62 (2013).

[9] R.-J. Lasheras, D. Paules, M. Escudero, J. Anzano, S. Legnaioli, S. Pagnotta, V. Palleschi, Quantitative analysis of major components of mineral particulate matter by calibration free laser-induced breakdown spectroscopy, Spectrochim. Acta Part B At. Spectrosc. 171 (2020) 105918.

[10] S. Pandhija, A.K. Rai, In situ multielemental monitoring in coral skeleton by CF-LIBS, Appl. Phys. B. 94 (2009) 545–552.

[11] V.K. Unnikrishnan, K. Mridul, R. Nayak, K. Alti, V.B. Kartha, C. Santhosh, G.P. Gupta, B.M. Suri, Calibration-free laser-induced breakdown spectroscopy for quantitative elemental analysis of materials, Pramana. 79 (2012) 299–310.

[12] L.M. John, R.C. Issac, S. Sankararaman, K.K. Anoop, Multi-element Saha Boltzmann plot (MESBP) coupled calibration-free laser-induced breakdown spectroscopy (CF-LIBS): an efficient approach for quantitative elemental analysis, J. Anal. At. Spectrom. 37 (2022) 2451–2460.

[13] E. Mal, R. Junjuri, M.K. Gundawar, A. Khare, Optimization of temporal window for application of calibration free-laser induced breakdown spectroscopy (CF-LIBS) on copper alloys in air employing a single line, J. Anal. At. Spectrom. 34 (2019) 319–330.

[14] D. Bulajic, M. Corsi, G. Cristoforetti, S. Legnaioli, V. Palleschi, A. Salvetti, E. Tognoni, A procedure for correcting self-absorption in calibration free-laser induced breakdown spectroscopy, Spectrochim. Acta Part B At. Spectrosc. 57 (2002) 339–353.

[15] H. Amamou, A. Bois, B. Ferhat, R. Redon, B. Rossetto, P. Matheron, Correction of self-absorption spectral line and ratios of transition probabilities for homogeneous and LTE plasma, J. Quant. Spectrosc.

Radiat. Transf. 75 (2002) 747–763.

[16] L. Sun, H. Yu, Correction of self-absorption effect in calibration-free laser-induced breakdown spectroscopy by an internal reference method, Talanta. 79 (2009) 388–395.

[17] F. Rezaei, P. Karimi, S.H. Tavassoli, Effect of self-absorption correction on LIBS measurements by calibration curve and artificial neural network, Appl. Phys. B. 114 (2014) 591–600.

[18] J. Dong, L. Liang, J. Wei, H. Tang, T. Zhang, X. Yang, K. Wang, H. Li, A method for improving the accuracy of calibration-free laser-induced breakdown spectroscopy (CF-LIBS) using determined plasma temperature by genetic algorithm (GA), J. Anal. At. Spectrom. 30 (2015) 1336–1344.

[19] I. Karnadi, M. Pardede, I. Tanra, R. Hedwig, A.M. Marpaung, Z.S. Lie, E. Jobiliong, D. Kwaria, M.M. Suliyanti, M. Ramli, Suppression of self-absorption in laser-induced breakdown spectroscopy using a double pulse orthogonal configuration to create vacuum-like conditions in atmospheric air pressure, Sci. Rep. 10 (2020) 1–9.

[20] Y. Zhang, Y. Lu, Y. Tian, Y. Li, W. Ye, J. Guo, R. Zheng, Quantitation improvement of underwater laser induced breakdown spectroscopy by using self-absorption correction based on plasma images, Anal. Chim. Acta. 1195 (2022) 339423.

[21] A. Taleb, V. Motto-Ros, M.J. Carru, E. Axente, V. Craciun, F. Pelascini, J. Hermann, Measurement error due to self-absorption in calibration-free laser-induced breakdown spectroscopy, Anal. Chim. Acta. 1185 (2021) 339070.

[22] T. Li, Z. Hou, Y. Fu, J. Yu, W. Gu, Z. Wang, Correction of self-absorption effect in calibration-free laser-induced breakdown spectroscopy (CF-LIBS) with blackbody radiation reference, Anal. Chim. Acta. 1058 (2019) 39–47.

[23] Z. Hu, F. Chen, D. Zhang, Y. Chu, W. Wang, Y. Tang, L. Guo, A method for improving the accuracy of calibration-free laser-induced breakdown spectroscopy by exploiting self-absorption, Anal. Chim. Acta. 1183 (2021) 339008.

[24] NIST Atomic Database, (n.d.). https://www.nist.gov/pml/atomic-spectra-database.

[25] J.P. Singh, S.N. Thakur, Laser-induced breakdown spectroscopy, Elsevier, 2020.

[26] D.A. Cremers, L.J. Radziemski, Handbook of laser-induced breakdown spectroscopy, John Wiley & Sons, 2013.

[27] A.K. Tarai, R. Junjuri, S.A. Rashkovskiy, M.K. Gundawar, Time-Dependent Intensity Ratio-Based Approach for Estimating the Temperature of Laser Produced Plasma, Appl. Spectrosc. (2022) 00037028221117534.

[28] N.M. Shaikh, S. Hafeez, B. Rashid, S. Mahmood, M.A. Baig, Optical emission studies of the mercury plasma generated by the fundamental, second and third harmonics of a Nd: YAG laser, J. Phys. D. Appl. Phys. 39 (2006) 4377.

[29] S.S. Harilal, G. V Miloshevsky, P.K. Diwakar, N.L. LaHaye, A. Hassanein, Experimental and computational study of complex shockwave dynamics in laser ablation plumes in argon atmosphere, Phys. Plasmas. 19 (2012).

[30] A. Miloshevsky, S.S. Harilal, G. Miloshevsky, A. Hassanein, Dynamics of plasma expansion and shockwave formation in femtosecond laser-ablated aluminum plumes in argon gas at atmospheric pressures, Phys. Plasmas. 21 (2014).

[31] S. Sai Shiva, C. Leela, P. Prem Kiran, C.D. Sijoy, S. Chaturvedi, The effects of electron thermal radiation on laser ablative shock waves from aluminum plasma into ambient air, Phys. Plasmas. 23 (2016).

[32] N. V Nedić, S. Bukvić, D. Dojić, L. Rajačić, M. Skočić, Observation of blackbody-like emission from laser-induced plasma at early times and implications for thermal equilibrium, Plasma Sources Sci. Technol. 31 (2022) 10LT02.

[33] M. Skočić, D. Dojić, S. Bukvić, Metallic surface temperature at the very beginning of the laser-induced breakdown obtained from black-body radiation, Phys. Rev. E. 105 (2022) 45211.

[34] J. Hermann, D. Grojo, E. Axente, V. Craciun, Local thermodynamic equilibrium in a laser-induced plasma evidenced by blackbody radiation, Spectrochim. Acta Part B At. Spectrosc. 144 (2018) 82–86.

[35] F. Poggialini, B. Campanella, B. Cocciaro, G. Lorenzetti, V. Palleschi, S. Legnaioli, Catching up on Calibration-Free LIBS, J. Anal. At. Spectrom. (2023).

[36] J. Jasik, J. Heitz, J.D. Pedarnig, P. Veis, Vacuum ultraviolet laser-induced breakdown spectroscopy analysis of polymers, Spectrochim. Acta Part B At. Spectrosc. 64 (2009) 1128–1134.

[37] S. Bollanti, R. Cotton, P. Di Lazzaro, F. Flora, T. Letardi, N. Lisi, D. Batani, A. Conti, A. Mauri, L. Palladino, Development and characterisation of an XeCl excimer laser-generated soft-X-ray plasma source and its applications, Nuovo Cim. D. 18 (1996) 1241–1255.

[38] J.-B. Sirven, B. Bousquet, L. Canioni, L. Sarger, Time-resolved and time-integrated single-shot laser-induced plasma experiments using nanosecond and femtosecond laser pulses, Spectrochim. Acta Part B At. Spectrosc. 59 (2004) 1033–1039.

[39] V. Margetic, A. Pakulev, A. Stockhaus, M. Bolshov, K. Niemax, R. Hergenröder, A comparison of nanosecond and femtosecond laser-induced plasma spectroscopy of brass samples, Spectrochim. Acta Part B At. Spectrosc. 55 (2000) 1771–1785.

[40] A.H. Galmed, M.A. Harith, Temporal follow up of the LTE conditions in aluminum laser induced plasma at different laser energies, Appl. Phys. B. 91 (2008) 651–660.

[41] J.S. Cowpe, J.S. Astin, R.D. Pilkington, A.E. Hill, Temporally resolved laser induced plasma diagnostics of single crystal silicon—effects of ambient pressure, Spectrochim. Acta Part B At. Spectrosc. 63 (2008) 1066–1071.

[42] R. Junjuri, S.A. Rashkovskiy, M.K. Gundawar, Dependence of radiation decay constant of laser produced copper plasma on focal position, Phys. Plasmas. 26 (2019) 122107.

[43] E. Tognoni, G. Cristoforetti, S. Legnaioli, V. Palleschi, Calibration-Free Laser-Induced Breakdown Spectroscopy: State of the art, Spectrochim. Acta - Part B At. Spectrosc. 65 (2010) 1–14. https://doi.org/10.1016/j.sab.2009.11.006.

Intentional Blank Page

Chapter 4

Dependence of Plasma Parameters on Material Hardness

This chapter explores the significance of material hardness in LIBS, providing a profound understanding of diverse industrial applications. Material hardness is an essential characteristic that determines how resistant a material is to deformation, indentation, and penetration. It is critical for building components and structures that are trustworthy. The chapter provides a thorough examination emphasizing the growing need for non-invasive techniques than the conventional approaches, particularly in difficult conditions. LIBS has been used to understand the dependence of various plasma parameters on material hardness. The experiment involves five iron-based alloy samples with same elemental composition and different hardness. The study explores the correlation of plasma parameters, plasma decay parameters, and surface morphology in relation to changes in material hardness. The results reveal a consistent linear correlation between the material's hardness and the plasma temperature, electron density, and initial plasma temperature. In addition, the analysis reveals a linear decrease in the radiative decay constant as the hardness increases. The chapter concludes by analyzing the correlation between crater diameter and material hardness, finding a consistent reduction in crater size as material hardness increases. This study improves the comprehension of the complex interactions between laser-induced plasma properties and material hardness.

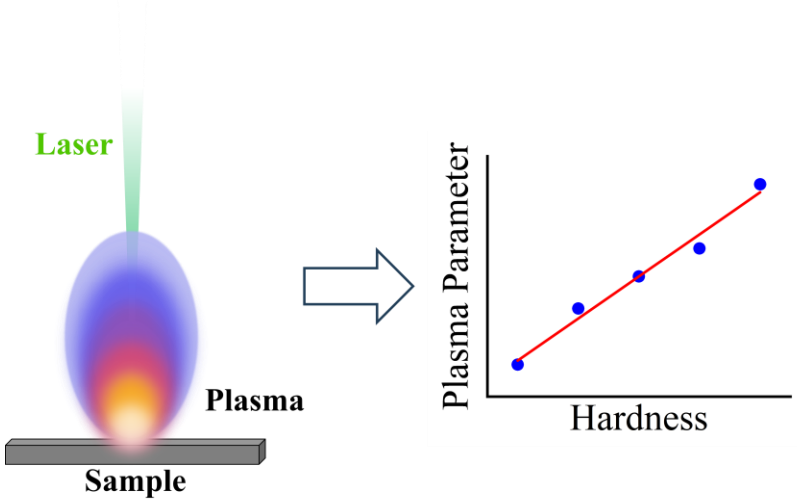

4.1 Introduction

The mechanical characteristics of materials significantly influence their applicability across diverse sectors[1]. Within this context, hardness emerges as a pivotal parameter of great relevance. Hardness, as a fundamental property of materials, provides insights into a material's ability to resist deformation, indentation, or penetration [2,3]. Understanding and characterization of material hardness stand as an essential endeavour in industry, scientific research, and engineering. Particularly, this is very important for the design and construction of robust, dependable components, devices, and structures.

Various techniques are available for measuring material hardness, including well-established techniques like Rockwell, Brinell, Knoop, and Vickers hardness tests, etc.[4]. Significantly, these methods mostly consist of mechanical techniques that need direct physical contact with the substance being analyzed. The demand for non-intrusive, remote techniques of hardness testing is increasing as materials are being used in more difficult situations such as space shuttles, TOKAMAKs, nuclear power plant vessels, etc.[5]. This requirement is particularly emphasized to minimize physical contact with materials, as ion irradiation, as evidenced by numerous studies, can cause significant damage to metals, hence affecting their hardness[6,7]. In recent years, LIBS has emerged as a new technique for evaluating material hardness[8–12]. It establishes a correlation between the variations in various parameters of laser-induced plasma (LIP) and the gradual enhancement in material hardness, providing a potential approach for estimating hardness.

Several researchers have investigated the application of LIBS to correlate the spectroscopic parameters of LIP with the hardness of various materials[8–11,13]. Abdel-Salam et al.[9] investigated the hardness of different calcified tissues. They discovered a direct correlation between the ionic to atomic emission intensities of calcium (Ca) and magnesium (Mg) and the hardness of the samples. Cowpe et al.[10] discovered a direct relationship between excitation temperature (Te) and sample hardness, highlighting the better consistency of LIBS compared to the traditional Vickers method in evaluating the surface hardness of apatite-based bio-ceramics. In 2014, Khalil et al.[11] discovered a direct correlation between the ionic to atomic emission intensity and sample density, which is inversely related to surface hardness. Nevertheless, this occurrence was ascribed to the distinctive characteristics of the zeolite samples. Yahiaoui et al.[12] made a significant contribution to the area by establishing a relationship between the surface hardness of α-alumina ceramics and several plasma parameters utilizing the LIBS diagnostic approach. The researchers confirmed the linear progression of the

ratio between the intensity of ionic and atomic lines, as well as the electronic temperature, in relation to the hardness of the sample's surface. In addition, they established a correlation between the electron density and vibrational temperature of AlO radicals. This correlation offers an approach to estimate the hardness of unknown α-alumina by utilizing these characteristics. Huang et al. [14] further developed this research by introducing an innovative calibration model for measuring hardness using LIBS. Their methodology consisted of establishing a correlation between the intensity of emission lines and the hardness of steel samples through the utilization of canonical correlation analysis and principal component analysis (PCA). The study determined that the combination of LIBS data with chemometrics presents a potent tool for examining the mechanical properties of steel samples, yielding a thorough comprehension of material hardness. Momcilovic et al. [15] conducted a study on cast iron samples to analyze the relationship between hardness and the atomic-to-ionic ratios of Mg lines. Furthermore, they investigated the correlation between plasma temperature and hardness. Also, they used calibration curve to estimate the hardness. Sattar et al. [16] investigated W-Ni-Fe alloy and reported that emission intensity doesn't depend linearly on hardness; however, it increases with increasing hardness up to a certain level. In addition, WII/WI intensity ratio and plasma temperature increases linearly with increasing hardness electron density decreases linearly with increasing hardness. Apart from these studies, some contradicting results were also observed in relation to the plasma parameters and material hardness. For example, Galmed et al. [5] conducted a study by considering both nanosecond (ns) and femtosecond (fs) lasers. They noticed an exponential pattern: as the hardness increased, the plasma temperature in nsLIBS increased exponentially, but in fsLIBS, it decreased exponentially. Similarly, the electron density decreases exponentially with increasing hardness in case of nsLIBS, but in fsLIBS, it increases exponentially. Yongqi et al. [13] observed decrease in plasma temperature with increasing hardness.

So far, no clear and definite pattern has been established regarding the changes in plasma parameters (e.g., plasma temperature) with changes in material hardness. The correlation between plasma properties and material hardness is still not fully understood and lacks complete clarity. To get a clear understanding, this chapter explores the relationship between plasma parameters, plasma decay parameters, and surface morphology in relation to variations in hardness. This study used five standard iron-based alloys that have the same chemical compositions but different material hardness.

4.2 Materials and Methods

For the experiment, a set of five iron-based alloy samples with same elemental composition and varying hardness levels were used. The hardness of each sample was estimated using the Vickers hardness test, and the corresponding results are displayed in table 4.1. The hardness values are determined by calculating the average of five measurements obtained from various locations on the sample. The reproducibility of the measurements was assessed by estimating the standard deviation.

Table 4.1. List of samples used in the present study, along with their respective hardness values determined through the Vickers hardness test.

Sample Name	Vickers Hardness (HV)	Standard Deviation
A1	270	7
A2	332	8
A3	631	7
A4	637	6
A5	649	4

The schematic of the LIBS experimental setup is shown in chapter 2 (figure 2.4). In brief, it comprises a picosecond laser (Ekspla, PL-2250 series) delivering energy of 20 mJ per pulse at 10 Hz repetition rate. The laser operated at its fundamental wavelength of 1064 nm with a pulse duration of ~30 ps. The laser pulse was focused on the sample surface through a plano-convex lens (focal length of 15 cm) to produce the plasma. An XY-translation stage controlled by a motion controller (Newport, ESP 300) was used to hold the sample to avoid deep crater formation at the same spot. The emissions from the plasma were collected by a collection optics assembly (Andor, ME OPT 007) and sent through an optical fiber of core diameter 600 μm to an echelle spectrograph (Andor, Mechelle ME-5000). The spectrograph has been equipped with an ICCD (Intensified charge-coupled device) camera as a detector (Andor, iSTAR DH334T-18U-E3). A delay generator (SRS-DG-645) was used to electronically trigger the ICCD with respect to photodiode to avoid electronic interference and jitters. The spectrograph covers the spectral range of 220-850 nm. Temporal kinetic series spectra of the alloys were recorded in ambient air at atmospheric pressure. Each spectrum was collected after an initial delay of 0.2 μs to avoid the high intensity of continuum radiation at the initial period of plasma formation. The ICCD gain was set to 3000 to obtain a strong signal. Time evolution spectra were collected in the 0.2 – 2 μs temporal window with a constant step and

gate width of 0.5 μs. Each spectrum was averaged over 10 spectra to increase the signal-to-noise ratio. Likewise, 7 sets of time evolution spectral data were recorded for each alloy.

4.3 Results and Discussion

The time-dependent LIBS spectra corresponding to sample A1 is graphically presented in figure 4.1. Originally, the spectrum was recorded in the wavelength range of 220 – 850 nm, where those wavelength ranges having intensity emission lines of interest (i.e., 220 – 600 nm) are depicted. All the spectral emission lines in the spectrum were identified with the help of the NIST atomic database[17]. Prominent emission lines of Fe at wavelengths at 278.82, 322.81, 344.11, 349.04, 357.01, 358.15, 361.88, 379.52, 380.67, 384.11, 385.00, and 386.01 nm were observed.

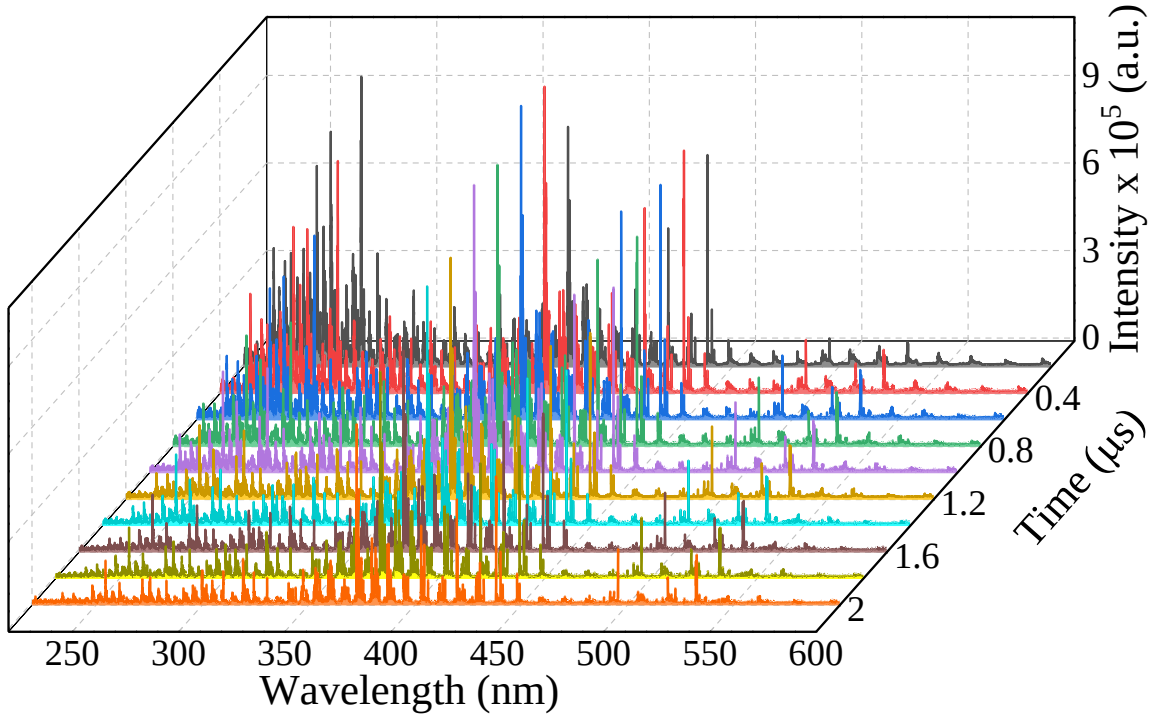

Figure 4.1. Time-dependent LIBS spectra corresponding to sample A1.

4.3.1 Dependence of Plasma Temperature and Electron Density on Hardness

In the domain of laser-induced plasma, the complex relationship between plasma temperature and material hardness emerges as a critical field of study, providing important insights into the underlying dynamics of laser-material interactions[15]. This scientific investigation explores the intricate relationship between the characteristics of materials and the subsequent thermal response that occurs during the formation of LIP.

The plasma temperatures for five alloy samples were calculated using the Boltzmann plot method. According to this method, the plasma temperature can be estimated from the slope of the ln(Iλ/Ag) vs E_k plot of the Boltzmann distribution which can be represented by [18,19],

$$\ln\left(\frac{I\lambda}{Ag}\right)=\frac{-E_k}{k_BT}+\ln\left(\frac{FC}{Z(T)}\right) \tag{4.1}$$

where I, λ, A, E_k, k_B, T, F, C and Z(T) represent the intensity of emission, wavelength of the emission, transition probability, upper energy level, Boltzmann constant, plasma temperature, experimental factor, elemental concentration of the species and partition function, respectively.

By plotting the RHS of equation 4.1 vs E_k, the plasma temperature can be estimated form the slope ($1/k_BT$). Detailed explanation regarding the estimation of plasma temperature can be found in section 3.4.2 of Chapter 3. For the estimation of plasma temperature five neutral emission lines of iron were considered based on literature[20]. The spectroscopic parameters of these emission lines are tabulated in table 4.2.

Table 4.2. Spectroscopic parameters of Fe emission lines considered for Boltzmann plot.

Sl. No.	λ (nm)	E_k (eV)	A (10^7 s^{-1})	g
1	346.59	3.686	1.19	3
2	361.88	4.415	7.72	7
3	425.08	4.473	1.02	7
4	426.05	5.308	3.99	11
5	432.58	4.473	5.16	7

The Boltzmann plot of Fe emission lines for all the alloy samples at 1.2 μs delay is depicted in figure 4.2. From the figure, it can be noticed that the straight line fitted well w.r.t. the experimental data and have high R square more than 0.7 for all the alloys. Figure 4.3 depicts a graphic representation of the relation between the hardness of a material and the temperature of plasma. Upon observation, it becomes evident that the plasma temperature shows a consistent increase as the material hardness values increase, following a linear pattern. The linear fit precisely matches the experimental data, demonstrating a high level of accuracy, as indicated by an R-squared value of 0.99. The strong alignment between the fitted line and experimental observations highlights the dependability and uniformity of the established correlation between material hardness and plasma temperature.

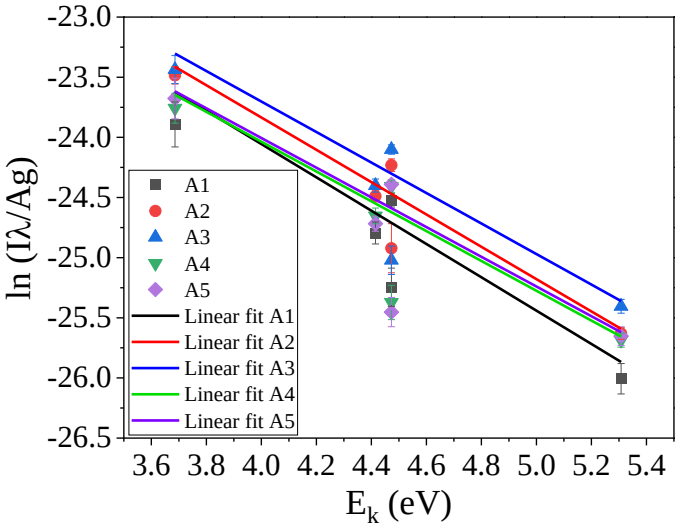

Figure 4.2. Boltzmann plot using Fe emission lines.

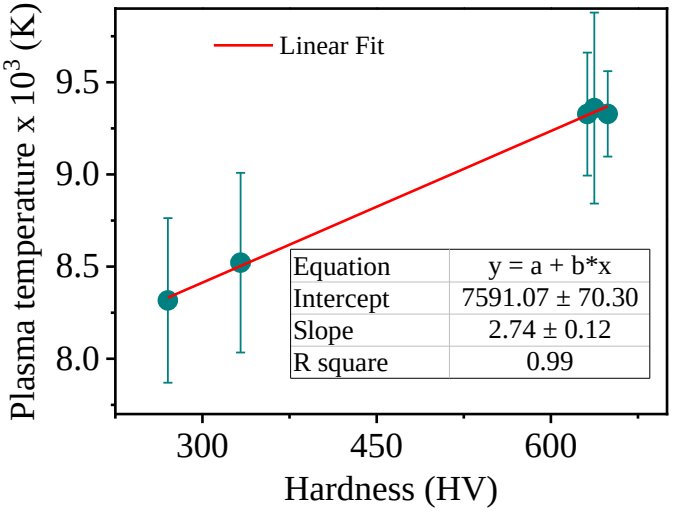

Figure 4.3. Dependence of plasma temperature on material hardness.

Electron number density is another characteristic parameter of LIP that need to be examined w.r.t. increasing hardness. The electron density can be determined from the full-width at half maximum (FWHM) of the spectral line. The main contribution in the broadening of the emission lines is due to Stark broadening. More details regarding the broadening of emission lines of LIP can be found in section 3.4.3 of Chapter 3. The FWHM of an emission line due to Stark broadening can be given by the equation [21,22],

$$\Delta\lambda_{1/2} = 2w\left(\frac{n_e}{10^{16}}\right) \tag{4.2}$$

where n_e and w are the electron impact width parameter and electron density respectively.

The electron density values at a 1.2 μs for all alloy samples were measured by using the emission lines of Fe at a wavelength of 538.33 nm. Figure 4.4 visually illustrates the

correlation between material hardness and electron number density. Upon careful examination, it becomes evident that electron density consistently increases as material hardness values increase, similar to plasma temperature. The linear fit precisely follows the experimental dataset, achieving a high level of accuracy shown by an R-squared value of 0.98. The strong agreement observed between the fitted line and experimental results highlights the dependability and uniformity of the established relationship between material hardness and electron number density.

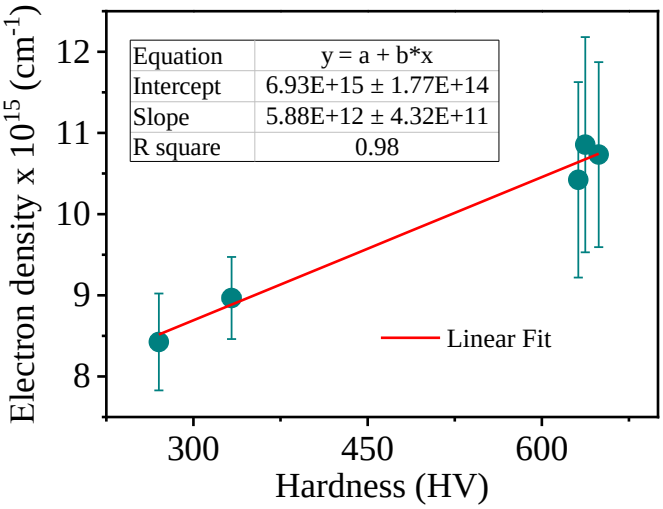

Figure 4.4. Dependence of electron density on material hardness.

As the hardness of a material increases, there is linear increase in the plasma temperature and electron density. This could be because of the reason that when harder materials are exposed to laser irradiation, they tend to undergo more ionization and excitation due to their higher densities. This phenomenon, known as electron excitation, enhances the efficiency of converting laser energy into thermal energy by facilitating the easy release and elevation of electrons to higher energy levels. In addition, the collisional processes occurring within the denser plasma produced by harder materials result in more vigorous interactions, hence promoting the thermalization of the plasma. As a result, the complex electrical and structural characteristics of harder materials contribute to an increased plasma temperature and electron density.

4.3.2 Dependence of Plasma Decay Parameters (PDPs) on Hardness

The expression for the temporal dependence of plasma temperature can be given by [18,23],

$$T(t) = T_m \left(1 + \frac{t}{\tau}\right)^{-\frac{1}{3}} \tag{4.3}$$

where T is the plasma temperature, T_m is the initial temperature of plasma, τ is the radiation decay constant and t is the time.

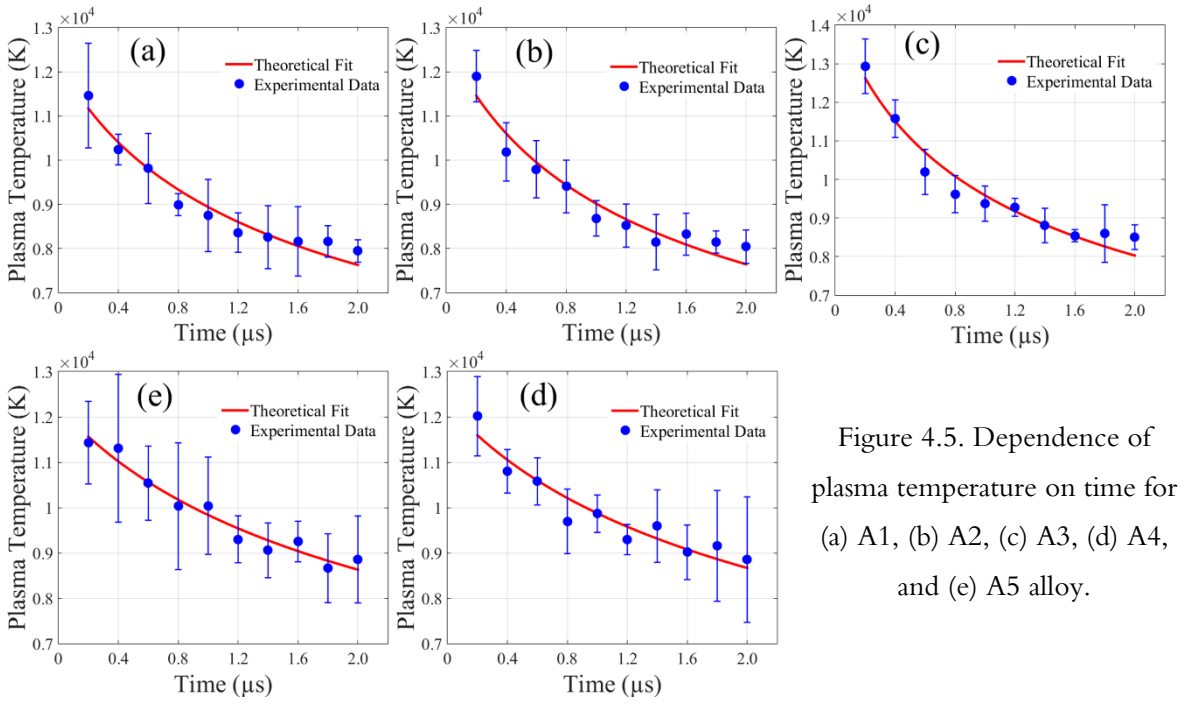

Figure 4.5. Dependence of plasma temperature on time for (a) A1, (b) A2, (c) A3, (d) A4, and (e) A5 alloy.

The value of PDPs (T_m and τ) can be estimated by comparing the theoretical dependence (equation 4.3) with temperature derived from experimental data using the Boltzmann plot (section 4.3.1). During data processing, T_m and τ can be considered as the fitting parameters and followed by fitting of experimental data as shown in figure 4.5. The detailed theory regarding the temporal dependence of plasma temperature can be found in section 3.4.4 of Chapter 3. From figure 4.5, it can be observed that the theoretical dependence fitted well with the experimental data. The value of PDPs estimated from the fitting is plotted against hardness as shown in figure 4.6.

From figure 4.6, it can be noticed that with increasing material hardness, the initial temperature of the plasma increases linearly. The linear fit precisely aligns with the experimental data, demonstrating a high level of accuracy, as indicated by an R-squared value of 0.90. Like the plasma temperature and electron density, strong correlation between material

hardness and the initial temperature of the plasma provides valuable parameter for predicting material hardness. However, from figure 4.6, it can also be observed that with increasing material hardness the radiative decay constant decreases linearly with R-square of 0.97. This is because with increasing hardness, the value of plasma temperature and initial plasma temperature increases. The enhanced thermal energy and excitation processes that occur at higher temperatures result in a faster radiative decay. Therefore, increasing hardness, the plasma relaxes faster which result in decrease in relaxation time or decay constant.

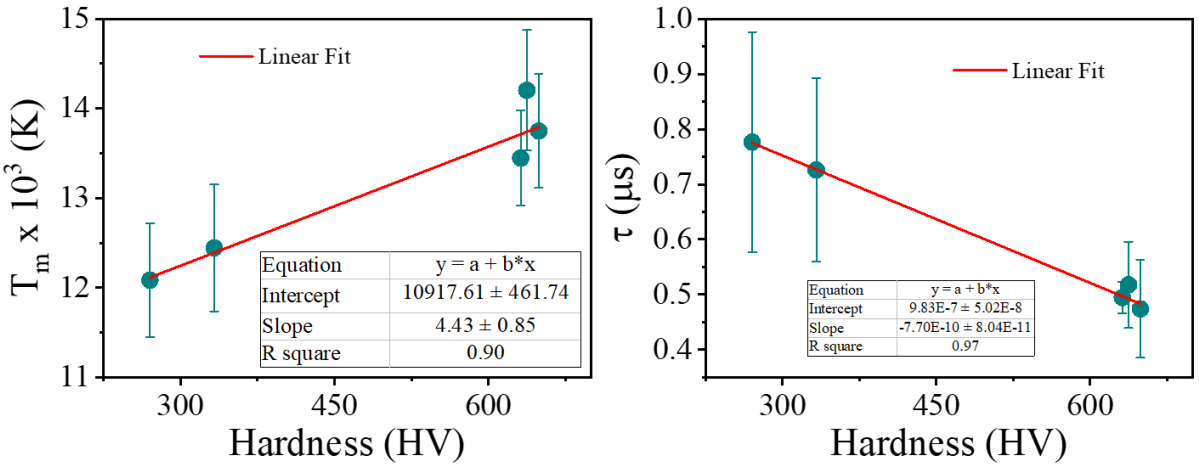

Figure 4.6. Dependence of PDPs on material hardness.

4.3.3 Dependence of Crater Diameter on Hardness

The dimensions of the crater formed in LIP are highly significant in relation to the properties of the material. The complexities of crater shape provide useful insights about the material's reaction to intense laser irradiation. Crater diameter and depth are parameters that directly indicate the efficacy of material ablation, providing insight into its vulnerability to laser-induced processes. In addition to its importance in characterizing fundamental properties of material, the dimensions of the crater generated during laser interactions are also important for understanding the hardness of the material. The shape of the crater serves as an indicator of a material's ability to withstand laser ablation. More durable materials frequently display unique crater profiles, which indicate their capacity to endure the high levels of heat and mechanical pressures caused by laser irradiation. An analysis of crater diameters in connection to material hardness offers a method to evaluate and distinguish materials based on their resilience and reaction to the processes of plasma formation and relaxation.

The diameter of craters formed by laser ablation on all alloy samples was measured by utilizing a surface profilometer (M/s. Ambios Technology, XP-200) equipped with a stylus tip

featuring a radius of 2 μm. Each ablation involved focusing of five laser pulses at a single spot. Likewise, five ablations were created for each sample at five separate places. The size of each crater was measured using the profilometer. Figure 4.7 visually depicts the crater profile acquired from a representative measurement, providing a detailed understanding of the laser-induced craters on the alloy samples.

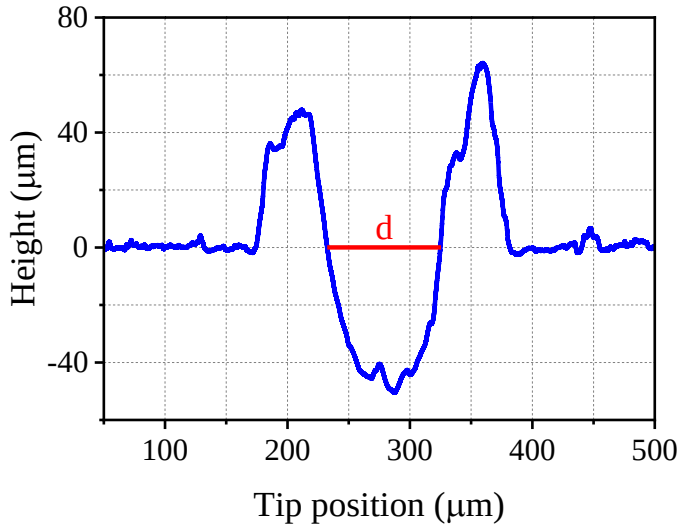

Figure 4.7. Profilometer measurement of crater. Zero on y-scale represents the sample surface. Here d represents the diameter of the crater.

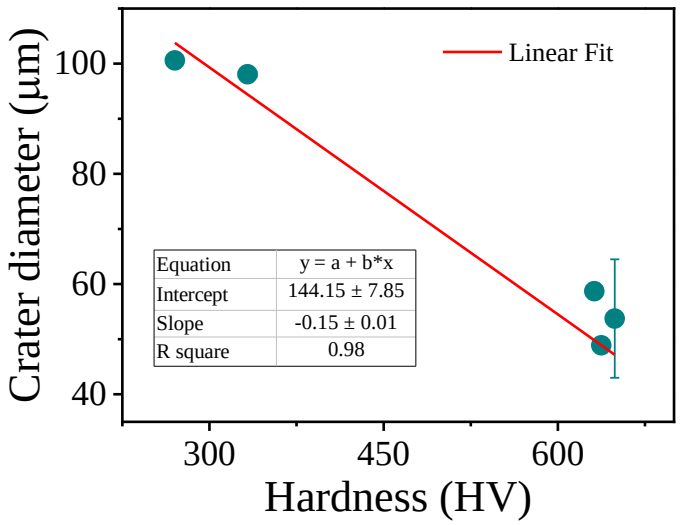

Figure 4.8. Dependence of crater diameter on material hardness.

The dependence of the crater diameter on the hardness of the material is discussed in figure 4.8. From the figure, it can be noticed that with increasing hardness, the diameter of the crater decreases linearly. The decrease in the size of craters as the hardness of the material increases in LIP interactions is a subtle process influenced by an intricate combination of thermal and mechanical factors. Materials with higher hardness likely results in more efficient energy

absorption, reduced lateral plasma expansion, and controlled material removal. The localized and precise nature of the ablation process on harder materials highlights the influence of their inherent features.

4.4 Summary

This chapter explores the crucial importance of material hardness, highlighting its significance across many industries. Hardness, as a fundamental characteristic, provides vital information about a material's ability to resist deformation, indentation, or penetration. This information is essential for building strong components, devices, and structures. The chapter provides an overview of well-established approaches for measuring hardness, with a particular emphasis on the increasing need for non-invasive procedures under difficult conditions. LIBS studies have shown that changes in the characteristics of LIP are closely related to variations in hardness. The experiment investigates the complex correlation between plasma parameters, plasma decay parameters, and surface morphology in connection to hardness variations. It involves testing five iron-based alloy samples with different levels of hardness. The findings demonstrate a direct relationship between the hardness of the material and the plasma temperature, electron density, and initial plasma temperature. Furthermore, the study reveals a correlation between increasing hardness and a decrease in the radiative decay constant. The chapter concludes by analyzing the correlation between crater diameter and material hardness, illustrating a consistent reduction in crater size as hardness increases.

4.5 References

[1] D.F. Mohamed, A.H. Galmed, O.A. Nassef, Determination of Surface Hardness of Ti -based Alloys via Laser Induced Breakdown Spectroscopy (LIBS), Arab J. Nucl. Sci. Appl. 50 (2017) 142–155. http://inis.iaea.org/search/search.aspx?orig_q=RN:49086904.

[2] Z. Ramezanian, S.M.R. Darbani, A.E. Majd, Effect of self-absorption correction on surface hardness estimation of Fe–Cr–Ni alloys via LIBS, Appl. Opt. 56 (2017) 6917–6922. https://doi.org/10.1364/AO.56.006917.

[3] S. Messaoud Aberkane, A. Bendib, K. Yahiaoui, S. Boudjemai, S. Abdelli-Messaci, T. Kerdja, S.E. Amara, M.A. Harith, Correlation between Fe–V–C alloys surface hardness and plasma temperature via LIBS technique, Appl. Surf. Sci. 301 (2014) 225–229. https://doi.org/https://doi.org/10.1016/j.apsusc.2014.02.046.

[4] P. Mencin, C.J. Van Tyne, B.S. Levy, A method for measuring the hardness of the surface layer on hot forging dies using a nanoindenter, J. Mater. Eng. Perform. 18 (2009) 1067–1072.

[5] A.H. Galmed, O. Balachninaite, O.A. Nassef, Effect of laser pulse duration on relative hardness

estimation using LIBS, Opt. Laser Technol. 161 (2023) 109184.

[6] H. Zhang, C. Zhang, Y. Yang, Y. Meng, J. Jang, A. Kimura, Irradiation hardening of ODS ferritic steels under helium implantation and heavy-ion irradiation, J. Nucl. Mater. 455 (2014) 349–353.

[7] X. Bai, S. Wu, P.K. Liaw, L. Shao, J. Gigax, Effect of heavy ion irradiation dosage on the hardness of SA508-IV reactor pressure vessel steel, Metals (Basel). 7 (2017) 25.

[8] K. Tsuyuki, S. Miura, N. Idris, K.H. Kurniawan, T.J. Lie, K. Kagawa, Measurement of concrete strength using the emission intensity ratio between Ca (II) 396.8 nm and Ca (I) 422.6 nm in a Nd: YAG laser-induced plasma, Appl. Spectrosc. 60 (2006) 61–64.

[9] Z.A. Abdel-Salam, A.H. Galmed, E. Tognoni, M.A. Harith, Estimation of calcified tissues hardness via calcium and magnesium ionic to atomic line intensity ratio in laser induced breakdown spectra, Spectrochim. Acta Part B At. Spectrosc. 62 (2007) 1343–1347.

[10] J.S. Cowpe, R.D. Moorehead, D. Moser, J.S. Astin, S. Karthikeyan, S.H. Kilcoyne, G. Crofts, R.D. Pilkington, Hardness determination of bio-ceramics using laser-induced breakdown spectroscopy, Spectrochim. Acta Part B At. Spectrosc. 66 (2011) 290–294.

[11] O.M. Khalil, I. Mingareev, T. Bonhoff, A.F. El-Sherif, M.C. Richardson, M.A. Harith, Studying the effect of zeolite inclusion in aluminum alloy on measurement of its surface hardness using laser-induced breakdown spectroscopy technique, Opt. Eng. 53 (2014) 14106.

[12] K. Yahiaoui, S.M. Aberkane, A. Naitbouda, Correlation between surface hardness of α-alumina samples and their spectroscopic parameters, Mater. Chem. Phys. 259 (2021) 124045.

[13] Y. He, Y. Deng, C. Yang, X. Wang, H. Mei, H. Liu, Z. Jia, Hardness Determination of Thin Film Structural Materials Using Laser-Induced Breakdown Spectroscopy, IEEE Trans. Plasma Sci. 51 (2023) 705–714.

[14] J. Huang, M. Dong, S. Lu, W. Li, J. Lu, C. Liu, J.H. Yoo, Estimation of the mechanical properties of steel via LIBS combined with canonical correlation analysis (CCA) and support vector regression (SVR), J. Anal. At. Spectrom. 33 (2018) 720–729.

[15] M. Momcilovic, J. Petrovic, J. Ciganovic, I. Cvijovic-Alagic, F. Koldzic, S. Zivkovic, Laser-induced plasma as a method for the metallic materials hardness estimation: An alternative approach, Plasma Chem. Plasma Process. 40 (2020) 499–510.

[16] H. Sattar, H. Ran, W. Ding, M. Imran, M. Amir, H. Ding, An approach of stand-off measuring hardness of tungsten heavy alloys using LIBS, Appl. Phys. B. 126 (2020) 1–11.

[17] NIST Atomic Database, (n.d.). https://www.nist.gov/pml/atomic-spectra-database.

[18] A.K. Tarai, R. Junjuri, S.A. Rashkovskiy, M.K. Gundawar, Time-Dependent Intensity Ratio-Based Approach for Estimating the Temperature of Laser Produced Plasma, Appl. Spectrosc. (2022) 00037028221117534.

[19] E. Mal, R. Junjuri, M.K. Gundawar, A. Khare, Optimization of temporal window for application of calibration free-laser induced breakdown spectroscopy (CF-LIBS) on copper alloys in air employing a single line, J. Anal. At. Spectrom. 34 (2019) 319–330.

[20] M.L. Shah, A.K. Pulhani, G.P. Gupta, B.M. Suri, Quantitative elemental analysis of steel using calibration-free laser-induced breakdown spectroscopy, Appl. Opt. 51 (2012) 4612–4621.

[21] E. Mal, R. Junjuri, M.K. Gundawar, A. Khare, Temporal characterization of laser-induced plasma of tungsten in air, Laser Part. Beams. 38 (2020) 14–24.

[22] E. Mal, R. Junjuri, M.K. Gundawar, A. Khare, Time and space-resolved laser-induced breakdown spectroscopy on molybdenum in air, Appl. Phys. B Lasers Opt. 127 (2021). https://doi.org/10.1007/s00340-021-07598-6.

[23] R. Junjuri, S.A. Rashkovskiy, M.K. Gundawar, Dependence of radiation decay constant of laser produced copper plasma on focal position, Phys. Plasmas. 26 (2019) 122107.

Chapter 5

Machine learning based classification using LIBS: Effect of feature selection and extraction

This chapter explores the integration of LIBS with machine learning techniques for effective detection of explosives and classification of post-consumer plastics. It describes the utilization of a picosecond LIBS (psLIBS) system, equipped with a low-cost CCD spectrometer, for real-time applications. The study employs a systematic approach to combine Artificial Neural Network (ANN) with various feature selection and extraction approaches. This integration aims to enhance accuracy, decrease computational time, and optimise resource allocation. The initial sections of this chapter involves detection of explosives where five explosive and twelve non-explosive samples were considered. For plastic classificaiton, two distinct approaches were explored. At first, a total of nine plastics were obtained from a local recycling unit and both training and testing were performed on the same samples. Nevertheless, this technique is not suitable for real-time application since in real-time scenario samples that are unknown to the trained model will be encountered. To address this, another study was performed on a set of 30 samples from six commonly used groups. 29 samples out of 30 are utilized for training and validation purposes, while the 30th sample, which is unfamiliar to the network, is employed for testing. The study thoroughly compares outcomes across several approaches, evaluating their accuracy, processing speed, and resource utilization to identify the most efficient approach for real-time identification of materials. This comprehensive analysis provides insights into the optimal method for accurate material identification while considering efficiency and resource allocation.

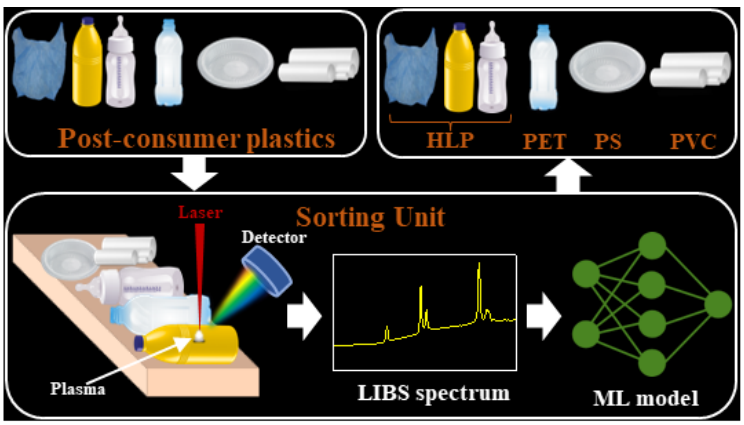

5.1. Introduction

The fusion of LIBS data with advanced computational techniques has far-reaching implications, extending its impact to diverse sectors, including metallurgy[1,2], geology[3–5], environmental science[6–8], defence applications[9–11], forensic investigations[12,13], archaeological survey[14–16], agriculture[17–19], medical diagnostics[20,21], art and cultural heritage[22,23], pharmaceuticals[24,25], manufacturing[26,27], etc. LIBS combined with machine learning have shown promising results in identification and classification of materials across various sectors. In metallurgy, LIBS has been extensively used to distinguish and categorize different metals and alloys[28], while in geology, it aids in the classification of rocks and minerals, thereby contributing significantly to mineral exploration and resource assessment[29]. Environmental monitoring benefits from its capability in several ways, from detecting pollutants and contaminants in soil and water samples to identifying/sorting various wastes produced from our day-to-day life[30,31]. It also serves as a potential tool for defence applications for the rapid detection of various explosives and high-energy materials (HEMs) in bulk and trace amounts[10,32]. Further, it is helpful in archaeological and forensic applications for investigating human body remains, material identification, etc.[33,34]. It also has various applications in medical diagnostics like classifying tissue samples and detecting abnormalities[20,35]. LIBS can also be applied in pharmaceutical and chemical analysis to identify and classify compounds, including impurities in drug formulations[24]. Last, but not the least, LIBS can be used efficiently in manufacturing and welding for quality control of materials, detecting defects, etc.[26,27].

This chapter explores the potential of LIBS in identifying and categorizing explosives and post-consumer plastics, utilizing machine learning techniques. Identifying and classifying explosives and post-consumer plastics are important in defense applications and waste management, respectively. The forthcoming sections will briefly elaborate on the importance of addressing the aforementioned samples of intrest. However, in the context of *in situ* application, an ideal classifying instrument should be cost-effective, compact, and reliable, capable of providing a fast identification rate with higher accuracy. The instrumentation of LIBS comprises two major components, i.e., the laser source and the detector. Most LIBS research dedicated to identifying explosives and post-consumer plastics utilizes nanosecond (ns) lasers as the excitation source. Femtosecond (fs) laser is used in very few studies[36].

The difference between ns, picosecond (ps), and fs laser ablation mechanisms are different due to a large variation in their pulse duration[36]. Ultrafast pulses (ps and fs) rapidly form a hot

plasma without a liquid phase and less damage threshold on the sample. In the case of the long pulse (ns pulse), ionization, sample heating, and vaporization occur during plasma formation. The matter undergoes a transient change in thermodynamic regime from solid to plasma state through liquid state[36]. Moreover, in the case of ns pulse, the material requires higher pulse energies, which forms scars on the material surface due to melting. Ultrafast interactions have exciting features including the absence of plasma shielding effect and negligible heat transfer form the laser interaction zone to the surrounding lattice, leading to improved sensitivity compared to long pulse[37]. Long pulses result in high temperature and dominance of atomic emissions at the initial time of the plasma formation, whereas ultrashort pulses form plasma with low temperature and favour molecular emissions [38]. In the case of ns lasers, emissions from organic samples like explosives, plastics, pharmaceuticals, biological specimens, etc., are confined to the atomic lines of C, H, N, and O, limiting the number of features in the LIBS spectra[39]. Ultrafast lasers yield more pronounced molecular emissions than ns lasers, potentially increasing the significant features in the spectra of organic samples, making them well-suited for the analysis. However, considering the real-time use, fs lasers pose challenges due to their substantial cost and larger physical dimensions than ps lasers. Therefore, the ps laser can be a better choice for this application as it provides more significant molecular emission compared to the ns laser. This chapter explores psLIBS for the identification and classification of explosives and post-consumer plastics. In terms of the detector, both ICCD and CCD based spectrometers have been used by researchers for classification studies of similar samples. Some comparative studies have been reported on spectrometers, focusing on their efficacy and robustness in classifying materials. For example, Rajendhar et al. demonstrated using a CCD spectrometer above ICCD for accurate discrimination of plastics, which also reduces the cost and time of analysis by many folds[8]. Also, the accuracy and testing time comparison between the single-shot ICCD, multi-shot ICCD, and single-shot CCD data acquisition were discussed. Therefore, in this study, the selection of CCD over ICCD was based on cost-effectiveness and compact size.

In LIBS, not all data points within the spectra possess high significance[8,40]. Focusing the study on the most significant features is beneficial, as it efficiently decreases the complexity of the data analysis. This strategy not only enhances the computational efficiency but also optimizes the resource usage. There are two approaches to reduce the dimension of the input data, i.e., 1) feature selection, where unwanted features are removed from the dataset manually or by using statistical/machine learning models, and 2) feature extraction, where machine learning algorithms are used to transform the original data into a new dataset. The purpose of

this transformation is to present the data in a concise manner, capturing the essential patterns or characteristics while reducing the dimension of the dataset. Feature selection/extraction is crucial in real-time application as it reduces the dimensionality of the data, improve model performance, mitigate overfitting, and expedite computational processes. Additionality, they enhance data interpretability, visualization and address multicollinearity, thus enabling more effective decision-making and insights. Various feature selection and feature extraction approaches have been explored in LIBS for the discrimination of materials. For example, in the worldwide contest held during the EMLIBS2019 conference for the classification of soils, several groups participated, explored the advantages of feature selection and feature extraction, and demonstrated various approaches to obtain higher classification rates[40]. *A. K. Myakalwar et al.* presented judicious feature selection by genetic algorithm approach for explosive detection[41]. *R. Junjuri et al.* have reported using random forest (RF) algorithm along with ANN to significantly decrease the analysis time with a minimal decrease in the classification accuracy of plastics[8]. *F. Ruan et al.* also used RF algorithm and hybrid filter/rapper method to classify archaeological samples[16]. *C. Huffman et al.* considered a statistical feature selection approach for classification problems in biological applications[42]. *T. Vance et al.* used PCA as a feature extraction tool for classifying different proteins[43]. These aforementioned studies stipulate that feature selection and feature extraction are useful in the case of *in situ* applications as higher accuracy can be achieved with minimal time.

This chapter explores the potential of a compact psLIBS setup for discrimination of explosives and post-consumer plastics using ANN coupled with various feature selection and feature extraction techniques. Among feature selection approaches, three manual feature selections (selection of sub-spectra) were considered, such as 1) wavelength ranges covering peak regions, 2) C, H, and N (CHN) peak regions, and 3) peak heights as input to ANN. Also, the RF algorithm was used to select the wavelength values with high feature importance. Apart from that, feature extraction techniques like principal component analysis (PCA) and linear discriminant analysis (LDA) were implemented on the original data with the aim of maximizing accuracy. The accuracy and analysis time obtained from various feature selection and extraction processes were compared with that of the original data. The flow chart of algorithm architecture is depicted in figure 5.1.

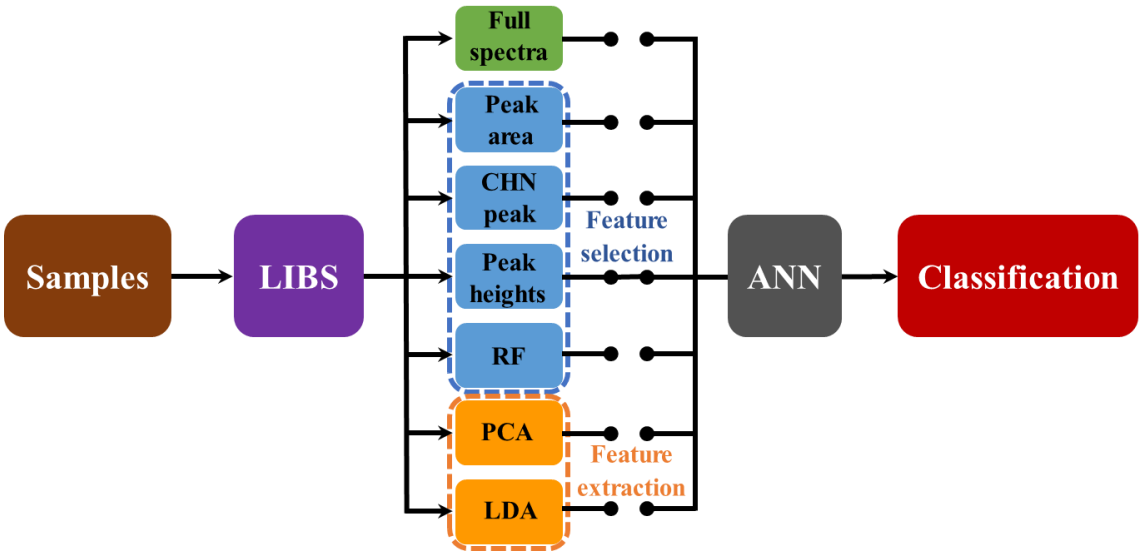

Figure 5.1. Flow chart of analysis protocol.

5.2. Experimental Details

The schematic of the experimental setup is shown in chapter 2 (figure 2.6). In brief, it comprises a picosecond laser (Ekspla, PL-2250 series) delivering energy of 10 mJ per pulse at 10 Hz repetition rate. The laser operated at its fundamental wavelength of 1064 nm with a pulse duration of ~30 ps. The laser pulse was focused on the sample surface through a plano-convex lens (focal length of 15 cm) to produce the plasma. An XY-translation stage controlled by a motion controller (Newport, ESP 300) was used to move the sample to avoid deep crater formation at the same spot. The emissions from the plasma were collected by a collection optics assembly (Andor, ME OPT 007) and sent through an optical fiber of core diameter 600 µm to a non-gated Czerny Turner CCD spectrometer (Avantes, AvaSpec – ULS2048L – USB2) of optical resolution of ~0.29 nm. The spectrometer produces the LIBS spectra in the 200 – 750 nm wavelength range. 200 spectra for each sample were acquired with an integration time of 500 ms.

5.3. Detection of explosives

In the last few decades, the threat to homeland security around the world, as well as in India, urged the need for an automated portable device for the rapid detection of high energy materials (HEMs), including explosives, improvised explosive devices (IEDs), etc. Especially in public places like airports, railway stations, metro stations, shopping malls, worship places, etc., an advanced explosive detection device based on modern analytical techniques is essential for detecting HEMs with high confidence. LIBS is a potential tool for the on-site detection of

explosives with numerous advantages over other techniques. These advantages include robust signal acquisition, standoff detection, trace level identification, rapid prediction, etc.

Since the first realization of LIBS application for detecting explosives and propellants in 2003[44], extensive researches have been carried out in this area. Over time, as LIBS advances to explore plasma evolution studies[45–47], molecular dynamics[48], etc., with growing development in data analysis by integrating machine learning, it has emerged as a potential fingerprint technique for rapid identification of explosives in real-time. Several research studies were devoted to literature for detecting explosives using LIBS combined with several analytical, statistical, and machine learning algorithms. The summary of the application of LIBS combined with various analytical methods for explosive detection is presented in table 5.1.

Table 5.1. Summary of LIBS studies devoted to literature for explosive detection.

S. No.	Reference & Year	Sample(s)	Method(s)	Results
1	[49] & 2023	H_2BTE, CL20, TNT, TATB, DNAN	k-means cluster analysis and SVM combined with PCA	Accuracy > 90%
2	[10] & 2020	DNT, TNT, RDX, NTO	2D scatter plot, PCA, ANN	Accuracy = 94.2%
3	[50] & 2019	HMX, CL20, RDX, TNT	semi-supervised learning algorithm	TP = 99. 8%, TN = 99. 9%
4	[51] & 2017	CL20, HMX, NTO, RDX, TNT	Ratiometric, PCA	Good separation observed
5	[52] & 2017	HMX, NTO, TNT, RDX, PETN	kNN-PCA, PLS-DA	Accuracy = kNN-PCA: 91.26%, PLS-DA: 90%
6	[53] & 2017	TNT, RDX, Propellant	PCA-ANN	Accuracy = 100%
7	[54] & 2016	PETN, UN, RDX, AN	Feature line recognition	Trace detected on various substrates
8	[55] & 2015	HMX, NTO, PETN, RDX, TNT	PLS-DA combined with genetic algorithm feature selection	Accuracy = 94.2%
9	[56] & 2015	DNT, RDX	SUSPECT methodology	Residues detected on various surfaces
10	[57] & 2014	AP, BPN, AN	Ratiometric	Good discrimination obsedrved
11	[58] & 2014	DNT, TNT, RDX, PETN	SVM	Accuracy =92%
12	[59] & 2013	DNT, TNT, RDX, PETN	Neural network classifier trained by the Levenberg-Marquardt rule	Accuracy = 88%, Precision =67%
13	[60] & 2012	TNT, RDX, HMX, PETN, AN	LDA, SVM	Accuracy = LDA: 85.9%, SVM: 96%
14	[61] & 2012	TNT	PLS-DA, PCA	PLS-DA shows good separation. PCA differentiates TNT from organic and non-organic materials but fails to differentiate from plastic.
15	[62] & 2012	TNT, RDX and a mixture of both	PLS-DA	TP = 99.5%, FP = 1.9%

16	[63] & 2011	DNT, TNT, RDX, PETN	Correlation coefficient	R_{DNT} = 0.623, R_{TNT} = 0.498, R_{RDX} = 0.436, R_{PETN} = 0.465
17	[64] & 2011	DNT, TNT, RDX, PETN	Correlation coefficient	R_{DNT} = 0.604, R_{TNT} = 0.420, R_{RDX} = 0.466, R_{PETN} = 0.460
18	[65] & 2009	RDX	PLS-DA	TP = 97.1%
19	[66] & 2009	DNT, TNT, C4 explosive, H15 explosive	Decision-making based on logical conjunction	Sensitivity to 8 shot =100%
20	[67] & 2007	RDX, TNT	PCA	TP = 96%, FP = 0%
21	[68] & 2006	TNT, RDX, PETN, C4, Comp B	Decision making strategy	Excellent prediction rate obtained

⋆ H_2BTE: Diazomethane, CL20: Hexanitrohexaazaisowurtzitane, TNT: Trinitrotoluene, TATB: Triaminotrinitrobenzene, DNAN: 2,4-Dinitroanisole, DNT: 2,4-Dinitrotoluene, RDX: 1,3,5-Trinitro-1,3,5-triazinane, NTO: Nitrotriazolone, ANN: Artificial neural network, HMX: 1,3,5,7-Tetranitro-1,3,5,7-tetrazocane, TP: True positive, TN: True negative, PETN: Pentaerythritol tetranitrate, kNN: k-nearest neighbours, PLS-DA: Partial least square discriminant analysis, UN: Urea nitrate, AN: ammonium nitrate, AP: Ammonium Perchlorate, BPN: Boron Potassium Nitrate, MNT: Mononitrotoluene, FP: False positive

As discussed in the introduction, feature selection and feature extraction can play crucial role in the identification/classification of materials using LIBS and machine learning. This aspect possess the potential to significantly improve the accuracy. However, very few research studies were devoted to literature for the identification of explosives by implementing feature selection or feature extraction approaches with machine learning to the LIBS data, as evidenced by the observation in table 5.1. The studies employing feature selection or extraction approaches tend to utilize only one or two methodologies. This chapter explores several feature selection and extraction approaches with ANN to determine the best analysis protocol for identifying explosives in terms of accuracy.

5.3.1. Sample Details

Five explosive and 12 non-explosive samples with similar atomic constituents were considered for this study. The details of the samples are presented in table 5.2. Before the LIBS experiment, the solid samples were first cleaned with water and then methanol to remove surface contaminants in case of plastics. The powder samples were first ground with mortar and pestle for 15 min. After that, circular pellets with a diameter of 10 mm were prepared for each sample by applying 2 tons of hydraulic pressure for 5 minutes. The pellets were prepared to give each sample a flat, uniform surface. In total, 3400 (17 × 200) spectra were recorded, i.e., 200 spectra for each sample.

Table 5.2. Details of the explosive and non-explosive sample used for the study.

Sl. No.	Name	Chemical Formula	Sample form	Group★ (E/NE)
1	Acrylonitrile butadiene styrene (ABS)	$(C_{15}H_{17}N)_n$	Solid	NE
2	Poly(methyl methacrylate), also called ACRYLIC	$(C_5O_2H_8)_n$	Solid	NE
3	DL_Alanine	$C_3H_7NO_2$	Powder	NE
4	DL_Histidine	$C_6H_9N_3O_2$	Powder	NE
5	High-density polyethylene (HDPE)	$(C_2H_4)_n$	Solid	NE
6	Low-density polyethylene (LDPE)	$(C_2H_4)_n$	Solid	NE
7	L_Leucine	$C_6H_{13}NO_2$	Powder	NE
8	NYLON	-	Solid	NE
9	Polycarbonate (PC)	$(C_{16}H_{14}O_3)$	Solid	NE
10	Polyethylene terephthalate (PET)	$(C_{10}H_8O_4)_n$	Solid	NE
11	Polypropylene (PP)	$(C_3H_6)_n$	Solid	NE
12	SIHET	-	Solid	NE
13	Ammonium nitrate (AN)	NH_4NO_3	Powder	E
14	Hexanitrohexaazaisowurtzitane (CL20)	$C_6N_{12}H_6O_{12}$	Powder	E
15	1,3,5,7-Tetranitro-1,3,5,7-tetrazocane (HMX)	$C_4H_8N_8O_8$	Powder	E
16	Nitrotriazolone (NTO)	$C_2H_2N_4O_3$	Powder	E
17	1,3,5-Trinitro-1,3,5-triazinane (RDX)	$C_3H_6N_6O_6$	Powder	E

★E: Explosive, NE: Non-explosive

5.3.2. Results

The normalized averaged LIBS spectra of all explosives and non-explosives acquired in the range of 200 – 750 nm are depicted in figure 5.2. All the emission spectral lines were identified with the aid of NIST atomic database. Prominent C, H, and N emission lines were observed in the spectral range of acquisition. Strong emission lines of Na are also observed in some samples due to the contamination. Also, the molecular structure of CN – violet and C_2 – swan bands were observed. The formation of molecules in LIP is complex to understand; however, extensive studies have reported that the molecular formation of CN band could be due to the recombination of C and N atoms [38,69]. The C_2 bond was observed due to the C = C linkage of the analyte [38,69].

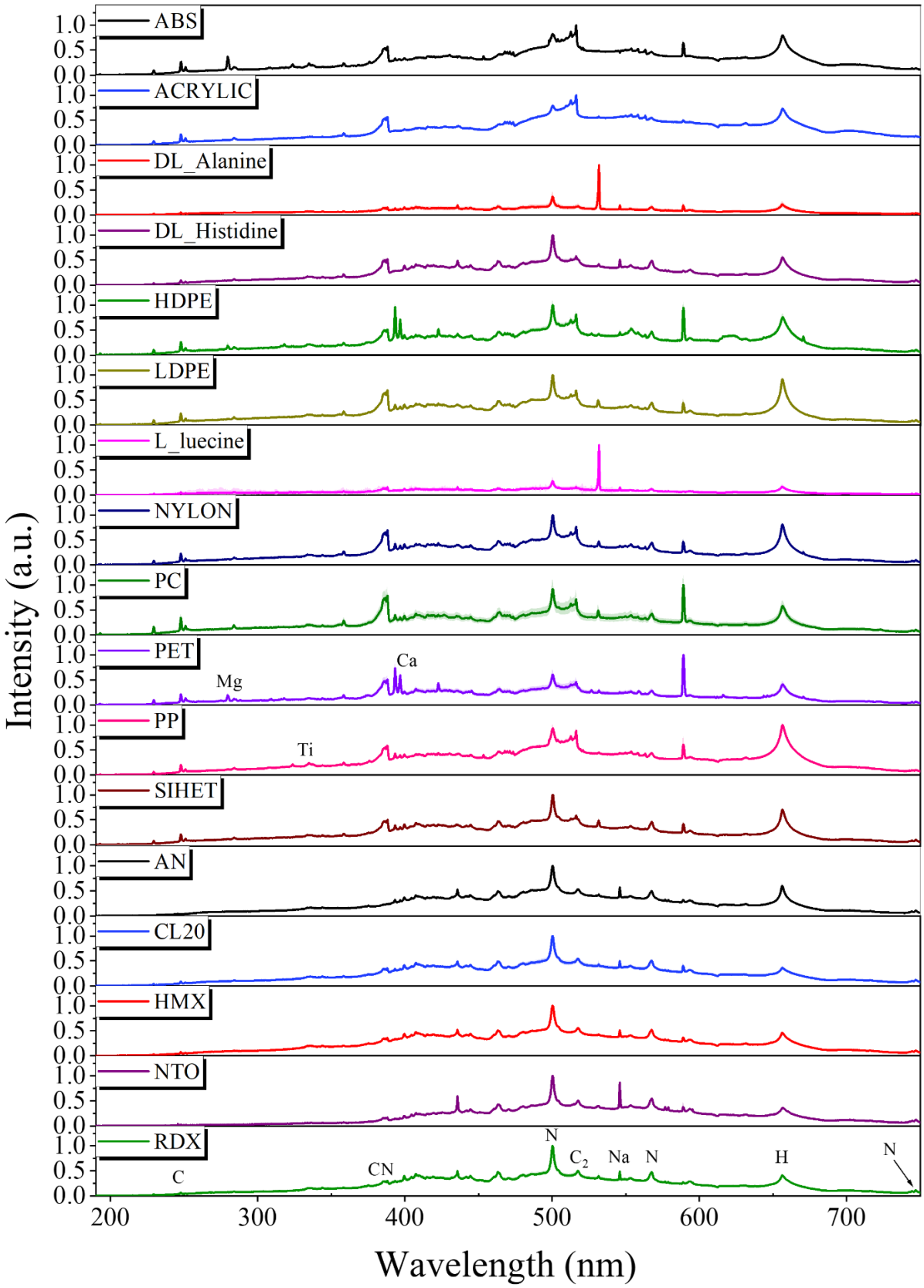

Figure 5.2. LIBS spectra of explosives and non-explosives.

From figure 5.2, it can be observed that all the spectra look similar due to their similar chemical composition. However, since the elemental compositions of C, H and N are

different in different plastics, the intensities corresponding to these species differ. Moreover, the intensities of impurities and contaminated species also differ.

5.3.2.1. ANN with full spectrum as input

ANN is a robust machine learning tool widely used for the classification of various materials, including explosives[10], plastics[8], metals[70], etc. The architecture and working procedure of ANN have been inspired by the nervous system of the human brain. The main components of ANN are the input layer, hidden layer, and output layer. The spectral data of plastics were fed to the input layer of the network. The scaled conjugate backpropagation algorithm was used to train the model. The number of neurons in the input layer is equal to the number of variables and in output layer is equal to the number of classes. The number of neurons in the hidden layer was optimized to 30 for a higher classification rate. The analysis was performed over 100 iterations and for each iteration, the total data (3400 spectra) was divided randomly for training (70%), validation (15%) and testing (15%). Initially, every spectrum within both the train and validation datasets is categorized into their respective groups, either explosive or non-explosive (refer to table 5.2). The test phase involves utilizing test data to predict whether a given spectrum corresponds to an explosive or non-explosive category. Following this, a separate training model is constructed specifically focusing on the explosive samples, which are labeled to explosive sample names. Once a spectrum is identified as explosive, it proceeds to a secondary model designed to determine the specific type of explosive it belongs. The overall classification accuracies for both the models obtained from the ANN analyses are presented in a confusion matrix in table 5.3.

Table 5.3. Results obtained from ANN for (a) explosives and non-explosives (b) within explosives.

(a)

		Predicted class	
		Non explosive	Explosive
Actual class	Non explosive	99.98	0.02
	Explosive	4	96

(b)

		Predicted class				
		AN	CL20	HMX	NTO	RDX
Actual class	AN	100	0	0	0	0
	CL20	0	99.98	0	0	0.02
	HMX	0	0	100	0	0
	NTO	1	0	0	99	0
	RDX	0.005	0.03	0.015	0	99.95

Table 5.3a shows that explosives are identified accurately at a rate of 96%, with 4% false alarm rate. Additionally, non-explosives are almost perfectly classified, close to 100% accuracy.

Moreover, table 5.3b reveals that the classification accuracy within explosives surpasses 99% for all six kinds of explosives.

In real-time applications, the testing time is also important in terms of speed and operational efficiency. The ANN demonstrates an average testing time of 150 ms when classifying explosive and non-explosive items. Conversely, the average testing time and ANN model size reduced significantly to 60 ms for predicting explosive type. Ensuring maximum accuracy (100%) and zero false alarms is imperative in the realm of explosive detection. The reliability of accurate explosive detection systems is pivotal in upholding public trust in security measures and the deployed systems safeguarding communities. Maintaining this accuracy reinforces confidence in the efficacy of security protocols and safety measures. In this scenario, each spectrum comprises 2048 features/variables/wavelength values. However, all the features (data points) are not significant since most represent noise. Therefore, it is beneficial to restrict the analyses to the selected features of interest by eliminating irrelevant and unwanted features. This will help in many ways, such as overfitting reduction, reducing dimension, improving generalization, enhancing model performance, etc. There are many ways of selecting relevant features by using feature selection and feature extraction approaches.

In this context, various feature selection and extraction approaches were explored with the aim of maximizing the accuracy further.

5.3.2.2. ANN with feature selection

Feature selection is a process that involves the recognition of important features in the original data. This can be achieved through manual selection of spectral regions based on the emission of elemental compositions or by employing multivariate statistical or machine learning techniques which offer insights into the significance of each variable. In this context, different approaches selecting different areas of the original spectra were used under manual feature selection. Additionally, random forest (RF) feature selection was leveraged with different spectra regions, selected based on different threshold values of feature importance.

5.3.2.2.1. Manual feature selection

In this section, ANN analyses were performed on some variables of interest that were selected manually. Three approaches for manual feature selection were considered. The first approach includes the spectral region of all the peaks observed in the spectra, which comprise 59% of the total data. Second, those areas where only C, H, and N-based peaks are present and these represent 17% of the total data, and lastly, only peak heights, i.e., one data point (maxima) for

each peak were considered, which comprises 3% of the total data. The three manual feature selection approaches adopted here are graphically presented in figure 5.3. Here, the full spectrum (black colored) is a reference spectrum depicted only for graphical demonstration.

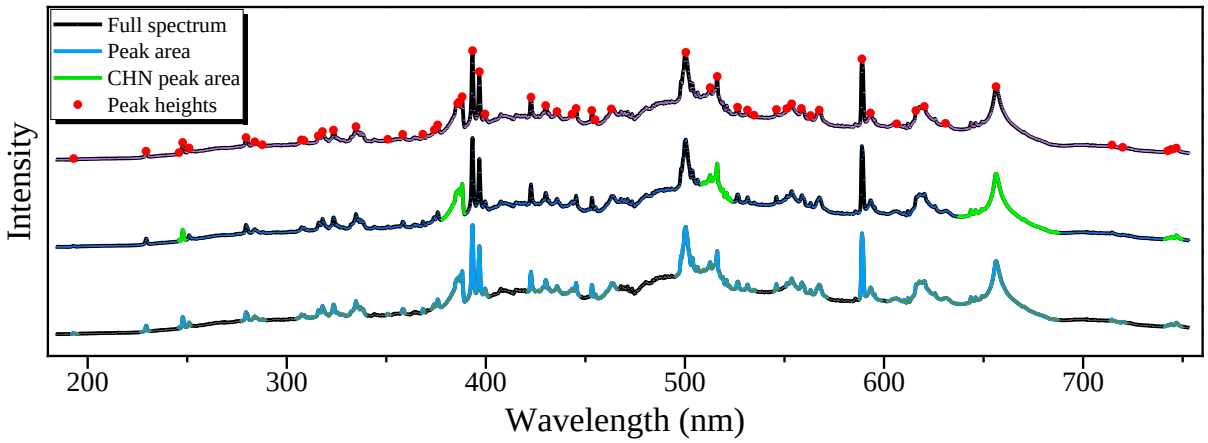

Figure 5.3. Graphical representation of features/variables considered under manual feature selection.

Table 5.4. Results obtained from ANN for (a) explosives and non-explosives (b) within explosives with manual feature selection approaches.

(a)	Prediction rate (%)		
	Peak area	CHN peak area	Peak height
Non-explosive	99.98	99.82	99.99
Explosive	99	99.99	95

(b)	Prediction rate (%)		
	Peak area	CHN peak area	Peak height
AN	100	97.8	92.68
CL20	100	99.99	93.01
HMX	99	98.74	89
NTO	100	99.99	92
RDX	99.99	99.24	85.96

The ANN analyses were performed in the same manner as in the case of the full spectrum. The ANN analyses have been performed on two datasets (i.e., explosive and non-explosive, within explosive). The ANN results obtained are discussed in table 5.4. From table 5.4a, it is evident that ANN shows excellent results in predicting explosives and non-explosives by leveraging peak area and CHN peak area as input to the ANN model. Nevertheless, a slightly lower prediction rate is observed when considering peak height as an input for the ANN model than the other two manual feature selection approaches. This disparity might be attributed because of the utilization of a very small dataset (only 3% of the total data) to train

the model, resulting in an underfitting scenario. Similar observations can be noticed in the case of classification within explosives (see table 5.4b).

5.3.2.2.2. Random Forest (RF) feature selection

RF is a sophisticated statistical algorithm comprised of tree-type classifiers. Each tree-type classifier within the RF employs a distinct training set generated through the bootstrap resampling method[71]. This algorithm has been popularly used as a classification technique. However, this is also often used as a feature selection tool by estimating the variable importance (VI) of each feature[8,40]. The VI value of each variable is obtained by calculating out-of-bag (OOB) error[71].

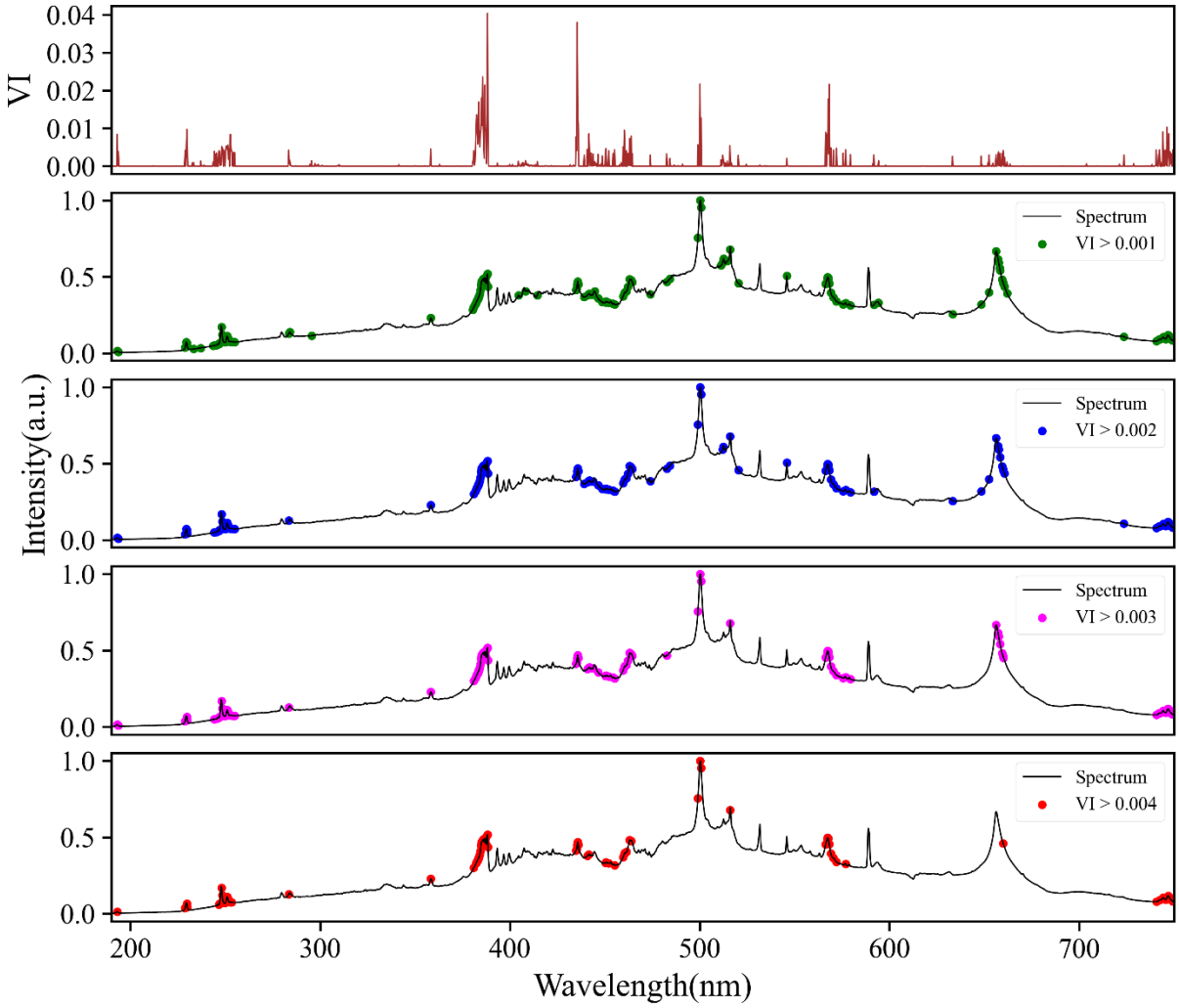

Figure 5.4. Variable importance (VI) estimated by RF model for explosive and non-explosive data. For visual purpose, each spectrum showcased in this figure represents the average of all spectra.

Here, the analyses were performed by considering only important features selected from VI as inputs to ANN for two datasets. Four sets of features were considered based on various VI

threshold values. The analyses were performed with features greater than VI values of 0.001, 0.002, 0.003 and 0.004 for each dataset. The four sets of features obtained from different VI thresholds are graphically presented in figure 5.4 and 5.5. The figures show that with the VI threshold of 0.001, the features include almost all the peak areas with some noise. As the VI threshold gradually increased, only C, H, N, Ca, and Na peaks were observed as important features. The results of ANN analyses obtained are presented in table 5.5. The table shows that in both cases, RF with VI > 0.002 exhibits the highest prediction rate, which is close to 100%.

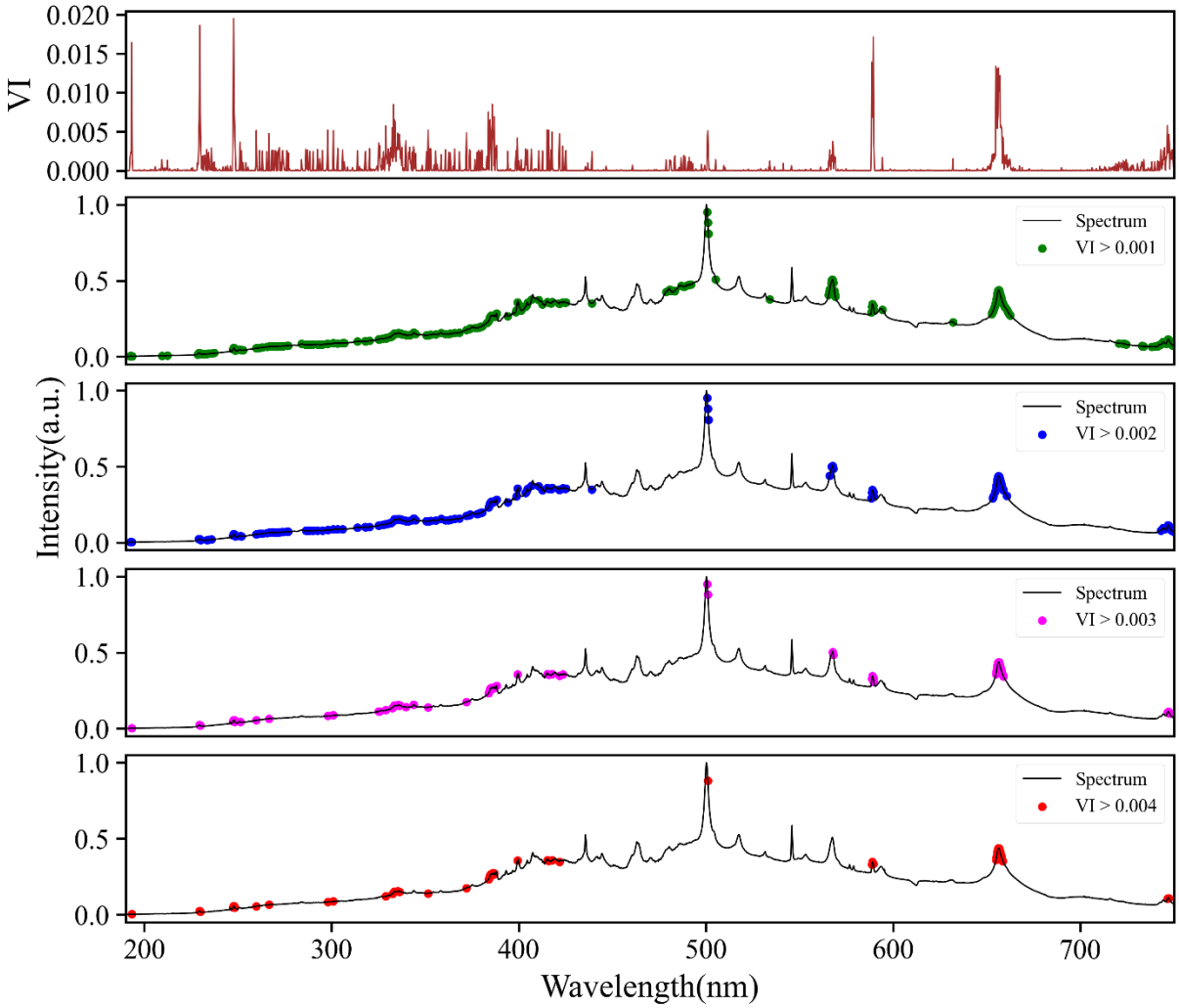

Figure 5.5. Variable importance (VI) estimated by RF model for explosive data. For visual purpose, each spectrum showcased in this figure represents the average of all spectra.

Table 5.5. Results obtained from ANN for (a) explosives and non-explosives (b) within explosives with RF feature selection.

(a)	Prediction rate (%)			
	VI >			
	0.001	0.002	0.003	0.004
Non-explosive	99.99	99.98	99.99	99.77
Explosive	92	99	95.11	96.98

(b)	Prediction rate (%)			
	VI >			
	0.001	0.002	0.003	0.004
AN	98.55	100	98	99
CL20	100	99	100	98
HMX	98.57	100	98	96
NTO	98	99	99	100
RDX	99.27	100	97	94.99

5.3.2.3. ANN with feature extraction

Feature extraction algorithms transform the original data into a new and smaller dataset based on the properties of data like variance. It provides a meaningful representation of the original data by highlighting the most important features and removing noisy and redundant information. In this context, two feature extraction approaches, PCA and LDA, are used to transform the original data for the input to the ANN algorithm.

5.3.2.3.1. Principal Component Analysis (PCA)

PCA is an unsupervised machine learning algorithm that transforms complex data in lower dimensions through dimensionality reduction. It transforms the original data into a new set of coordinates that are orthogonal to each other called principal components (PCs). The transformed data in the PC space is called scores. The PCs explain the variance in the original data in a gradient manner i.e., the first PC explains highest variance, followed by the second, third, and so on.

Figures 5.6 and 5.7 represent 3D score and variance plot, respectively. Figure 5.6 shows that the explosives make compact and separate clusters with no overlap with the non-explosives, indicating that they can be classified based on the scores rather than the original data. Also, there are multiple overlapping clusters within non-explosives. Figure 5.7 shows that the first three PCs explain 80, 8 and 7 % of the total variance, respectively, and the first ten collectively explain 99.5 % of the total variance.

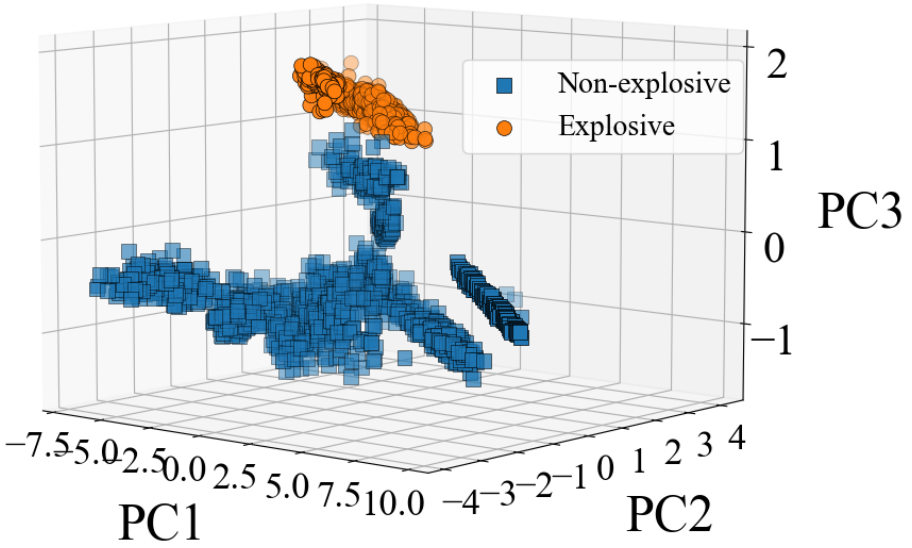

Figure 5.6. 3D score plot of first three PCs for explosive and non-explosive data.

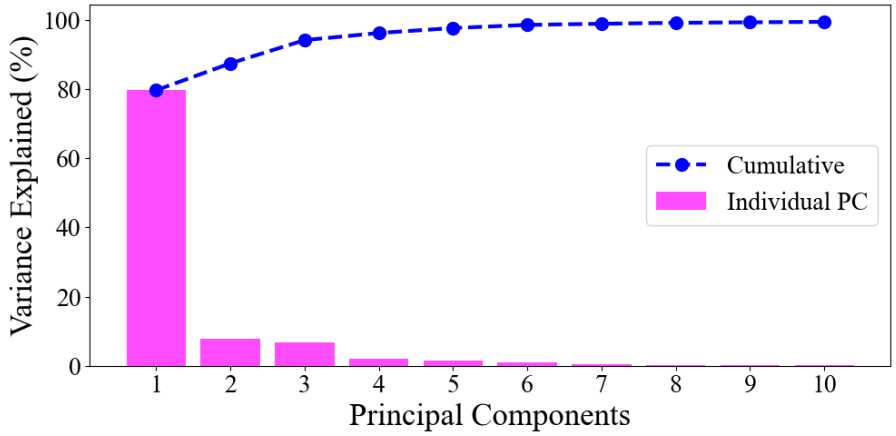

Figure 5.7. Variance plot of first ten PCs for explosive and non-explosive data.

Further, PCA was performed on the spectra corresponding to five explosives separately. Figures 5.8 and 5.9 represent 3D score and variance plot, respectively. From figure 5.8, it can be observed that NTO makes compact and separate clusters with no overlap with others. AN and CL20 also make separate clusters with minimal overlap and some spread, whereas a partial overlap between HMX and RDX is observed. The score plot also indicates the possibility of classification between them using the scores. Figure 5.9 shows that the first three PCs explain 76, 16 and 5 % of the total variance, respectively and the first ten PCs collectively explain 98.97 % of the total variance.

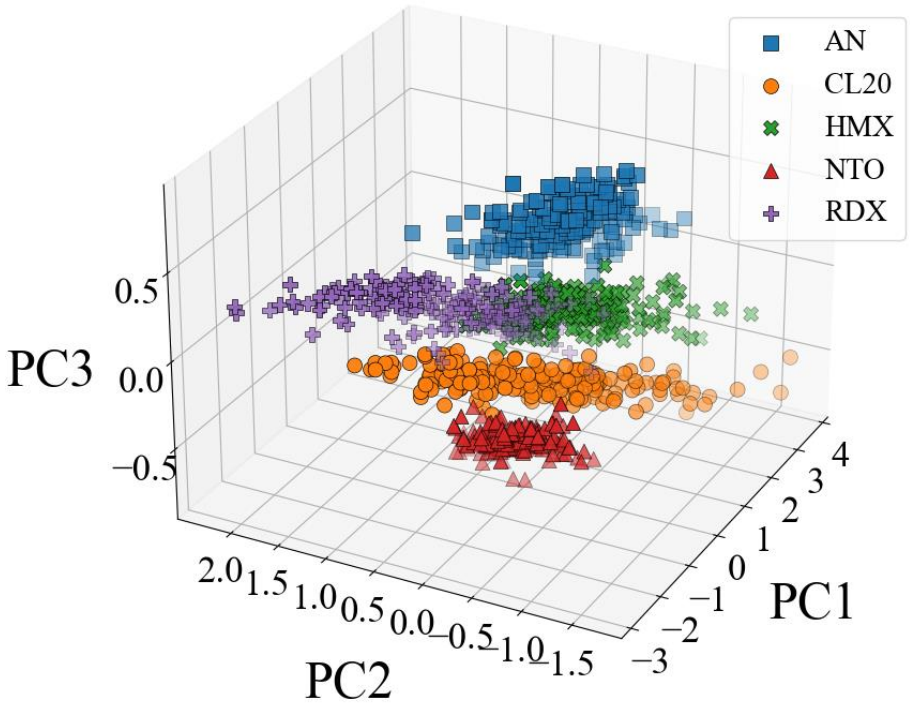

Figure 5.8. 3D score plot of first three PCs for explosive data.

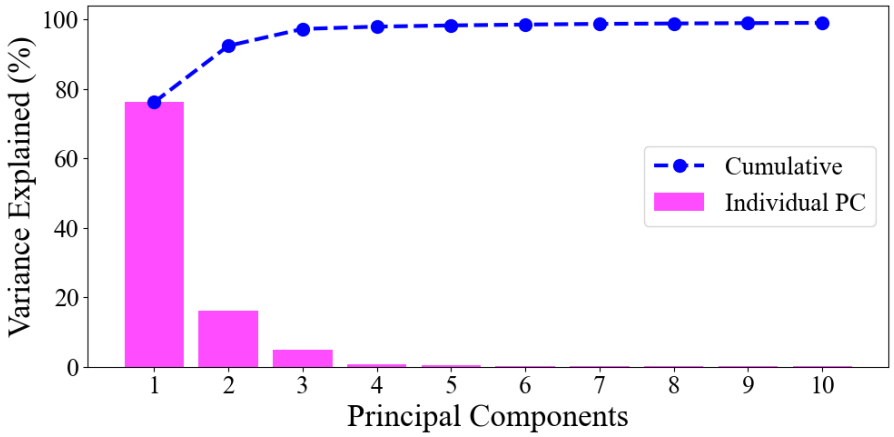

Figure 5.9. Variance plot of first ten PCs for explosive data.

Further, the ANN analyses were employed on the scores obtained from PCA analysis in a similar manner as before. ANN was employed by considering only the scores corresponding to the first PC as input data; then, collectively, the first 2, 4, 8, 10, 20, 40, 60, 80 and 100 scores were used as input to ANN. The average prediction rate of plastics obtained considering different sets of scores is shown in a bar chart in figure 5.10. From the figure, it can be noticed that the accuracy of the prediction increases with increasing the number of scores as input to the ANN but up to a certain value. After 8 scores, the increase in the number of scores doesn't significantly affect the classification accuracy between explosive and non-explosive.

Similarly, the accuracy becomes almost consistent for classification within explosive after 40 scores as input to the ANN model.

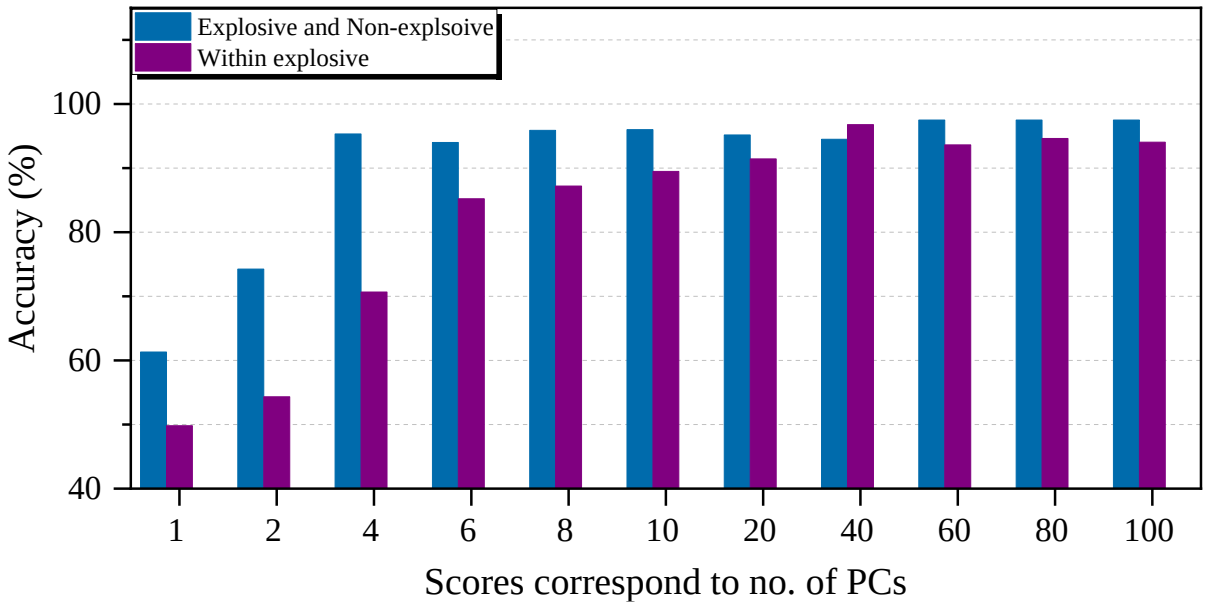

Figure 5.10. Prediction using different scores as input to ANN.

5.3.2.3.2. Linear Discriminant Analysis (LDA)

LDA is a supervised machine learning algorithm that effectively projects high-dimensional data into a lower-dimensional space by optimizing the separation of classes, thus efficiently extracting classification information while reducing the feature dimensionality [72]. The projection principle is set to ensure the minimum variance between interclass samples and the maximum variance between intraclass samples, i.e., LDA tries to project the sample onto a straight line. Unlike PCA, which maintains the information as much as possible, LDA makes the data points more distinguishable after dimension reduction. LDA is a good feature extraction technique that leads to a good separation in the feature space. The newly transformed coordinates are called linear discriminants (LDs), and the number of LDs depend on the number of classes, i.e., for n number of classes, the number of LDs are n-1. In a binary classification scenario distinguishing between explosive and non-explosive, only one LD is involved. However, when classifying within the explosives, the maximum number of LDs is four.

Figure 5.11 represents the 2D and 3D plots of the initial LDs classifying within explosives. A clear separation between different explosives with minimal variance between the interclass spectra was observed. After LDA, ANN analysis was employed on the only LD for predicting

explosive and non-explosive. For prediction within explosive, the ANN analyses were employed on the first LD, first two LDs, and so on up to the four LDs.

For explosive and non-explosive prediction, 100% accuracy was achieved. In case of within explosive prediction, the accuracy obtained from ANN analyses was shown in the bar chart in figure 5.12. From the figure, it can be noticed that the classification accuracy corresponding to the first LD is minimal and with increasing number of cumulative LDs, the accuracy increases and is maximum for all 4 LDs. However, for all the cases, the accuracy is below 90%.

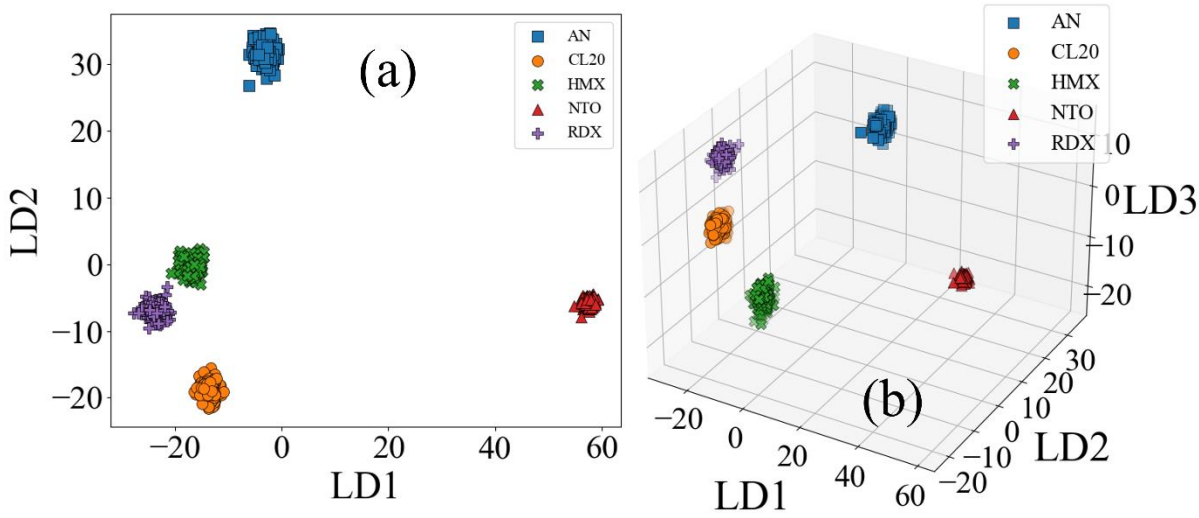

Figure 5.11. (a) 2D and (b) 3D plot of initial LDs classifying within explosives.

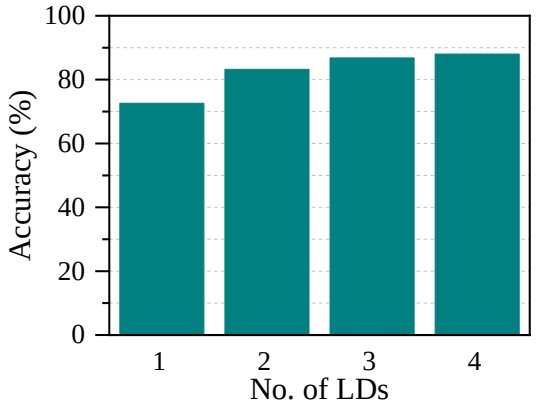

Figure 5.12. Prediction using different LDs as input to ANN.

5.3.3. Discussion

In this study, ANN analyses coupled with various feature selection and feature extraction methods were performed for the purpose of explosive detection. At first, ANN analyses were performed to classify explosives and non-explosive. Further, ANN analyses were performed only on explosives data to identify particular explosive types. The classification accuracies obtained from all the approaches are summarized in figure 5.13.

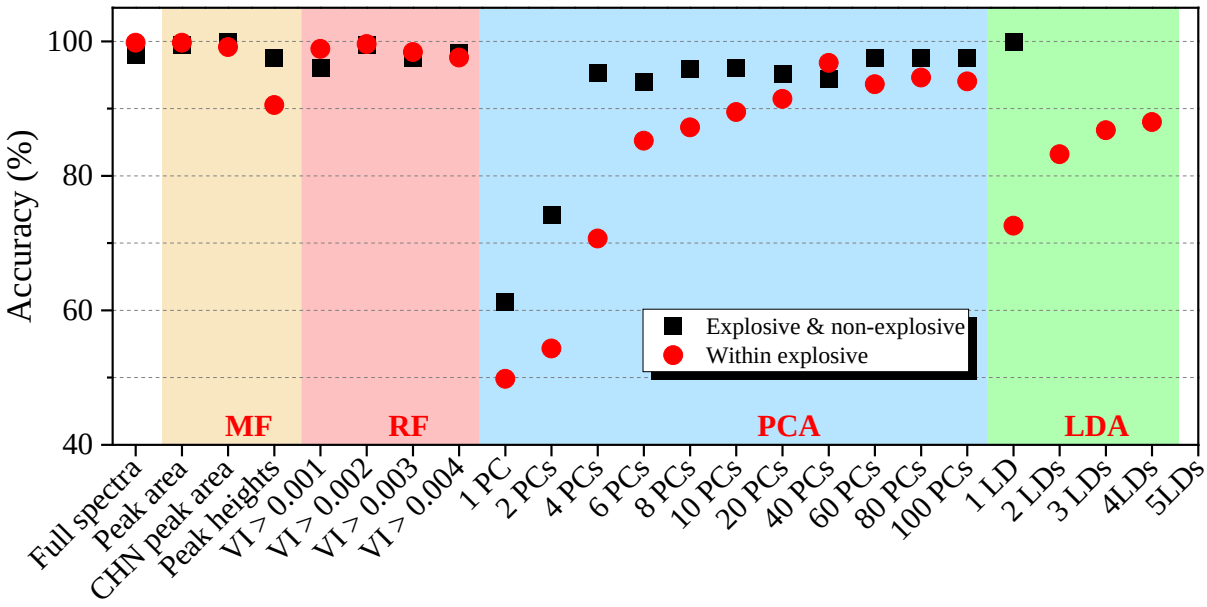

Figure 5.13. Classification accuracies obtained from various feature selection and feature extraction methods. Here MF represents manual feature selection.

The classification accuracy for distinguishing between explosive and non-explosive showcased remarkable performance across various feature extraction and selection methods. ANN combined with LDA feature extraction achieved a flawless 100% accuracy. Meanwhile, feature selection via manual and RF methods consistently achieved more than 96% accuracy. In the case of PCA feature extraction, results corresponding to initial PCs are poor, possibly due to the underfitting of the ANN model due to smaller datasets. However, the classification accuracy becomes more than 94% for PCs with more than four as input. The maximum accuracy (97.5%) is obtained for 60 PCs and more as input to the ANN model.

In classification within explosives, maximum accuracy (99.8%) was obtained for full spectrum and manual feature selection with peak area. Feature selection via manual RF methods consistently achieved more than 90% accuracy. Similar to the earlier case, poor results were observed when employing PCA feature extraction with fewer PCs as input for the model. However, for PCs with more than 20 as input, the classification accuracy becomes more than 91% and the maximum accuracy (96.8%) is obtained for 40 PCs as input to the ANN model. LDA demonstrates poor performance, consistently falling below 90%. However, a clear separation between different classes of explosives has been observed in the case of LDA (figure 5.11) as compared to PCA (figure 5.8). This is because PCA tries to preserve the feature information as much as possible in the new space, where LDA makes the data more distinguishable after dimensionality reduction [72]. Moreover, the number of LDs obtained from LDA is limited to the number of classes, and the dataset is too small compared to PCA to

train the ANN model, which might lead to the underfitting of the model. Therefore, the accuracies are low in the case of LDA compared to PCA. Furthermore, the testing time consistently remains between 20 – 150 ms across all methodologies. This swift testing time significantly expedites the process of real-time detection.

In this study, both the training and testing were performed on the LIBS spectra obtained from the same samples. However, in real-world scenarios, the model encounters unknown samples that haven't been seen by the trained model during the training process. Given the limited quantity of explosive samples available, the training and testing were conducted using the same set of samples. The next section explores the effect of testing on a new sample by considering a large set of plastic samples.

5.4. Identification of post-consumer plastics

With increasing population and modernization, the widespread adaptation of plastics in our day-to-day lives has experienced a substantial surge. Human society heavily relies on plastics as it is widely used in packaging, food safety, domestic equipment, industry, transport, electronics, etc. Its demand and use are continuously increasing because of its notable advantages such as cost-effectiveness, durability, low weight, flexibility in shape, etc. [73]. On the contrary, due to its high durability and low-degrading nature, it generates millions of tons of waste every year [74]. Thus, the management of plastic waste has now become essential. Traditional plastic waste management techniques like incineration and landfills are inconvenient as they cause colossal resource waste and adverse effects on the environment and human beings. Also, the toxic substances released in these processes severely harm soil, water, and air. Therefore, recycling is the most viable way to reduce final waste output. Classification/sorting of post-consumer plastics is the most critical step in the recycling process. The sorting process is essential to retain the quality and properties of recycled plastics [75]. For easy and convenient sorting, the Society for Plastic Industries (now called the Plastics Industry Association) instituted a labeling system that encodes different plastics [76]. Based on the labeling, manual sorting by visual inspection is the most common process, which is labor-intensive, more time-consuming, and error-prone. Also, it is harmful to the workers in case of hazardous contamination. Other classification techniques based on the physical properties are also developed, like the floating technique [77], an electrostatic technique [78], differential scanning calorimetric (DSC) [79], etc. These conventional methods greatly depend on the physical state of the sample and are more time-consuming and prone to errors. Most of these

techniques are confined to limited types of plastics. Thus, there is a need for an automated process that can increase the recycling rate without involving a large workforce.

Over the past few years, laser-induced breakdown spectroscopy (LIBS) combined with machine learning has shown increasing interest in the rapid identification of plastics regardless of the size, shape, and color of the material [8,38,73]. Several analytical approaches have been reported for the classification of plastics using LIBS signals. R. Junjuri et al. have investigated post-consumer plastics by exploiting atomic and molecular intensity ratios [38]. J. Anzano et al. [80–83] and V. K. Unnikrishnan et al. [84] have explored various statistical approaches like Euclidean distance, Receiver Operating Characteristic (ROC) analysis, Pearson's correlation coefficient, etc. Also, different machine learning algorithms have been widely used for the identification of plastics with higher accuracy. Some recent studies reported the classification of plastics using principal component analysis (PCA), partial least square discriminant analysis (PLS-DA), artificial neural network (ANN), etc. [8,30,38,84–88]. Table 5.6 provides a comprehensive summary of LIBS studies conducted in the past years, focusing on the identification of plastics.

Table 5.6. Summary of LIBS studies devoted to literature for identification/sorting of plastics. A: Sl. No., B: Reference & Year, C: Samples used, D: Sample collection source, E: Methods used for Identification/ Classification, F: Is testing performed on unknown sample?, G: Average accuracy (%).

A	B	C	D	E	F	G
1	[89] & 2022	PET, HDPE, LDPE, PP	NA	kNN and SVM	No	~ 100
2	[90] & 2022	POM, PVC, PA,ABS, PP, and PE	Industry	NCA, PCA and SVM	No	> 91
3	[7] & 2021	ABS, PA, PC, PMMA, POM, PTFE, PU, PP, PS, and PVC	Manufacturer	PCA and kNN	No	99.6
4	[91] & 2021	ABS, PA, PMMA, and PVC	Manufacturer	Residual network	Yes	73.34
5	[8] & 2020	HIP, SIHET, PC, PP, PS, HDPE, PET, LDPE, ABS, and PPCP	Recycling unit	RF and ANN	No	> 99
6	[30] & 2019	HIP, LDPE, ABS, PP, PS, HDPE, SIHET, PC, PET, and PPCP	Recycling unit	Ratiometric, correlation, and PLS-DA	No	> 93
7	[86] & 2019	HDPE, LDPE, PP, PVC, PS, ABS, PTFE, PC, PMMA, PU, and POM	Industry	PLS-DA	No	99.55

8	[38] & 2019	PET, HDPE, LDPE, PP, and PS	Recycling unit	ANN	No	~ 100
9	[92] & 2018	ABS, PA, PMMA, PVC, PC, PE, POM, PP, PS, PTFE, and PU	Industry	SOM, K - means	No	99.2
10	[93] & 2018	PP, PS, and ABS	Recycling centre	PCA and ICA	No	> 95
11	[94] & 2018	PE, PP, PVC, PS, ABS, PTFE, PA, PC, PMMA, PU, and POM	Industry	K-means clustering	No	99.6
12	[95] & 2017	ABS, PS, PE, PC, PP PA	E-waste recycling company	kNN and SIMCA	No	> 90
13	[96] & 2014	PP, PE, PS, PVC, PU, PTFE, ABS, POM and PMMA	NA	SVM	No	~ 100
14	[97] & 2013	ABS, PP and HIP	Commercial	Ratiometric	No	NA
15	[84] & 2013	PET, HDPE, PP, and PS	NA	PCA and MD	No	> 91
16	[98] & 2012	HDPE, LPDE, PP, PET, PS, and PVC	Commercial	DFA	No	99
17	[88] & 2011	PP, PE, PC, PVC, POM, PA, and PMMA	NA	ANN	No	~ 100

⋆NA: Not available, kNN: k-nearest neighbors, PCA: principal component analysis, PLS: partial least-square, PLS-DA: partial least-square discriminant analysis, SVM: support vector machine, NCA: nearest component analysis, SIMCA: soft independent modeling of class analogy, PU: polyurethane, PVC: polyvinylchloride, POM: polyvinylchloride, PA: polyamide, PE: polyethylene, PS: polystyrene, PU: polyurethane, PTFE: polytetrafluoroethylene, PMMA: polymethylmethacrylate, HIP: high impact polystyrene, POE: polyoxyethylene, PBT: polybutylene terephthalate, SOM: self-organizing maps, DFA: discriminant function analysis, ICA: independent component analysis, RBFNN: residual basis function neural networks, PPCP: polypropylene copolymer, MD: Mahalanobis distance.

Table 1 reveals that most research studies achieve outstanding identification and classification accuracy, exceeding 90% and even approaching 100%. However, the majority of these research studies lack practical relevance in real-world circumstances. A closer look at table 1 reveals that most research relies on neatly structured samples, often consisting of commercial or standard materials purchased directly from manufacturers or industrial suppliers. In contrast, real-time applications demand the classification of post-consumer/used plastics. Only a handful of research endeavours have delved into the classification of post-consumer/used plastics [8,30,38,93,95]. Along with these, in almost all research, the training set and testing set data came from the same sample, making the classification meaningless for practical application. In an attempt to address this challenge, X. Peng et al. employed distinct sets of samples for testing; however, they also faced limitations by using standard samples and achieved a

maximum average accuracy of only 73.34% [91]. Furthermore, it is worth noting that their study focused on four specific types of plastics: ABS (acrylonitrile butadiene styrene), PA (polyamide), PMMA (polymethyl methacrylate), and PVC (polyvinyl chloride). Notably, these plastics, particularly ABS, PA, and PMMA, do not account for much plastic waste compared to commonly used plastics such as PET, HDPE, LDPE, PS etc. [99].

Analogous to the investigations carried out in explosive detection, ANN was utilized, incorporating various feature selection and extraction methods. Their performances were compared in accuracy, testing time, data size, and model size to find the most effective strategy. The study explores two separate approaches for classifying post-consumer plastics. Firstly, nine different post-consumer plastics were collected from a local recycling unit, and both training and testing were performed on the same sample. Secondly, 30 post-consumer plastics representing six commonly used types (HDPE, LDPE, PP, PET, PS, and PVC) and five samples from each category were collected from garbage. Testing was performed on unknown plastic, mimicking real-world scenarios for identifying unfamiliar post-consumer plastics.

5.4.1. Post-consumer plastics from the recycling unit (Testing on same sample)

The experiment was called for nine post-consumer plastics, namely, Acrylonitrile butadiene styrene (ABS), Poly(methyl methacrylate), also called ACRYLIC, High-density polyethylene (HDPE), Low-density polyethylene (LDPE), NYLON, Polycarbonate (PC), Polyethylene terephthalate (PET), Polypropylene (PP) and SIHET. One sample from each category has been considered in this study. The details of the samples are provided in table 5.7. All the samples were collected from a local recycling unit. Each sample was first cleaned with water, followed by methanol in order to remove the contaminations from the surface. Two hundred spectra from each sample (a total of 1800 spectra) were acquired with 500 ms integration time. The normalized LIBS spectra of plastics acquired in the range of 200 – 750 nm are depicted in figure 5.14. All the emission spectral lines were identified with the aid of NIST atomic database. Prominent emission lines from C, H, and N were detected within the acquired spectral range. Additionally, strong emission lines of Na were commonly observed in many plastics, potentially indicating contamination since post-consumer plastics were utilized in the study. Low-intense emission lines of some elements like Ca and Mg were also noticed, which were added as traces during the manufacturing process to increase the hardness and lower the

production cost. Also, the molecular structure of CN – violet and C_2 – swan bands were observed.

Table 5.7. Details of the nine different post-consumer plastic samples.

S. No.	Scientific Name	Chemical formula	Recycling No. (#)
1	Acrylonitrile butadiene styrene (ABS)	$(C_{15}H_{17}N)_n$	7
2	Poly(methyl methacrylate), also called ACRYLIC	$(C_5O_2H_8)_n$	7
3	High-density polyethylene (HDPE)	$(C_2H_4)_n$	2
4	Low-density polyethylene (LDPE)	$(C_2H_4)_n$	4
5	NYLON	-	7
6	Polycarbonate (PC)	$(C_{16}H_{14}O_3)$	7
7	Polyethylene terephthalate (PET)	$(C_{10}H_8O_4)_n$	1
8	Polypropylene (PP)	$(C_3H_6)_n$	5
9	SIHET	-	7

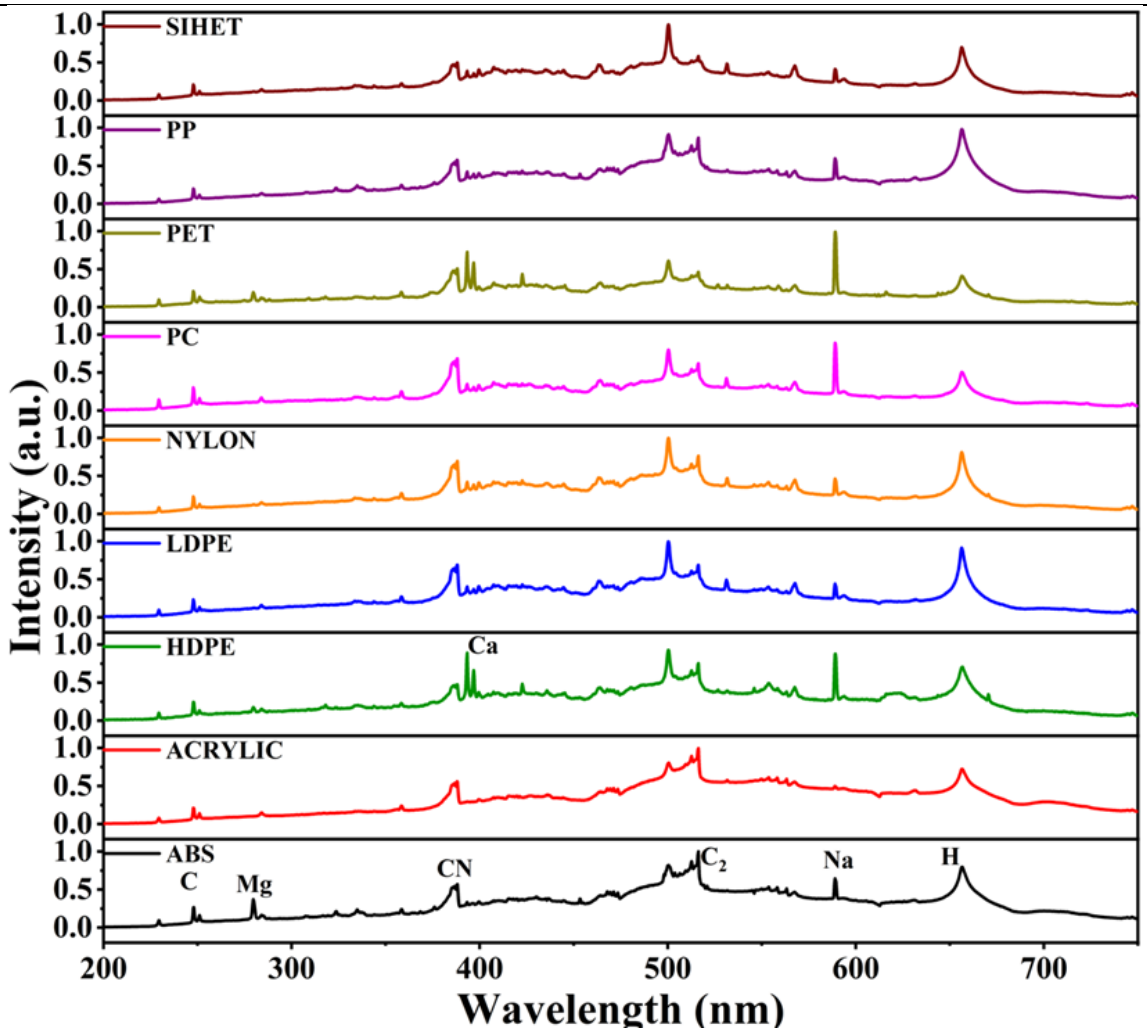

Figure 5.14. LIBS spectra of plastics acquired in the range of 200 – 750 nm.

From figure 5.14, it has been observed that all the plastic spectra look similar due to similar chemical composition. However, since the elemental compositions of C, H and N are different in different plastics, the intensities corresponding to these species differ from one another. Moreover, the intensities of impurities and contaminated species also differ from one another.

5.4.1.1. ANN with total data

The ANN analysis was performed over 100 iterations, and for each iteration, the total data (1800 spectra) was divided randomly into 70 + 15 + 15 % for training, validation and testing, respectively. The target data comprises class labels of nine different plastics. The overall classification accuracies of each sample obtained from the ANN analysis for the test data are presented in the form of a confusion matrix in table 5.8. More than 90% of classification accuracy was observed in the case of all the plastics and most of them are ~97%, with an average prediction rate of 96.43%. The average training and testing times taken for the ANN operation are 4436 and 8.44 ms, respectively.

Table 5.8. ANN results for classification of nine different post-consumer plastics.

		Predicted Class								
		ABS	ACRYLIC	HDPE	LDPE	NYLON	PC	PET	PP	SIHET
Actual Class	ABS	97	1.15	0.63	0.64	0.1	0	0	0.47	0.01
	ACRYLIC	3	96.99	0	0	0	0	0	0.01	0
	HDPE	0.12	0.23	96.99	0.44	0.17	0.2	0.17	0.82	0.85
	LDPE	0.03	0.1	0.5	92	3.32	1.06	0.1	1.34	1.54
	NYLON	0	0	0.12	1.31	97	0	0.4	0.69	0.49
	PC	0	0	0	0	0	100	0	0	0
	PET	0	0	0	0	0	0	99.86	0	0.14
	PP	2.83	1.35	2.14	1.81	1.29	0	0	90	0.6
	SIHET	0	0	0.71	0.48	0.09	0	0.72	0	98

5.4.1.2. ANN with feature selection

5.4.1.2.1. Manual feature selection

The same manual feature selection was employed, as discussed in section 5.3.2.2. The ANN analyses were performed in the same manner as in the case of total data. The data was split into 70% training, 15% validation and 15% testing sets. The results obtained from ANN analyses are summarized in table 5.9. The high average accuracy obtained is for the peak area and CHN peak area. The accuracy corresponding to peak heights is poor compared to the

other two. This might be attributed to the limited number of features utilized in training the model, potentially resulting in the underfitting of the ANN model. Comparing the training and testing time, the peak heights as input has lower training and testing time than others due to a smaller dataset, and the peak area as input shows higher training and testing time than the other two.

Table 5.9. Results obtained from ANN for classification of nine post-consumer plastics with manual feature selection.

Sl. No.	Plastic	Accuracy (%)		
		Peak area	CHN peak area	Peak height
1	ABS	98	94.98	82.94
2	ACRYLIC	98.01	99.79	89
3	HDPE	95.95	87.29	87.98
4	LDPE	89.97	86.96	73.61
5	NYLON	93.98	84.86	81.9
6	PC	98.57	95.8	91.01
7	PET	99.73	98.45	93.34
8	PP	93	95.8	80.05
9	SIHET	88	90.98	75.17
Average		95.02	92.77	83.89
Testing time (ms)		4.64	4.4	3.12
Fraction of total data (%)		59	17	3

5.4.1.2.2. Random Forest (RF) feature selection

Here, the analyses were performed by selecting only important features based on the variable importance (VI). A total of three sets of features were considered based on various VI threshold values. The analyses were performed on three sets of data with features greater than VI values of 0.001, 0.002 and 0.003. The three sets of features obtained from three VI thresholds are graphically presented in figure 5.15. The figure shows that with the VI threshold of 0.001, the features include almost all the peak areas with some noise. As the VI threshold gradually increased, only C, H, N, Ca, and Na peaks were observed as important features. The results of ANN analyses obtained by considering three different features are presented in table 5.10.

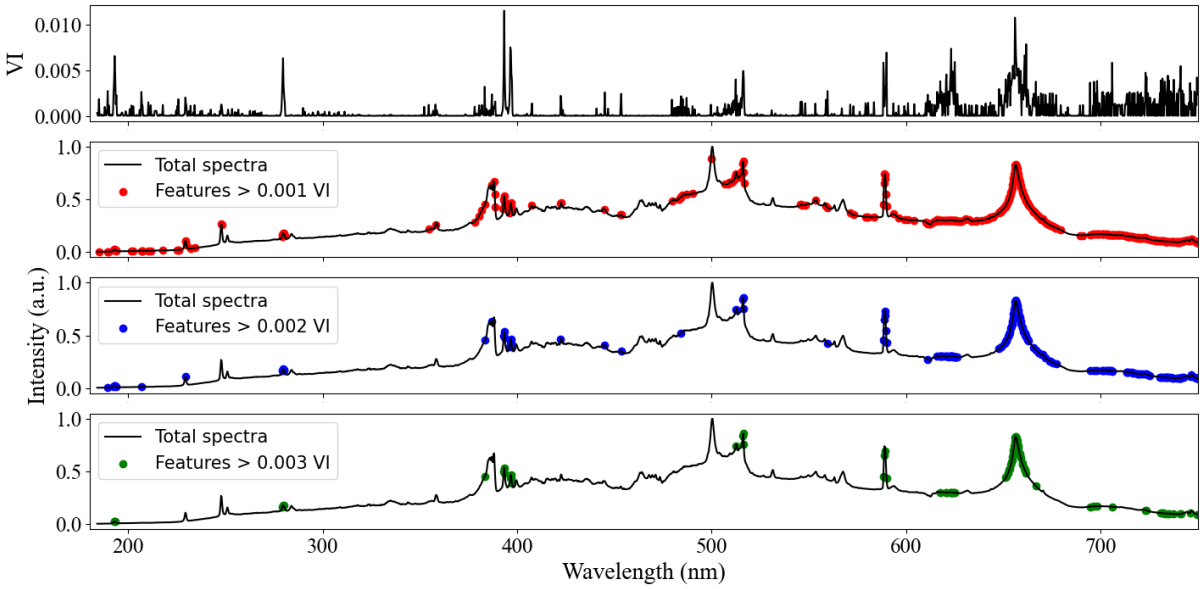

Figure 5.15. Variable importance (VI) estimated by RF model for LIBS data of nine different post-consumer plastics.

Table 5.10. Results obtained from ANN for classification of nine post-consumer plastics with RF feature selection.

Sl. No.	Plastic	Correct classification rate (%)		
		VI> 0.001	VI> 0.002	VI >0.003
1	ABS	95.97	91.00	85.00
2	ACRYLIC	99.98	92.05	97.96
3	HDPE	93.97	88.98	89.94
4	LDPE	92.00	83.93	77.95
5	NYLON	91.90	78.00	88.97
6	PC	98.03	96.02	93.00
7	PET	99.80	97.84	99.75
8	PP	93.00	87.00	82.00
9	SIHET	93.98	91.00	76.95
Average		95.40	89.53	87.95
Testing time (ms)		3.71	3.51	3.32
Fraction of total data (%)		18.51	8.54	4.05

The training and testing time is higher in the case of VI > 0.001 as the fraction of total data is high. Here, the time taken for RF analysis was added to the training time, representing overall time required to train the ANN model, including preprocessing. Also, the highest classification was observed in this case as compared to the other two cases. This is because the VI > 0.001 covers all important features, including almost all peak areas. A similar observation was also

observed in the case of manual feature selection, where the classification rate was highest in the case of all peak areas as input. The testing times are similar to the training time for all three cases where VI > 0.003 represents the fastest prediction.

5.4.1.3. ANN with feature extraction

5.4.1.3.1. Principal Component Analysis (PCA)

Here PCA was employed for the total data comprised of 1800 spectra. Figure 5.16 and 5.17 represent the score plot and variance plot, respectively. From figure 5.16, it can be noticed that the different types of plastics make separate clusters with minimal overlap among them. Among all, ABS and ACRYLIC make compact and separate clusters with no overlap with others, whereas there are some overlaps between other types of plastics. The score plot represents that they can be classified based on the scores rather than the original data. Figure 5.17 shows the variance explained by the first ten PCs. Here the first three PCs explain 78.05, 12.86 and 3.6 % of the total variance, respectively and the first ten collectively explain 99.5 % of the total variance. Since the PCs explain the variances in the original data, based on the variances, the scores can be used as extracted features. In other words, the scores are nothing but the extracted features from the original data and the most important features are the scores corresponding to initial PCs.

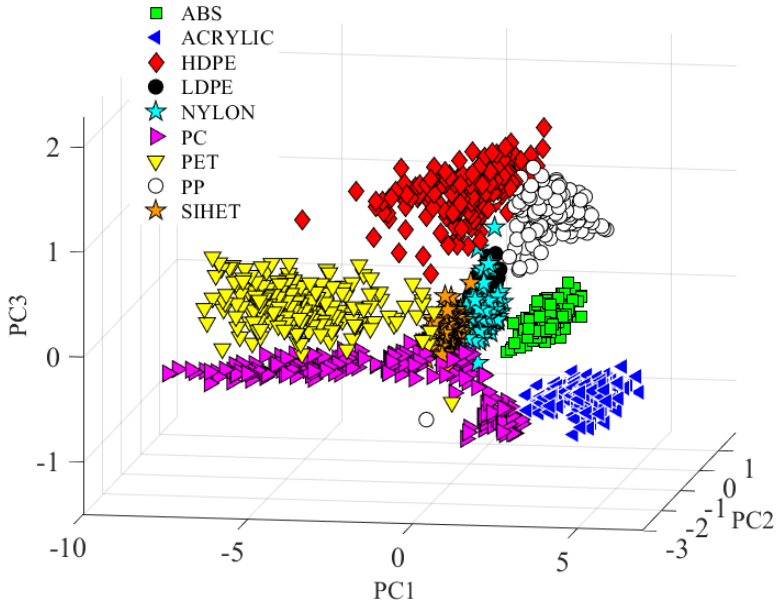

Figure 5.16. 3D score plot of first three PCs for nine post-consumer plastics.

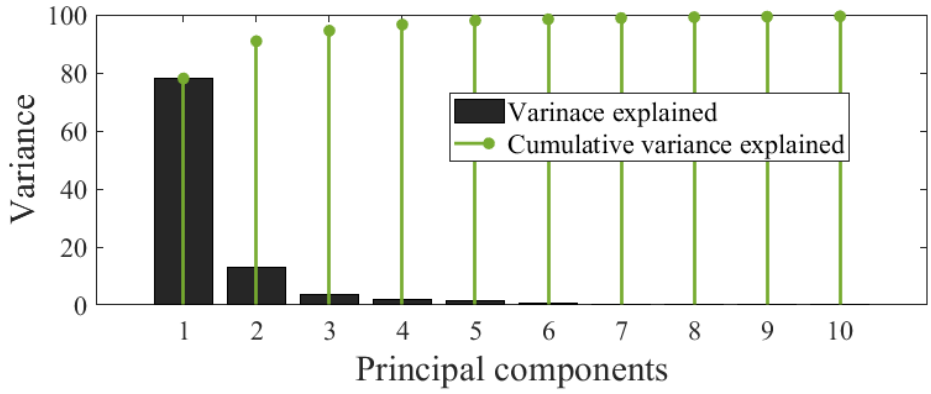

Figure 5.17. Variance plot of first ten PCs for nine post-consumer plastics.

The ANN analyses were employed on the scores obtained from PCA analysis in a similar manner as in case of explosive detection. At first, ANN was employed by considering only the scores corresponding to the first PC as input data; then, collectively, the first 10, 20, 30, 40, 50, 60, 70, 80, 90 and 100 scores were used as input to ANN. The average prediction rate of plastics obtained considering different sets of scores is shown in a bar chart in figure 5.18. The figure shows that the accuracy of the prediction increases with increasing the number of scores as input to the ANN but up to a certain value. After 30 scores, the increase in the number of scores doesn't affect the accuracy significantly.

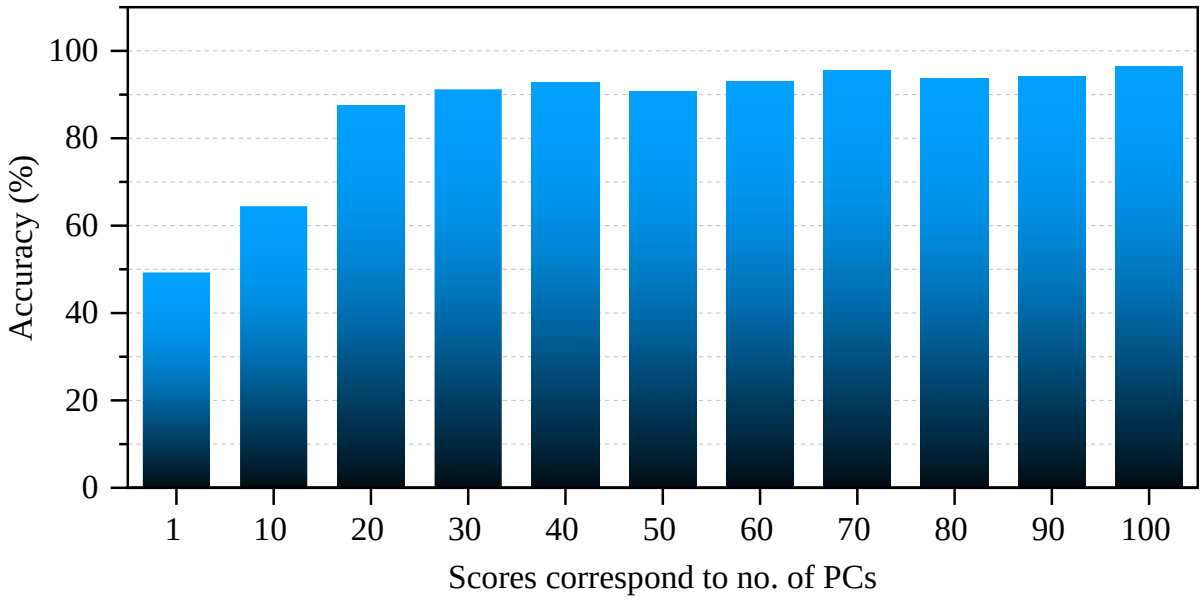

Figure 5.18. Classification accuracy of nine post-consumer plastics by considering different scores as input to ANN.

5.4.1.3.2. Linear Discriminant Analysis (LDA)

In this section, LDA was employed on the LIBS spectra corresponding to nine different post-consumer plastics categories. Figure 5.19 represents the 2D plot of the first two LDs, which show a clear separation between different classes of plastics. Moreover, the minimal variance between the interclass spectra was also observed.

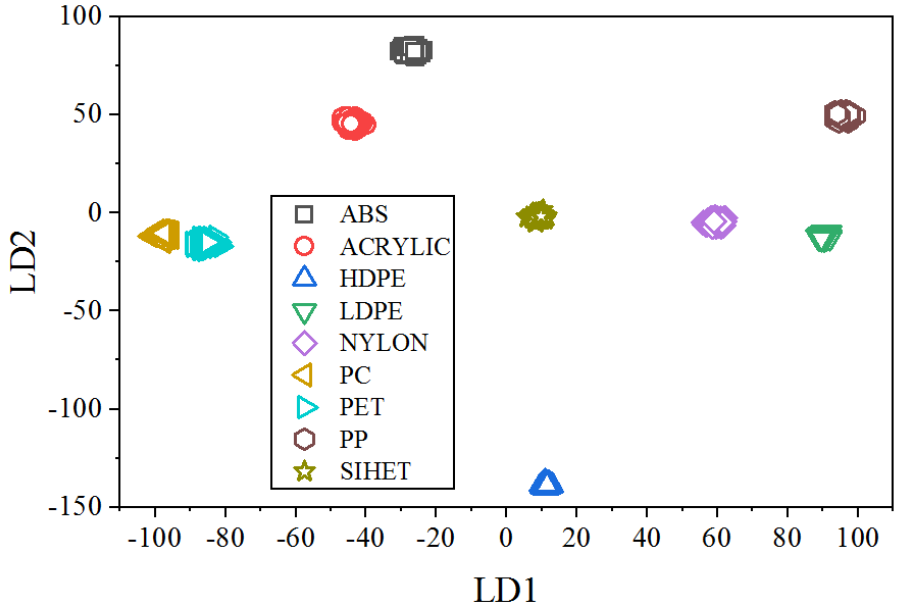

Figure 5.19. 2D LDA plot of first two LDs for nine post-consumer plastics.

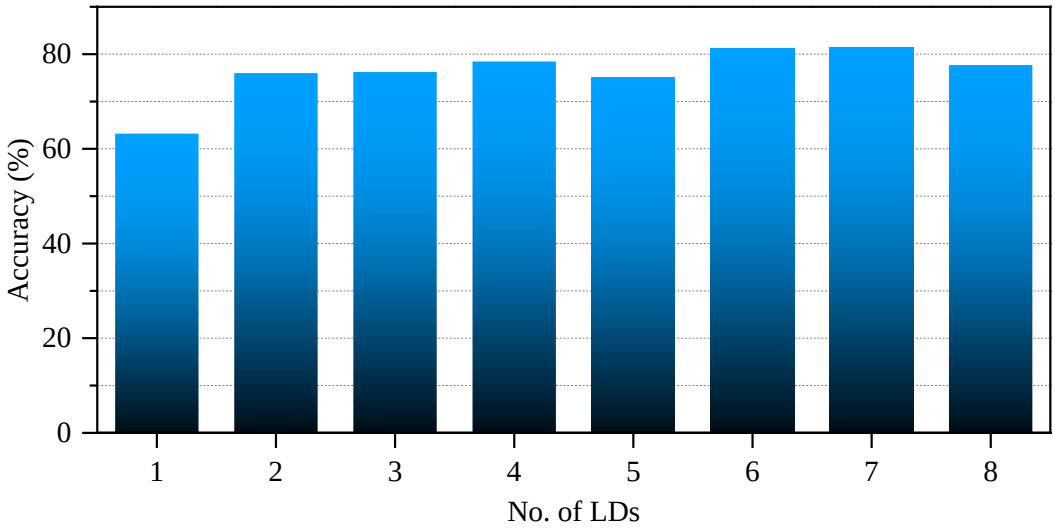

Figure 5.20. Classification accuracy of nine post-consumer plastics by considering different LDs as input to ANN.

After LDA, ANN analyses were employed on the first LD, first two LDs and so on, up to the first eight LDs. The average classification accuracies obtained from ANN analyses were shown in the bar chart in figure 5.20. The figure shows that the classification accuracy corresponding

to the first LD is minimal, whereas, for all other cumulative LDs, it is almost similar. However, for all the cases, the accuracy in the prediction of plastics is around 80 %. This is again due to the underfitting of the ANN model since fewer data variables are considered for training.

5.4.1.4. Discussion

In this study, ANN analyses were performed on LIBS data of nine post-consumer plastics with various feature selection and feature extraction methods. The classification accuracies obtained from all the approaches are summarized in figure 5.21.

From the figure, it can be noticed that the total data as input to the ANN shows maximum accuracy. In the case of feature selection techniques, peak heights, RF with VI > 0.002 and VI > 0.003 show comparatively lower classification accuracies than peak areas, CHN peak areas and RF with VI > 0.001 as input to the ANN model which represent more than 90% classification rate closer to the total data as input. The lowest classification rate is observed in the case of peak heights as input which could be due to the underfitting of the ANN model. Similar observations were also observed in the case of PCA and LDA feature extraction. The score corresponding to the first PC shows a poor prediction rate and scores corresponding to PCs up to 20 PCs represent prediction accuracies lower than 90%, possibly due to the underfitting of the ANN model. Moreover, as compared to PCA, LDA as input to ANN shows poor classification rates similar to the case of explosive detection (figure 5.12).

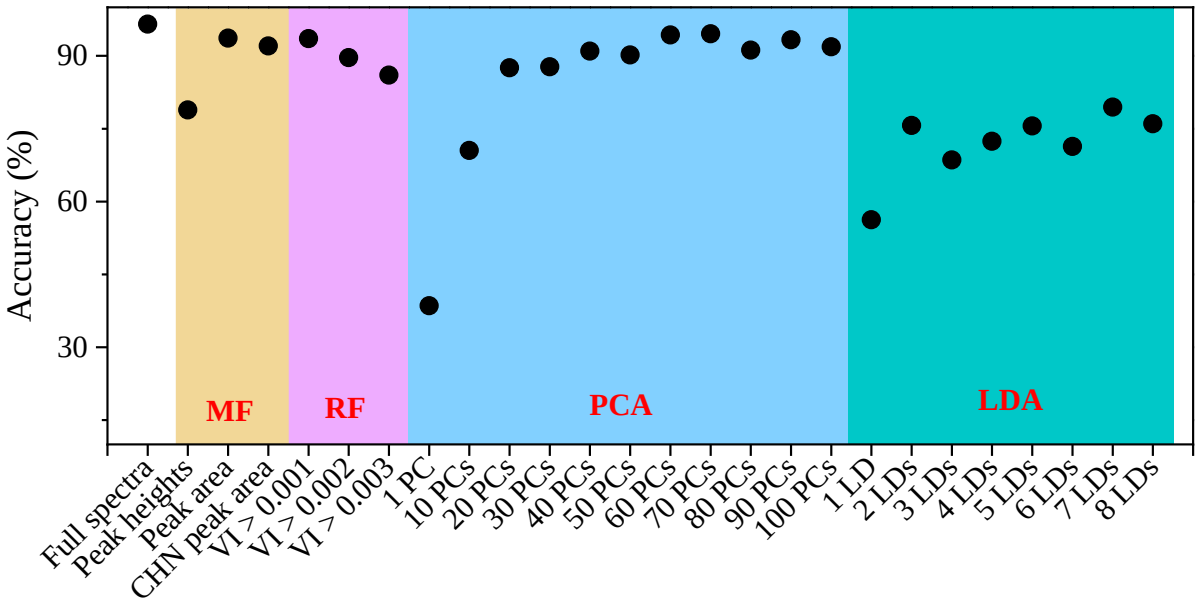

Figure 5.21. Classification accuracies obtained from various feature selection and feature extraction methods. Here MF represents manual feature selection.

In a real-time application, classification accuracy plays a crucial role in plastic sorting. The accuracy in sorting has to be as maximum as possible in order to maintain the quality of the recycled plastics and reduce the production cost. Moreover, mixing different kinds of plastics undergoes unwanted chemical reactions which release toxic substances very harmful to the environment and ecosystem. In this study, full spectra as an input to ANN yields maximum accuracy and is the best choice if only accuracy is considered.

Along with accuracy, computational time also plays a very important role in plastic sorting. In a real-time scenario, tons of plastic waste have to be sorted for recycling. In industrial sorting units, the use of a conveyor belt is a very efficient way of transporting plastics towards classifying instruments. Furthermore, the computational time of the instrument should be compatible with the speed of the conveyor belt. Also, the faster the speed of the conveyor belt, the faster the sorting process. In such a layout, even milliseconds difference in the computational time can make greater differences on a large scale. The average training and testing times for one iteration correspond to various feature selection and extraction approaches are described in table 5.11. Among the training and testing time, training time is really not important as the model has to be trained prior to the testing and on the testing site only the speed of the testing matters. In table 5.11, the testing times that correspond to feature selection techniques (manual and RF feature selection) are the times taken by ANN only. Whereas, in the case of feature extraction approaches (PCA and LDA), the testing time are the sum of transforming time taken for transforming the spectrum to PC and LD spaces added to the time taken by ANN, respectively. The time taken by the manual and RF feature selection is not considered here because the preprocessing by feature selection will be performed during the training process and the same wavelength ranges of spectra can be remembered, and the same fraction can be extracted without requiring any additional time every time. During the comparison of testing times, only those approaches that represent more than 90 % of classification accuracies are considered. Comparing all the testing times (with accuracy > 90%), the features corresponding to RF VI > 0.001 reflect faster prediction with accuracy close to the total spectra.

Apart from accuracy and computational time, the size of the training model and input data are important parameters for discussion. The sizes of input data considered to train the ANN model and the size of the ANN model are also described in table 5.11. In this case, a total of 1800 spectra were considered; therefore, the input data size ranges from hundreds to a few thousand KB for different subsets. But, in practical use, the input data to the model will be a single spectrum which is typically 70 – 80 KB in size. The size of the trained ANN model

ranges between 16 – 25158 KB. The combined data and classification model requires less than 26 MB of storage. Since no big data is being analyzed during the testing process and the overall storage requirement is very low, there is no need for any computer or workstation. This can be replaced with compact and low-cost microcontrollers capable of performing ANN operations like Arduino[100], Raspberry Pi[101], etc. This will fascilate the development of a handy, robust, low-cost LIBS setup for identifying post-consumer plastics.

Table 5.11. Comparison of various feature selection and extraction approaches for classification of nine post-consumer plastics.

		Classification accuracy (%)	Testing time (ms)	Input data size (MB)	Training model size (KB)	Classification index (% ms^{-1} MB^{-1})
	Full spectra	96.43	8.44	28.71	25.16	0.45
MF	Peak area	95.02	4.64	10.86	7.91	2.59
	CHN peak area	92.77	4.4	6.41	5.35	3.94
	Peak heights	83.89	3.12	0.41	0.34	78.62
RF	VI > 0.001	95.4	3.71	5.46	4.62	5.57
	VI > 0.002	89.53	3.51	2.53	2.18	11.68
	VI > 0.003	87.95	3.32	1.99	1.02	26.1
PCA	1 PC	49.28	3.69	0.87	0.02	834.69
	10 PCs	64.44	3.88	1.02	0.14	116.96
	20 PCs	87.53	3.9	1.19	0.28	79.03
	30 PCs	91.21	3.95	1.36	0.42	54.59
	40 PCs	92.76	3.86	1.53	0.57	42.46
	50 PCs	90.75	4.36	1.70	0.7	29.73
	60 PCs	92.9	4.5	1.88	0.84	24.55
	70 PCs	95.43	4.76	2.05	0.99	20.17
	80 PCs	93.57	5.83	2.22	1.12	14.3
	90 PCs	94.13	5.4	2.39	1.26	13.8
	100 PCs	96.31	5.71	2.56	1.4	12.02
LDA	1 LD	63.21	3.7	0.07	0.02	899.15
	2 LDs	76	3.79	0.1	0.03	607.66
	3 LDs	76.22	3.75	0.12	0.05	432.45
	4 LDs	78.44	4.03	0.14	0.06	319.08
	5 LDs	75	4.53	0.17	0.08	220.75
	6 LDs	81.11	4.44	0.19	0.09	202.98
	7 LDs	81.33	4.63	0.22	0.1	168.9
	8 LDs	77.68	4.51	0.25	0.12	145.97

★The blue colour indicates the approaches with classification accuracies greater than 90%.

In order to find the best approach among all feature selection and extraction approaches, an index called classification index is defined that simultaneously considers the accuracy, testing

time, and ANN model size and provides the best analysis protocol. The classification index is defined as,

$$Classification\ index = \frac{Accuracy\ (\%)}{Testing\ time\ (ms) \times Model\ size\ (MB)} \tag{1}$$

The limit of the classification index ranges from 0 to ∞, i.e., when accuracy is 0%, or the model consumes infinite time or size then the index value is zero.And when the model doesn't consume any time or storage space for prediction, then the classification index is infinite. The classification index estimated for all the approaches is listed in table 5.11. Table shows that in terms of classification index, LDA feature extraction with 1 LDs followed by ANN gives the best overall result; however, the accuracy is poor, i.e., 63.21%. Considering better accuracy, i.e., at least more than 90%, the best analysis protocol can be PCA with 30 PCs as input to the ANN model.

5.4.2. Locally collected post-consumer plastics (Testing on unknown sample)

The last section, excellent accuracy in identifying each plastic category has been achieved with optimized computational time and resource usage. However, in the study only one sample from each category was considered and both training and testing were poerfomed on the same sample. This approach is irrelevant in terms of real-time application as numerous samples from each category will be encountered in recycling unit and the testing samples will be completely unknown to the training model. Therefore, to mimic the real-time application scenario, in this section, multiple samples were collected from each category and the testing was performed on the unknown samples which has not been seen by the model earlier.

Post-consumer plastics from six commonly used categories, namely, HDPE, LDPE, PP, PET, PS and PVC were collected for the experiment. Details of these types of plastics can be found in table 5.12. From each group/category, five different samples used in our day-to-day life were collected and identified based on their recycling number. These samples were first cleaned with water and then methanol to remove surface contaminants. The photograph of 30 plastic samples (6 groups × 5 samples) is depicted in figure 5.22. 200 spectra from each sample (a total of 6000 spectra) were acquired with 500 ms integration time.

The normalized averaged LIBS spectra of six kinds of plastics acquired in the range of 200 – 750 nm are depicted in figure 5.23. Similar emission lines are observed as earlier, i.e., prominent C, H, N, and Na atomic lines were observed along low intense emission lines of Ca, Mg, Ti, and molecular emissions of CN – violet and C_2 – swan bands.

Table 5.12. Details of the six categories of post-consumer plastics.

S. No.	Name	Chemical structure	Chemical formula	Recycle No. (#)
1	High-density polyethylene (HDPE)	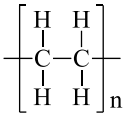	$(C_2H_4)_n$	2
2	Low-density polyethylene (LDPE)			4
3	Polypropylene (PP)	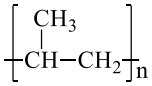	$(C_3H_6)_n$	5
4	Polyethylene terephthalate (PET)	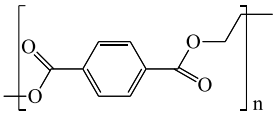	$(C_{10}H_8O_4)_n$	1
5	Polystyrene (PS)	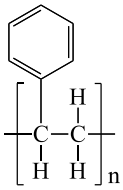	$(C_8H_8)_n$	6
6	Polyvinyl Chloride (PVC)	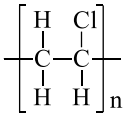	$(C_2H_3Cl)_n$	3

Figure 5.22. Photograph of 30 post-consumer plastics used for the study.

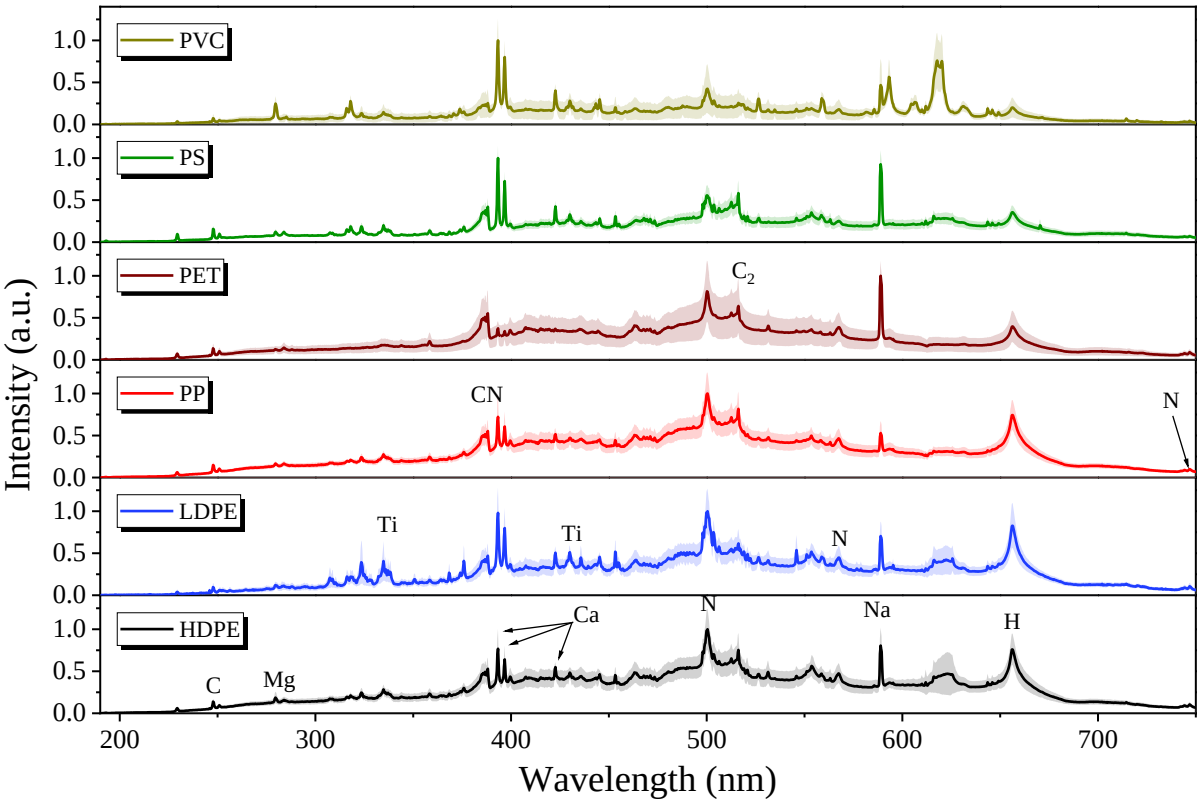

Figure 5.23. LIBS spectra of plastics acquired in the 200 – 750 nm range. Each spectrum was averaged over 1000 spectra (5 samples × 200 spectra). The shaded bands respresent the standard deviation of 200 measurements.

5.4.2.1. ANN with total data

The ANN model has been developed to mimic the real-time application scenario where the sample subjected to the test is never a part of the training. Notably, one sample (out of 30) was reserved as an 'unknown,' while the neural network was trained using the remaining 29 samples. Out of the 6000 spectra obtained from the 30 samples, 200 spectra corresponding to one sample were designated for testing. The remaining 5800 spectra were randomly split into 80% for training and 20% for validation data. This process was repeated iteratively 30 times. The schematic of the training–testing architecture is described in figure 5.24.

For each iteration, the number of neurons in the input layer equals the number of features in the data, while the number of neurons in the output layer matches the number of classes. The number of hidden layers is optimized by using grid search cross-validation (GridSearchCV) along with the number of epochs by minimizing the loss function (categorical cross entropy) of the validation data [102]. The overall classification accuracies of each sample obtained from the ANN analysis for the test data are presented in the form of a confusion matrix in table 5.12.

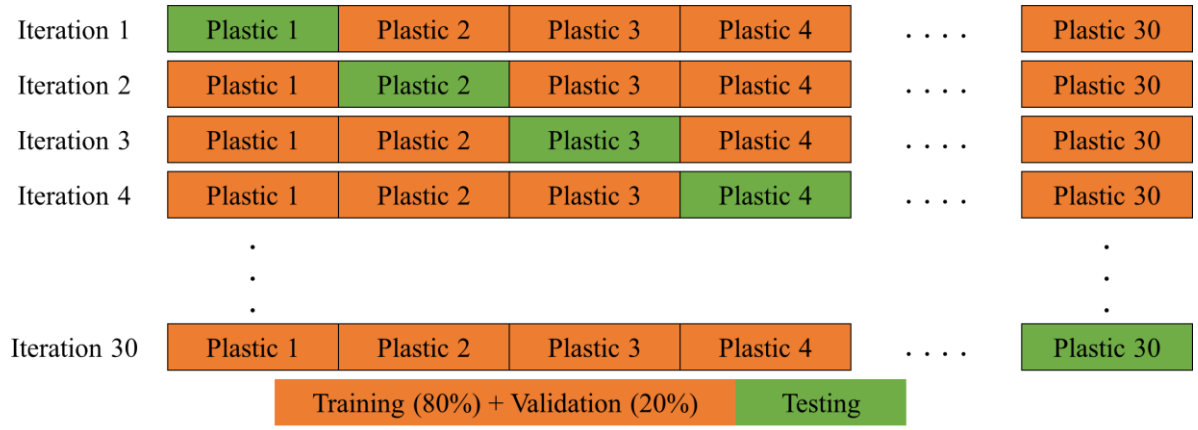

Figure 5.24. Schematic of the training–testing architecture of the data.

Table 5.13 shows that in the case of PS and PVC, the classification accuracy is maximum and the classification rate of PET is high. However, HDPE, LDPE and PP are misclassified largely among themselves. This discrepancy can be attributed to their similar chemical structures and spectral signatures (discussed in table 5.7 and figure 5.23).

The current ANN algorithm is not able to differentiate between HDPE, LDPE and PP along with other plastics. To resolve this, HDPE, LDPE and PP are grouped as single class HLP. The dataset containing HLP, PET, PS and PVC is named 'global dataset'. The ANN analyses were performed on global dataset and when a spectrum is identified as HLP, it undergoes another ANN model, which is trained with only HDPE, LDPE and PP (3 groups) named as 'local dataset'. The initial dataset consisting of six groups is referred to as the 'original dataset.'

Table 5.13. Confusion matrix representing the classification accuracy (%) of 30 post–consumer plastics obtained from ANN analysis.

		Predicted Class					
		HDPE	LDPE	PP	PET	PS	PVC
Actual Class	HDPE	19.5	0.3	75	4.4	0.8	0
	LDPE	9.6	57.5	32.4	0	0	0.5
	PP	64.3	0.2	35.4	0	0.1	0
	PET	0	0	5.5	94.5	0	0
	PS	0	0	0	0	100	0
	PVC	0.1	0	0	0	0	99.9

Again, the ANN analyses were performed on global and local dataset. The same training, validation and testing architecture was employed as before. The confusion matrices obtained from ANN analyses for two different approaches are discussed in table 5.14. By considering

HDPE, LDPE, and PP as a group, the overall accuracy of global dataset increases significantly and becomes close to 100% (see table 5.14a). Compared to table 5.13, the classification accuracy of PET increases significantly and accuracy of PVC becomes maximum and HLP also give excellent prediction rate. However, for local dataset, the classification approach doesn't work, representing failure of ANN model in distinguishing between LIBS spectra of HDPE, LDPE and PP (see table 5.14b). The testing time of each plastic spectrum for global dataset is 137 ms and for the local dataset it is 133 ms. The size of the ANN model is ~1560 KB for both cases.

Table 5.14. Confusion matrix representing the classification accuracy (%) of (a) global dataset and (b) local dataset obtained from ANN analysis.

(a)

		Predicted class			
		HLP	PET	PS	PVC
Actual class	HLP	99.37	0.57	0.07	0
	PET	0.3	99.7	0	0
	PS	0	0	100	0
	PVC	0	0	0	100

(b)

		Predicted class		
		HDPE	LDPE	PP
Actual class	HDPE	21.4	10	68.6
	LDPE	36.9	35.7	27.4
	PP	56.3	7.3	36.4

5.4.2.2. ANN with feature selection

5.4.2.2.1. Manual feature selection

In this case, the same manual feature selection was employed as discussed before (section 5.3.2.2 and 5.4.1.2). The ANN analyses were performed on three datasets (i.e., original dataset, global dataset and local dataset) in the same manner as in the case of the full spectrum. It has been observed that excellent classification accuracy obtained for all three manual feature selection approaches corresponds to the global dataset, as discussed in table 5.15. However, poor classification accuracies are obtained in the case of the original and local dataset, resulting in the failure of ANN to classify between HDPE, LDPE and PP. Also, a significant increase in PET, PS and PVC accuracy was observed in the global dataset for all three feature selection approaches compared to the original dataset. Additionally, there is no discernible change observed in testing time when employing reduced input data. There are several factors because of which the overall testing time doesn't reduce significantly, even using a smaller test dataset. Further elaboration on this topic can be found in the discussion section.

Table 5.15. The ANN results for manual feature selection correspond to (a) original, (b) global and (c) local dataset.

(a)	Classification accuracy (%)		
	A	B	C
HDPE	2.8	0	3.7
LDPE	34.5	26.4	35.9
PP	40.9	34	29.4
PET	96.1	85.6	98.5
PS	99.8	100	98.7
PVC	96.2	85.5	78.8
D	61.7	55.2	57.5
E	130	127	125
F	59	17	3

(b)	Classification accuracy (%)		
	A	B	C
HLP	98.5	97.3	95.6
PET	100	93.9	100
PS	100	100	99.8
PVC	100	97.9	98.5
D	99.6	97.3	98.5
E	126	140	125
F	59	17	3

(c)	Classification accuracy (%)		
	A	B	C
HDPE	2.2	0.2	15.4
LDPE	33.5	27.4	43.9
PP	32.1	30.9	32.6
D	22.6	19.5	30.6
E	128	126	128
F	59	17	3

*A: Peak area, B: CHN peak area, C: Peak height, D: Average, E: Testing time (ms), F: Fraction of total data (%)

5.4.2.2.2. Random Forest (RF) feature selection

Here, the analyses were performed by selecting only important features based on VI threshold as inputs to ANN for the three datasets. A total of four sets of features were considered based on various VI threshold values. The analyses were performed on four sets of data with features greater than VI values of 0.001, 0.002, 0.003 and 0.004 for each dataset. The four sets of features obtained from three VI thresholds for original, local and global dataset are graphically presented in figure 5.25, 5.26 and 5.27, respectively.

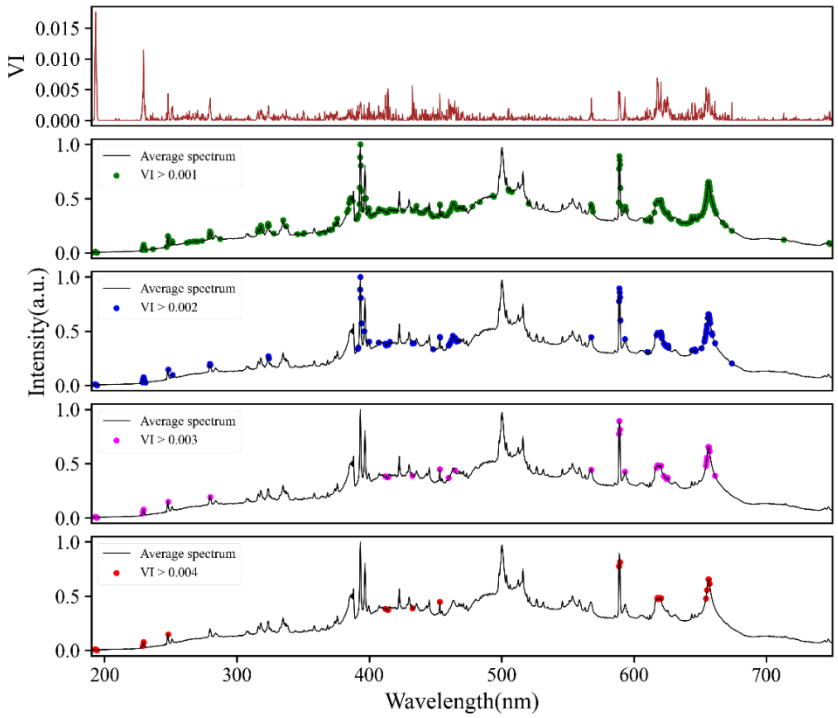

Figure 5.25. Variable importance (VI) estimated by RF model for original dataset.

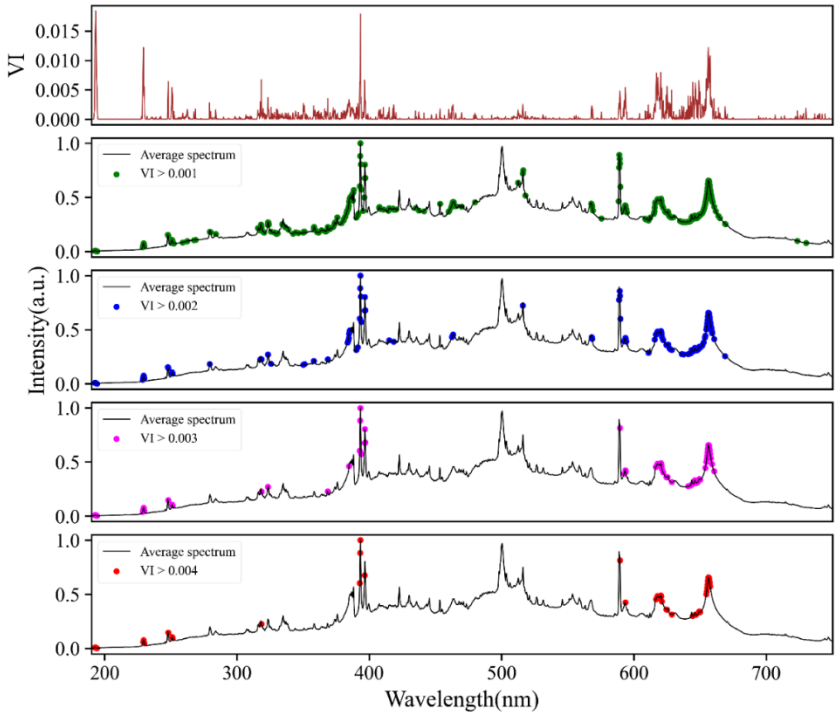

Figure 5.26. Variable importance (VI) estimated by RF model for global dataset.

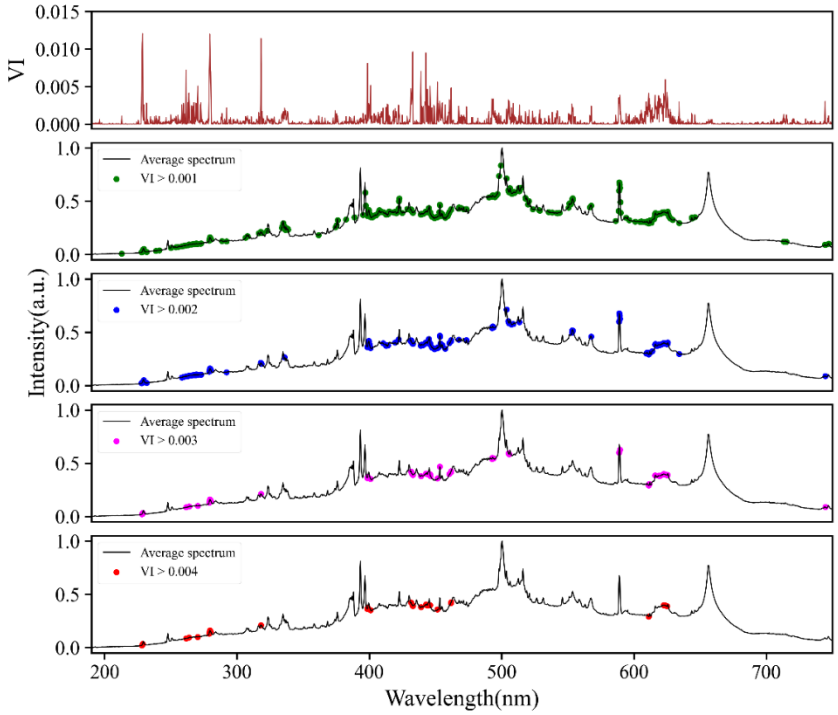

Figure 5.27. Variable importance (VI) estimated by RF model for local dataset.

The figures show that with increasing VI threshold, the number of important features decreasing gradually. In figures 5.25 and 5.26, with VI threshold of 0.001, the features include almost all the peak areas with some noise. With increasing VI threshold, only C, H, N, Ca, and Na peaks were noticed as important features. The results of ANN analyses obtained by considering four different sets of features are presented in table 5.16.

Table 5.16. The ANN results for RF feature selection correspond to (a) original, (b) global and (c) local dataset.

(a)	CA			
	V1	V2	V3	V4
HDPE	5.2	4.6	3.8	6.4
LDPE	34.8	33.1	51.2	67.8
PP	40.9	40.4	34.9	44.6
PET	95.3	99.3	99.2	99.9
PS	99.9	99.7	99.9	99.7
PVC	93.7	89.3	92.6	79.9
D	61.6	61.1	63.6	66.4
E	124	123	122	123
F	13	5	2.25	1.37

(b)	CA			
	V1	V2	V3	V4
HLP	98.1	93.3	95.2	96.8
PET	98.8	92.6	99.7	100
PS	99.9	99.9	99.7	99.7
PVC	99.9	99.3	98.2	97.3
D	99.2	96.3	98.2	98.4
E	128	124	125	124
F	13	7	4	2.5

(c)	CA			
	V1	V2	V3	V4
HDPE	2.7	12	4.4	6.1
LDPE	36.4	30.2	35.8	42
PP	34.4	32.2	30.9	18.5
D	24.5	24.8	23.7	22.2
E	125	123	128	126
F	14	7	2.7	1.5

⋆CA: Classification accuracy (%), V1: VI>0.001, V2: VI>0.002, V3: VI>0.003, V4: VI>0.005, D: Average, E: Testing time (ms), F: Fraction of total data (%)

No significant change was observed in testing time by considering the RF feature selection approach. However, there is a significant reduction in the data size. Also, like manual feature selection and full spectrum as input, there is no improvement in classification accuracy for original and local datasets. However, the classification accuracy of global dataset is excellent in case of all four feature selection approaches, i.e., close to 100%. The highest classification was observed for VI > 0.001.

5.4.2.3. ANN with feature extraction

5.4.2.3.1. Principal Component Analysis (PCA)

Here, PCA was employed on the training dataset, and the resulting transformed data were used to train and validate the ANN model. Before testing, the testing data underwent the same PCA transformation using the parameters obtained during the transformation of the training dataset. The score plots in figure 5.28 represent the distribution of the first two and first three PCs for original datasets during one iteration. The same graphs for global and local datasets are depicted in figures 5.29 and 5.30, respectively.

From figure 5.29, it can be noticed that PS makes a compact cluster as compared to other types of plastics. On the other hand, PET makes two clusters, i.e., one corresponding to a single sample and the other encompassing four other samples. In the case of HLP and PVC, multiple clusters were observed. Also, some overlaps were noticed between all four categories of plastics. Furthermore, when test data, such as spectra corresponding to PVC 5, are transformed using the same PCA parameters as the training data, they align with the trained

PVC data. Similarly, the test data align with its kind in the original and local dataset (figures 5.28 & 5.30) with overlap between different kinds and no obvious clusters can be observed.

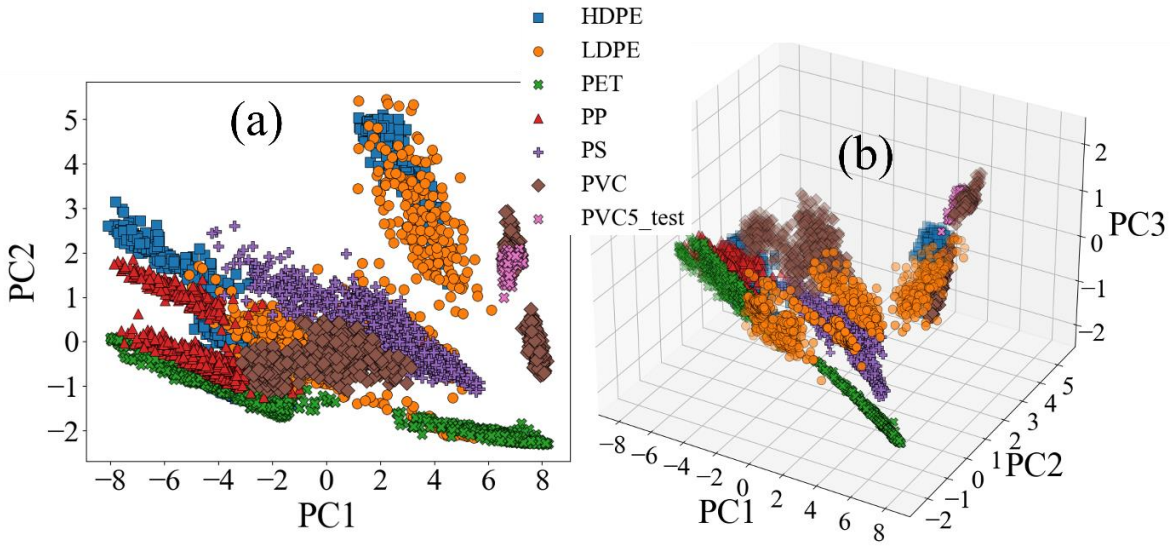

Figure 5.28. (a) 2D and (3D) score plot of initial PCs for original dataset.

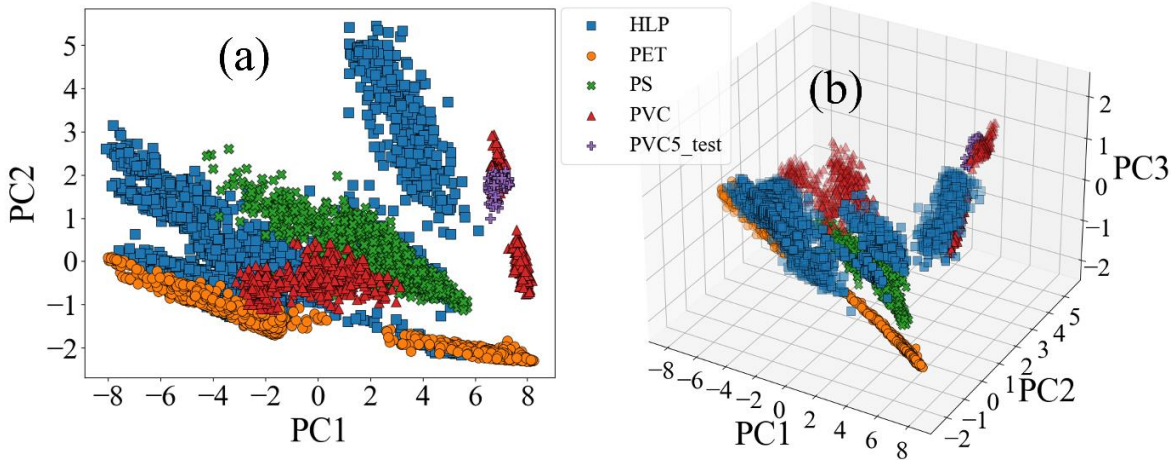

Figure 5.29. (a) 2D and (3D) score plot of initial PCs for global dataset.

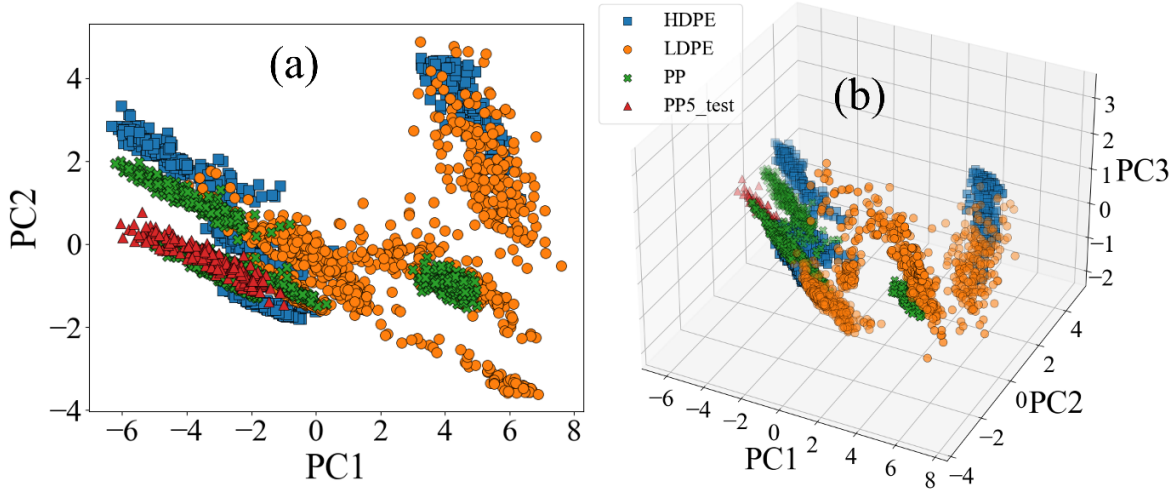

Figure 5.30. (a) 2D and (3D) score plot of initial PCs for local dataset.

The ANN analyses were employed on the scores obtained from PCA analysis following the similar architecture as before. At first, ANN was employed by considering only the scores corresponding to the first PC as input data; then, collectively, the first 2, 4, 6, 8, 10, 20, 40, 60, 80 and 100 scores were used as input to ANN. The classification accuracy obtained by considering different sets of scores for all three datasets is shown in a bar chart in figure 5.31. From the figure, it can be noticed that for the global dataset, the prediction accuracy increases with increasing the number of scores as input to the ANN. After six scores, the accuracy becomes more than 90% and with further increasing in the number of scores, the accuracy remains similar, i.e., more than 90% and close to 100%. Moreover, after implementing PCA feature extraction, the ANN failed to classify between HDPE, LDPE, and PP in the original and local datasets.

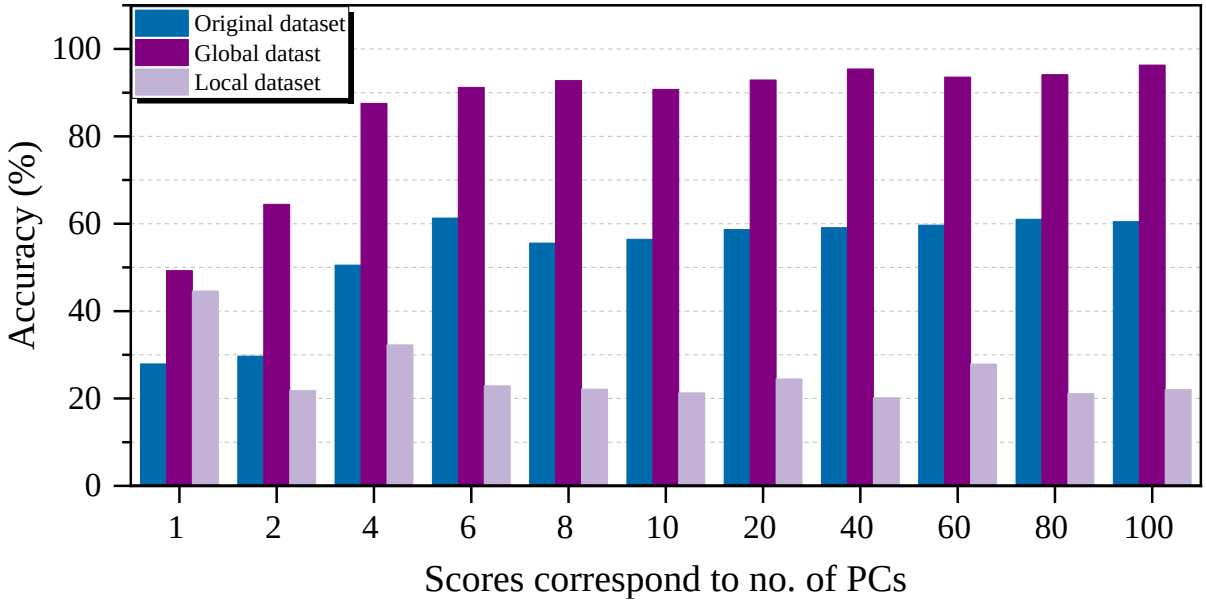

Figure 5.31. Classification of post-consumer plastics by considering different scores as input to ANN.

5.4.2.3.2. Linear Discriminant Analysis (LDA)

In this case, LDA was employed similarly to PCA, i.e., it was implemented on the training data and the testing data was transformed with the same transformation parameters for each iteration. Figure 5.32 represents the 2D and 3D plots of the LDs corresponding to the original dataset; the plots corresponding to global and local datasets are shown in figures 5.33 & 5.34, respectively.

In the original dataset, partial overlap between LDPE, HDPE, and PP and between PET and PS was observed in the 2D plot (figure 5.32). However, the test data makes a good cluster with its kind with minimal variance. Figure 5.33 shows excellent separation between different

classes of plastics with minimal variance between the interclass spectra. Also, the test data makes cluster with the same type with minimal variation, representing the possibility of good classification after LDA feature extraction. Similarly, a very good separation and minimal variance between LDPE, HDPE and PP is observed in the local dataset (figure 5.34). Also, the test dataset makes cluster around its actual training type but has a larger spread than the global dataset. Despite the similarities observed between HDPE, LDPE and PP in former analyses, LDA can separate them for global and local datasets.

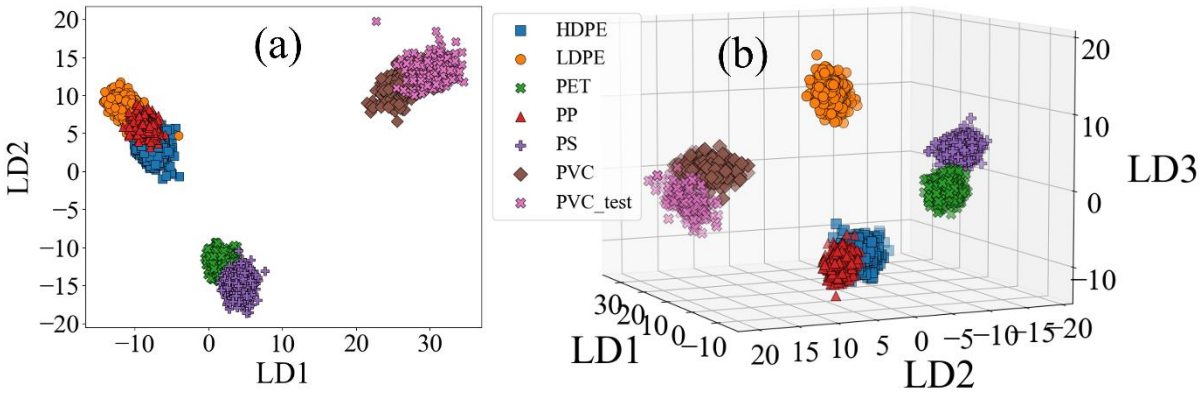

Figure 5.32. (a) 2D and (b) 3D plot of initial LDs correspond to original dataset.

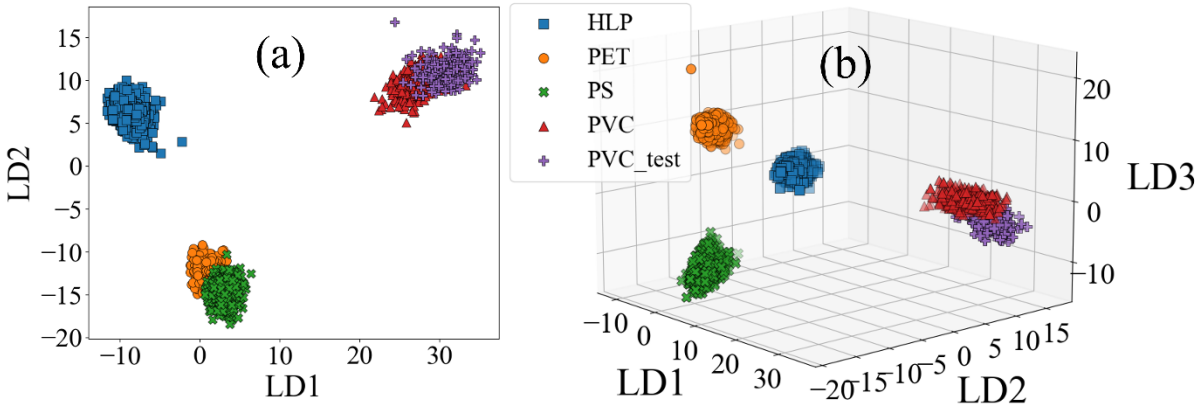

Figure 5.33. (a) 2D and (b) 3D plot of initial LDs correspond to global dataset.

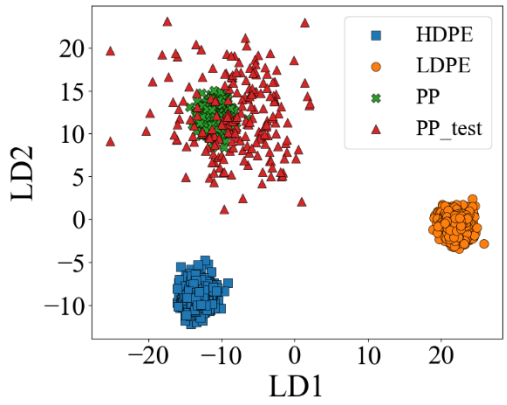

Figure 5.34. 2D plot of first two LDs correspond to local dataset.

After LDA, ANN analyses were employed on the first LD, first two LDs and so on up to the maximum number of LDs. The average classification accuracies obtained from ANN analyses were shown in figure 5.35. From the figure, it can be noticed that for the global dataset, the classification accuracy corresponding to the first LD and first two cumulative LDs are comparatively low, i.e., less than 90%, which could be due to the underfitting of the ANN model as number of data points for training is very small. However, the input of three cumulative LDs result in very good classification accuracy close to 100%. Furthermore, for the local dataset, the accuracy in classification remains as poor as in the earlier cases. Also, in the original dataset, the accuracy is poor due to the misclassification between HDPE, LDPE, and PP.

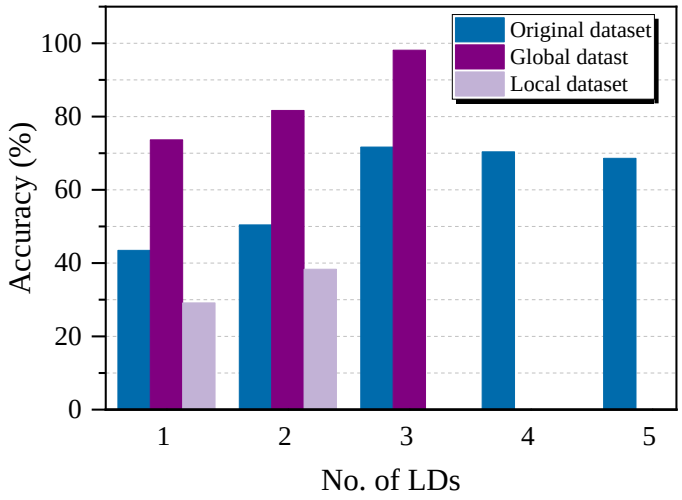

Figure 5.35. Classification of post-consumer plastics by considering different LDs as input to ANN.

5.4.2.4. Discussion

Identification of unknown post-consumer plastics is demonstrated. For the experiment, 30 post-consumer plastics from widely used six categories i.e. five from each were collected and subjected to LIBS experiment. ANN analyses were performed to differentiate six groups of plastics. The ANN model has been developed to mimic the real-time application scenario where the sample subjected to the test is never a part of the training. Notably, one sample out of 30 was reserved as an 'unknown,' while the neural network was trained using the remaining 29 samples. This process was repeated iteratively 30 times to each sample. At first, ANN analysis was performed on the total data considering six groups. However, the ANN model fails to differentiate between HDPE, LDPE and PP due to their high similarity in chemical structure and spectral signature. To resolve this, HDPE, LDPE and PP were grouped

as single class HLP and the dataset containing HLP, PET, PS and PVC is called 'global dataset' where the original dataset containing six groups was remained as 'original dataset'. The ANN analyses were performed on global dataset and when a spectrum is identified as HLP, it undergoes another ANN model, which is trained with only HDPE, LDPE and PP (local dataset). This methodology is repeated for all above-discussed feature selection and feature extraction approaches. After all the analyses, it is concluded that the prediction accuracy for the global dataset is high for most of the feature selection and feature extraction approaches. However, not even a single feature selection or extraction approach could classify correctly between HDPE, LDPE, and PP for the original and local datasets. This section discussed the results obtained from the global dataset while delving into the potential for real-time implementation of this technique and exploring future prospects.

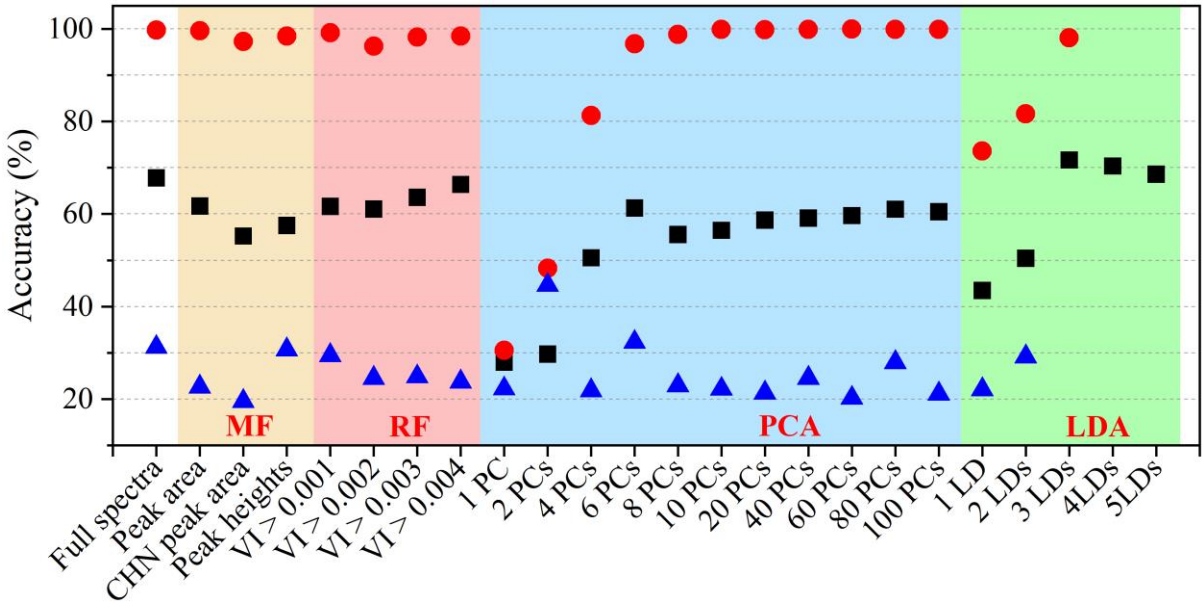

Figure 5.36. Overall averaged classification accuracies obtained from various feature selection and feature extraction methods. Here MF represents manual feature selection. The black square, red circle and blue triangle represent the result corresponding to original, global and local dataset, respectively.

The averaged classification accuracies obtained from all the feature selection and extraction approaches for the global dataset are summarized in figure 5.36. From the figure, it can be noticed that the full spectra as input result in excellent accuracy (99.77%). In the case of all the feature selection approaches (manual and RF) more than 96% classification accuracy has been achieved. In the case of PCA feature extraction, results corresponding to initial PCs are poor, possibly due to the underfitting of the ANN model due to smaller datasets. However, for PCs with more than six as input, the classification accuracy becomes more than 90%, and the maximum accuracy (99.97%) is obtained for 60 PCs as input to the ANN model among all the

feature selection and extraction approaches. Similarly, in the LDA feature extraction approach, the initial two LDs result in lower accuracy (< 90%) likewise initial PCs. Moreover, compared to PCA, LDA as input to ANN shows poor classification rate. In terms of accuracy, PCA followed by 60 PCs as an input to ANN yields maximum accuracy and is the best choice for global dataset.

Table 5.17. Comparison of various feature selection and extraction approaches for classification of post-consumer plastics for global dataset.

		Classification accuracy (%)	Testing time (ms)	Input data size (MB)	ANN model size (MB)	Classification index
Full spectra		99.77	137	143	1.56	0.47
MF	Peak area	99.62	126	84	1.37	0.58
	CHN peak area	97.27	140	25	0.29	2.40
	Peak heights	98.48	125	4	0.07	10.65
RF	VI > 0.001	99.17	129	19	0.23	3.41
	VI > 0.002	96.28	125	10	0.13	6.04
	VI > 0.003	98.21	125	6	0.09	9.13
	VI > 0.004	98.44	124	4	0.06	12.41
PCA	1 PC	30.49	130	143	0.03	9.00
	2 PCs	48.28	131	143	0.03	13.66
	4 PCs	81.29	127	143	0.03	22.00
	6 PCs	96.82	130	143	0.03	22.58
	8 PCs	98.81	134	143	0.04	20.41
	10 PCs	99.9	132	143	0.04	19.92
	20 PCs	99.86	129	143	0.05	16.86
	40 PCs	99.94	129	143	0.06	14.03
	60 PCs	99.97	147	143	0.08	9.05
	80 PCs	99.93	128	143	0.09	8.59
	100 PCs	99.92	131	143	0.11	7.24
LDA	1 LD	73.64	130	143	0.02	23.55
	2 LDs	81.66	129	143	0.03	24.27
	3 LDs	98.13	150	143	0.03	23.31

★The blue colour indicates the approaches with classification accuracies greater than 90%.

The testing time, input data size, ANN model size and classification index for all the feature selection and extraction approaches are discussed in table 5.17. In terms of testing time, RF with VI threshold 0.004 reflect the fastest prediction with an accuracy of 98.44%. However, no significant difference is observed in the testing time of all the approaches even though data size is reduced, as several factors contribute to the overall testing time apart from the size of

the input data. For example, in the present work, the ANN algorithm undergoes GridSearchCV to optimize hyperparameters such as number of neurons and epochs, which vary each time while training the model with a new dataset. The variations in optimized hyperparameters for different models can influence the testing time differently. Additionally, since each ANN model utilizes many steps, it might take a significant amount of time, irrespective of the input data size. Furthermore, ANN algorithm has some inherent overhead, including model initialization, loading weights, model compilation, making predictions, etc., which consume approximately the same time for each analysis. Moreover, the hardware limitations and underutilization of the computational device's multiple-core parallelism can overshadow the reduced time due to a smaller dataset. Therefore, when considering these factors collectively, the significant impact on the overall testing time is low.

Table 5.17 shows that in terms of classification index, LDA feature extraction with 2 LDs followed by ANN gives the best overall result; however, the accuracy is below 90%, i.e., 81.66%. This approach can be useful in some specific applications where the instrument needs to be cost effective and fast and more than 80% accuracy is acceptable. However, considering better accuracy, i.e., at least more than 90%, the best analysis protocol will be LDA with 3 LDs.

5.5. Summary

This chapter demonstrates the efficacy of employing a fusion of LIBS data and machine learning algorithms for the swift and precise identification of explosives and different types of post-consumer plastics. The study utilized a psLIBS setup incorporating a low-cost, compact CCD spectrometer. Material classification was executed using ANN and diverse feature selection and extraction methodologies. The results obtained from these diverse approaches were thoroughly compared, encompassing accuracy, computational time, and resource utilization measures. This comprehensive analysis provides insights into the optimal method for accurate material identification while considering efficiency and resource allocation.

For explosive detection, two steps were considered. Initially, each sample underwent scrutiny to ascertain its classification as either explosive or non-explosive. Subsequently, samples identified as explosive underwent a secondary classification process to determine their specific type. Among various feature selection approaches, ANN combined with LDA feature extraction achieved a flawless 100% accuracy for classifying between explosive and non-explosive. In the case of classification within explosives, maximum accuracy (99.8%) was obtained for full spectrum and manual feature selection with peak area. However, both the

training and testing were performed on the LIBS spectra obtained from the same samples. In real-world scenarios, the model encounters unknown samples that hasn't been seen by the trained model during the training process. Given the limited quantity of explosive samples available, the training and testing were conducted using the same set of samples. Multiple spectra were recorded and then randomly divided for training, validation and testing purposes. This study can further be extended by considering a large set of samples.

Further, to explore the effect of testing on a new sample, the study was extended to a large number of plastic samples. For the identification of post-consumer plastics, two sets of samples were considered. Firstly, nine different post-consumer plastics were collected from a local recycling unit, and both training and testing were performed on the same sample. Secondly, 30 post-consumer plastics representing six commonly used types (HDPE, LDPE, PP, PET, PS, and PVC), five samples from each category were collected from garbage and testing was performed on unknown plastic, mimicking real-world scenarios for identifying unfamiliar post-consumer plastics. In the first case, PCA with 30 PCs as input to the ANN model represents the best classification in terms of accuracy, computational time and storage requirement. However, in the subsequent case (30 plastics), ANN fails to classify between HDPE, LDPE and PP even using various feature selection and extraction approaches due to their high degree of similarity in chemical and spectral signature. Therefore, by considering these three plastics as a single group, results show classification with a high degree of confidence with many feature selection and extraction approaches. In particular, LDA feature extraction with 3 LDs as input to the ANN was found to have the best results in terms of accuracy, computation time, and storage.

By comparing two approaches considered for discrimination of plastics, better results obtained in the prior case where the training and testing were performed on the same sample. However, this approach is meaningless in terms of real-time application as the testing samples will be completely unknown to the training model. Therefore, the second approach represents the real-time application scenario, but it fails to distinguish between three categories of plastics out of six. Therefore, in real-time scenario, this technique can be used to differentiate between HLP, PET, PS, and PVC. The classification between HDPE, LDPE and PP can performed by using the conventional technique for the time being. This will reduce the workforce requirement by half as three plastic categories out of six can be sorted efficiently.

Further, to improve the classification accuracy between HDPE, LDPE and PP, these studies might be extended by employing other powerful machine learning classifiers like

convolutional neural network (CNN), extreme gradient boosting (XGBoost), etc. Also, more statistical approaches can be implemented for feature selection or feature extraction like genetic algorithm (GA), successive projection algorithm (SPA) and stepwise formulation(SW), analysis of variance (ANOVA), etc. in order to further increase the prediction accuracy and lower the testing time. The ANN performances in terms of computation time can be explored with low-cost microcontrollers like Arduino, Raspberry Pi, etc.

5.6. Reference

[1] D.J. Díaz-Romero, S. Van den Eynde, W. Sterkens, A. Eckert, I. Zaplana, T. Goedemé, J. Peeters, Real-time classification of aluminum metal scrap with laser-induced breakdown spectroscopy using deep and other machine learning approaches, Spectrochim. Acta Part B At. Spectrosc. 196 (2022) 106519.

[2] P. Wang, N. Li, C. Yan, Y. Feng, Y. Ding, T. Zhang, H. Li, Rapid quantitative analysis of the acidity of iron ore by the laser-induced breakdown spectroscopy (LIBS) technique coupled with variable importance measures-random forests (VIM-RF), Anal. Methods. 11 (2019) 3419–3428.

[3] S.-L. Lui, A. Koujelev, Accurate identification of geological samples using artificial neural network processing of laser-induced breakdown spectroscopy data, J. Anal. At. Spectrom. 26 (2011) 2419–2427.

[4] G. Yang, S. Qiao, P. Chen, Y. Ding, D. Tian, Rock and soil classification using PLS-DA and SVM combined with a laser-induced breakdown spectroscopy Library, Plasma Sci. Technol. 17 (2015) 656.

[5] M.D. Assefa, A.K. Chaubey, A.T. Hailu, A.Y. Hibstie, Multi-elemental INAA and CF-LIBS techniques for analysis of rocks of Ethiopian Tropical forest area of Tepi, Eur. Phys. Journal-Applied Phys. 62 (2013).

[6] R.J. Harper, J.R. Almirall, K.G. Furton, Identification of dominant odor chemicals emanating from explosives for use in developing optimal training aid combinations and mimics for canine detection, Talanta. 67 (2005) 313–327. https://doi.org/10.1016/j.talanta.2005.05.019.

[7] X. Yan, X. Peng, Y. Qin, Z. Xu, B. Xu, C. Li, N. Zhao, J. Li, Q. Ma, Q. Zhang, Classification of plastics using laser-induced breakdown spectroscopy combined with principal component analysis and K nearest neighbor algorithm, Results Opt. 4 (2021) 100093.

[8] R. Junjuri, M.K. Gundawar, A low-cost LIBS detection system combined with chemometrics for rapid identification of plastic waste, Waste Manag. 117 (2020) 48–57.

[9] E.M.A. Ali, H.G.M. Edwards, I.J. Scowen, Raman spectroscopy and security applications: the detection of explosives and precursors on clothing, J. Raman Spectrosc. An Int. J. Orig. Work All Asp. Raman Spectrosc. Incl. High. Order Process. Also Brillouin Rayleigh Scatt. 40 (2009) 2009–2014.

[10] R. Junjuri, A.P. Gummadi, M.K. Gundawar, Single-shot compact spectrometer based standoff LIBS configuration for explosive detection using artificial neural networks, Optik (Stuttg). 204 (2020) 163946.

[11] Y. Zhao, Q.Q. Wang, X. Cui, G. Teng, K. Wei, H. Liu, Laser-Induced Breakdown Spectroscopy for the Discrimination of Explosives Based on the ReliefF Algorithm and Support Vector Machines, Front. Phys. 9 (2021) 277.

[12] M. Tofanelli, L. Pardini, M. Borrini, F. Bartoli, A. Bacci, A. D'Ulivo, E. Pitzalis, M.C. Mascherpa, S. Legnaioli, G. Lorenzetti, Spectroscopic analysis of bones for forensic studies, Spectrochim. Acta Part B

At. Spectrosc. 99 (2014) 70–75.

[13] D. Higgins, J.J. Austin, Teeth as a source of DNA for forensic identification of human remains: a review, Sci. Justice. 53 (2013) 433–441.

[14] A. Giakoumaki, K. Melessanaki, D. Anglos, Laser-induced breakdown spectroscopy (LIBS) in archaeological science—applications and prospects, Anal. Bioanal. Chem. 387 (2007) 749–760.

[15] S. Awasthi, R. Kumar, G.K. Rai, A.K. Rai, Study of archaeological coins of different dynasties using libs coupled with multivariate analysis, Opt. Lasers Eng. 79 (2016) 29–38.

[16] F. Ruan, L. Hou, T. Zhang, H. Li, A novel hybrid filter/wrapper method for feature selection in archaeological ceramics classification by laser-induced breakdown spectroscopy, Analyst. 146 (2021) 1023–1031.

[17] J. Ren, Y. Zhao, K. Yu, LIBS in agriculture: A review focusing on revealing nutritional and toxic elements in soil, water, and crops, Comput. Electron. Agric. 197 (2022) 106986.

[18] A. Erler, D. Riebe, T. Beitz, H.-G. Löhmannsröben, R. Gebbers, Soil nutrient detection for precision agriculture using handheld laser-induced breakdown spectroscopy (LIBS) and multivariate regression methods (PLSR, Lasso and GPR), Sensors. 20 (2020) 418.

[19] H. Duan, L. Han, G. Huang, Quantitative analysis of major metals in agricultural biochar using laser-induced breakdown spectroscopy with an adaboost artificial neural network algorithm, Molecules. 24 (2019) 3753.

[20] R. Gaudiuso, E. Ewusi-Annan, N. Melikechi, X. Sun, B. Liu, L.F. Campesato, T. Merghoub, Using LIBS to diagnose melanoma in biomedical fluids deposited on solid substrates: Limits of direct spectral analysis and capability of machine learning, Spectrochim. Acta Part B At. Spectrosc. 146 (2018) 106–114.

[21] X. Chen, Y. Zhang, X. Li, Z. Yang, A. Liu, X. Yu, Diagnosis and staging of multiple myeloma using serum-based laser-induced breakdown spectroscopy combined with machine learning methods, Biomed. Opt. Express. 12 (2021) 3584–3596.

[22] L. Pagnin, L. Brunnbauer, R. Wiesinger, A. Limbeck, M. Schreiner, Multivariate analysis and laser-induced breakdown spectroscopy (LIBS): a new approach for the spatially resolved classification of modern art materials, Anal. Bioanal. Chem. 412 (2020) 3187–3198.

[23] D. Anglos, V. Detalle, Cultural heritage applications of LIBS, in: Laser-Induced Break. Spectrosc. Theory Appl., Springer, 2014: pp. 531–554.

[24] A.K. Myakalwar, S. Sreedhar, I. Barman, N.C. Dingari, S.V. Rao, P.P. Kiran, S.P. Tewari, G.M. Kumar, Laser-induced breakdown spectroscopy-based investigation and classification of pharmaceutical tablets using multivariate chemometric analysis, Talanta. 87 (2011) 53–59.

[25] A.H. Farhadian, S.S. Mousavifard, M. Mollaei, A novel approach in pharmaceutical analysis by laser induced breakdown spectroscopy combined with chemometric methods and artificial neural network, Laser Phys. 32 (2022) 85601.

[26] J. Lin, J. Yang, Y. Huang, X. Lin, Defect identification of metal additive manufacturing parts based on laser-induced breakdown spectroscopy and machine learning, Appl. Phys. B. 127 (2021) 1–10.

[27] J.J. Valdiande, M. Martínez-Minchero, A. Cobo, J.M. Lopez-Higuera, J. Mirapeix, On-line monitoring and defect detection of arc-welding via plasma optical spectroscopy and LIBS, Spectrochim. Acta Part B At. Spectrosc. 194 (2022) 106474.

[28] L.M. Narla, S.V. Rao, Identification of metals and alloys using color CCD images of laser-induced breakdown emissions coupled with machine learning, Appl. Phys. B. 126 (2020) 113.

[29] T. Chen, T. Zhang, H. Li, Applications of laser-induced breakdown spectroscopy (LIBS) combined with machine learning in geochemical and environmental resources exploration, TrAC Trends Anal. Chem. 133 (2020) 116113.

[30] R. Junjuri, C. Zhang, I. Barman, M.K. Gundawar, Identification of post-consumer plastics using laser-induced breakdown spectroscopy, Polym. Test. 76 (2019) 101–108.

[31] X. Zhang, F. Zhang, H. Kung, P. Shi, A. Yushanjiang, S. Zhu, Estimation of the Fe and Cu contents of the surface water in the Ebinur Lake basin based on LIBS and a machine learning algorithm, Int. J. Environ. Res. Public Health. 15 (2018) 2390.

[32] J. Serrano, J. Moros, C. Sánchez, J. Macías, J.J. Laserna, Advanced recognition of explosives in traces on polymer surfaces using LIBS and supervised learning classifiers, Anal. Chim. Acta. 806 (2014) 107–116.

[33] P. Siozos, N. Hausmann, M. Holst, D. Anglos, Application of laser-induced breakdown spectroscopy and neural networks on archaeological human bones for the discrimination of distinct individuals, J. Archaeol. Sci. Reports. 35 (2021) 102769.

[34] S. Moncayo, S. Manzoor, T. Ugidos, F. Navarro-Villoslada, J.O. Caceres, Discrimination of human bodies from bones and teeth remains by laser induced breakdown spectroscopy and neural networks, Spectrochim. Acta Part B At. Spectrosc. 101 (2014) 21–25.

[35] X. Lin, H. Sun, X. Gao, Y. Xu, Z. Wang, Y. Wang, Discrimination of lung tumor and boundary tissues based on laser-induced breakdown spectroscopy and machine learning, Spectrochim. Acta Part B At. Spectrosc. 180 (2021) 106200.

[36] J.R. Freeman, S.S. Harilal, P.K. Diwakar, B. Verhoff, A. Hassanein, Comparison of optical emission from nanosecond and femtosecond laser produced plasma in atmosphere and vacuum conditions, Spectrochim. Acta Part B At. Spectrosc. 87 (2013) 43–50.

[37] T. Gunaratne, M. Kangas, S. Singh, A. Gross, M. Dantus, Influence of bandwidth and phase shaping on laser induced breakdown spectroscopy with ultrashort laser pulses, Chem. Phys. Lett. 423 (2006) 197–201.

[38] R. Junjuri, M.K. Gundawar, Femtosecond laser-induced breakdown spectroscopy studies for the identification of plastics, J. Anal. At. Spectrom. 34 (2019) 1683–1692.

[39] J. Ding, T. Zhang, H. Li, Recent advances in laser-induced breakdown spectroscopy for explosive analysis, TrAC Trends Anal. Chem. (2023) 117197.

[40] J. Vrábel, E. Képeš, L. Duponchel, V. Motto-Ros, C. Fabre, S. Connemann, F. Schreckenberg, P. Prasse, D. Riebe, R. Junjuri, Classification of challenging Laser-Induced Breakdown Spectroscopy soil sample data-EMSLIBS contest, Spectrochim. Acta Part B At. Spectrosc. 169 (2020) 105872.

[41] A. Kumar Myakalwar, N. Spegazzini, C. Zhang, S. Kumar Anubham, R.R. Dasari, I. Barman, M. Kumar Gundawar, Less is more: Avoiding the LIBS dimensionality curse through judicious feature selection for explosive detection, Sci. Rep. 5 (2015) 1–10.

[42] C. Huffman, H. Sobral, E. Terán-Hinojosa, Laser-induced breakdown spectroscopy spectral feature selection to enhance classification capabilities: A t-test filter approach, Spectrochim. Acta Part B At. Spectrosc. 162 (2019) 105721.

[43] T. Vance, N. Reljin, A. Lazarevic, D. Pokrajac, V. Kecman, N. Melikechi, A. Marcano, Y. Markushin,

S. McDaniel, Classification of LIBS protein spectra using support vector machines and adaptive local hyperplanes, in: 2010 Int. Jt. Conf. Neural Networks, IEEE, 2010: pp. 1–7.

[44] F.C. De Lucia, R.S. Harmon, K.L. McNesby, R.J. Winkel, A.W. Miziolek, Laser-induced breakdown spectroscopy analysis of energetic materials, Appl. Opt. 42 (2003) 6148–6152.

[45] M.J. Witte, C.G. Parigger, N.A. Bullock, J.A. Merten, S.D. Allen, Carbon Swan spectra measurements following breakdown of nitro compound explosive simulants, Appl. Spectrosc. 68 (2014) 367–370.

[46] E.N. Rao, S. Sunku, S.V. Rao, Femtosecond laser-induced breakdown spectroscopy studies of nitropyrazoles: the effect of varying nitro groups, Appl. Spectrosc. 69 (2015) 1342–1354.

[47] E.N. Rao, P. Mathi, S.A. Kalam, S. Sreedhar, A.K. Singh, B.N. Jagatap, S.V. Rao, Femtosecond and nanosecond LIBS studies of nitroimidazoles: correlation between molecular structure and LIBS data, J. Anal. At. Spectrom. 31 (2016) 737–750.

[48] S. Sreedhar, E.N. Rao, G.M. Kumar, S.P. Tewari, S.V. Rao, Molecular formation dynamics of 5-nitro-2, 4-dihydro-3H-1, 2, 4-triazol-3-one, 1, 3, 5-trinitroperhydro-1, 3, 5-triazine, and 2, 4, 6-trinitrotoluene in air, nitrogen, and argon atmospheres studied using femtosecond laser induced breakdown spectroscopy, Spectrochim. Acta Part B At. Spectrosc. 87 (2013) 121–129.

[49] X. Wang, Y. He, Y. Zhang, A. Li, X. Zhang, X. Guo, T. Zhang, W. Guo, R. Liu, Y. Yao, Discrimination and classification of high explosives and other organic materials based on laser-induced plasma spectroscopy, J. Anal. At. Spectrom. (2023).

[50] Q. Wang, G. Teng, C. Li, Y. Zhao, Z. Peng, Identification and classification of explosives using semi-supervised learning and laser-induced breakdown spectroscopy, J. Hazard. Mater. 369 (2019) 423–429.

[51] M.K. Gundawar, R. Junjuri, A.K. Myakalwar, Standoff detection of explosives at 1 m using laser induced breakdown spectroscopy, Def. Sci. J. 67 (2017) 623.

[52] S.K. Anubham, R. Junjuri, A.K. Myakalwar, M.K. Gundawar, An Approach to Reduce the Sample Consumption for LIBS based Identification of Explosive Materials., Def. Sci. J. 67 (2017).

[53] A.H. Farhadian, M.K. Tehrani, M.H. Keshavarz, S.M.R. Darbani, Energetic materials identification by laser-induced breakdown spectroscopy combined with artificial neural network, Appl. Opt. 56 (2017) 3372–3377.

[54] S. Almaviva, A. Palucci, V. Lazic, I. Menicucci, M. Nuvoli, M. Pistilli, L. De Dominicis, Laser-induced breakdown spectroscopy for the remote detection of explosives at level of fingerprints, in: Opt. Sens. Detect. IV, SPIE, 2016: pp. 172–180.

[55] A.K. Myakalwar, N. Spegazzini, C. Zhang, S.K. Anubham, R.R. Dasari, I. Barman, M.K. Gundawar, Less is more: Avoiding the LIBS dimensionality curse through judicious feature selection for explosive detection, Sci. Rep. 5 (2015) 1–10.

[56] J. Moros, J.J. Laserna, A spectral sieve-based strategy for sensing inorganic and organic traces on solid surfaces using laser-induced breakdown spectroscopy, Anal. Methods. 7 (2015) 7280–7289.

[57] S. Sreedhar, M.K. Gundawar, S.V. Rao, Laser Induced Breakdown Spectroscopy for Classification of High Energy Materials using Elemental Intensity Ratios., Def. Sci. J. 64 (2014).

[58] I. Gaona, J. Serrano, J. Moros, J.J. Laserna, Range-adaptive standoff recognition of explosive fingerprints on solid surfaces using a supervised learning method and laser-induced breakdown spectroscopy, Anal. Chem. 86 (2014) 5045–5052.

[59] J. Moros, J. Serrano, F.J. Gallego, J. Macías, J.J. Laserna, Recognition of explosives fingerprints on objects for courier services using machine learning methods and laser-induced breakdown spectroscopy, Talanta. 110 (2013) 108–117.

[60] D.W. Pinkham, J.R. Bonick, M.D. Woodka, Feature optimization in chemometric algorithms for explosives detection, in: Detect. Sens. Mines, Explos. Objects, Obs. Targets XVII, SPIE, 2012: pp. 485–492.

[61] Q.-Q. Wang, K. Liu, H. Zhao, Multivariate analysis of laser-induced breakdown spectroscopy for discrimination between explosives and plastics, Chinese Phys. Lett. 29 (2012) 44206.

[62] F.C. De Lucia, J.L. Gottfried, Classification of explosive residues on organic substrates using laser induced breakdown spectroscopy, Appl. Opt. 51 (2012) B83–B92.

[63] J. Moros, J.A. Lorenzo, J.J. Laserna, Standoff detection of explosives: critical comparison for ensuing options on Raman spectroscopy–LIBS sensor fusion, Anal. Bioanal. Chem. 400 (2011) 3353–3365.

[64] J. Moros, J.J. Laserna, New Raman–laser-induced breakdown spectroscopy identity of explosives using parametric data fusion on an integrated sensing platform, Anal. Chem. 83 (2011) 6275–6285.

[65] J.L. Gottfried, F.C. De Lucia Jr, A.W. Miziolek, Discrimination of explosive residues on organic and inorganic substrates using laser-induced breakdown spectroscopy, J. Anal. At. Spectrom. 24 (2009) 288–296.

[66] R. González, P. Lucena, L.M. Tobaria, J.J. Laserna, Standoff LIBS detection of explosive residues behind a barrier, J. Anal. At. Spectrom. 24 (2009) 1123–1126.

[67] J.L. Gottfried, F.C. De Lucia Jr, C.A. Munson, A.W. Miziolek, Double-pulse standoff laser-induced breakdown spectroscopy for versatile hazardous materials detection, Spectrochim. Acta Part B At. Spectrosc. 62 (2007) 1405–1411.

[68] C. Lopez-Moreno, S. Palanco, J.J. Laserna, F. DeLucia Jr, A.W. Miziolek, J. Rose, R.A. Walters, A.I. Whitehouse, Test of a stand-off laser-induced breakdown spectroscopy sensor for the detection of explosive residues on solid surfaces, J. Anal. At. Spectrom. 21 (2006) 55–60.

[69] S.A. Kalam, N.L. Murthy, P. Mathi, N. Kommu, A.K. Singh, S.V. Rao, Correlation of molecular, atomic emissions with detonation parameters in femtosecond and nanosecond LIBS plasma of high energy materials, J. Anal. At. Spectrom. 32 (2017) 1535–1546.

[70] H. Kim, J. Lee, E. Srivastava, S. Shin, S. Jeong, E. Hwang, Front-end signal processing for metal scrap classification using online measurements based on laser-induced breakdown spectroscopy, Spectrochim. Acta Part B At. Spectrosc. 184 (2021) 106282.

[71] J. Liang, M. Li, Y. Du, C. Yan, Y. Zhang, T. Zhang, X. Zheng, H. Li, Data fusion of laser induced breakdown spectroscopy (LIBS) and infrared spectroscopy (IR) coupled with random forest (RF) for the classification and discrimination of compound salvia miltiorrhiza, Chemom. Intell. Lab. Syst. 207 (2020) 104179.

[72] J. Yu, Z. Hou, S. Sheta, J. Dong, W. Han, T. Lu, Z. Wang, Provenance classification of nephrite jades using multivariate LIBS: a comparative study, Anal. Methods. 10 (2018) 281–289.

[73] U.K. Adarsh, V.B. Kartha, C. Santhosh, V.K. Unnikrishnan, Spectroscopy: A promising tool for plastic waste management, TrAC Trends Anal. Chem. (2022) 116534.

[74] Q. Zeng, J.-B. Sirven, J.-C.P. Gabriel, C.Y. Tay, J.-M. Lee, Laser induced breakdown spectroscopy for plastic analysis, TrAC Trends Anal. Chem. 140 (2021) 116280.

[75] J.A. Brydson, Plastics materials, Elsevier, 1999.

[76] E.A. Bruno, Automated sorting of plastics for recycling, Infohouse. P2ric. Org. (2000).

[77] S. Pongstabodee, N. Kunachitpimol, S. Damronglerd, Combination of three-stage sink–float method and selective flotation technique for separation of mixed post-consumer plastic waste, Waste Manag. 28 (2008) 475–483.

[78] G.L. Hearn, J.R. Ballard, The use of electrostatic techniques for the identification and sorting of waste packaging materials, Resour. Conserv. Recycl. 44 (2005) 91–98.

[79] B. Luijsterburg, H. Goossens, Assessment of plastic packaging waste: Material origin, methods, properties, Resour. Conserv. Recycl. 85 (2014) 88–97.

[80] J. Anzano, R.-J. Lasheras, B. Bonilla, J. Casas, Classification of polymers by determining of C1: C2: CN: H: N: O ratios by laser-induced plasma spectroscopy (LIPS), Polym. Test. 27 (2008) 705–710.

[81] J. Anzano, B. Bonilla, B. Montull-Ibor, R.-J. Lasheras, J. Casas-Gonzalez, Classifications of plastic polymers based on spectral data analysis with leaser induced breakdown spectroscopy, J. Polym. Eng. 30 (2010) 177–188.

[82] J.M. Anzano, I.B. Gornushkin, B.W. Smith, J.D. Winefordner, Laser-induced plasma spectroscopy for plastic identification, Polym. Eng. Sci. 40 (2000) 2423–2429.

[83] J. Anzano, M.-E. Casanova, M.-S. Bermúdez, R.-J. Lasheras, Rapid characterization of plastics using laser-induced plasma spectroscopy (LIPS), Polym. Test. 25 (2006) 623–627.

[84] V.K. Unnikrishnan, K.S. Choudhari, S.D. Kulkarni, R. Nayak, V.B. Kartha, C. Santhosh, Analytical predictive capabilities of laser induced breakdown spectroscopy (LIBS) with principal component analysis (PCA) for plastic classification, Rsc Adv. 3 (2013) 25872–25880.

[85] J. Anzano, B. Bonilla, B. Montull-Ibor, J. Casas-González, Plastic identification and comparison by multivariate techniques with laser-induced breakdown spectroscopy, J. Appl. Polym. Sci. 121 (2011) 2710–2716.

[86] K. Liu, D. Tian, H. Wang, G. Yang, Rapid classification of plastics by laser-induced breakdown spectroscopy (LIBS) coupled with partial least squares discrimination analysis based on variable importance (VI-PLS-DA), Anal. Methods. 11 (2019) 1174–1179.

[87] R. Sattmann, I. Monch, H. Krause, R. Noll, S. Couris, A. Hatziapostolou, A. Mavromanolakis, C. Fotakis, E. Larrauri, R. Miguel, Laser-induced breakdown spectroscopy for polymer identification, Appl. Spectrosc. 52 (1998) 456–461.

[88] M. Boueri, V. Motto-Ros, W.-Q. Lei, L.-J. Zheng, H.-P. Zeng, Identification of polymer materials using laser-induced breakdown spectroscopy combined with artificial neural networks, Appl. Spectrosc. 65 (2011) 307–314.

[89] J. Kang, J. Lee, M. Bak, S. Im, Pre-Processing Effects on Laser-Induced Breakdown Spectroscopy with Machine Learning for Plastic Classification, Available SSRN 4211206. (n.d.).

[90] J. Nie, X. Wen, X. Niu, Y. Chu, F. Chen, W. Wang, D. Zhang, Z. Hu, J. Xiao, L. Guo, Identification of different colored plastics by laser-induced breakdown spectroscopy combined with neighborhood component analysis and support vector machine, Polym. Test. 112 (2022) 107624.

[91] X. Peng, B. Xu, Z. Xu, X. Yan, N. Zhang, Y. Qin, Q. Ma, J. Li, N. Zhao, Q. Zhang, Accuracy improvement in plastics classification by laser-induced breakdown spectroscopy based on a residual

network, Opt. Express. 29 (2021) 33269–33280.

[92] Y. Tang, Y. Guo, Q. Sun, S. Tang, J. Li, L. Guo, J. Duan, Industrial polymers classification using laser-induced breakdown spectroscopy combined with self-organizing maps and K-means algorithm, Optik (Stuttg). 165 (2018) 179–185.

[93] S.-B. Roh, S.-B. Park, S.-K. Oh, E.-K. Park, W.Z. Choi, Development of intelligent sorting system realized with the aid of laser-induced breakdown spectroscopy and hybrid preprocessing algorithm-based radial basis function neural networks for recycling black plastic wastes, J. Mater. Cycles Waste Manag. 20 (2018) 1934–1949.

[94] G.U.O. Yangmin, T. Yun, D.U. Yu, T. Shisong, G.U.O. Lianbo, L.I. Xiangyou, L.U. Yongfeng, Z. Xiaoyan, Cluster analysis of polymers using laser-induced breakdown spectroscopy with K-means, Plasma Sci. Technol. 20 (2018) 65505.

[95] V.C. Costa, F.W.B. Aquino, C.M. Paranhos, E.R. Pereira-Filho, Identification and classification of polymer e-waste using laser-induced breakdown spectroscopy (LIBS) and chemometric tools, Polym. Test. 59 (2017) 390–395.

[96] Y. Yu, L.B. Guo, Z.Q. Hao, X.Y. Li, M. Shen, Q.D. Zeng, K.H. Li, X.Y. Zeng, Y.F. Lu, Z. Ren, Accuracy improvement on polymer identification using laser-induced breakdown spectroscopy with adjusting spectral weightings, Opt. Express. 22 (2014) 3895–3901.

[97] S. Barbier, S. Perrier, P. Freyermuth, D. Perrin, B. Gallard, N. Gilon, Plastic identification based on molecular and elemental information from laser induced breakdown spectra: a comparison of plasma conditions in view of efficient sorting, Spectrochim. Acta Part B At. Spectrosc. 88 (2013) 167–173.

[98] M. Banaee, S.H. Tavassoli, Discrimination of polymers by laser induced breakdown spectroscopy together with the DFA method, Polym. Test. 31 (2012) 759–764.

[99] R. Geyer, J.R. Jambeck, K.L. Law, Production, use, and fate of all plastics ever made, Sci. Adv. 3 (2017) e1700782.

[100] G. Parker, M. Khan, Distributed neural network: Dynamic learning via backpropagation with hardware neurons using arduino chips, in: 2016 Int. Jt. Conf. Neural Networks, IEEE, 2016: pp. 206–212.

[101] B.H. Ugalde, AN INTEGRATED ARTIFICIAL NEURAL NETWORK PROTOTYPE ENABLING REAL-TIME OBJECT DETECTION USING RASPBERRY PI, Turkish J. Physiother. Rehabil. 32 (n.d.) 3.

[102] H. Dong, L. Sun, L. Qi, H. Yu, P. Zeng, A lightweight convolutional neural network model for quantitative analysis of phosphate ore slurry based on laser-induced breakdown spectroscopy, J. Anal. At. Spectrom. 36 (2021) 2528–2535.

Intentional Blank Page

Chapter 6

Machine learning in Raman spectroscopy for quantification of explosive mixtures

Detection of explosives and their residues in real time is of paramount importance to homeland security and military. In real-time applications, the suspected materials may contain several chemical compounds making the detection even more challenging. This chapter demonstrates a compact portable Raman spectroscopic tool for quantitative detection of constituent explosives in a binary mixture using machine learning. For the experiment, two samples (1,3,5-trinitroperhydro-1,3,5-triazine (RDX) and ammonium nitrate (AN)) were considered and mixed at different weight percentages. Various regression models such as linear regression, partial least square regression (PLSR), support vector regression (SVR), decision tree regression (DTR) and random forest regression (RFR) were employed to quantify the amount of RDX and AN. The Raman spectra were analyzed with and without background correction. Further, various feature/variable selection strategies were explored to find out the best analysis protocol. The analyses show that the background correction of the spectra does not improve the accuracy significantly. Among various feature selection techniques in conjunction with various regression models, RDX peaks as input for the RFR model yield the best result in terms of accuracy. However, after considering multiple factors such as slope, intercept, and testing time, it was observed that the DTR model using only peak areas with background correction is the most optimal strategy. The results demonstrate that Raman spectroscopy combined with machine learning can be used as a reliable, compact, and fast tool for the real-time investigation of explosive mixtures.

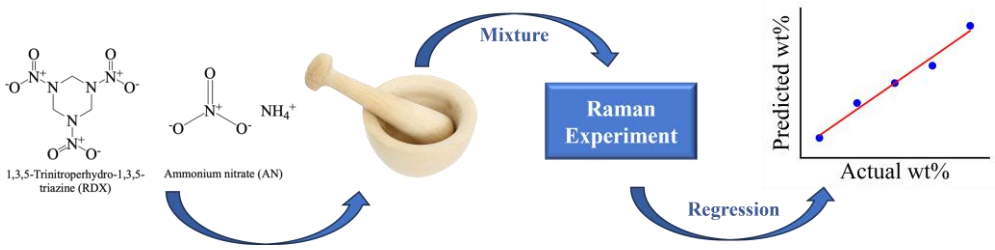

6.1 Introduction

In the last few decades, the threat to homeland security around the world urged the need for an automated portable device for the rapid detection of explosives and high energy materials (HEMs) in the real field. Especially in public places like airports, railway stations, metro stations, shopping malls, worship places, etc., an advanced explosive detection device based on modern analytical techniques is essential for detecting HEMs, particularly explosive mixtures, with high confidence.

Several spectroscopic techniques have been developed for the detection of explosives, including laser induced breakdown spectroscopy[1], Raman spectroscopy[2], laser induced fluorescence[3], terahertz spectroscopy[4], mid-infrared laser spectroscopy[5], etc. Raman spectroscopy is a powerful molecular spectroscopic technique renowned for its ability to interrogate and identify the vibrational states of the molecules. It is one of the most popular analytical technique widely used for the identification of HEMs. In this method, a monochromatic light is focused onto a sample and analyses the scattered light to reveal molecular vibrations unique to different chemical bonds and structures. By detecting the energy shifts in the scattered light, Raman spectroscopy serves as an invaluable analytical tool for molecular fingerprinting and monitoring changes in molecular bond structure within a wide range of materials, including solids, liquids, and gases. Raman spectroscopy has various advantages over other analytical techniques, including low-cost experimental setup[6], compact and portable instrument[7], capable of molecular detection without requiring any sample preparation, standoff detection capability with the use of pulsed laser[2,8], etc. Raman spectroscopy is widely used in various research areas such as environmental monitoring[9], quality control of food items[10], explosive detection[11,12], etc.

Several researchers across the globe use Raman spectroscopy as a potential tool for the detection of explosives and hazardous materials. For example, D. Diaz and D. W. Hahn reported the detection of AN commonly used for the manufacture of improvised explosive devices (IEDs) in various mixtures, such as AN-soil and AN-water mixtures[13]. K. K. Gulati et al. have used a standoff Raman configuration using a pulsed laser to detect p-nitro benzoic acid (PNBA) and AN deposited on various background surfaces[2]. Using time-gated Raman spectroscopy, the same group also studied PNBA mixed with different materials like sand and soil. C. Byram et al. demonstrated instant detection of various explosives using surface-enhanced Raman spectroscopy (SERS), using gold nanoparticles and nanostructures as SERS platforms[14]. M. Gaft and L. Nagli have also demonstrated standoff detection of various

explosives using Raman spectroscopy[8]. Several other works have also been devoted to literature for bulk and trace detection of explosives using Raman spectroscopy[15–19]. However, most of the research has been performed for bulk and trace detection of explosives. A few studies were focused on the bulk detection of explosives mixed with other materials[13].

This chapter explores quantitative detection of RDX mixed with AN at different weight percentages. The choice of RDX and AN mixtures has specific significance in real-time as its mixtures are not only used as military and commercial explosives but also for IEDs[20–23]. More importantly, AN is popularly used as fertilizers for farming and is easily accessible; in such cases, identification and quantification of explosives like RDX become crucial if mixed with AN. Here, a low-cost, compact, and portable Raman spectroscopic setup is used to detect explosive mixtures. For the experiment, RDX and AN were mixed at different concentrations. Subsequently, several regression techniques were employed on the Raman spectra to investigate the weight percentage of each sample. In addition, various manual feature selection approaches were examined to determine the most effective analysis protocol.

6.2 Materials and Methods

Two explosives, viz., RDX and AN, and their mixtures were considered for the present experiment. Figure 6.1 illustrates the molecular structures of RDX and AN. A total of six samples were prepared, consisting of two pure samples and four mixtures of RDX and AN at varying weight percentage ratios. Table 6.1 contains comprehensive information about the composition of the mixed samples.

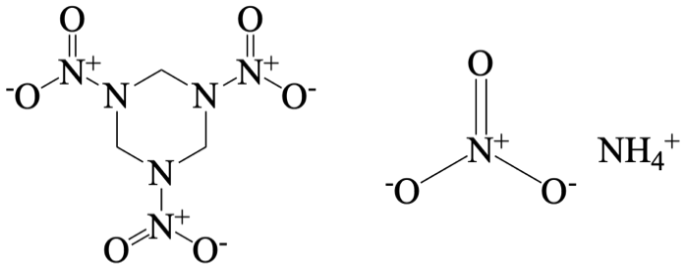

Figure 6.1. Molecular structure of RDX and AN.

For each sample, the proportion of RDX and AN (Table 1) were first mixed and then ground with mortar and pestle for 15 mins to make each mixture homogeneous. After that, circular pellets of diameter 10 mm were prepared for each sample by applying 2 tons of hydraulic pressure for 5 mins. The pellets were prepared to give each sample a flat, uniform surface.

Table 6.1. Details of the mixture samples mixed at different concentrations.

Sample No.	RDX		AN	
	Quantity (mg)	Concentration (wt %)	Quantity (mg)	Concentration (wt %)
1	200	100	0	0
2	160	80	40	20
3	120	60	80	40
4	80	40	120	60
5	40	20	160	80
6	0	0	200	100

The schematic diagram of the experimental setup is shown in figure 2.7 of chapter 2. In detail, a compact portable diode-pumped continuous-wave (CW) laser (M/s, OceanOptics – I0785MM0350MS) emitting monochromatic light at 785 nm and delivering a maximum power of ~350 mW was used. The laser light was focused onto the sample surface using a Raman probe (M/s, (OceanOptics – RIP-RPB-785-FC-SMA) of a working distance of 7.5 mm and spectral range of 300 – 3900 cm^{-1}. The same probe collected the Raman scattering and delivered them to a Czerny-Turner CCD spectrometer (M/s, Ocean Optics – QEPro) with a detection range of 300 – 3000 cm^{-1} and optical resolution of 11 cm^{-1}. Under this experimental setting, 50 Raman spectra were acquired from each sample (total: 6 × 50 = 300 spectra). All the spectra were recorded with an integration time of 10 seconds.

6.3 Spectral Interpretation

The Raman spectra of RDX mixed with AN at different ratios are depicted in figure 6.2. Figure 6.3 shows the typical background correction. All the spectra were normalized w.r.t. to the total area, i.e., each intensity value divided by the total area of the spectrum. All the vibrational signatures of RDX and AN were identified and assigned based on earlier reports[13,24]. The Raman shift at 856 cm^{-1} is attributed to the C – N – C stretching vibrations of RDX, and the band at 894 cm^{-1} is due to the CH_2 bending. Other strong bands were also observed in RDX, i.e., the band at 1223 cm^{-1} was noticed due to the stretching of N – C – N, and the bands at 1281 and 1315 cm^{-1} were observed due to the stretching of the N – NO_2 band. An intensity band is also observed in RDX at 1352 cm^{-1} which is due to the axial stretching of N – NO_2. Similarly, some Raman modes were also observed in the AN. For instance, the AN mode associated with the NO_3^- ion in-plane deformation was observed at 723 cm^{-1}. Similarly, the AN mode associated with the NO_3^- ion symmetric stretching is

located at 1050 cm^{-1}. These are the Raman modes observed in the present work; however, these have been reported at slightly different locations in the literature, which may be due to the different optical resolutions of different spectrometers used[13,24].

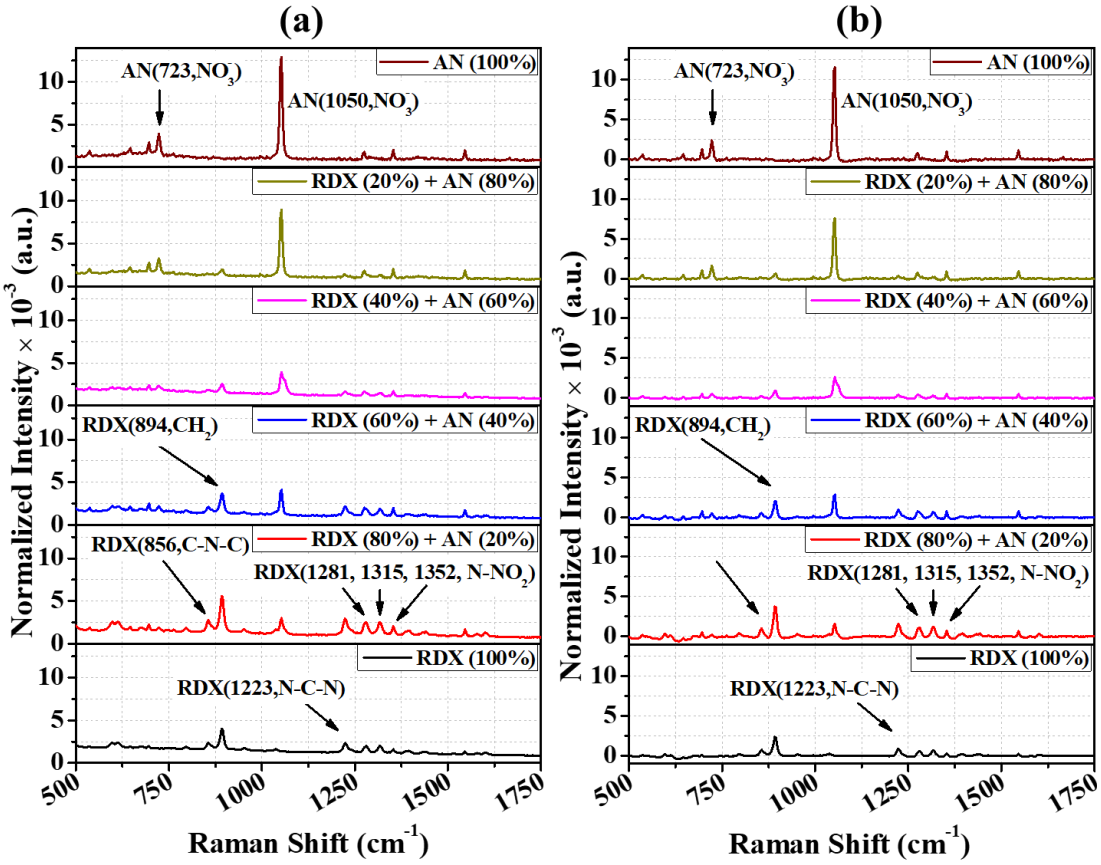

Figure 6.2. Normalized Raman spectra of RDX and AN mixtures mixed at different wt% (a) before and (b) after background correction.

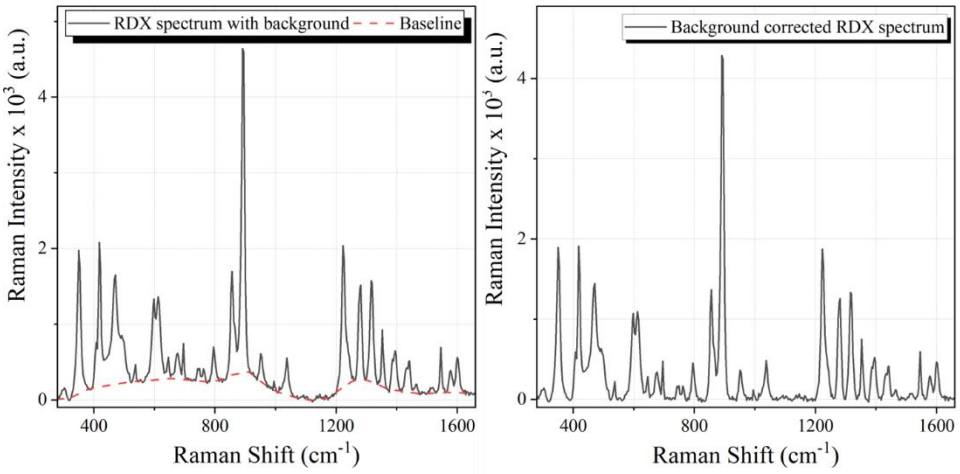

Figure 6.3. RDX spectrum with background (left) and after background removal (right).

From figure 6.2, it can be observed that with increasing the concentration of RDX, the intensities of Raman peaks corresponding to RDX increase gradually and vice-versa. Similarly, with increasing AN concentration, the Raman intensities of AN bands increases and vice-

versa. Apart from that, it also has been observed that the background of the whole spectrum increases with increasing RDX concentration and decreasing AN concentration.

Except for pure RDX and AN, all four mixtures' spectra look similar as they represent the vibrational signatures of both; therefore, it is not possible to quantify the amount of RDX and/ or AN in the mixtures from the spectral observations alone. However, the intensities of each peak differ from sample to sample, which is proportional to the concentrations of that element in the sample; hence, quantitative analysis is necessary to detect the amount of RDX and AN proportion present in each mixture sample.

6.4 Quantitative Analysis

The quantitative analysis of Raman spectroscopy is divided into uni- (and bi-variate) and multivariate analysis. Uni- or bi-variate analysis considers intensity at one or two wavenumbers as variables/features from the Raman spectrum to extract the quantitative information. Conversely, multivariate analysis employs intensities at many wavenumbers as variables. The advantages of univariate analysis are that it is less time-consuming and more straightforward calculation. However, multivariate analysis has its own advantages as it considers multiple features corresponding to the analytes of interest rather than one/two intensity values. In this context, to quantify the explosive mixtures, various machine learning algorithms such as linear regression (univariate and multivariate), partial least square regression (PLSR), support vector regression (SVR), decision tree regression (DTR) and random forest regression (RFR) were employed. Further, regression analyses were also performed using various manual feature selection approaches.

6.4.1 Linear Regression Analysis

The univariate analysis using linear regression is called simple linear regression (SLR) and the multivariate analysis is called multiple linear regression (MLR).

SLR estimates the relationship between a single explanatory variable (X) and dependent variable (Y) and constructs a regression line/model. Then the regression line is used to predict the value of Y for an unknown X. In SLR, the relationship between the explanatory variable and dependent variable is represented by the following equation[25]:

$$Y = \beta_0 + \beta X + e \tag{6.1}$$

Where β_0 and β_1 are the intercept and slope of the regression line, respectively, and e is the error term.

MLR is used to predict the dependent variable (Y_i) values for a given N number of explanatory variables (X_1, X_2, X_3, …, X_N). In MLR, the relationship between the explanatory variable and dependent variable is represented by the following equation[25]:

$$Y_i = \beta_0 + \beta_1 X_{1i} + \beta_2 X_{2i} + \beta_3 X_{3i} + ... + \beta_N X_{Ni} + e \tag{6.2}$$

Where β_0 is the constant term and β_1, β_2, β_3, …, β_N are the coefficients of N explanatory variables, respectively. Here, the intensities at different wavenumbers are the variables.

Hence, MLR is an extension of the SLR, which considers multiple explanatory variables/features simultaneously to construct the regression model, and SLR is a special case of MLR, where N = 1.

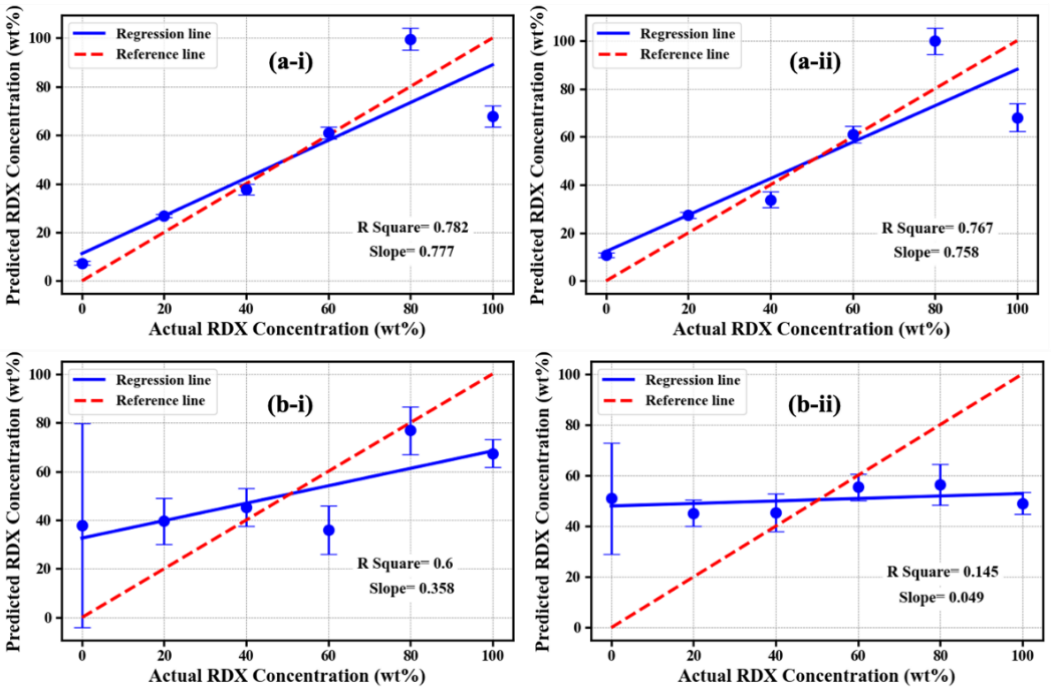

Figure 6.4. SLR prediction of RDX concentrations in RDX and AN mixtures using (a) RDX Raman peak height at 894 cm^{-1} and (b) AN Raman peak height at 1050 cm^{-1}. (i) represents the SLR prediction by considering the spectra without background correction and (ii) represents the results from background corrected spectra.

The univariate quantitative analysis using SLR was performed separately on the two most intense Raman peaks, i.e., 894 and 1050 cm^{-1} correspond to RDX and AN, respectively. SLR is used in both cases because the number of features is one. For each analysis, a total of 300 spectra were considered. The data was first split randomly into 80% for training and 20% for

testing. The training data is used to train/construct the SLR model and the testing data is used to predict the concentrations of RDX mixed with AN. A total of 100 iterations were performed for the training, followed by testing. The algorithm for the complete analysis was designed and programmed in Python. Figure 6.4 represents the prediction of RDX concentrations in the mixtures from the SLR of RDX peak height and AN peak height, respectively. The red dashed line in each graph represents the reference line representing the actual concentrations of RDX and the solid blue line represents the regression line of concentration prediction.

From figure 6.4, it can be observed that the SLR doesn't yield a good result for both raw spectra and background corrected spectra. It estimates a slope of 0.777 and 0.758 for the regression lines constructed using raw and background corrected RDX Raman peak height, respectively. In the case of AN Raman peak height as input to the SLR model, the results are worse for both raw and background corrected spectra. Therefore, SLR model fails to predict the concentrations of RDX and/ or AN in their mixtures.

Further, MLR was employed on the Raman spectra of all the mixture. At first, the MLR analysis was performed by considering the full spectra as input, and further four manual feature selection approaches were employed, which provide four different sub-spectra to the input of the MLR algorithm. The details of the Raman shift ranges and the number of features associated with various approaches are represented in table 6.2.

Table 6.2. Various feature selection approaches considered for regression analysis.

Sl. No.	Feature selected spectrum	Features included	Range of Raman shift (cm^{-1})	Number of features	Fraction of total data (%)
1	S1	Full Spectrum	300 - 3000	1044	100
2	S2	Peak range	703 - 1369	219	21
3	S3	Only peaks	703 - 746, 830 - 932, 1028 - 1080, 1199 - 1369	125	12
4	S4	RDX peaks	830 - 932, 1199 - 1369	93	9
5	S5	AN peaks	703 - 746,1028 - 1080	32	3

In this case, the sub-spectra were selected manually based on the Raman peak region. S1 represents the full spectrum. The sub-spectra S2 represents the range of the spectra where Raman peaks are present, sub-spectra S3 represents only those areas where the peaks are present, sub-spectra S4 and sub-spectra S5 represent the spectral area where only RDX and AN peaks are present respectively. Figure 6.5 visualizes the feature-selected areas of one of the

mixture spectra. From figure 6.5, it can be observed that various manual feature selection approaches involve different numbers of features. The number of features associated with each feature selection approach is represented in table 6.2. From table 6.2, it can be noticed that in comparison to the full Raman spectrum, all four feature-selected sub-spectra contain a much smaller number of features.

Finally, MLR analyses were employed on S1 – S5 under similar conditions as SLR. Like the univariate analysis, the total data were randomly split into 80% training, and 20% testing data, and 100 iterations were performed for training and testing. The regression lines obtained from all MLR analyses are represented in figure 6.6. Figure 6.6 shows that the MLR analyses yielded a very good result compared to the SLR analyses with R – square and slope of ~1 for both raw and background corrected spectra. However, the nature of the regression lines is similar in all cases and there is not much difference between the raw and background corrected spectra.

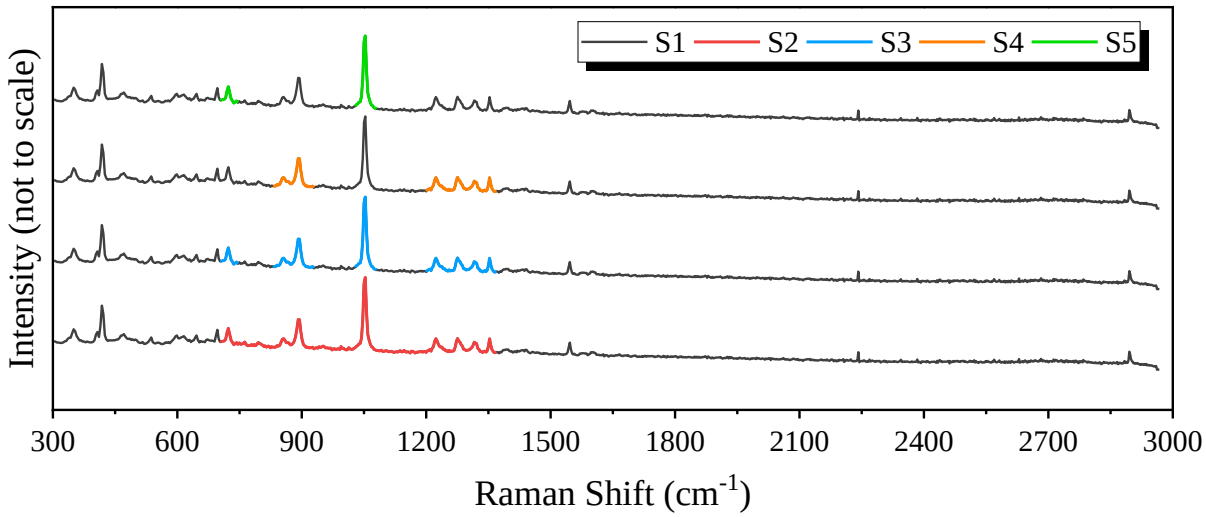

Figure 6.5. Raman spectrum (S1) and various feature selected sub-spectra (S2 – S5) of RDX and AN mixture.

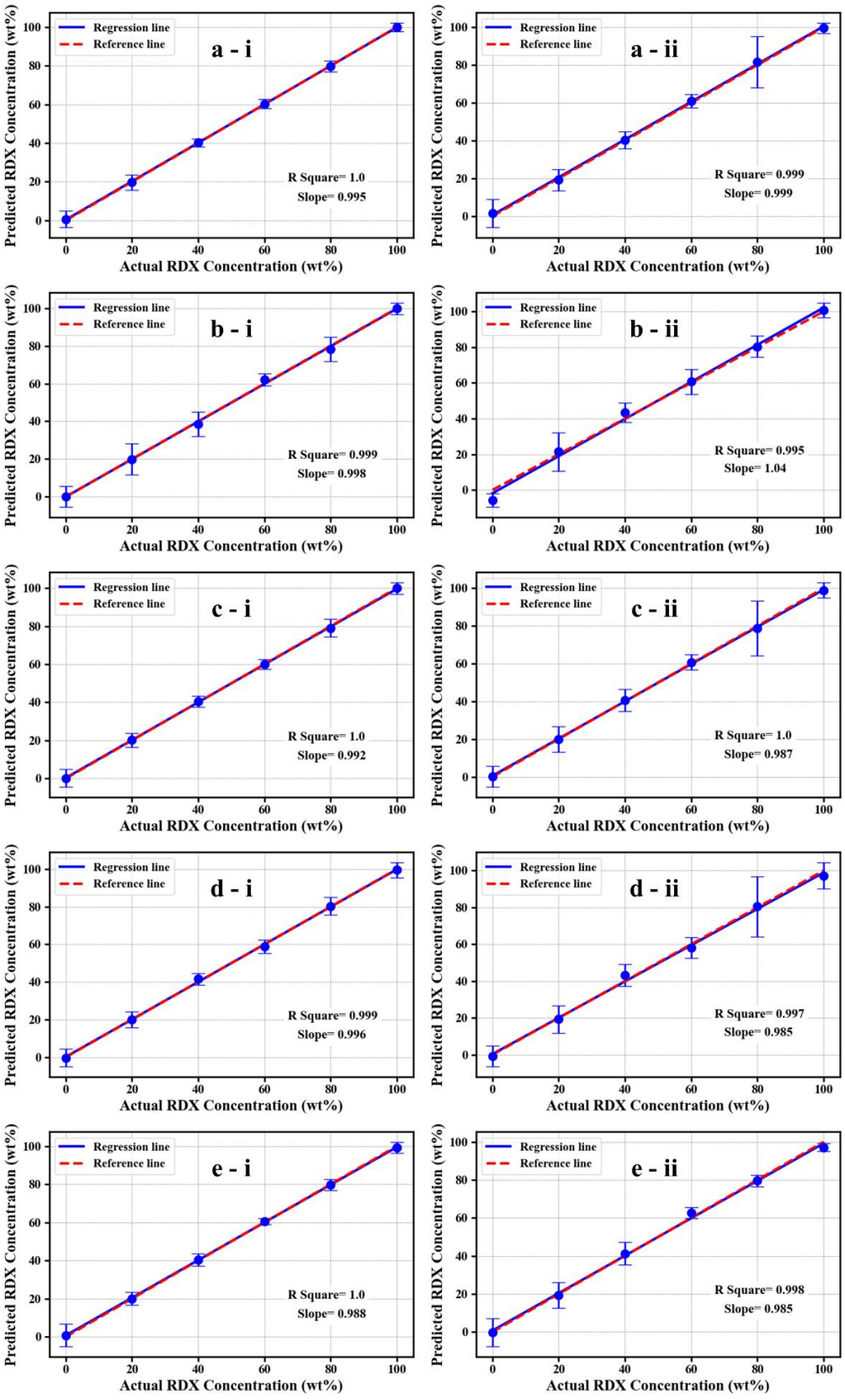

Figure 6.6. MLR prediction of RDX concentrations in RDX and AN mixtures using (a) S1, (b) S2, (c) S3, (d) S4, and (e) S5 as input. (i) represents the MLR prediction by considering the spectra without background correction and (ii) represents the results from background corrected spectra.

6.4.2 Partial Least Square Regression (PLSR) Analysis

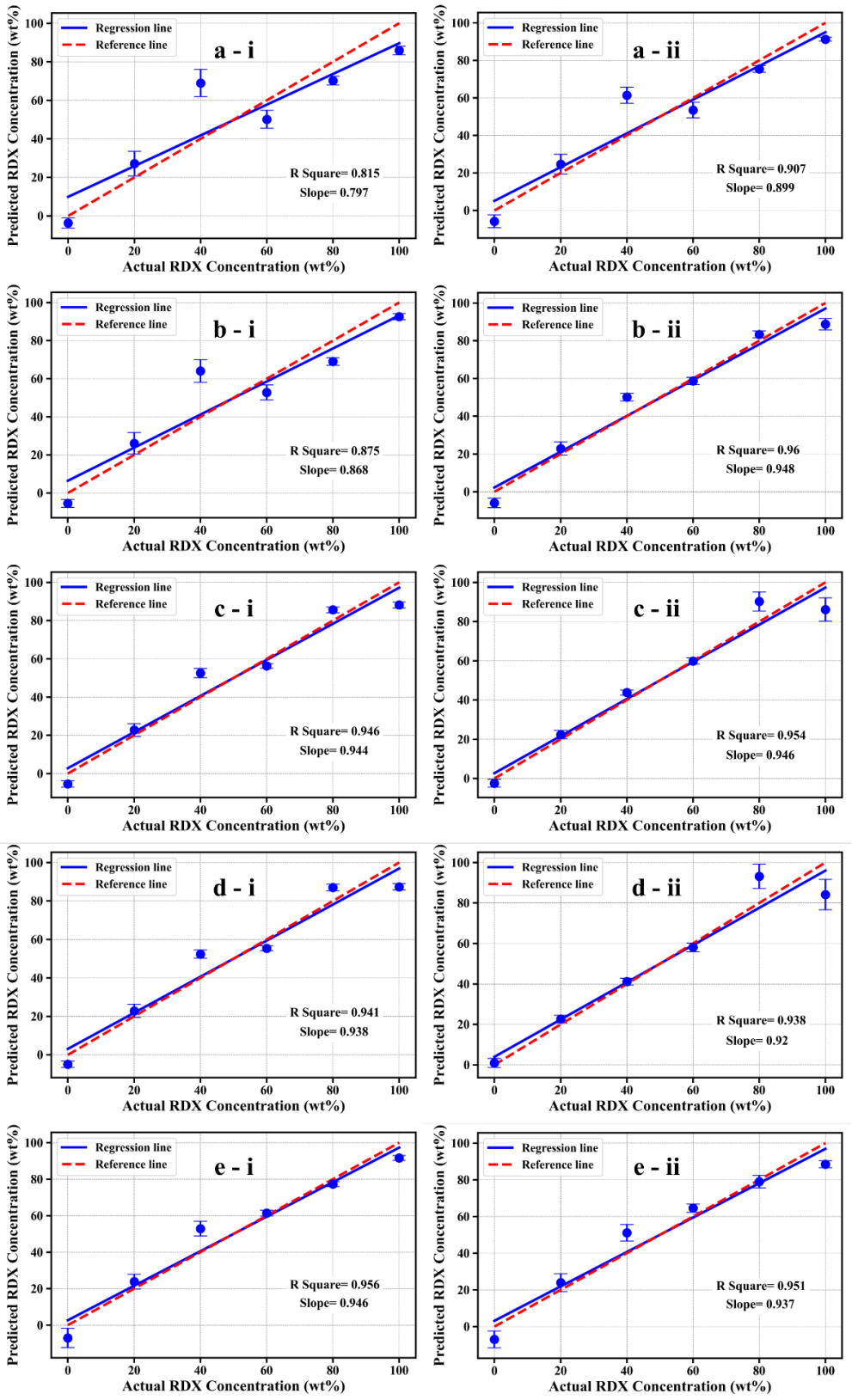

Figure 6.7. PLSR prediction of RDX concentrations in RDX and AN mixtures using (a) S1, (b) S2, (c) S3, (d) S4, and (e) S5 as input. (i) represents the PLSR prediction by considering the spectra without background correction and (ii) represents the results from background corrected spectra.

PLSR is a powerful machine learning approach that combines regression analysis with dimensionality reduction. PLSR was created as a flexible approach for dealing with complicated datasets, and it is especially beneficial when dealing with high-dimensional, multicollinear, or noisy data. Unlike traditional regression methods that focus solely on finding relationships between predictors and a response variable, PLSR simultaneously considers both predictor and response variables, effectively extracting and highlighting patterns in the data. This method is widely employed in conjunction with Raman spectroscopy for various applications[26–29].

PLSR was employed on full spectra and various feature selected sub-spectra (see table 6.2), mirroring the methodology applied in MLR. The examinations were conducted on Raman spectra, both with and without background correction.

Figure 6.7 visualizes the regression lines obtained by employing various feature selection approaches for Raman spectra, considering the presence or absence of background correction in the analysis. From the figure, it can be noticed that the performance in predicting the RDX concentration is significantly inferior as compared to MLR. In contrast to the results obtained using MLR, the reference lines had significantly lower R-square and slope values a little far from zero, indicating poor results. Furthermore, there are cases where the predicted values differ significantly from the actual values, for example, in Fig. 6.6 (a – i), where the actual concentration is at 40 wt%.

6.4.3 Support Vector Regression (SVR) Analysis

SVR is a popular machine learning method for regression analysis that excels at handling both linear and non-linear data. SVR is a modification of the support vector machine (SVM) algorithm. Instead of trying to minimize errors like traditional regression algorithms, SVR focuses on fitting a defined margin of tolerance around the predicted values within a predetermined threshold of deviation or error. The core principle of SVR involves mapping the input data to higher dimensional space in order to find the optimal hyperplane that fits well for the data points. This method enables the model to effectively handle outliers and complex variable interactions by allowing for adjustments within a specific range known as the epsilon tube or margin of tolerance. This strategy facilitates the management of fluctuations or deviations, allowing the model to capture intricate relationships between variables more accurately and effectively identify outliers.

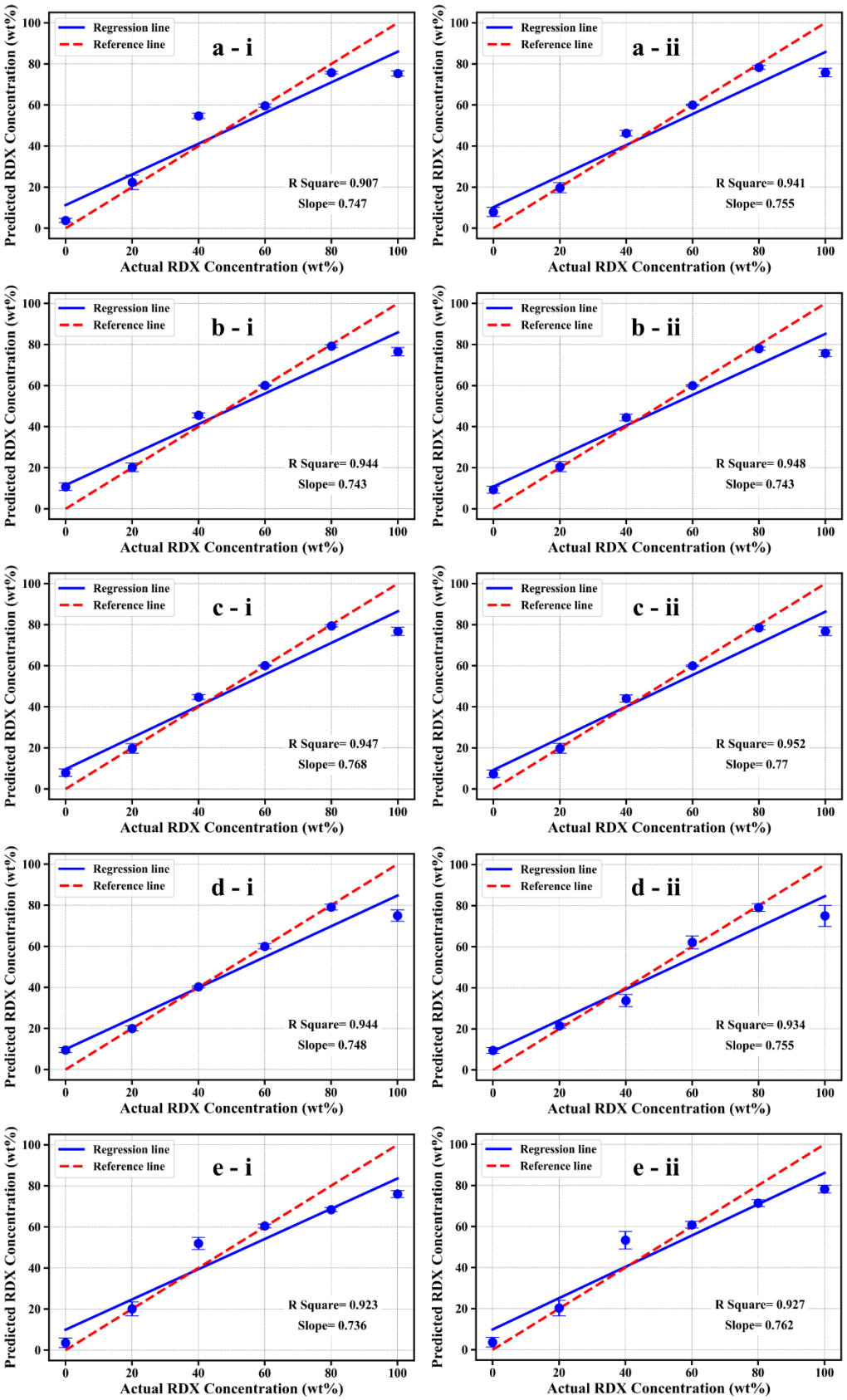

Figure 6.8. SVR prediction of RDX concentrations in RDX and AN mixtures using (a) S1, (b) S2, (c) S3, (d) S4, and (e) S5 as input. (i) represents the PLSR prediction by considering the spectra without background correction and (ii) represents the results from background corrected spectra.

In SVR, the main idea is to maximize the margin between the epsilon tube and the actual data points by finding the hyperplane. This ensures a balance between the complexity of the model and its generalizability. Through the utilization of kernel functions, SVR is able to deal effectively with variable relationships that are not linear. This is achieved by implicitly projecting the input data into a higher-dimensional space while constructing a linear model. SVR is used in various applications of Raman spectroscopy[30–32].

In this context, SVR was employed on full spectra and various feature selected sub-spectra of mixtures in a similar manner as MLR and PLSR i.e., on both raw and background corrected spectra. The results obtained from full spectra and various feature-selected sub-spectra as input to the SVR model are described in figure 6.8.

The figure indicates a significant discrepancy between the results and the ones obtained using MLR and PLSR. Specifically, the slope of the regression lines is below 0.8, where the ideal value should be 1. Not only that, but the R-squared values are also lower in comparison to MLR and PLSR. Additionally, there are many cases where the predicted values significantly differ from the anticipated values, highlighting significant inconsistency in the model's prediction.

6.4.4 Decision Tree Regression (DTR) Analysis

DTR is one of the most effective and user-friendly machine learning methods for predictive modeling and analysis. The working principle involves iteratively constructing a tree-like structure by partitioning the feature space into smaller sections or nodes, guided by the input feature values. Each internal node denotes a decision point based on features, while each leaf node is associated with a predicted value. The building process of the tree involves binary splitting at each node that divides the data by minimizing the variance of the target variable. This process is repeated until a stopping criterion/threshold is not satisfied. The stopping point is achieving a maximum tree depth where the reduction in variance saturates. The interpretability of decision tree regression is a major advantage since it helps to visualize and comprehend the decision-making procedure. In addition to being resilient to outliers, decision trees can process both numerical and categorical data.

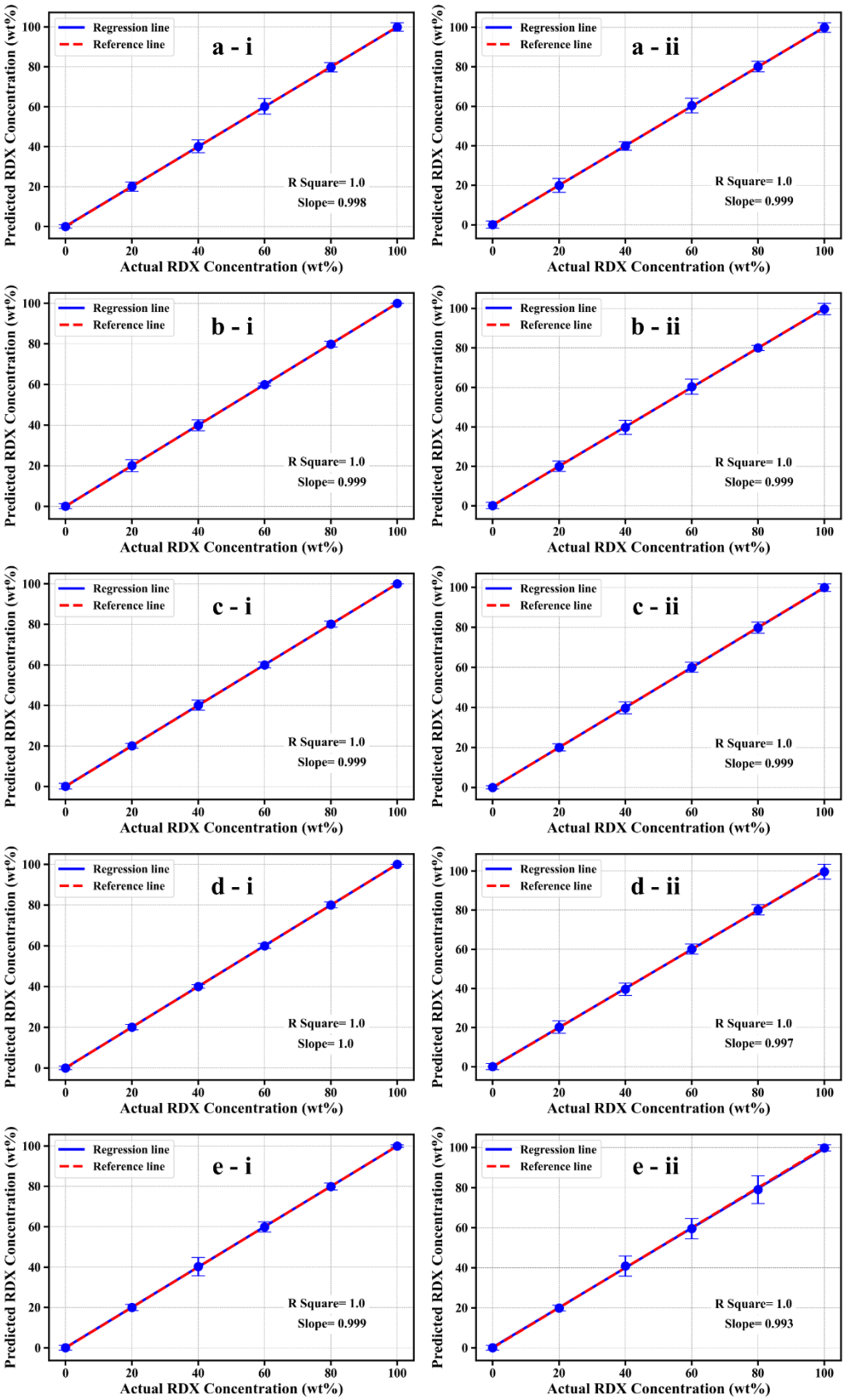

Figure 6.9. DTR prediction of RDX concentrations in RDX and AN mixtures using (a) S1, (b) S2, (c) S3, (d) S4, and (e) S5 as input. (i) represents the PLSR prediction by considering the spectra without background correction and (ii) represents the results from background corrected spectra.

On the other hand, decision trees can easily suffer overfitting when they grow too large and start to capture the noise data. Pruning, reducing tree depth, or employing ensemble approaches such as Gradient Boosting or Random Forests can improve the model's performance and reduce the likelihood of overfitting.

DTR is useful in many scientific fields where it is necessary to identify and evaluate interactions between variables in order to do predictive modeling and analysis. Several researches were devoted in literature to process Raman spectroscopic data using DTR for various applications[33,34].

Like previous regression methods, DTR was employed for the quantitative investigation of explosive mixtures here. The regression model was applied to the raw and background corrected spectra, as well as to various feature subsets. Figure 6.9 illustrates the results obtained by DTR under varying input data.

The figure illustrates the impressive accuracy of the predictions obtained from DTR analyses for different sets of input data. There is a high degree of agreement between the actual and predicted values since the slope and R-squared values are almost 1 for each case. In comparison to previous regression analyses, the standard deviation (error) in calculating each concentration is significantly smaller, signifying heightening precision in the predictions.

6.4.5 Random Forest Regression (RFR) Analysis

RFR has become an important ensemble learning method in predictive modeling and analysis because of its adaptability and resilience when faced with complicated datasets. For regression problems, it works by building numerous decision trees and combining their predictions for more stable and reliable outcomes. Random forest comprises ensembles of decision trees, each trained on a section of the dataset and employing a random selection of features. Unlike a single decision tree, the ensemble method aggregates predictions from all the trees, which helps reduce the risk of overfitting and improves generalization.

During the training process, the original dataset selects random samples with replacement (bootstrap samples) and constructs each tree individually. Also, a random subset of features is taken into account for splitting at each node of the tree, which adds diversity and randomization to the different trees. By averaging the predictions produced by all the trees in the forest, RFR determines the final outcome.

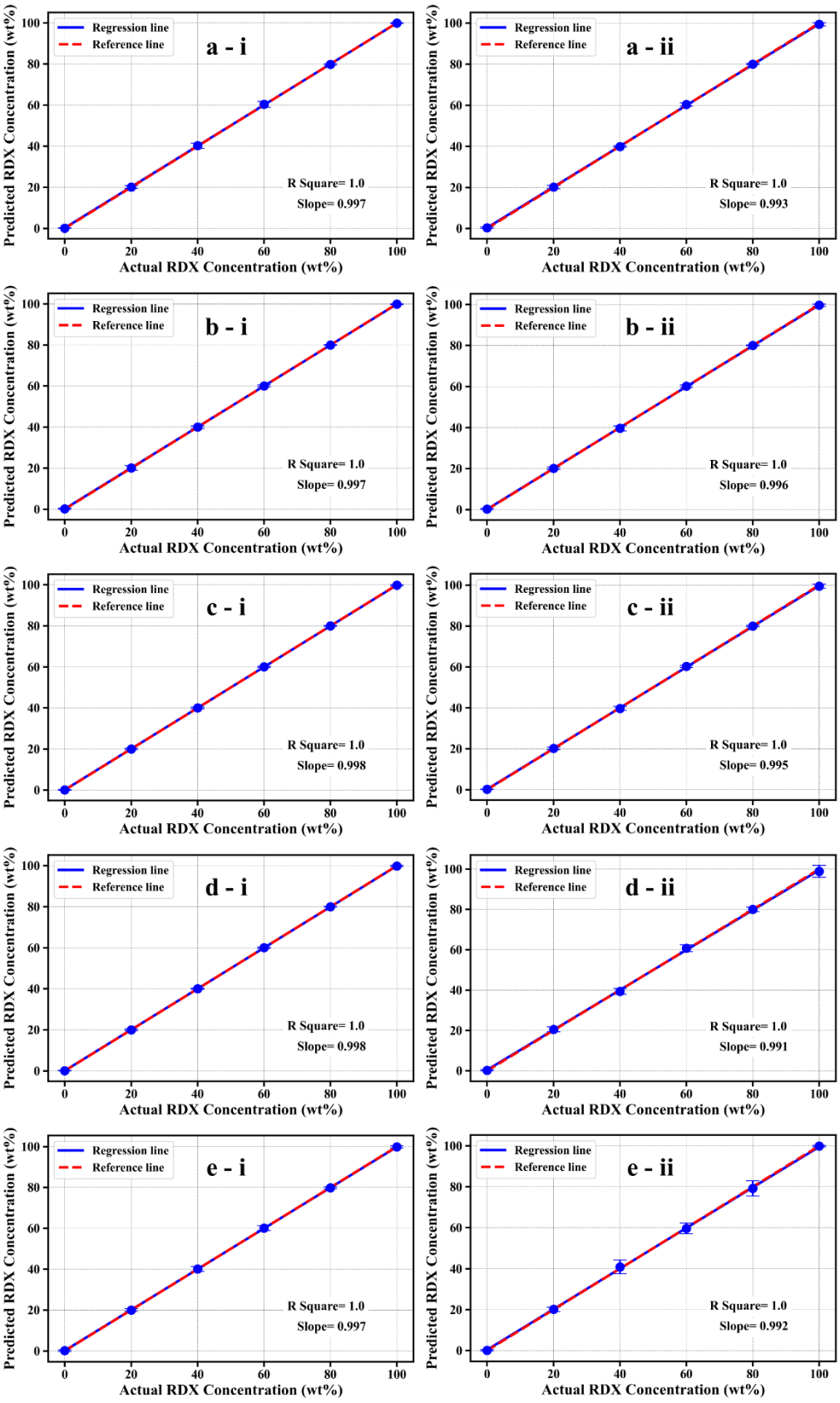

Figure 6.10. RFR prediction of RDX concentrations in RDX and AN mixtures using (a) S1, (b) S2, (c) S3, (d) S4, and (e) S5 as input. (i) represents the PLSR prediction by considering the spectra without background correction and (ii) represents the results from background corrected spectra.

In particular, this aggregation approach produces more robust and accurate results when working with high-dimensional or noisy data or with variables that exhibit non-linear correlations. One of the major advantages of RFR is successful handling of big datasets with several features while minimizing overfitting. In addition, it provides insights into the significance of features, which helps to determine which variables are most important for making predictions. Therefore, random forest is also used as a potential method for feature selection. RFR has numerous applications in diverse areas of research. It is also widely used in conjunction with Raman spectroscopy for various quantitative applications[35–38].

The results obtained from the RFR analyses for different sets of input data are described in figure 6.10. Similar to DTR, RFR stands out for its outstanding performance. In this case, the slopes and R-squared values are close to one, suggesting a strong correlation between the actual and predicted values. Furthermore, since the predictive error at individual concentrations is significantly less, the model's predictions are accurate and precise.

The results obtained by each regression method are compared in the next section, which also evaluates their performance in terms of accuracy and computational time.

6.5 Discussion

Raman spectroscopy has been used for the quantitative detection of explosives within mixtures. Samples with varied concentrations were prepared for this study by mixing RDX and AN at various weight percentages. The experiment was conducted using a portable, small, and low-cost Raman spectroscopic setup that allowed for the recording of multiple spectra for each sample. Various machine learning regression techniques were utilized to evaluate the concentration of RDX in the mixtures. These techniques include linear regression, PLSR, SVR, DTR, and RFR. The analyses were performed on both spectra with or without background correction. In addition, the study explored different feature selection methods that strive to maximize accuracy while minimizing the computing time for faster and more robust prediction. The former section meticulously presented the results obtained from different methodologies employed. This subsequent section is dedicated to a thorough dissection and comparison of all parameters, endeavoring to discern the most proficient approach.

In order to evaluate the effectiveness and precision of a regression model, the parameters of the regression line (slope and intercept) showing actual vs projected concentrations in regression analysis are crucial. A steeper slope indicates a stronger correlation between the predictor and response variables, while a flatter slope indicates no change in the anticipated

values relative to the actual values. Minimal projected response without the predictor is shown by an intercept near zero. These parameters are essential for evaluating and improving the regression model, as they show how well the model predicts concentrations and how strongly they are related. Figure 6.11 represents the value of the slope and intercept obtained from all regression approaches. The Y-scale of the figure represent the distance of resulted slope of the regression line from the expected slope (slope of 1). Within the figure, the marker size represents the absolute value of the intercept—where larger markers denote more deviated intercept from zero, and smaller markers correspond to the intercepts close to zero. By comparing the regression lines corresponding to all the models with varying input data, it has been observed that the utilization of only peaks (S3) as input for the DTR model with background correction resulted in a remarkable slope of 0.999 and intercept of 0.007. This particular regression line stands out as the most optimal in terms of slope and intercept. Moreover, upon close observation of the figure, it becomes evident that, except PLSR and SVR, other methodologies demonstrate significantly better results in terms of both slope and intercept.

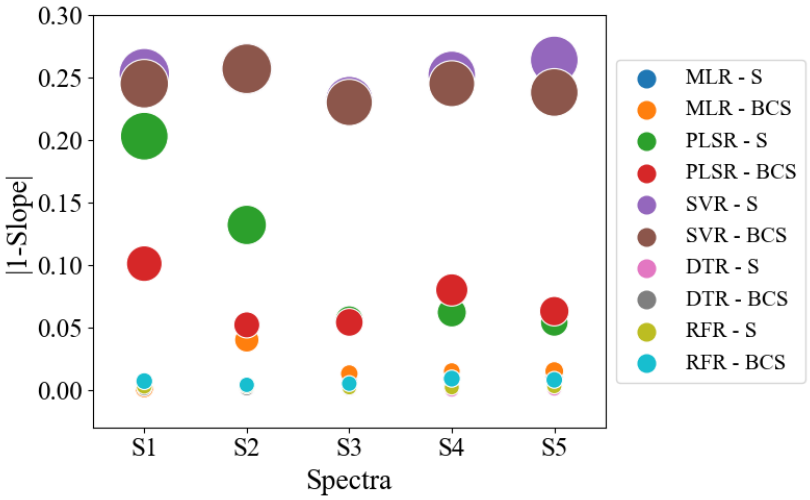

Figure 6.11. Comparison of slope and intercept obtained from regression analyses. S represents spectra without background correction and BCS represents background corrected spectra. The size of the markers are scaled to the absolute value of intercept (abs(intercept)), i.e., the smallest marker represents the intercept closer to 0.

Apart from regression line parameters, root mean square error (RMSE) is important in regression analysis, offering multifaceted insights into model performance and practical applicability. RMSE serves as a fundamental measure of the average magnitude of differences between actual and predicted values. RMSE can be defined as,

$$RMSE = \sqrt{\frac{\sum_{i=1}^{N}(Predicted_i - Actual_i)^2}{N}} \tag{6.3}$$

where N is the total number of observations.

A lower RMSE indicates higher accuracy, meaning the model's predictions closely match the actual data points. This demonstrates improved precision and superior performance.

Additionally, computational efficiency becomes crucial in practical situations when quick decision-making or instant predictions are required. The importance of training time is very low compared to testing time, as models can be pre-trained before deployment, guaranteeing their preparedness for real-time testing situations. Therefore, the crucial factor is the effectiveness of the testing duration, which directly influences the model's practical usefulness in real-time decision-making or live prediction settings.

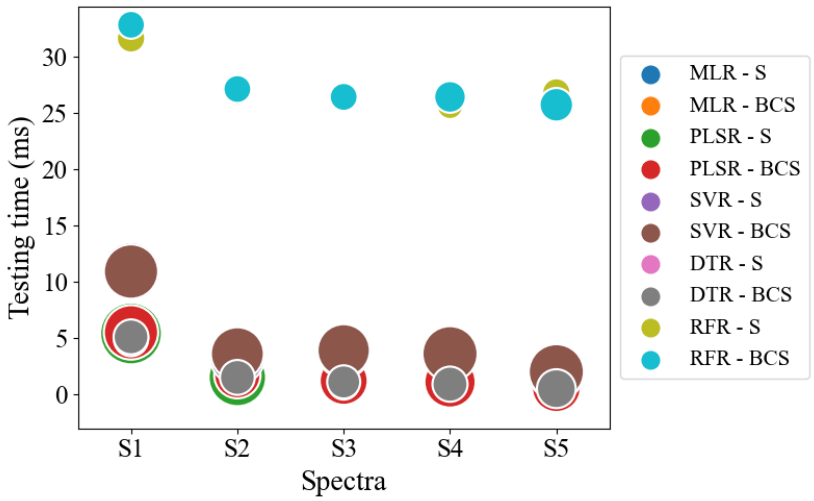

Figure 6.12. Comparison of testing time and RMSE obtained from regression analyses. S represents spectra without background correction and BCS represents background corrected spectra. The size of the markers is scaled to the RMSE value, i.e., the smaller markers represent low RMSE.

Figure 6.12 depicts the duration of testing acquired from all regression methods for a single iteration. The sizes of the markers in the figure correlate to the RMSE of the predictions. Smaller markers represent lower RMSE values, while larger markers represent higher RMSE values. Remarkably, testing times remain low, consistently staying below 35 ms. When comparing the different models, all models except for RFR show similar time consumption, taking up to 15 ms. Among all the methods examined, employing AN peaks (S5) with background correction markedly decreases the computational time needed for the DTR

model. Notably, this approach requires only 0.5 ms, making it the fastest among all the examined approaches. PLSR and SVR have relatively greater levels of RMSE, indicating a lower prediction accuracy. However, all methods exhibit similar RMSE values, with the lowest value obtained by RFR when using only RDX peaks (S4) without background correction as input. The comprehensive examination in Figure 6.12 offers a sophisticated comprehension of testing durations and predictive precision across different regression models. This analysis gives useful insights for selecting and optimizing models to predict RDX concentration.

After carefully analyzing the parameters such as slope, intercept, RMSE and testing time for all the models in combination with diverse input data, it is clear that finding a single model or combination that consistently predicts all parameters accurately is challenging. The intricacy of selecting the best model for all characteristics presents difficulties in defining the superior analysis protocol. In order to simplify and make this process of making decisions more efficient, a comprehensive indicator known as the "regression index" is proposed. The index combines all pertinent parameters, resulting in a numerical number that acts as a definitive criterion for choosing the most efficient analysis protocol. The regression index can be defined as,

$$Regression\ Index = \frac{1}{|1 - Slope| \times |Intercept| \times RMSE \times Testing\ time\ (ms)} \tag{6.4}$$

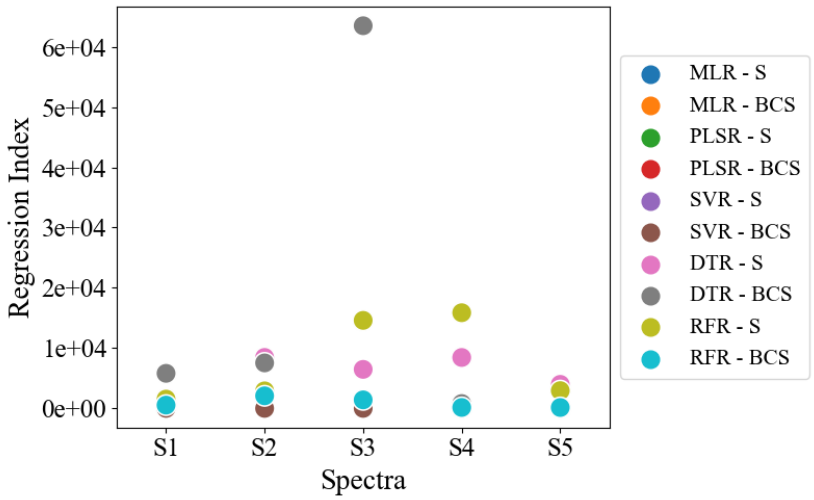

Figure 6.13. Regression indices obtained from all the analyses. S represents spectra without background correction and BCS represents background corrected spectra.

A higher regression index indicates superior performance across multiple metrics, including slope, intercept, RMSE, and testing time. Figure 6.13 displays the regression index achieved

for all approaches. The figure shows that using S3 of the background-corrected spectra as input to the DTR model produces the best results from all aspect.

In the present study, only RDX, AN, and their mixtures were considered for the Raman experiment, followed by regression analysis. However, in a real-life scenario, only a mixture sample will be available, and the matrix elements will be unknown. The sample can be a mixture of two, three, or many materials, including some explosives and some non-explosives. In such cases, the detection becomes more challenging as the first step is determining how many materials are mixed and what they are. The materials present in the mixture can be identified based on the peaks from the Raman spectra of mixtures. However, some materials can have a high similarity in the Raman spectra due to some common vibrational signatures. In such cases, other statistical and analytical techniques, like correlation, ordinary least squares, etc., may be used for the identification of matrix elements in a mixture.

6.6 Summary

This chapter presents a robust framework for the accurate detection of explosives in mixtures by using a portable Raman spectroscopic setup combined with machine learning techniques. In order to carry out the experiment, pure RDX and AN and their mixtures with different weight ratios were considered. Using a cost-effective portable Raman spectroscopic setup, spectra were recorded and analyzed by using both univariate and multivariate regression techniques.

For the univariate analysis, SLR was employed on both raw and background-corrected spectra. The input for the SLR model was the peak height of the prominent Raman peaks of RDX and AN. Nevertheless, SLR demonstrated unsatisfactory predictive outcomes. Afterward, different multivariate regression models such as MLR, PLSR, SVR, DTR, and RFR were deployed. At first, the inputs consisted of entire spectra, both with and without background correction were considered and significantly higher predictive accuracy obtained in comparison to univariate techniques.

To improve the analysis efficiency with retaining higher accuracy, various manual feature selection approaches were considered for the multivariate approaches. Nevertheless, no noticeable accuracy improvement was observed after feature selection. Furthermore, the application of background correction did not have a substantial effect on the accuracy of prediction. Of all the methods examined, using simply the RDX peaks (S4) as input for the RFR model resulted in the highest level of accuracy. However, after evaluating multiple

factors such as slope, intercept, and testing time. it was observed that the DTR model using S3 with background correction is the most effective strategy.

To summarize, this chapter demonstrates the efficacy of a portable Raman spectroscopic device for accurate identification and quantification of explosives in mixtures. This technology has significant potential for use in homeland security and military applications.

6.7 References

[1] R. Junjuri, A.P. Gummadi, M.K. Gundawar, Single-shot compact spectrometer based standoff LIBS configuration for explosive detection using artificial neural networks, Optik (Stuttg). 204 (2020) 163946.

[2] K.K. Gulati, S. Gulia, T. Gambhir, N. Kumar, V. Gambhir, M.N. Reddy, Standoff detection and identification of explosives and hazardous chemicals in simulated real field scenario using time gated Raman spectroscopy, Def. Sci. J. 69 (2019) 342–347.

[3] C.M. Wynn, S. Palmacci, R.R. Kunz, M. Rothschild, Noncontact detection of homemade explosive constituents via photodissociation followed by laser-induced fluorescence, Opt. Express. 18 (2010) 5399–5406.

[4] M.R. Leahy-Hoppa, M.J. Fitch, R. Osiander, Terahertz spectroscopy techniques for explosives detection, Anal. Bioanal. Chem. 395 (2009) 247–257.

[5] C. Bauer, A.K. Sharma, U. Willer, J. Burgmeier, B. Braunschweig, W. Schade, S. Blaser, L. Hvozdara, A. Müller, G. Holl, Potentials and limits of mid-infrared laser spectroscopy for the detection of explosives, Appl. Phys. B. 92 (2008) 327–333.

[6] W. Zhu, B.-Y. Wen, L.-J. Jie, X.-D. Tian, Z.-L. Yang, P.M. Radjenovic, S.-Y. Luo, Z.-Q. Tian, J.-F. Li, Rapid and low-cost quantitative detection of creatinine in human urine with a portable Raman spectrometer, Biosens. Bioelectron. 154 (2020) 112067.

[7] M. Gnyba, J. Smulko, A. Kwiatkowski, P. Wierzba, Portable Raman spectrometer-design rules and applications, Bull. Polish Acad. Sci. Tech. Sci. 59 (2011) 325–329.

[8] M. Gaft, L. Nagli, UV gated Raman spectroscopy for standoff detection of explosives, Opt. Mater. (Amst). 30 (2008) 1739–1746.

[9] D. Wang, P. He, Z. Wang, G. Li, N. Majed, A.Z. Gu, Advances in single cell Raman spectroscopy technologies for biological and environmental applications, Curr. Opin. Biotechnol. 64 (2020) 218–229.

[10] M. Petersen, Z. Yu, X. Lu, Application of raman spectroscopic methods in food safety: a review, Biosensors. 11 (2021) 187.

[11] K.K. Gulati, V. Gambhir, M.N. Reddy, Detection of nitro-aromatic compound in soil and sand using time gated Raman spectroscopy, Def. Sci. J. 67 (2017) 588.

[12] K.K. Gulati, T. Gambhir, N. Kumar, V. Gambhir, Standoff detection of liquid explosives and hazardous chemicals concealed in translucent plastic bottles using nanoseconds time gated Raman spectroscopy, Def. Sci. J. 69 (2019) 342.

[13] D. Diaz, D.W. Hahn, Raman spectroscopy for detection of ammonium nitrate as an explosive precursor used in improvised explosive devices, Spectrochim. Acta Part A Mol. Biomol. Spectrosc. 233 (2020) 118204.

[14] C. Byram, S.S.B. Moram, V.R. Soma, SERS based detection of multiple analytes from dye/explosive

mixtures using picosecond laser fabricated gold nanoparticles and nanostructures, Analyst. 144 (2019) 2327–2336.

[15] A. Hakonen, P.O. Andersson, M.S. Schmidt, T. Rindzevicius, M. Käll, Explosive and chemical threat detection by surface-enhanced Raman scattering: A review, Anal. Chim. Acta. 893 (2015) 1–13.

[16] B.A. Eckenrode, E.G. Bartick, S.D. Harvey, M.E. Vucelick, B.W. Wright, R.A. Huff, Portable Raman spectroscopy systems for field analysis, Forensic Sci. Commun. 3 (2001).

[17] N. Nuntawong, P. Eiamchai, S. Limwichean, B. Wong-Ek, M. Horprathum, V. Patthanasettakul, A. Leelapojanaporn, S. Nakngoenthong, P. Chindaudom, Trace detection of perchlorate in industrial-grade emulsion explosive with portable surface-enhanced Raman spectroscopy, Forensic Sci. Int. 233 (2013) 174–178.

[18] J.D. Santillán, C.D. Brown, W. Jalenak, Advances in Raman spectroscopy for explosive identification in aviation security, in: Opt. Photonics Glob. Homel. Secur. III, SPIE, 2007: pp. 124–131.

[19] R. Gillibert, J.Q. Huang, Y. Zhang, W.L. Fu, M.L. de La Chapelle, Explosive detection by surface enhanced Raman scattering, TrAC Trends Anal. Chem. 105 (2018) 166–172.

[20] R.J. Harper, J.R. Almirall, K.G. Furton, Identification of dominant odor chemicals emanating from explosives for use in developing optimal training aid combinations and mimics for canine detection, Talanta. 67 (2005) 313–327. https://doi.org/10.1016/j.talanta.2005.05.019.

[21] C.L. Mader, Equation of state for nonideal explosives.[For ammonium nitrate-loaded RDX and TNT explosives], Los Alamos National Lab.(LANL), Los Alamos, NM (United States), 1975.

[22] J. Hershkowitz, J. Rigdon, P.A.D. NJ, Evaluation by a Modified Cylinder Test of Metal Acceleration by Non-Ideal Explosives Containing Ammonium Nitrate, Picatinny Arsenal, Dover, New Jersey, Tech. Rep. 4611 (1974).

[23] I. Akst, J. Hershkowitz, Explosive performance modification by cosolidification of ammonium nitrate with fuels, Picatinny Arsenal, Dover, NJ, Picatinny Arsenal Tech. Rep. 4987 (1976).

[24] R. Infante-Castillo, L.C. Pacheco-Londoño, S.P. Hernández-Rivera, Monitoring the $\alpha \rightarrow \beta$ solid–solid phase transition of RDX with Raman spectroscopy: A theoretical and experimental study, J. Mol. Struct. 970 (2010) 51–58.

[25] M. Tranmer, M. Elliot, Multiple linear regression, Cathie Marsh Cent. Census Surv. Res. 5 (2008) 1–5.

[26] F. Chen, C. Chen, W. Li, M. Xiao, B. Yang, Z. Yan, R. Gao, S. Zhang, H. Han, C. Chen, Rapid detection of seven indexes in sheep serum based on Raman spectroscopy combined with DOSC-SPA-PLSR-DS model, Spectrochim. Acta Part A Mol. Biomol. Spectrosc. 248 (2021) 119260.

[27] S. Guo, R. Heinke, S. Stöckel, P. Rösch, J. Popp, T. Bocklitz, Model transfer for Raman-spectroscopy-based bacterial classification, J. Raman Spectrosc. 49 (2018) 627–637.

[28] K.H. Wong, V. Razmovski-Naumovski, K.M. Li, G.Q. Li, K. Chan, The quality control of two Pueraria species using Raman spectroscopy coupled with partial least squares analysis, J. Raman Spectrosc. 46 (2015) 361–368.

[29] M.A. Flórez, J.E. Guerrero, R. Cabanzo, E. Mejía-Ospino, SARA analysis and Conradson carbon residue prediction of Colombian crude oils using PLSR and Raman spectroscopy, J. Pet. Sci. Eng. 156 (2017) 966–970.

[30] P. Li, J. Ma, N. Zhong, Raman spectroscopy combined with support vector regression and variable

selection method for accurately predicting salmon fillets storage time, Optik (Stuttg). 247 (2021) 167879.

[31] K. Noack, B. Eskofier, J. Kiefer, C. Dilk, G. Bilow, M. Schirmer, R. Buchholz, A. Leipertz, Combined shifted-excitation Raman difference spectroscopy and support vector regression for monitoring the algal production of complex polysaccharides, Analyst. 138 (2013) 5639–5646.

[32] S. XuanYuan, H. Hao, C. Hu, J. Lan, T. Song, C. Xie, Quantitative analysis of solid and liquid contents in reactive crystallization by in-situ Raman with support vector regression, J. Cryst. Growth. 587 (2022) 126641.

[33] Y. Chen, Y. Su, L. Ou, C. Zou, Z. Chen, Classification of nasopharyngeal cell lines (C666-1, CNE2, NP69) via Raman spectroscopy and decision tree, Vib. Spectrosc. 80 (2015) 24–29.

[34] W. Gao, L. Zhou, S. Liu, Y. Guan, H. Gao, B. Hui, Machine learning prediction of lignin content in poplar with Raman spectroscopy, Bioresour. Technol. 348 (2022) 126812.

[35] X. Du, P. Wang, L. Fu, H. Liu, Z. Zhang, C. Yao, Determination of chlorpyrifos in pears by Raman spectroscopy with random forest regression analysis, Anal. Lett. 53 (2020) 821–833.

[36] A. Amjad, R. Ullah, S. Khan, M. Bilal, A. Khan, Raman spectroscopy based analysis of milk using random forest classification, Vib. Spectrosc. 99 (2018) 124–129.

[37] M. Li, Y. Xu, J. Men, C. Yan, H. Tang, T. Zhang, H. Li, Hybrid variable selection strategy coupled with random forest (RF) for quantitative analysis of methanol in methanol-gasoline via Raman spectroscopy, Spectrochim. Acta Part A Mol. Biomol. Spectrosc. 251 (2021) 119430.

[38] S. Khan, R. Ullah, A. Khan, A. Sohail, N. Wahab, M. Bilal, M. Ahmed, Random forest-based evaluation of Raman spectroscopy for dengue fever analysis, Appl. Spectrosc. 71 (2017) 2111–2117.

[39] A. Shrivastava, V.B. Gupta, Methods for the determination of limit of detection and limit of quantitation of the analytical methods, Chron. Young Sci. 2 (2011) 21–25.

Intentional Blank Page

Chapter 7

Conclusion and Future Scope

This chapter presents the summary of the inferences derived from the research carried out in the thesis, while also delineating the future exploration of the work. The initial work focuses on developing a new method for elemental analysis using LIBS and understanding the dependence of plasma parameters on the material hardness. Furthermore, the investigation expands into the domain of machine learning combined with LIBS for the identification/classification of explosives and post-consumer plastics, with the objective of implementing them in real-time scenarios. Finally, the chapter presents a way of quantitatively detecting explosive mixtures by combining Raman spectroscopy with machine learning techniques. This novel methodology offers improved accuracy and effectiveness in identifying compositions, hence enhancing capabilities in homeland security and the military. The chapter covers a range of investigations, providing valuable insights into the current state of study. It also paves the way for future improvements and explorations in the integration of spectroscopic analysis and machine learning. The research aims to expand the limits of knowledge and practical applications in several domains, such as materials science and national security, by strategically combining scientific investigation and technology advancement.

7.1 Conclusion

The thesis focuses on the fundamental studies of LIBS towards development of Simplified LIBS-based Intensity-ratio approach for Concentration Estimation (SLICE) and harnessing machine learning for the classification of materials such as explosives and post-consumer plastics. It also discusses the dependence of various plasma parameters on the hardness of materials. Moreover, it delves into the applications of machine learning in Raman spectroscopy, aiming for the quantitative detection of explosives in mixtures. The following are the major conclusion of the thesis work.

1. In Chapter 3, a new method based on LIBS was proposed for elemental analysis, namely the SLICE. For the experiment, two Cu-based alloy samples, one binary and one ternary, were considered. A detailed study of thermodynamic equilibrium was provided, along with the calculation of plasma parameters and plasma decay parameters (PDPs). The temporal dynamics of LIP were thoroughly investigated by modeling the temporal decay of plasma temperature and intensity ratio, providing valuable insights into plasma behavior. The elemental analysis was performed using SLICE, CF-LIBS and EDS. The elemental concentrations estimated by SLICE showed remarkable consistency with those obtained using CF-LIBS and EDS. Furthermore, the chapter briefly explored the advantages and limitations of the SLICE technique in comparison with CF-LIBS. The SLICE has remarkable advantages over CF-LIBS as it can offset the major bottlenecks for elemental analysis using LIBS. *[A part this published in Applied Spectroscopy,2022 [1]].*
2. Chapter 4 explores the significance of material hardness, providing a profound understanding of diverse industrial applications. Material hardness is an essential characteristic that determines how resistant a material is to deformation, indentation, and penetration. It is critical for building components and structures that are trustworthy. The chapter provides a thorough examination emphasizing the growing need for non-invasive techniques than the conventional approaches, particularly in difficult conditions. LIBS has been used to understand the dependence of various plasma parameters on material hardness. The experiment involves five iron-based alloy samples with same elemental composition and different hardness. The study investigates the correlation of plasma parameters, plasma decay parameters, and surface morphology in relation to changes in material hardness. The results demonstrate a constant linear relationship between the hardness of the material and the temperature of the plasma, the density of electrons, and the initial temperature of the plasma. In addition, the analysis reveals a linear decrease in

the radiative decay constant as the hardness increases. The chapter concludes by analyzing the correlation between crater diameter and material hardness, finding a consistent reduction in crater size as material hardness increases. This study improves the comprehension of the complex interactions between laser-induced plasma properties and material hardness.

3. Chapter 5 explores the integration of LIBS with machine learning techniques for effective detection of explosives and classification of post-consumer plastics. It describes the utilization of a picosecond LIBS (psLIBS) system, equipped with a low-cost CCD spectrometer, for real-time applications. The study employs a systematic approach to combine ANN with various feature selection and extraction approaches. This integration aims to enhance accuracy, decrease computational time, and optimize resource allocation.

   The initial sections of this chapter involve the detection of explosives, where five explosive and twelve non-explosive samples were considered. In this case, two approaches were considered. Initially, each sample underwent scrutiny to ascertain its classification as either explosive or non-explosive. Subsequently, samples identified as explosive underwent a secondary classification process to determine their specific type. Among various feature selection approaches, ANN combined with LDA feature extraction achieved a flawless 100% accuracy for classifying between explosive and non-explosive. In the case of classification within explosives, maximum accuracy (99.8%) was obtained for full spectrum and manual feature selection with peak area.

   For the identification of post-consumer plastics, two sets of samples were considered. Firstly, nine different post-consumer plastics were collected from a local recycling unit, and both training and testing was performed on the same sample. PCA with 30 PCs as input to the ANN model represents the best classification in terms of accuracy, computational time and storage requirement. Nevertheless, this technique is not suitable for real-time application since in real-time scenario samples that are unknown to the trained model will be encountered. To address this, another study was performed on a set of 30 post-consumer plastics representing six commonly used types (HDPE, LDPE, PP, PET, PS, and PVC). Five samples from each category were collected from garbage and testing was performed on unknown plastic, mimicking real-world scenarios for identifying unfamiliar post-consumer plastics. 29 samples out of 30 are utilized for training and validation purposes, while the 30th sample, which is unfamiliar to the network, is employed for testing. Here, ANN fails to classify between HDPE, LDPE, and PP, even using various feature selection and extraction approaches due to their high degree of

similarity in chemical and spectral signatures. Therefore, by considering these three plastics as a single group, results show classification with a high degree of confidence with many feature selection and extraction approaches. In particular, LDA feature extraction with 3 LDs as input to the ANN was found to have the best results in terms of accuracy, computation time, and storage.

By comparing two approaches considered for discrimination of plastics, better results obtained in the former case where the training and testing were performed on the same sample. However, this approach is meaningless in terms of real-time application as the testing samples will be completely unknown to the training model. Therefore, the second approach represents the real-time application scenario, but it fails to distinguish between three categories of plastics out of six. Therefore, in real-time scenario, this technique can be used to differentiate between HLP (HDPE, LDPE & PP), PET, PS, and PVC. The classification between HDPE, LDPE and PP can performed by using the conventional technique for the time being. This will reduce the workforce requirement by half as three plastic categories out of six can be sorted efficiently.

4. Chapter 6 demonstrates a compact portable Raman spectroscopic tool for quantitative detection of constituent explosives in a binary mixture using machine learning. For the experiment, two samples (1,3,5-trinitroperhydro-1,3,5-triazine (RDX) and ammonium nitrate (AN)) were considered and mixed at different weight percentages. Various regression models such as linear regression, partial least square regression (PLSR), support vector regression (SVR), decision tree regression (DTR) and random forest regression (RFR) were employed to quantify the amount of RDX and AN. The Raman spectra were analyzed with and without background correction. Further, various feature/variable selection strategies were explored to find out the best analysis protocol. The analyses show that the background correction of the spectra does not improve the accuracy significantly. Among various feature selection techniques in conjunction with various regression models, RDX peaks as input for the RFR model yield the best result in terms of accuracy. However, after considering multiple factors such as slope, intercept, and testing time, it was observed that the DTR model using only peak areas with background correction is the most optimal strategy. The results demonstrate that Raman spectroscopy combined with machine learning can be used as a reliable, compact, and fast tool for the real-time investigation of explosive mixtures. *[A part this published in Journal of Optics,2023 [2]]*

7.2 Future Scope

1. The thesis presents SLICE, a novel approach for elemental analysis, with a particular focus on its pilot study and experimental verification using alloy samples with bulk elemental composition. The current study is an initial investigation that emphasizes the ability of the technique to be applied to a wide range of materials with different matrix elements and compositions, including trace elements. This suggests that the method has promise for broader use. The thesis promotes additional exploration of the capabilities of SLICE, highlighting the importance of thorough comprehension and validation to fully unleash its potential in elemental analysis.

   Further the SLICE is based on the radiative relaxation mechanism of the laser induced plasma where the collisional decay is considered negligible. However, at the initial stage of the plasma relaxation, the plasma will show radiative decay only as the shockwave protects the plasma from the interaction of environmental atoms with the plasma emissions. But with time, the shockwave becomes weak gradually due to expansion which allows the outside atoms to interact with the atoms/ions of the plasma resulting in collisional decay. Thus, considering the temporal range where the contribution of collisional decay is negligible, the elemental analysis can be performed with better accuracy and precision; hence, optimization of the temporal window is important. Also, optimization of other parameters like ambient gas and pressure are important as they affect the broadening of spectral lines and plasma relaxation [3,4]. Therefore, future work can be devoted to optimize different parameters like the temporal window for data acquisition, ambient gas, and pressure, etc.
2. Comprehending the relationship between plasma parameters and material hardness is a significant area of focus in LIBS research. This is particularly important due to the increasing need for non-invasive and remote methods of testing hardness, especially in demanding settings like space shuttles, TOKAMAKs, nuclear power plant vessels, etc. [5]. This thesis investigates the correlation between plasma parameters, plasma decay features, and surface morphology in relation to changes in material hardness. Although the initial findings show promise, discrepancies noted by other researchers necessitate further investigation. To get more understanding, expanding the study to encompass a larger and more diverse sample set, encompassing a wider range of hardness values, could yield more profound insights into this correlation. In addition, expanding the range of materials used beyond alloys could provide a more thorough comprehension of the phenomena, thereby enhancing the practicality and resilience of hardness testing procedures based on LIBS.

3. In the domain of explosive detection using LIBS, the combination of machine learning, feature selection, and extraction has shown remarkable accuracy. However, the current limitation of this study is its inability to be applied in real-time situations. This analysis was performed on a restricted collection of explosive samples, with both training and testing performed on the same sample due to constraints in sample availability. In order to improve practicality, future research efforts could encompass a wider variety of both explosive and non-explosive samples, extending analysis to unknown samples to mimic real-time scenarios effectively. Furthermore, enhancing the efficiency of the equipment configuration shows potential for practical implementation in the field, with possible approaches including reducing size and lowering expenses. Contemporary, small-sized, and economical lasers that are easily accessible at present offer practical choices. Additionally, incorporating data collection and processing into microcontrollers such as Arduino or Raspberry Pi could simplify operations and reduces size and cost, making it easier to deploy and use in real-life scenarios.
4. A significant problem that persists is enhancing the ability to identify different types of plastics is classifying between HDPE, LDPE, and PP, using LIBS, especially when dealing with unknown samples. In order to improve the accuracy of classification, future research can incorporate advanced machine learning classifiers such as convolutional neural networks (CNN) and extreme gradient boosting (XGBoost). Additionally, additional statistical methods like genetic algorithms (GA), successive projection algorithms (SPA), stepwise formulations (SW), analysis of variance (ANOVA), etc. can be utilized for feature selection and feature extraction. Furthermore, the investigation of data fusion approaches through the integration of LIBS with complementary technologies such as Raman spectroscopy has the potential to provide improved plastic sorting capabilities. Investigations should encompass a wider variety of samples, such as e-waste, in order to fully explore its potential for reuse. Additionally, it is important to consider the effects of additives on the accuracy and measurement of categorization in industrial applications. It is essential to consider practical factors, such as the implementation of laser beam cleaning shots to eliminate dust and debris for immediate measurements, as well as the optimization of sample transportation using a conveyor belt model, in order to conduct real-time investigations effectively. In addition, utilizing microcontrollers such as Arduino and Raspberry Pi for the purpose of recording, analyzing, and making decisions based on data

can make the system cost-efficient and small in size, thereby making it more suitable for real-time applications.

5. Finally, for quantitative detection of explosives, mixture samples of RDX and AN were considered followed by regression analyses. However, in a real-life scenario, only a mixture sample will be available, and the matrix elements will be unknown. The sample can be a mixture of two, three, or many materials, including some explosives and some non-explosives. In such cases, the detection becomes more challenging as the first step is determining how many materials are mixed and what they are. The materials present in the mixture can be identified based on the peaks from the Raman spectra of mixtures. However, some materials can have a high similarity in the Raman spectra due to some common vibrational signatures. In such cases, other statistical and analytical techniques, like correlation, ordinary least squares, etc., may be used for the identification of matrix elements in a mixture. Moreover, extending the same study to incorporate LIBS presents a promising avenue, given its rapidity, robust signal acquisition capabilities, minimal or negligible sample preparation requirements, and ability to conduct standoff measurements. LIBS emerges as a potential tool for such investigations, offering unique advantages that align well with the demands of the research objectives.

7.3 Reference

[1] A.K. Tarai, R. Junjuri, S.A. Rashkovskiy, M.K. Gundawar, Time-Dependent Intensity Ratio-Based Approach for Estimating the Temperature of Laser Produced Plasma, Appl. Spectrosc. (2022) 00037028221117534.

[2] A.K. Tarai, M.K. Gundawar, Raman spectroscopy combined with machine learning for the quantification of explosives in mixtures, J. Opt. (2023) 1–9.

[3] E.J. Kautz, A. Xu, A. V Harilal, M.P. Polek, A.M. Casella, D.J. Senor, S.S. Harilal, Influence of ambient gas on self-reversal in Li transitions relevant to isotopic analysis, Opt. Express. 31 (2023) 3549–3564.

[4] S.S. Harilal, M.C. Phillips, D.H. Froula, K.K. Anoop, R.C. Issac, F.N. Beg, Optical diagnostics of laser-produced plasmas, Rev. Mod. Phys. 94 (2022) 35002.

[5] A.H. Galmed, O. Balachninaite, O.A. Nassef, Effect of laser pulse duration on relative hardness estimation using LIBS, Opt. Laser Technol. 161 (2023) 109184.

Intentional Blank Page

List of Publications

1. **Tarai, A. K.,** Rashkovskiy, S. A., & Gundawar, M. K. Simplified LIBS- based intensity-ratio approach for concentration estimation (SLICE): an approach for elemental analysis using laser induced breakdown spectroscopy. **Optics Express (In Press)**. **(Chapter 3)**
2. **Tarai, A. K.,** Junjuri, R., Dhobley, A., & Gundawar, M. K. (2023). Classification of human tooth using laser-induced breakdown spectroscopy combined with machine learning. **Journal of Optics**, 1-11.
3. **Tarai, A. K.,** & Gundawar, M. K. (2023). Raman spectroscopy combined with machine learning for the quantification of explosives in mixtures. **Journal of Optics**, 1-9. **(Chapter 6)**
4. **Tarai, A. K.,** Junjuri, R., Rashkovskiy, S. A., & Gundawar, M. K. (2022). Time- Dependent Intensity Ratio-Based Approach for Estimating the Temperature of Laser Produced Plasma. **Applied Spectroscopy**, 76(11), 1300-1306. **(Chapter 3)**
5. **Tarai, A. K.,** & Gundawar, M. K. (2022). Possibility of Plastic Discrimination using Picosecond Laser Induced Breakdown Spectroscopy. In 2022 Workshop on Recent Advances in Photonics (WRAP) (pp. 1-2). **IEEE**. **(Chapter 5)**
6. **Tarai, A. K.,** Junjuri, R., & Gundawar, M. K. (2021). Advances in applications of LIBS in India: A Review. **Asian Journal of Physics**, 30(6), 871-888.

Co-authored Publications

7. John, B., Joseph, G., Aryadevi, G., **Tarai, A. K.,** Gundawar, G. M. K., Navya, S., & Ginson, P. J. (2024). Tweaking Bis Thiourea Cadmium Chloride single crystals for Optoelectronic applications by L-Valine. **Journal of Materials Science: Materials in Electronics,** 35(135).

8. Gupta, V., Rai, A. K., Kumar, T., **Tarai, A.,** Gundawar, G. M. K., & Rai, A. K. (2023). Compositional analysis of copper and iron-based alloys using LIBS coupled with chemometric method. **Analytical Sciences**, 1-13.

9. Gupta, V., Rai, A. K., Kumar, R., **Tarai, A. K.,** Gundawar, M. K., & Rai, A. K. (2023). Compositional quantification of binary ternary and quaternary metallic alloy-based coins using laser-induced breakdown spectroscopy. **Journal of Optics**, 52(3), 1245-1257.

10. Gazali, Z., Gupta, V., Kumar, T., Kumar, R., **Tarai, A. K.,** Rai, P. K., ... & Rai, A. K. (2023). Effect of mineral elements on the formation of gallbladder stones using spectroscopic techniques. **Analytical and Bioanalytical Chemistry**, 1-11.

11. Dubey, D., Kumar, R., Gupta, V., **Tarai, A. K.,** Gundawar, M. K., & Rai, A. K. (2022). Investigation of Hazardous Materials in Firecrackers using LIBS Coupled with a Chemometric Method and FTIR Spectroscopy. **Defence Science Journal**, 72(4), 618.

12. Mishra, P., Kumar, R., **Tarai, A. K.,** Kumar, M., & Rai, A. K. (2022). Characterization of toxic substances present in smoking tobacco using different spectroscopic techniques. **Journal of Laser Applications**, 34(2).

13. Junjuri, R., **Tarai, A. K.,** Dhobley, A., & Gundawar, M. K. (2019). Identification of the calcified tissues using laser induced breakdown spectroscopy. In 2019 Workshop on Recent Advances in Photonics (WRAP) (pp. 1-3). **IEEE**.

Awards/Achievements

1. **Science and Engineering Research Board – International Travel Scheme (SERB – ITS)** sanctioned to attend "12th Euro-Mediterranean Symposium on Laser-induced Breakdown Spectroscopy (EMS LIBS 2023)" held at Porto, Portugal during 4 – 7th Sep 2023.
2. **Institute of Eminence – University of Hyderabad – International Travel Grant (IoE – UoH – ITG)** received to attend "XII Laser Induced Breakdown Spectroscopy (LIBS 2022)" held at Bari, Italy during 5 – 9th Sep 2022.
3. **Best Poster Award** received for presenting work entitled "Laser induced breakdown spectroscopy combined with machine learning: An efficient tool for plastic waste sorting", at Frontiers in Physics (FIP 2023), organized by University of Hyderabad, Hyderabad, India during 3 – 4th Mar 2023.

Workshops/Schools selected

1. "Machine learning workshop 2022" organized by University of Hyderabad, India during 26 – 28th Oct 2022.
2. "National Workshop on Explosive Detection (NWED 2020)" organized by High Energy Materials Research Laboratory (HEMRL), Pune, India during 1 – 2nd Mar 2020.
3. "Workshop on advances in optics and photonics 2019" organized by University of Hyderabad, India during 18 – 23rd Mar 2019.
4. "Workshop on photonics for detonics 2019" organized by Terminal Ballistics Research Laboratory (TBRL), Chandigarh, India during 1 – 2nd Mar 2019.

Conference presentations (National and International)

1. **Poster presentation** entitled "Laser induced breakdown spectroscopy combined with machine learning: An efficient tool for plastic waste sorting" at "Frontiers in Physics (FIP 2023)" organized by University of Hyderabad, Hyderabad, India during 3 – 4th Mar 2023.
2. **Poster presentation** entitled "Effect of feature selection and extraction in identification of post-consumer plastics using picosecond laser induced breakdown spectroscopy" at "XII Laser Induced Breakdown Spectroscopy (LIBS 2022)" held at Bari, Italy during 5 – 9th Sep 2022.
3. **Poster presentation** entitled "Quantitative estimation of ammonium nitrate in mixtures using portable Raman spectroscopy" at "13th International High Energy Materials Conference & Exhibits (HEMCE 2022)" organized by Terminal Ballistics Research Laboratory (TBRL), Chandigarh, India during 26 – 28th May 2022.
4. **Poster presentation** entitled "Possibility of Plastic Discrimination using Picosecond Laser Induced Breakdown Spectroscopy" at "5th IEEE Workshop on Recent Advances in Photonics (WRAP 2022)" held at Mumbai, India (Virtual) during 4 – 6th Mar 2022.
5. **Contributed Oral Presentation** entitled "Estimation of radiation decay constant of laser produced brass plasma from its emission intensities" at 47th IEEE International Conference on Plasma Science (ICOPS 2020) held at Singapore (Virtual) during 6 – 10th Dec 2020.
6. **Poster presentation** entitled "Standoff detection of explosives using laser induced breakdown spectroscopy" at "12th International High Energy Materials Conference & Exhibits (HEMCE 2019)" organized by Indian Institute of Technology Madras (IIT – Madras), Chennai, India during 16 – 18th Dec 2019.

Development of a novel LIBS-based Technique for Elemental Analysis and Harnessing Machine Learning for Real-time Applications using LIBS and Raman Spectroscopy

by Akash Kumar Tarai

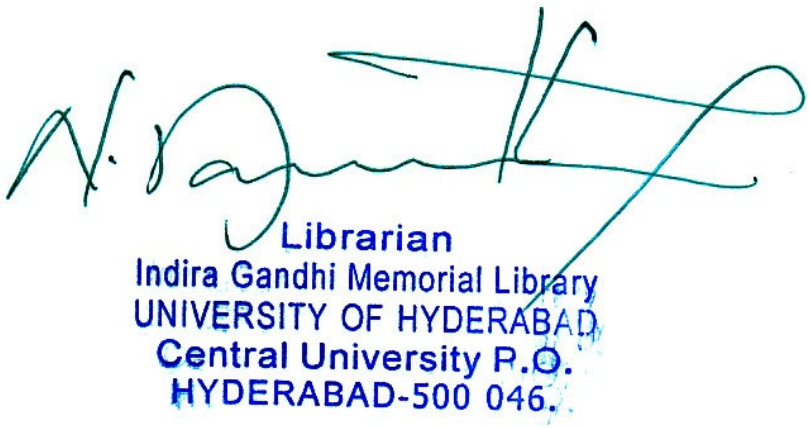

Development of a novel LIBS-based Technique for Elemental Analysis and Harnessing Machine Learning for Real-time Applications using LIBS and Raman Spectroscopy

ORIGINALITY REPORT

19%	5%	17%	3%
SIMILARITY INDEX	INTERNET SOURCES	PUBLICATIONS	STUDENT PAPERS

PRIMARY SOURCES

1	Akash Kumar Tarai, Manoj Kumar Gundawar. "Raman spectroscopy combined with machine learning for the quantification of explosives in mixtures", Journal of Optics, 2023 Publication	7%
2	Akash Kumar Tarai, Rajendhar Junjuri, Sergey A. Rashkovskiy, Manoj Kumar Gundawar. "Time Dependent Intensity Ratio-Based Approach for Estimating Temperature of Laser Produced Plasma", Applied Spectroscopy, 2022 Publication	2%
3	Submitted to University of Hyderabad, Hyderabad Student Paper	1%
4	Akash Kumar Tarai, Rajendhar Junjuri, Sergey A. Rashkovskiy, Manoj Kumar Gundawar. "Time-Dependent Intensity Ratio-Based	1%

Prof. G. MANOJ KUMAR
ACRHEM
DRDO Industry Academic
Centre of Excellence (DIA-COE)
School of Physics
University of Hyderabad
Hyderabad-500 046. Telangana, INDIA.

1/5

Prof. G. MANOJ KUMAR
ACRHEM
DRDO Industry Academic
Centre of Excellence (DIA-COE)
School of Physics
University of Hyderabad
Hyderabad-500 046. Telangana, INDIA.

2/5

Prof. G. MANOJ KUMAR
ACRHEM
DRDO Industry Academic
Centre of Excellence (DIA-COE)
School of Physics
University of Hyderabad
Hyderabad-500 046. Telangana, INDIA.

3/5

Prof. G. MANOJ KUMAR
ACRHEM
DRDO Industry Academic
Centre of Excellence (DIA-COE)
School of Physics
University of Hyderabad
Hyderabad-500 046. Telangana, INDIA.

4/5

It is certified that S.nos 1-5 are Student's own publications.

Prof. G. MANOJ KUMAR
ACRHEM
DRDO Industry Academic
Centre of Excellence (DIA-COE)
School of Physics
University of Hyderabad
Hyderabad-500 046. Telangana, INDIA.

Approach for Estimating the Temperature of Laser Produced Plasma", Applied Spectroscopy, 2022
Publication

5	Akash Kumar Tarai, Manoj Kumar Gundawar. "Possibility of Plastic Discrimination using Picosecond Laser Induced Breakdown Spectroscopy", 2022 Workshop on Recent Advances in Photonics (WRAP), 2022 Publication	1 %
6	epdf.tips Internet Source	<1 %
7	"Laser Induced Breakdown Spectroscopy (LIBS)", Wiley, 2023 Publication	<1 %
8	Humera Ghani, Shahram Salekzamankhani, Bal Virdee. "Chapter 32 Critical Analysis of 5G Networks' Traffic Intrusion Using PCA, t-SNE, and UMAP Visualization and Classifying Attacks", Springer Science and Business Media LLC, 2024 Publication	<1 %
9	Rajendhar Junjuri, Manoj Kumar Gundawar. "A low-cost LIBS detection system combined with chemometrics for rapid identification of plastic waste", Waste Management, 2020 Publication	<1 %

10	Rajendhar Junjuri, Sergey A. Rashkovskiy, Manoj Kumar Gundawar. "Dependence of radiation decay constant of laser produced copper plasma on focal position", Physics of Plasmas, 2019 Publication	<1 %
11	pubs.rsc.org Internet Source	<1 %
12	Rajendhar Junjuri, Akash Kumar Tarai, Arun Prakash G, Akshay Dhobley, Manoj Kumar Gundawar. "Identification of the calcified tissues using laser induced breakdown spectroscopy", 2019 Workshop on Recent Advances in Photonics (WRAP), 2019 Publication	<1 %
13	www.mdpi.com Internet Source	<1 %
14	Ting-Yu Huang, Jorn Chi Chung Yu. "Development of Crime Scene Intelligence Using a Hand-Held Raman Spectrometer and Transfer Learning", Analytical Chemistry, 2021 Publication	<1 %
15	David A. Cremers, Leon J. Radziemski. "Handbook of Laser-Induced Breakdown Spectroscopy", Wiley, 2013 Publication	<1 %

16	Bitto John, Geethu Joseph, Aryadevi G., Manoj Kumar Gundawar, Akash Kumar Tarai, Navya Shaji, Ginson P. Joseph. "l-valine refines bis(thiourea) cadmium chloride single crystals for optoelectronic applications", Journal of Materials Science: Materials in Electronics, 2024 Publication	<1 %
17	U.K. Adarsh, V.B. Kartha, C. Santhosh, V.K. Unnikrishnan. "Spectroscopy: A Promising Tool for Plastic Waste Management", TrAC Trends in Analytical Chemistry, 2022 Publication	<1 %
18	mdpi-res.com Internet Source	<1 %
19	Rajendhar Junjuri, Chi Zhang, Ishan Barman, Manoj Kumar Gundawar. "Identification of post-consumer plastics using laser-induced breakdown spectroscopy", Polymer Testing, 2019 Publication	<1 %
20	Jianming Ding, Tianlong Zhang, Hua Li. "Recent advances in laser-induced breakdown spectroscopy for explosive analysis", TrAC Trends in Analytical Chemistry, 2023 Publication	<1 %
21	eprints.kfupm.edu.sa Internet Source	

		<1%
22	www.science.gov Internet Source	<1%
23	"Industrial Plasma Technology", Wiley, 2010 Publication	<1%
24	www.researchgate.net Internet Source	<1%
25	stars.library.ucf.edu Internet Source	<1%
26	Rajendhar Junjuri, Manoj Kumar Gundawar. "Femtosecond laser-induced breakdown spectroscopy studies for the identification of plastics", Journal of Analytical Atomic Spectrometry, 2019 Publication	<1%
27	eprints.utm.my Internet Source	<1%
28	"Laser-Induced Breakdown Spectroscopy", Springer Nature, 2014 Publication	<1%
29	Akash Kumar Tarai, Rajendhar Junjuri, Akshay Dhobley, Manoj Kumar Gundawar. "Classification of human tooth using laser-induced breakdown spectroscopy combined	<1%

with machine learning", Journal of Optics, 2023
Publication

30	Senesi, Giorgio S.. "Laser-Induced Breakdown Spectroscopy (LIBS) applied to terrestrial and extraterrestrial analogue geomaterials with emphasis to minerals and rocks", Earth-Science Reviews, 2014. Publication	<1 %
31	M. Achouri, T. Baba-Hamed, S. A. Beldjilali, A. Belasri. "Determination of a brass alloy concentration composition using calibration-free laser-induced breakdown spectroscopy", Plasma Physics Reports, 2015 Publication	<1 %
32	edoc.ub.uni-muenchen.de Internet Source	<1 %
33	fastercapital.com Internet Source	<1 %
34	Submitted to Higher Education Commission Pakistan Student Paper	<1 %
35	Submitted to Queen's University of Belfast Student Paper	<1 %
36	Girma Moges, Kevin McDonnell, Mulugeta Admasu Delele, Addisu Negash Ali, Solomon Workneh Fanta. "Development and	<1 %

comparative analysis of ANN and SVR-based models with conventional regression models for predicting spray drift", Environmental Science and Pollution Research, 2022
Publication

---

37 Qiang Zeng, Jean-Baptiste Sirven, Jean-Christophe P. Gabriel, Chor Yong Tay, Jong-Min Lee. "Laser induced breakdown spectroscopy for plastic analysis", TrAC Trends in Analytical Chemistry, 2021 <1%
Publication

---

38 Rikizo Hatakeyama. "Nanocarbon materials fabricated using plasmas", Reviews of Modern Plasma Physics, 2017 <1%
Publication

---

39 studyres.com <1%
Internet Source

---

40 N. Mavrikakis, C. Detlefs, P.K. Cook, M. Kutsal et al. "A multi-scale study of the interaction of Sn solutes with dislocations during static recovery in α-Fe", Acta Materialia, 2019 <1%
Publication

---

41 N. Mavrikakis, W. Saikaly, P.R. Calvillo, A.P.C. Campos, S. Jacomet, N. Bozzolo, D. Mangelinck, M. Dumont. "How Sn addition influences texture development in single-phase Fe alloys: Correlation between local chemical information, microstructure and <1%

recrystallisation", Materials Characterization, 2022
Publication

42	Stefanie Kern, Christine Kern, Marcus Rohnke. "Mass spectra database of polymers for bismuth-cluster ToF-SIMS", Surface Science Spectra, 2019 Publication	<1 %
43	C. A. Murthy. "Bridging Feature Selection and Extraction: Compound Feature Generation", IEEE Transactions on Knowledge and Data Engineering, 2017 Publication	<1 %
44	addi.ehu.es Internet Source	<1 %
45	Eshita Mal, Rajendhar Junjuri, Manoj Kumar Gundawar, Alika Khare. "Spatial characterization of ns-laser induced Tungsten plasma in air using laser induced breakdown spectroscopy", Fusion Engineering and Design, 2021 Publication	<1 %
46	www.diva-portal.se Internet Source	<1 %
47	"Laser Ablation and its Applications", Springer Science and Business Media LLC, 2007 Publication	<1 %

48	cyberleninka.org Internet Source	<1 %
49	Harse Sattar, Zhenlin Hu, Wen Zheng, Jiayuan Zhou, Muhammad Khuram Shahzad, Fahad Rehman, Lianbo Guo, Wei Luo. "Exploring the potential and recent advancement in laser Opto-ultrasonic detection for material characterization: A state-of-the-art review", Optics & Laser Technology, 2024 Publication	<1 %
50	Richard E. Russo, X.L. Mao, J. Yoo, J.J. Gonzalez. "Laser ablation", Elsevier BV, 2007 Publication	<1 %
51	Submitted to University of Ulster Student Paper	<1 %
52	ijiset.com Internet Source	<1 %
53	Jian Yang, Yu-Peng Xu, Pu Chen, Jing-Yan Li, Dan Liu, Xiao-Li Chu. "Combining spectroscopy and machine learning for rapid identification of plastic waste: Recent developments and future prospects", Journal of Cleaner Production, 2023 Publication	<1 %
54	Jiankui Gao, Juan Kang, Runhua Li, Yuqi Chen. "Application of calibration-free high repetition rate laser-ablation spark-induced breakdown	<1 %

spectroscopy for the quantitative elemental analysis of a silver alloy", Applied Optics, 2020
Publication

55	M.A. Wahab. "Symmetry Representations of Molecular Vibrations", Springer Science and Business Media LLC, 2022 Publication	<1 %
56	Submitted to University of Canberra Student Paper	<1 %
57	Andrew R. Webb. "Statistical Pattern Recognition", Wiley, 2002 Publication	<1 %
58	wrap.warwick.ac.uk Internet Source	<1 %
59	Narahara Chari Dingari, Ishan Barman, Ashwin Kumar Myakalwar, Surya P. Tewari, Manoj Kumar Gundawar. "Incorporation of Support Vector Machines in the LIBS Toolbox for Sensitive and Robust Classification Amidst Unexpected Sample and System Variability", Analytical Chemistry, 2012 Publication	<1 %
60	T.U. Rahman, Z.U. Rehman, S. Ullah, H. Qayyum, B. Shafique, R. Ali, U. Liaqat, A.H. Dogar, A. Qayyum. "Laser-induced plasma-assisted ablation (LIPAA) of glass: Effects of the laser fluence on plasma parameters and	<1 %

crater morphology", Optics & Laser Technology, 2019
Publication

61	Juan Kang, Yuqi Chen, Runhua Li. "Calibration-free elemental analysis combined with high repetition rate laser-ablation spark-induced breakdown spectroscopy", Spectrochimica Acta Part B: Atomic Spectroscopy, 2019 Publication	<1 %
62	Qi Shi, Huihui Zhao, Jianxin Chen, Youlin Li, Zhongfeng Li, Juan Wang, Wei Wang. "Study on Qi Deficiency Syndrome Identification Modes of Coronary Heart Disease Based on Metabolomic Biomarkers", 'Hindawi Limited', 2014 Internet Source	<1 %
63	Snigdha Agrawal, Ramesh Kumar Agrawal, S. Senthil Kumaran, Achal Kumar Srivastava, Manpreet Kaur Narang. "Fusion of 3D feature extraction techniques to enhance classification of spinocerebellar ataxia type 12", International Journal of Information Technology, 2023 Publication	<1 %
64	hdl.handle.net Internet Source	<1 %
65	link.springer.com Internet Source	<1 %

66	Adolf Giesen. "Thin Disk Lasers – Power scalability and beam quality", Laser Technik Journal, 2005 Publication	<1 %
67	Richard J. Morris. "Statistical pattern recognition for macromolecular crystallographers", Acta Crystallographica Section D Biological Crystallography, 2004 Publication	<1 %
68	eeer.org Internet Source	<1 %
69	Ali Safi, S. Hassan Tavassoli, Gabriele Cristoforetti, Stefano Legnaioli et al. "Determination of Excitation Temperature in Laser-Induced Plasmas Using Columnar Density Saha-Boltzmann Plot", Journal of Advanced Research, 2019 Publication	<1 %
70	Submitted to Texas Christian University Student Paper	<1 %
71	research.usq.edu.au Internet Source	<1 %
72	worldwidescience.org Internet Source	<1 %
73	"Laser-Induced Breakdown Spectroscopy in Biological, Forensic and Materials Sciences",	<1 %

	Springer Science and Business Media LLC, 2022 Publication	
74	Giovanna Bitossi, Rodorico Giorgi, Marcello Mauro, Barbara Salvadori, Luigi Dei. "Spectroscopic Techniques in Cultural Heritage Conservation: A Survey", Applied Spectroscopy Reviews, 2005 Publication	<1 %
75	Submitted to Indian Institute of Technology Guwahati Student Paper	<1 %
76	Rajendhar Junjuri, Arun Prakash Gummadi, Manoj Kumar Gundawar. "Single-shot compact spectrometer based standoff LIBS configuration for explosive detection using artificial neural networks", Optik, 2020 Publication	<1 %
77	Selke, Susan. "Food Packaging : Plastics", Food Science and Technology, 2005. Publication	<1 %
78	e-space.mmu.ac.uk Internet Source	<1 %
79	thesis.library.caltech.edu Internet Source	<1 %
80	"Proceedings of Eighth International Congress on Information and Communication	<1 %

Technology", Springer Science and Business Media LLC, 2024
Publication

---

81 Francesco Poggialini, Beatrice Campanella, Bruno Cocciaro, Giulia Lorenzetti, Vincenzo Palleschi, Stefano Legnaioli. "Catching up on Calibration-Free LIBS", Journal of Analytical Atomic Spectrometry, 2023
Publication

<1 %

---

82 Mohammad Siddiqui. "Identification of different type of polymers in plastics waste", Journal of Environmental Science and Health Part A, 09/2008
Publication

<1 %

---

83 Rochman, Chelsea M., Eunha Hoh, Brian T. Hentschel, and Shawn Kaye. "Long-Term Field Measurement of Sorption of Organic Contaminants to Five Types of Plastic Pellets: Implications for Plastic Marine Debris", Environmental Science & Technology, 2013.
Publication

<1 %

---

84 Tesfaye F. Bedane, Long Chen, Francesco Marra, Shaojin Wang. "Experimental study of radio frequency (RF) thawing of foods with movement on conveyor belt", Journal of Food Engineering, 2017
Publication

<1 %

---

85 Submitted to University of Florida

	Student Paper	<1%
86	digitalarchive.boun.edu.tr Internet Source	<1%
87	escholarship.org Internet Source	<1%
88	etd.uwc.ac.za Internet Source	<1%
89	libjncir.jncasr.ac.in Internet Source	<1%
90	uir.unisa.ac.za Internet Source	<1%
91	Dheerendra Yadav, Raj K. Thareja. "Laser ablated zirconium plasma: A source of neutral zirconium", Physics of Plasmas, 2010 Publication	<1%
92	Hengcong Zhang, Jianmin Wu, Yin Luo, Zhong Qin. "High temperature properties of composite modified light-colored synthetic asphalt binders", Materials Research Express, 2021 Publication	<1%
93	Ton Duc Thang University Publication	<1%

94	Yaroshchyk, P.. "A semi-quantitative standard-less analysis method for laser-induced breakdown spectroscopy", Spectrochimica Acta Part B: Atomic Spectroscopy, 200602 Publication	<1 %
95	archive.org Internet Source	<1 %
96	cpb-us-w2.wpmucdn.com Internet Source	<1 %
97	oak.ulsan.ac.kr Internet Source	<1 %
98	www.demagoprint.eu Internet Source	<1 %
99	www.jameco.com Internet Source	<1 %
100	Ali Kassab, Dawood Al Nabhani, Pravansu Mohanty, Christopher Pannier, Georges Y. Ayoub. "Advancing Plastic Recycling: Challenges and Opportunities in the Integration of 3D Printing and Distributed Recycling for a Circular Economy", Polymers, 2023 Publication	<1 %
101	Submitted to Cranfield University Student Paper	<1 %

Lecture Notes in Computer Science, 2006.

102	Publication	<1 %
103	O. Peleg. "Parameters of the plasma produced at the surface of a ferroelectric cathode by different driving pulses", Journal of Applied Physics, 2005 Publication	<1 %
104	Z. Zakaria, S. K. Kamarudin. "Performance of quaternized poly(vinyl alcohol)-based electrolyte membrane in passive alkaline DEFCs application: RSM optimization approach", Journal of Applied Polymer Science, 2019 Publication	<1 %
105	tesis.pucp.edu.pe Internet Source	<1 %
106	www.applied-science-innovations.com Internet Source	<1 %

Exclude quotes	On	Exclude matches	< 14 words
Exclude bibliography	On		